

A Shock Tube Study of NCN and HCO Radical Reactions Related to the NO_x Formation in Combustion Processes

Dissertation zur Erlangung des Doktorgrades der
Mathematisch-Naturwissenschaftlichen Fakultät der
Christian-Albrechts-Universität zu Kiel

vorgelegt von Johannes Dammeier
aus Köln

Institut für Physikalische Chemie
der Christian-Albrechts-Universität zu Kiel
Kiel, 2011

Referent: Prof. Dr. Gernot Friedrichs
Korreferent: Prof. Dr. Friedrich Temps

Tag der mündlichen Prüfung: 01.12.2011
Zum Druck genehmigt: 01.12.2011

gez. Prof. Dr. Lutz Kipp

Im Kleinen geschieht das
Wachsen, Gelten und Fallen von
Theorien tagtäglich, und was
heute wertvolle Erkenntnis ist, ist
morgen schon Plunder, kaum
eines historischen Rückblickes
wert.

(Max Born)

Abstract

The rate constants of seven elementary reactions associated with the formation of nitrogen oxides have been directly measured at combustion relevant temperatures behind shock waves. Nitrogen oxides (NO and NO₂, together: NO_x) are main pollutants of combustion processes. One of several pathways yielding NO_x involves the cyanonitrene (NCN) radicals as a key intermediate. In order to optimise mechanistic models of NO_x formation, the rate constants of the investigated NCN reactions $\text{NCN} + \text{M} \rightarrow \text{C} + \text{N}_2 + \text{M}$, $\text{NCN} + \text{NCN} \rightarrow 2 \text{CN} + \text{N}_2$, $\text{NCN} + \text{O} \rightarrow \text{CN} + \text{NO}$, $\text{NCN} + \text{NO} \rightarrow \text{CN} + \text{N}_2\text{O}$ and $\text{NCN} + \text{NO}_2 \rightarrow \text{NCNO} + \text{NO}$ have to be accurately known. Despite the importance of the high temperature chemistry of NCN, apart from the reaction $\text{NCN} + \text{M}$, none of these rate constants had been measured at combustion relevant temperatures, before. NCN was sensitively and quantitatively detected in its triplet ground state and in its first electronically excited singlet state by a new difference amplification laser absorption set-up. As a prerequisite of the NCN measurements, the suitability of cyanogen azide (NCN₃) as an NCN precursor has been thoroughly investigated. It could be proved that a direct synthesis of the explosive NCN₃ in high purities > 99% is possible. Rate constants of the thermal decomposition of NCN₃, $\text{NCN}_3 + \text{M} \rightarrow \text{NCN} + \text{N}_2 + \text{M}$, have been determined and it turned out that this unimolecular reaction serves as an almost ideal source of stable NCN plateau concentrations. Actually, the precursor initially yields NCN in its excited electronic singlet ¹NCN state, which is subsequently deactivated to the combustion relevant triplet ³NCN ground state by a collision-induced intersystem crossing (CIISC) process. Surprisingly low CIISC rate constants have been extracted from experiments involving the detection of NCN in both electronic states. These measurements constitute the first quantitative investigation of a CIISC process behind shock waves. Finally, for the quantitative detection of NCN, high temperature spectra of ¹NCN and ³NCN have been measured and temperature dependent absolute narrow-bandwidth absorption cross-sections have been derived for the first time for both species. Next to NCN chemistry, the high temperature kinetics of the reactions of NO and NO₂ with the formyl radical $\text{HCO} + \text{NO} \rightarrow \text{HNO} + \text{CO}$ and $\text{HCO} + \text{NO}_2 \rightarrow \text{products}$ have been measured for the first time, as well. In the case of the reaction $\text{HCO} + \text{NO}_2$ product branching ratios have been determined by detailed simulations of HCO concentration-time profiles. The relevance of HCO reactions stems from the fact that HCO lies on the main oxidation pathway of hydrocarbons and thus is a very important species in combustion systems.

Kurzzusammenfassung

Die Geschwindigkeitskonstanten von sieben für die Stickoxidbildung wichtigen Reaktionen wurden bei verbrennungsrelevanten Temperaturen hinter Stoßwellen direkt gemessen. Die Stickoxide (NO und NO₂, zusammen: NO_x) gehören zu den wichtigsten luftverschmutzenden Stoffen, die bei Verbrennungsprozessen entstehen. Unter anderem werden sie in einem Reaktionszyklus gebildet, der als entscheidendes Zwischenprodukt Cyanonitren beinhaltet. Um die NO_x-Bildung über diesen Reaktionsweg modellieren zu können, wurden in dieser Arbeit die Geschwindigkeitskonstanten der Reaktionen $\text{NCN} + \text{M} \rightarrow \text{C} + \text{N}_2 + \text{M}$, $\text{NCN} + \text{NCN} \rightarrow 2 \text{CN} + \text{N}_2$, $\text{NCN} + \text{O} \rightarrow \text{CN} + \text{NO}$, $\text{NCN} + \text{NO} \rightarrow \text{CN} + \text{N}_2\text{O}$ und $\text{NCN} + \text{NO}_2 \rightarrow \text{NCNO} + \text{NO}$ untersucht. Mit Ausnahme der Reaktion $\text{NCN} + \text{M}$, sind zuvor für keine dieser Reaktionen Geschwindigkeitskonstanten bei verbrennungsrelevanten Temperaturen experimentell bestimmt worden. Für den empfindlichen Nachweis von NCN-Radikalen wurde ein neues Differenzlaserabsorptionsspektrometer aufgebaut und es wurde zunächst detailliert untersucht, ob Cyanazid (NCN₃) als NCN-Quelle geeignet ist. Dazu wurden Geschwindigkeitskonstanten des thermischen Zerfalls von NCN₃, $\text{NCN}_3 + \text{M} \rightarrow \text{NCN} + \text{N}_2 + \text{M}$, gemessen. Es zeigte sich, dass dieser unimolekulare Zerfall eine nahezu perfekte NCN-Radikalquelle darstellt, da im Experiment stabile NCN-Plateaukonzentrationen eingestellt werden konnten. Wichtig war es außerdem, einen Syntheseweg zu finden, über den das explosive NCN₃ direkt und in hoher Reinheit (> 99%) sicher hergestellt werden konnte. Der Zerfall des Vorläufermoleküls bildet NCN zunächst im elektronisch angeregten Singulettzustand, der nachfolgend durch stoßinduziertes Intersystem Crossing (CIISC) zum Triplett-Grundzustand relaxiert. Durch den Nachweis sowohl von ¹NCN als auch von ³NCN gelang es, Geschwindigkeitskonstanten für den überraschend langsamen CIISC-Prozess zu erhalten. In diesen Messungen wurde einerseits ¹NCN erstmals bei hohen Temperaturen nachgewiesen und andererseits erstmals ein CIISC-Prozess quantitativ hinter Stoßwellen untersucht. Um die quantitative Messung von NCN-Konzentrationen zu ermöglichen, wurden zunächst Hochtemperaturspektren und temperaturabhängige absolute Absorptionsquerschnitte von ¹NCN und ³NCN bestimmt. Ergänzend zu den NCN-Untersuchungen wurde zudem die Hochtemperaturkinetik zweier Stickoxidreaktionen mit dem Formylradikal, $\text{HCO} + \text{NO} \rightarrow \text{HNO} + \text{CO}$ und $\text{HCO} + \text{NO}_2 \rightarrow \text{Produkte}$, untersucht. Dabei konnten nicht nur die Geschwindigkeitskonstanten beider Reaktionen direkt aus HCO Konzentrations-Zeit-Profilen gewonnen werden, sondern auch das Kanalverzweigungsverhältnis der Reaktion $\text{HCO} + \text{NO}_2$ aufgeklärt werden. Reaktionen des Formylradikals sind von entscheidender Bedeutung, da HCO auf dem Hauptoxidationsweg von Kohlenwasserstoffen liegt und deshalb eine der wichtigsten Intermediate in Verbrennungsprozessen darstellt.

Contents

1	Introduction	1
1.1	The significance of combustion as an energy source	1
1.2	Nitrogen oxides (NO_x) as pollutants	3
1.3	Pathways to NO_x in combustion processes	5
1.4	High temperature NCN chemistry	7
1.5	High temperature HCO chemistry	9
1.6	Scope of this work	10
2	Experimental	17
2.1	The shock tube method	17
2.1.1	Theory of shock wave propagation	18
2.1.2	The Kiel shock tube	21
2.1.3	The test gas mixing system	23
2.2	Spectroscopic methods	24
2.2.1	The difference laser absorption setup	24
2.2.2	The Frequency Modulation (FM) setup	27
2.3	Numerical methods	28
2.3.1	Data reduction	28
2.3.2	Quantum mechanical and statistical methods	29
2.4	Precursors	31
2.4.1	Cyanogen azide (NCN_3) synthesis	31
2.4.2	FTIR analysis	32
2.4.3	Glyoxal ($(\text{CHO})_2$) preparation	35
2.5	Supplement: Program for the calculation of $\langle \Delta E \rangle_{\text{all}}$ and $\langle \Delta E \rangle_{\text{down}}$	39
3	The Thermal Decomposition of NCN_3 as a High Temperature NCN Radical Source: Singlet-Triplet Relaxation and Absorption Cross Section of $\text{NCN}(^3\Sigma)$	43
3.1	Introduction	44
3.2	Experimental	46
3.3	Results and discussion	49
3.3.1	Room temperature photolysis	49
3.3.2	High temperature absorption cross section	51

3.3.3	Singlet-triplet relaxation and unimolecular decomposition of NCN_3	56
3.4	Conclusion	60
4	A Consistent Model for the Thermal Decomposition of NCN_3 and the Singlet-Triplet Relaxation of NCN	67
4.1	Introduction	68
4.2	Experimental	71
4.3	Results and discussion	72
4.3.1	Room temperature measurements	72
4.3.2	High temperature measurements	78
4.4	Conclusion	85
4.5	Supporting information	90
5	Direct Measurements of the High Temperature Rate Constants of the Reactions $\text{NCN} + \text{O}$, $\text{NCN} + \text{NCN}$, and $\text{NCN} + \text{M}$	95
5.1	Introduction	96
5.2	Experimental section	99
5.3	Results and discussion	101
5.3.1	NCN mechanism	101
5.3.2	The reaction $\text{NCN} + \text{O}$	107
5.4	Conclusion	111
5.5	Supporting information	117
6	Direct Measurements of the Rate Constants of the Reactions $\text{NCN} + \text{NO}$ and $\text{NCN} + \text{NO}_2$ Behind Shock Waves	119
6.1	Introduction	120
6.2	Experimental	123
6.3	Results and discussion	125
6.3.1	$\text{NCN} + \text{NO}$	125
6.3.2	$\text{NCN} + \text{NO}_2$	130
6.4	Conclusion	137
6.5	Supporting information	142
7	Wide Temperature Range ($T = 295 \text{ K}$ and $770\text{-}1305 \text{ K}$) Study of the Kinetics of the Reactions $\text{HCO} + \text{NO}$ and $\text{HCO} + \text{NO}_2$ using Frequency Modulation Spectroscopy	145
7.1	Introduction	146
7.2	Experimental section	148
7.2.1	Shock tube and slow flow reactor	148
7.2.2	Gas mixtures	149

7.2.3	Quantitative detection of HCO radicals	149
7.3	Glyoxal photolysis	150
7.4	The reaction HCO + NO	152
7.4.1	Room temperature measurements	152
7.4.2	High temperature measurements	155
7.4.3	Discussion	156
7.5	The reaction HCO + NO ₂	160
7.5.1	Product branching ratios	161
7.5.2	Room temperature measurements	165
7.5.3	High temperature measurements	167
7.5.4	Discussion	170
7.6	Conclusion	171
7.7	Supporting information	178
8	Summary and outlook	183

1 Introduction

1.1 The significance of combustion as an energy source

In a world relying on easily accessible energy, combustion processes do not cease to be the by far most important source of heat and electrical as well as mechanical power. Figure 1.1 shows the sources of primary energy used in the world (left) and in Germany (right). In the graph, energy sources based on combustion are shown as grey areas. The most important combustible is oil, which is used for heating as well as to power engines in the transport sector and for the generation of electrical power. Gas is also used for heating and electrical power production. In Germany, coal is almost exclusively used to fuel power plants, whereas it is still widely used for heating in other parts of the world. The combustion of renewable resources (e.g., wood, waste or plant oil), according to international treaties, is supposed to reduce Germany's green house gas emissions. In large parts of the world, however, plants are burned in simple open fires with very low efficiency. "Other" sources (B8 in the right graph) mainly comprise industrial waste heat. It is obvious that the non-combustion sources, perhaps except for nuclear power, contribute only slightly to the statistics. The reason for this dominating role of combustion as a means of making energy available lies in the fact that most combustibles are relatively easy to transport, to use, versatile and offer a high density of chemical energy that can easily be released. On the downside, combustion processes are accompanied by a range of undesired secondary effects. (i) As far as fossil combustibles are concerned, their resources

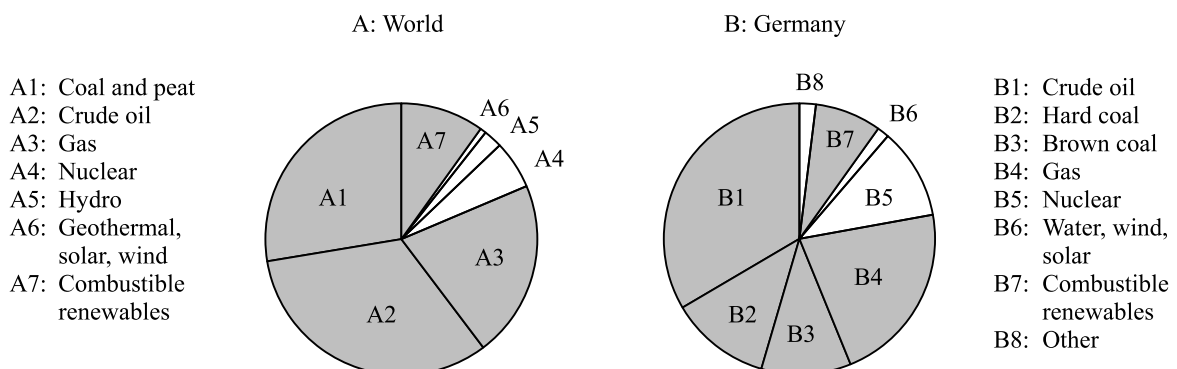


Figure 1.1: Significance of primary energy sources in the world (left, 2008)¹ and in Germany (right, 2010).² Grey: Combustion as energy source.

are limited. (ii) Combustion processes themselves produce pollutants, which have a negative influence on our environment. The most important of these pollutants are carbon dioxide (CO_2), which is a cause of global warming;³ soot and polycyclic aromatic hydrocarbons (PAH), which are a hazard to human health especially in our cities;^{4,5} sulfates (SO_2), which cause acid rain;⁴⁻⁷ and nitrogen oxides (NO_x) with several negative consequences, which will be discussed in more detail, below.

Therefore, efforts are undertaken to strengthen the role of alternative energy sources. Nuclear power, however, though having a quite large margin in the generation of energy (see Figure 1.1) comes with the disadvantages of a risk of a nuclear catastrophe and the production of dangerous waste. For these reasons, it is not predicted to contribute more than 10% to the total primary energy in the year 2030 (2008: 6%),¹ whereas the combustion of fossil fuels is still supposed to account for three quarters of the total energy production, then.

As a potential way to reduce the greenhouse gas emissions, renewable energies are supposed to play a major role. As it is obvious from Figure 1.1, most of the renewable energy is produced by the combustion of either biomass or waste, which are subsumed under the term “combustible renewables” in the graph. Predictions of the composition of renewables in the year 2050, when Germany is supposed to cover 50% of its requirement of energy from renewable sources, show that the combustion of biomass may have a share of approximately 70% of the renewables.⁸ Whereas biomass as a fuel may indeed contribute to the conservation of resources and perhaps even help with the reduction of carbon dioxide emissions, its combustion continues to lead to the production of pollutants. Altogether, despite all efforts to find new energy sources, the dominating role of combustion is neither in well-developed countries like Germany nor in the world as a whole going to be diminished, soon. Along these lines, combustion research must find ways to reduce the negative consequences connected with combustion processes.

Combustion science covers a great variety of topics from the construction of large industrial facilities to elementary kinetics of small molecules. Therefore, different disciplines including physics, chemistry and engineering are involved in this interdisciplinary research field. Scientists of the different subjects must work hand in hand in order to optimise combustion processes and facilities. For example, engineers use simulations of combustion processes to gain knowledge of temperature, pressure and the concentration of different species at a certain point in a reaction sequence. In this way, strategies to suppress pollutant forming reactions by controlling the reaction conditions can be developed.

Simulation of the ensuing complex reaction sequences of the combustion of even small combustibles like methane (CH_4), or ethane (C_2H_6) requires a detailed understanding of the many elementary steps of the reaction sequence. Hence, measurements of the rate constants of these reactions, of which the most important are the reactions of small (i.e., 2 – 3 atoms) radicals⁹ have to be performed. In this spirit, this thesis will be concerned with the investigation of different elementary reactions associated with the formation of nitrogen oxides (NO_x).

1.2 Nitrogen oxides (NO_x) as pollutants

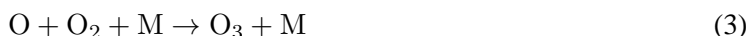
Nitric oxide (NO) and nitrogen dioxide (NO₂) (together termed NO_x) are main pollutants of combustion processes.^{4,5,10,11} Their relevance stems from the fact that they can damage the environment in several ways.

(i) Acid rain arises from HNO₃ dissolved in H₂O droplets. Several pathways lead from NO₂ to HNO₃, the most important is

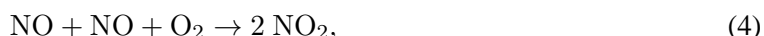


HNO₃ is then washed out of the air and acidifies the ground.

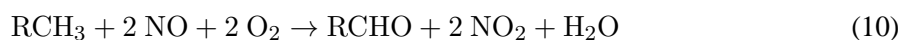
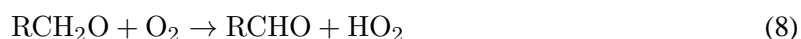
(ii) Photochemical smog is defined as an oxidising form of air pollution, which causes breathing problems, eye irritation, plant damage and a degradation of sight. The oxidising properties are caused by pollutants of which the most important are ozone (O₃), NO₂ and peroxyacetyl nitrate (CH₃COO₂NO₂, PAN). Nitrogen oxides are involved in all known tropospheric ozone forming processes. A prerequisite of photochemical smog is the irradiation of mixtures of hydrocarbons and NO_x by solar light. Then, ozone is produced by the reaction sequence



The regeneration of nitrogen dioxide by the reaction



alone is not sufficient to account for the high NO₂ levels observed during high ozone episodes in polluted air. Instead, NO₂ is generated by a reaction sequence following the attack of OH on a hydrocarbon yielding peroxy radicals as intermediates, as well:

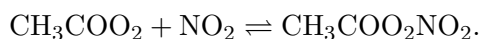


This reaction sequence explains why smog is mainly observed in the polluted areas of big cities, where

next to NO_x many hydrocarbon pollutants are available. In principle, the reaction



also produces NO_2 , but simultaneously removes ozone on such that is in not able to raise ozone levels. PAN is present in the equilibrium



Towards lower temperatures, this equilibrium is shifted to the right-hand side such that it is a means of transferring NO_x from cooler to warmer regions.

(iii) In the stratosphere, in contrast to its role in the troposphere, NO_x contributes to the destruction of the ozone layer. Responsible are the two reaction cycles



and



(iv) Finally, N_2O , a secondary product of NO_x is an effective green house gas and thus worsens the problem of global warming. It has a 300 times higher global warming potential than CO_2 .³ Besides being produced from nitrogen containing biomass fuels, it can be generated in combustion processes by the reaction of amino radicals (NH_2) with NO_2 ¹²



Amino radicals stem from ammonia (NH_3) or other NH_2 sources such as urea, which are often added in combustion processes to reduce NO_x according to the reaction



The production of N_2O through reaction 18 is one of several disadvantages of these methods of reducing NO_x emissions and leads to significant N_2O emissions.¹³

1.3 Pathways to NO_x in combustion processes

Four main pathways leading to the production of nitrogen oxides in combustion processes are known.^{6,7,9,14} (i) Especially in not too rich mixtures with fuel-air equivalent ratios $\phi < 1.3$, nitrogen contents in the combustibles can be oxidised to form NO and NO₂ by a reaction sequence according to¹⁵



This *Fuel-N-conversion* is of particular interest in the combustion of coal, since coal contains large amounts (> 1%) of nitrogen.

(ii) *Thermal-NO* can be formed from molecular nitrogen and oxygen contained in the combustion air according to the Zeldovich mechanism:^{16,17}



Since reaction 20 exhibits a high activation barrier due to the stable N-N bond, very high temperatures are needed to overcome this barrier and initiate the reaction sequence.

(iii) Furthermore, NO can be generated via N₂O with the help of a stabilising collision partner M:^{18,19}



This reaction becomes important at lower temperatures and leaner conditions. Of course, high pressures promote this reaction sequence due to the recombination step (23).

(iv) Finally, in the *Fenimore mechanism* so called *prompt* NO is formed from the attack of small hydrocarbon radicals on N₂ stemming from the combustion air. According to Fenimore,²⁰ the spin-forbidden reaction 25,



is the initiating step of the reaction sequence. However, the intersystem crossing (ISC) probability from the doublet to the quartet potential energy surface is low and thus theoretically predicted rate constants are lower than experimentally measured.^{6,21} In the year 2000, Moskaleva and Lin^{22,23} shed new light on the Fenimore mechanism by introducing the spin-allowed reaction 26,



The feasibility of this reaction was predicted based on quantum chemical exploration of the potential

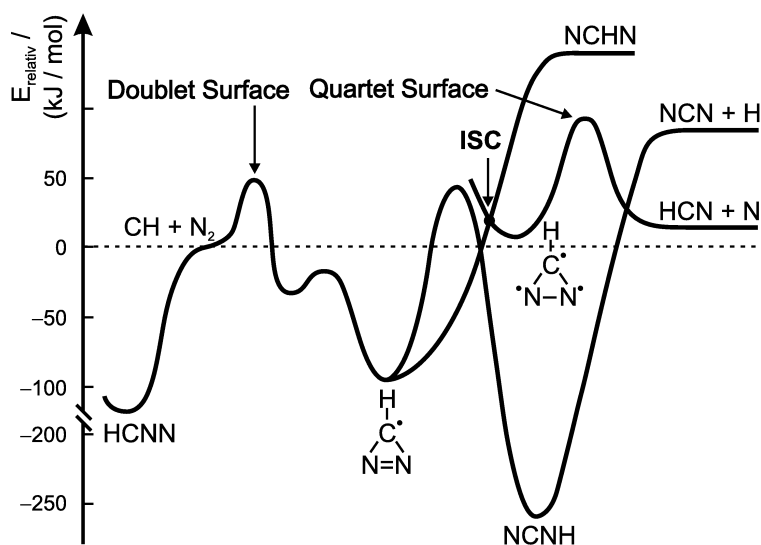


Figure 1.2: CH + N₂ potential energy surface as calculated by Moskaleva and Lin.²²

energy surface (PES) and subsequent RRKM calculations and master equation modelling. A scheme of the PES is shown in figure 1.2. It is discernible that NCN + H, although thermodynamically less stable than HCN + N, are accessible over a somewhat lower threshold than the products of reaction 25. Moreover, in the light of the required spin-forbidden ISC process for reaction 25, reaction 26 can be assumed to be the main reaction channel. In the scheme, ISC denotes the intersystem crossing point between the doublet surface (containing CH + N₂ as well as NCN + H) and the quartet surface (comprising HCN + N). Whereas the low ISC probability in forward direction limits the accessibility of this channel, according to Moskaleva and Lin, the intersystem crossing probability is 1 for the backward reaction. This is due to the fact that in contrast to the reactants, the energy of the molecules entering the system from the product side is significantly higher than the energy of the ISC point. Therefore, HCN + N are likely products of the back reaction. However, both the branching ratio and the total rate constant of the reaction NCN + H (28) is subject to ongoing discussions.^{22,24,25}

Besides studies dating from the years 2007 and 2008, which clearly showed that measured NCN concentrations in flames are correlated to CH concentrations,^{26–28} it was a shock tube study²⁴ that ultimately proved that the branching fraction of reaction 26 is indeed > 70%. By now, the reaction CH + N₂ is commonly accepted to yield more or less quantitatively NCN + H. Of course, changing the products of this textbook reaction from HCN + N to NCN + H brought the properties and reactions of the cyonitrene radical (NCN) into the focus of attention of combustion research. Before the identification of reaction 26 as a key reaction in the *prompt* NO formation, NCN high temperature chemistry had been completely unknown. Even at room temperature, apart from a few spectroscopic studies,^{29–37} NCN properties and reactions had not been investigated.

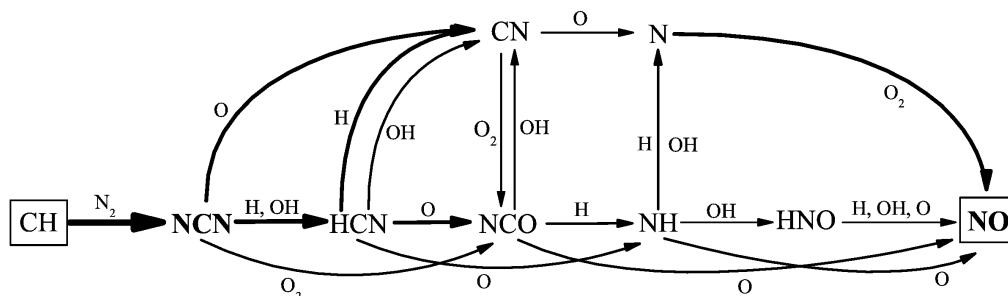


Figure 1.3: Reaction pathway of the NCN oxidation taken from Lamoureux *et al.*⁴²

1.4 High temperature NCN chemistry

Having introduced NCN as a reaction product of the initiating step of the prompt NO formation mechanism, several attempts have been made to adjust widely used reaction mechanisms, accordingly. In the year 2006, El Bakali *et al.*³⁸ introduced reaction 26 into the GDF-Kin 3.0 mechanism. To account for high temperature NCN chemistry, they used an estimated set of NCN reaction rate constants as proposed by Glarborg *et al.*¹⁵ several years before. Despite the fact that the used rate constants were not accurately known, the introduction of reaction 26 still lead to much better results regarding NO and CH concentrations measured in low pressure methane, ethane and propane - O₂/N₂ flames. Similarly, Gersen *et al.* measured HCN profiles of methane - air flames and corrected the GRI-Mech. 3.0³⁹ for reaction 26. They also succeeded in optimising the agreement between simulations and their experiments. The GRI-Mech is a commonly accepted mechanism consisting of 325 reactions, of which rate constants have been optimised to model natural gas combustion.

Already in the year 2000, Moskaleva and Lin²² proposed a rather extensive set of NCN reaction rate constants, which were calculated by Rice-Ramsperger-Kassel-Marcus (RRKM) theory combined with master equation (ME) modelling. Input parameters were based on quantum chemical (QM) calculations. In 2008, in a comparative study, Sutton *et al.*^{27,40} used this set of rate constants as well as the estimated values of Glarborg *et al.* to model NCN and NO concentrations measured in methane/N₂-O₂ flames. They found much better agreement between measured and simulated NO and NCN profiles when using the parameters from Moskaleva and Lin instead of the estimation Glarborg recommended. In 2009 and 2010, thorough analyses of the NCN reaction system were performed by Konnov⁴¹ and Lamoureux *et al.*⁴² Both used Moskaleva and Lin's set of rate constants and came up with similar results on the sensitivity of modelled NCN and NO concentrations with regard to the different NCN reactions. The updated pathways leading from CH + N₂ to NO are sketched in the reaction flow diagram shown in figure 1.3. Sensitivity analyses reveal that the reactions NCN + O

(27), $\text{NCN} + \text{H}$ (28), $\text{NCN} + \text{O}_2$ (29) and $\text{NCN} + \text{OH}$ (30) are the most important ones. Overall, a trend towards higher sensitivities of the oxygen containing reactions with larger combustibles and leaner (stoichiometric) mixtures has been reported. As it is discernible in the scheme, the reactions of NCN with H (28) and OH (30) yield HCN , which had formally been believed to be the product of the reaction $\text{CH} + \text{N}_2$ (26). HCN is then oxidised to form HCN , NCO , NH , HNO , and finally NO . Overall, this part of the scheme is identical to the outdated reaction pathway. However, a different pathway exists: The reaction $\text{NCN} + \text{O}$ (27) generates $\text{CN} + \text{NO}$. CN is further oxidised and also forms NO via N atoms. Thus, taking into account this new route, overall NO yields are higher compared to the older models. It depends on the reaction conditions (temperature, pressure, fuel - air ratio, nature of the fuel), which of the two pathways is more important.

Even with the new mechanism at hand, the interpretation of NCN measurements in flames is still complicated due to the fact that no reliable high temperature absorption cross section data for NCN are available in the literature. So far, only indirectly determined values by Vasudevan *et al.*²⁴ and spectral simulations by Lamoureux *et al.*⁴³ provide a rough estimate of its absorption cross section.

To further improve the reaction mechanisms, direct measurements of NCN reaction rate constants at combustion relevant temperatures of $T \gtrsim 1000$ K are desirable. At the outset of this work, only reaction 28, $\text{NCN} + \text{H}$, had been investigated by Vasudevan *et al.* behind shock waves. Later, the unimolecular decomposition of NCN , $\text{NCN} + \text{M}$ was addressed by Busch⁴⁴⁻⁴⁶ using the shock tube technique, as well. Some additional experimental investigations are available for lower temperatures. All other high temperature rate constant data of NCN reactions still rely on theoretical work, alone. Details of these studies will be given in the later sections of this work. Most of the studies have been performed by the M.-C. Lin group addressing the reactions $\text{NCN} + \text{O} \rightarrow \text{CN} + \text{NO}$ (27),⁴⁷ $\text{NCN} + \text{H} \rightarrow \text{HCN} + \text{N}$ (28),²² $\text{NCN} + \text{O}_2 \rightarrow \text{NCO} + \text{NO}$ (29)⁴⁸ and $\text{NCN} + \text{OH} \rightarrow \text{NCNO} + \text{H}$ (30).⁴⁹ Moreover, theoretical results are available for the reactions $\text{NCN} + \text{NO} \rightarrow \text{CN} + \text{N}_2\text{O}$ (32)^{50,51} and $\text{NCN} + \text{NO}_2 \rightarrow \text{NCNO} + \text{NO}$ (33).^{52,53} An overview of reported high temperature rate constant data is given by Faßheber,²⁵ in terms of the Arrhenius diagram shown in Figure 1.4. It is discernible that the reactions $\text{NCN} + \text{O}$ (27) and $\text{NCN} + \text{OH}$ (30) proceed close to the collision limit, whereas the reaction $\text{NCN} + \text{H}$ (28) is somewhat slower. Although the reaction $\text{NCN} + \text{O}_2$ (29) has a very low rate constant, it is very important due to high O_2 mole fractions present in the combustion air. The reactions of NCN with NO (32) and NO_2 can be supposed to be important in combustion systems with nitrogen containing propellants like nitromethane. In these systems, NO and NO_2 reactions are usually among the most important ones.⁵⁴

Finally, low temperature ($T < 600$ K) experimental studies exist for the reactions 32, $\text{NCN} + \text{NO}$ ^{50,51,55} and 33, $\text{NCN} + \text{NO}_2$.^{52,53} Additionally, upper limits have been recommended for the rate constants of reaction 29, $\text{NCN} + \text{O}_2$ and the reaction $\text{NCN} + \text{C}_2\text{H}_4$ (34).⁵⁵

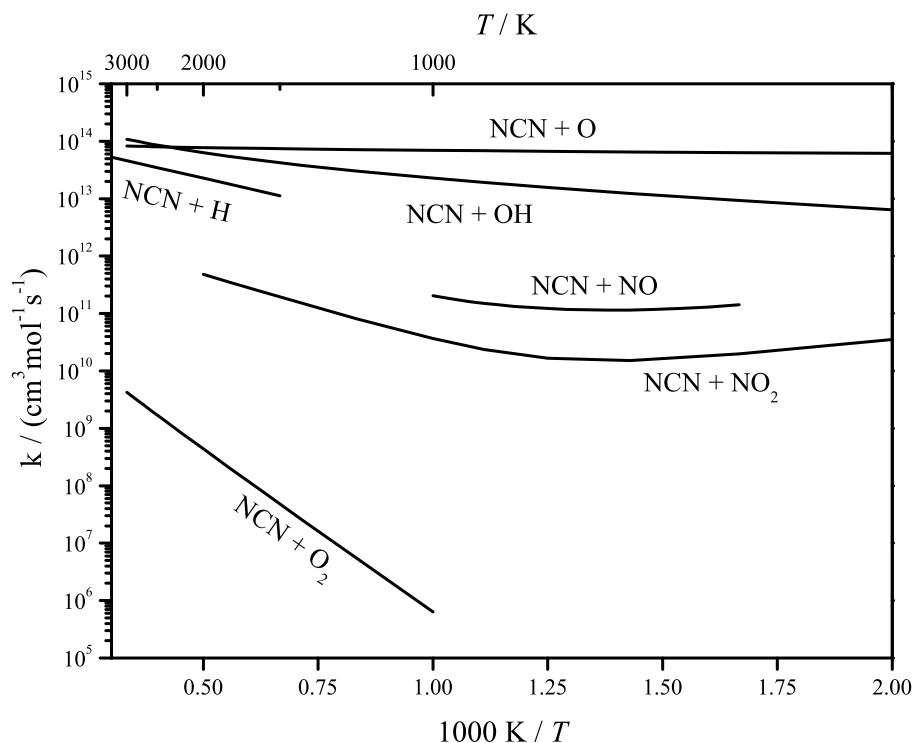


Figure 1.4: Arrhenius expressions of bimolecular NCN reaction rate constants. The plot has been adopted from Faßheber.²⁵

1.5 High temperature HCO chemistry

Next to NCN chemistry, many other reactions have to be considered to model overall NO_x formation rates. For example, the direct reactions of the key combustion intermediates with nitrogen containing species have to be taken into account. In this context, bimolecular HCO reactions are of interest, because the formyl radical HCO is a key intermediate in combustion chemistry and lies on the main oxidation pathway of hydrocarbons. A scheme of the most important reactions in the methane (CH_4) oxidation is shown in Figure 1.5. HCO radicals are mainly produced in the reactions of O, OH, H and CH_3 with formaldehyde. Important HCO consuming reactions are the reactions with H, OH, O_2 and H_2O . The produced CO is subsequently converted to CO_2 . Reactions with nitrogen oxides become most important in nitrogen-rich flames. Corresponding examples are the nitromethane (CH_3NO_2) flame,⁵⁴ or the combustion of mixtures of fuel and nitrogen oxides.⁵⁷ Under these conditions, the reactions $\text{HCO} + \text{NO}$ (35) and $\text{HCO} + \text{NO}_2$ (36) belong to the most important reactions. Because of the small high-temperature absorption cross section of HCO, which makes HCO measurements exceedingly difficult, no direct measurements of reaction rate constants at combustion relevant temperatures

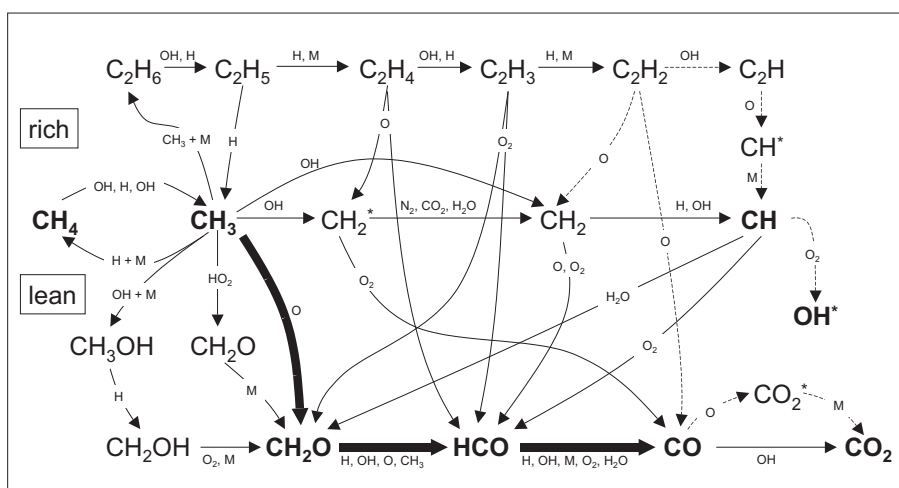


Figure 1.5: Reaction scheme of the methane oxidation according to Najm et al.⁵⁶

of either reaction are available, yet.

1.6 Scope of this work

The aim of this work was to develop an experimental strategy to directly measure the high temperature rate constants of bimolecular NCN reactions as well as to provide rate constant data for the reactions of HCO with NO and NO_2 . Measured data will serve as an experimental basis to further improve our understanding of NO_x formation pathways in combustion processes.

Whereas for HCO a radical source, namely the photolysis of the precursor molecule glyoxal, $(\text{CHO})_2$, as well as high temperature absorption cross sections were already available from previous studies performed in the workgroup of Friedrichs,^{58–60} in the case of NCN a suitable precursor was yet to be found and characterised. Furthermore, NCN absorption cross sections had to be determined at combustion-relevant temperatures. Therefore, a new spectroscopic set-up to allow for the sensitive and quantitative detection of NCN had to be established, first.

Briefly, this cumulative thesis is structured as follows: In the experimental part (chapter 2) the detection scheme for NCN radicals is outlined and some details are given on the shock tube technique, the performed statistical rate calculations and the synthesis of the precursor molecules. The formation mechanism of NCN following the decomposition of the precursor as well as the absolute NCN absorption cross section at combustion relevant temperatures are investigated in chapters 3 and 4 (paper 1: The Thermal Decomposition of NCN_3 as a High Temperature NCN Radical Source: Singlet-Triplet Relaxation and Absorption Cross Section of $\text{NCN}(^3\Sigma)$, paper 2: A Consistent Model for the Thermal Decomposition of NCN_3 and the Singlet-Triplet Relaxation of NCN). In chapter 5 (paper 3: Direct

Measurements of the High Temperature Rate Constants of the Reactions $\text{NCN} + \text{O}$, $\text{NCN} + \text{NCN}$, and $\text{NCN} + \text{M}$, the rate constants for the self reaction of NCN , the unimolecular decomposition of NCN and the important reaction $\text{NCN} + \text{O}$ (27) will be reported. Moreover, in chapter 6 (paper 4: Direct Measurements of the Rate Constants of the Reactions $\text{NCN} + \text{NO}$ and $\text{NCN} + \text{NO}_2$ Behind Shock Waves), rate constants of the reactions of NCN with NO and NO_2 (32,33) are measured and the temperature and pressure dependencies of these reactions are discussed in the framework of complex-forming bimolecular reactions. Finally, the kinetics of the reactions of the important intermediate HCO with NO and NO_2 (35,36) are investigated at room temperature and at high temperatures in chapter 7 (paper 5: Wide Temperature Range ($T = 295 \text{ K}$ and $770 - 1305 \text{ K}$) Study of the Kinetics of the Reactions $\text{HCO} + \text{NO}$ and $\text{HCO} + \text{NO}_2$ using Frequency Modulation Spectroscopy).

Bibliography

- [1] International Energy Agency, Key World Energy Statistics, <http://www.iea.com>, **2011**.
- [2] Bundesministerium für Wirtschaft und Technologie, Referat III C 3, Zahlen und Fakten: Energiedaten, Nationale und Internationale Entwicklung, <http://www.bmwi.de/BMWi/Navigation/Energie/Statistik-und-Prognosen/energiedaten.html>, **2011**.
- [3] P. Forster, V. Ramaswamy, P. Artaxo, T. Berntsen, R. Betts, D. Fahey, J. Haywood, J. Lean, D. Lowe, G. Myhre, J. Nganga, R. Prinn, G. Raga, M. Schulz, and R. V. Dorland, Changes in Atmospheric Constituents and in Radiative Forcing, in S. Solomon, D. Qin, M. Manning, Z. Chen, M. M. K. Averyt, M. Tignor, and H. Miller, editors, *Climate Change 2007: The Physical Science Basis. Contribution of Working Group I to the Fourth Assessment Report of the Intergovernmental Panel on Climate Change*, chapter 2, Cambridge University Press, Cambridge, United Kingdom, **2007**.
- [4] R. P. Wayne, *Chemistry of Atmospheres*, Oxford University Press, **2000**.
- [5] C. Baird, *Environmental Chemistry*, W. H. Freeman and Company, New York, **1995**.
- [6] J. Warnatz, U. Maas, and R. W. Dibble, *Combustion*, Springer, Berlin/Heidelberg, 3. edition, **2001**.
- [7] W. C. Gardiner, Jr, editor, *Combustion Chemistry*, Springer-Verlag, New York, **1984**.
- [8] Prognos AG, EWI - Energiewissenschaftliches Institut and der Universität zu Köln, and Gesellschaft für Wirtschaftliche Strukturforchung mbH (GWS), Studie Energiszenarien für ein Energiekonzept der Bundesregierung, **2010**.
- [9] J. F. Griffiths and J. A. Barnard, *Flame and Combustion*, Blackie Academic and Professional, London, Weinheim, New York, Tokyo, Melbourne, Madras, 3. edition, **1995**.

- [10] H. B. Singh, editor, *Composition, Chemistry, and Climate of the Atmosphere*, Van Nostrand Reinhold, New York, **1995**.
- [11] R. M. Harrison, editor, *Principles of Environmental Chemistry*, RSC Publishing, Cambridge, **2007**.
- [12] J. A. Miller and P. Glarborg, Modeling the Thermal De-NO_x Process: Closing in on a Final Solution, *Int. J. Chem. Kinet.* **1999**, *31*, 757–765.
- [13] R. Zellner and GDCh - Gesellschaft Deutscher Chemiker e. V., editors, *Chemie über der Wolken ... und darunter*, Wiley-VCH Verlag, Weinheim, **2011**.
- [14] J. C. Jones, *Combustion Science, Principles and Practice*, Millenium Books, Newtown, **1993**.
- [15] P. Glarborg, M. U. Alzueta, K. Dam-Johansen, and J. A. Miller, Kinetic Modeling of Hydrocarbon/Nitric Oxide Interactions in a Flow Reactor, *Combust. Flame* **1998**, *115*, 1–27.
- [16] Y. B. Zeldovich, The Oxidation of Nitrogen in Combustion and Explosions, *Acta Physicochim. USSR* **1946**, *21*, 577–628.
- [17] D. L. Baulch, C. J. Cobos, A. M. Cox, P. Frank, G. Hayman, Th. Just, J. A. Kerr, T. Murrels, M. J. Pilling, J. Troe, R. W. Walker, and J. Warnatz, Evaluated Kinetic Data for Combustion Modelling Supplement I, *Int. J. Phys. Chem. Ref. Data* **1994**, *23*, 847–1033.
- [18] J. Wolfrum, Bildung von Stickoxiden bei der Verbrennung, *Chemie-Ingenieur-Technik* **1972**, *44*, 656–659.
- [19] P. C. Malte and D. T. Pratt, Measurement of Atomic Oxygen and Nitrogen Oxides in Jet-Stirred Combustion, *Proc. Comb. Inst.* **1974**, 1061–1070.
- [20] C. P. Fenimore, Formation of Nitric Oxide in Premixed Hydrocarbon Flames, *Proc. Combust. Inst.* **1971**, *13*, 373–380.
- [21] Q. Cui, K. Morokuma, J. M. Bowman, and S. J. Klippenstein, The Spin-Forbidden Reaction CH(²Π) + N₂ → HCN + N(⁴S) Revisited. II. Nonadiabatic Transition State Theory and Application, *J. Chem. Phys.* **1999**, *110*, 9469–9482.
- [22] L. V. Moskaleva and M. C. Lin, The Spin-Conserved Reaction CH + N₂ → H + NCN: A Major Pathway to Prompt NO Studied by Quantum/Statistical Theory Calculations and Kinetic Modeling of Rate Constant, *Proc. Combust. Inst.* **2000**, *28*, 2393–2401.
- [23] L. V. Moskaleva, W. S. Xia, and M. C. Lin, The CH + N₂ Reaction Over the Ground Electronic Doublet Potential Energy Surface: A Detailed Transition State Search, *Chem. Phys. Lett.* **2000**, *331*, 269–277.

- [24] V. Vasudevan, R. K. Hanson, C. T. Bowman, D. M. Golden, and D. F. Davidson, Shock Tube Study of the Reaction of CH with N₂: Overall Rate and Branching Ratio, *J. Phys. Chem. A* **2007**, *111*, 11818–11830.
- [25] N. Faßheber, Stoßwellenuntersuchungen zur Bestimmung der Hochtemperatur-Geschwindigkeitskonstanten der Reaktionen NCN + H und NCN + H₂, Diplomarbeit, Christian-Albrechts-Universität zu Kiel, **2010**.
- [26] G. P. Smith, Evidence of NCN as a Flame Intermediate for Prompt NO, *Chem. Phys. Lett.* **2003**, *367*, 541–548.
- [27] J. A. Sutton, B. A. Williams, and J. W. Fleming, Laser-Induced Fluorescence Measurements of NCN in Low-Pressure CH₄/O₂/N₂ Flames and Its Role in Prompt NO Formation, *Combust. Flame* **2008**, *153*, 465–478.
- [28] R. J. H. Klein-Douwel, N. J. Dam, and J. J. ter Meulen, Laser-Induced Fluorescence of NCN in Low and Atmospheric Pressure Flames, *Optics Lett.* **2008**, *33*, 2620–2622.
- [29] G. Herzberg and D. N. Travis, The Spectrum and Structure of the Free NCN Radical, *Can. J. Phys.* **1964**, *42*, 1658–1675.
- [30] D. E. Milligan, M. E. Jacox, and A. M. Bass, Matrix-Isolation Study of the Photolysis of Cyanogen Azide. The Infrared and Ultraviolet Spectra of the Free Radical NCN, *J. Chem. Phys.* **1965**, *43*, 3149–3160.
- [31] H. W. Kroto, Singlet and Triplet States of NCN in the Flash Photolysis of Cyanogen Azide, *J. Chem. Phys.* **1966**, *44*, 831–832.
- [32] H. W. Kroto, The $^1\Pi_u \leftarrow ^1\Delta_g$ Electronic Spectrum of NCN, *Can. J. Phys.* **1967**, *45*, 1439–1450.
- [33] H. Okabe and A. Mele, Photodissociation of NCN₃ in the Vacuum-Ultraviolet: Production of CN B²Σ and NCN A³Π*, *J. Chem. Phys.* **1969**, *51*, 2100–2106.
- [34] H. W. Kroto, T. F. Morgan, and H. H. Sheena, Flash Photolysis of Cyanogen Azide, NCN₃, *Trans. Faraday Soc.* **1970**, *66*, 2237–2243.
- [35] S. A. Beaton and J. M. Brown, Laser Excitation Spectroscopy of the $\tilde{A}^3\Pi_u - \tilde{X}^3\Sigma_g^-$ -Transition of the NCN Radical. 2. The ν_2 Hot Band, *J. Mol. Spectrosc.* **1997**, *183*, 347–359.
- [36] R. T. Bise, H. Choi, and D. M. Neumark, Photodissociation Dynamics of the Singlet and Triplet States fo the NCN Radical, *J. Chem. Phys.* **1999**, 4923–4932.
- [37] G. P. Smith, R. A. Coppeland, and D. R. Crosley, Electronic Quenching, Fluorescence Lifetime, and Spectroscopy of the A³Π_u State of NCN, *J. Chem. Phys.* **1989**, *91*, 1987–1993.

- [38] A. El Bakali, L. Pillier, P. Desgroux, B. Lefort, L. Gasnot, J. F. Pauwels, and I. da Costa, NO Prediction in Natural Gas Flames Using GDF-Kin 3.0 Mechanism. NCN and HCN Contribution to Prompt-NO Formation, *Fuel* **2006**, 85, 896–909.
- [39] G. P. Smith, D. M. Golden, M. Frenklach, N. W. Moriarty, B. Eiteneer, M. Goldenberg, C. T. Bowman, R. K. Hanson, S. Song, W. C. G. Jr., V. V. Lissanski, and Z. Qin, GRI-MECH 3.0, http://www.me.berkeley.edu/gri_mech/.
- [40] J. A. Sutton and J. W. Fleming, Towards Accurate Kinetic Modeling of Prompt NO Formation in Hydrocarbon Flames via the NCN Pathway, *Combust. Flame* **2008**, 154, 630–636.
- [41] A. A. Konnov, Implementation of the NCN Pathway of Prompt-NO Formation in the Detailed Reaction Mechanism, *Combust. Flame* **2009**, 156, 2093–2105.
- [42] N. Lamoureux, P. Desgroux, A. El Bakali, and J. F. Pauwels, Experimental and Numerical Study of the Role of NCN in Prompt-NO Formation in Low-Pressure CH₄-O₂-N₂ and C₂H₂-O₂-N₂ Flames, *Combust. Flame* **2010**, 157, 1923–1941.
- [43] N. Lamoureux, X. Mercier, C. Western, J. F. Pauwels, and P. Desgroux, NCN Quantitative Measurement in a Laminar Low Pressure Flame, *Proc. Combust. Inst.* **2009**, 32, 937–944.
- [44] A. Busch and M. Olzmann, Shock-Tube Study of the Thermal Decomposition of NCN, Vienna, paper p810138, Proc. European Combust. Meeting, **2009**.
- [45] A. Busch, N. González-García, and M. Olzmann, Thermal Decomposition of NCN: Shock-Tube Study and Master-Equation Modeling, Savonlinna, poster abstract, 30th Int. Symp. on Free Radicals, **2009**.
- [46] A. Busch, *Stoßwellenuntersuchungen zum Zerfall stickstoffhaltiger Verbindungen mit spektroskopischen Methoden*, Ph.D. thesis, Karlsruher Institut für Technologie, **2010**.
- [47] R. S. Zhu and M. C. Lin, Ab Initio Study on the Oxidation of NCN by O(³P): Prediction of the Total Rate Constant and Product Branching Ratios, *J. Phys. Chem. A* **2007**, 111, 6766–6771.
- [48] R. S. Zhu and M. C. Lin, Ab Initio Study on the Oxidation of NCN by O₂, *Int. J. Chem. Kinet.* **2005**, 37, 593–598.
- [49] R. S. Zhu, M. T. Nguyen, and M. C. Lin, Ab Initio Study on the Oxidation of NCN by OH: Prediction of the Individual and Total Rate Constants, *J. Phys. Chem. A* **2009**, 113, 298–304.
- [50] C.-L. Huang, S. Y. Tseng, T. Y. Wang, N. S. Wang, Z. F. Xu, and M. C. Lin, Reaction Mechanism and Kinetics of the NCN + NO Reaction: Comparison of Theory and Experiment, *J. Chem. Phys.* **2005**, 122, 184321.

- [51] O. Welz, *Laserspektroskopische Untersuchungen und molekularkinetische Modellierung der Kinetik von Radikalreaktionen in der Gasphase*, Ph.D. thesis, Universität Karlsruhe (TH), **2009**.
- [52] T.-J. Yang, N. S. Wang, L. C. Lee, Z. F. Xu, and M. C. Lin, Kinetics and Mechanism of the NCN + NO₂ Reaction Studied by Experiment and Theory, *J. Phys. Chem. A* **2008**, *112*, 10185–10192.
- [53] C. Kappler, *Untersuchungen komplexbildender bimolekularer Reaktionen in der Gasphase mit laserspektroskopischen Methoden und statistischer Reaktionstheorie*, Ph.D. thesis, Karlsruher Institut für Technologie, **2010**.
- [54] K. Zhang, Y. Li, T. Yuan, J. Cai, P. Glarborg, and F. Qi, An Experimental and Kinetic Modeling Study of Premixed Nitromethane Flames at Low Pressure, *Proc. Combust. Inst.* **2011**, *33*, 407–414.
- [55] R. E. Baren and J. F. Hershberger, Kinetics of the NCN Radical, *J. Phys. Chem. A* **2002**, *106*, 11093–11097.
- [56] H. Najm, P. Paul, C. Müller, and P. Wyckoff, On the Adequacy of Certain Experimental Observables as Measurements of Flame Burning Rate, *Combust. Flame* **1998**, *113*, 312–332.
- [57] J. Gimnez-López, M. U. Alzueta, C. T. Rasmussen, P. Marshall, and P. Glarborg, High Pressure Oxidation of C₂H₄/NO Mixtures, *Proc. Combust. Inst.* **2011**, *33*, 449–457.
- [58] M. Colberg and G. Friedrichs, Room Temperature and Shock Tube Study of the Reaction HCO + O₂ Using the Photolysis of Glyoxal as an Efficient HCO Source, *J. Phys. Chem. A* **2006**, *110*, 160–170.
- [59] M. Colberg, *Aufbau und Charakterisierung einer Stoßwellenapparatur zur Untersuchung von Hochtemperaturreaktionen des Formylradikals*, Ph.D. thesis, Christian-Albrechts-Universität zu Kiel, **2006**.
- [60] G. Friedrichs, M. Colberg, J. Dammeier, T. Bentz, and M. Olzmann, HCO Formation in the Thermal Unimolecular Decomposition of Glyoxal: Rotational and Weak Collision Effects, *Phys. Chem. Chem. Phys.* **2008**, *10*, 6520–6533.

2 Experimental

To investigate high temperature NCN and HCO reactions, several conditions must be fulfilled. On the one hand, known concentrations of the reactants must be generated at the desired combustion relevant temperatures. Since both NCN and HCO are not stable species, they must be generated from precursor molecules. On the other hand, either the reactants or the products must be quantitatively detected in a time-resolved manner with high sensitivity to suppress secondary chemistry. Afterwards, measured concentration-time profiles must be evaluated in order to extract the desired rate constant data.

A gas mixing system equipped with calibrated mass flow controllers allowed for the preparation of the test gas mixtures. High temperature conditions were achieved by shock heating of the test gas. Following a pressure and temperature jump on the ns time scale, stable conditions were achieved for approximately 1.5 ms. As a sensitive spectroscopic method either difference amplification of narrow bandwidth laser absorption or frequency modulation (FM) spectroscopy have been used. Data reduction was performed by fitting analytical functions or by performing numerical simulations. Rate constants were varied in order to match the simulated concentration-time profiles with the measured ones.

In the experimental section of this thesis, the shock tube method will be introduced followed by the description of the experimental set-up. The used spectroscopic and numerical methods will also be described. Finally, experimental procedures and calibration measurements will be outlined.

2.1 The shock tube method

The shock heating of gases is known since 1899 when Vieille¹ generated the first shocks in a 6 m long tube. This shock tube consisted of a high pressure section and a low pressure section divided by a diaphragm. The high pressure section was filled with air until that diaphragm burst. The resulting shock wave propagated through the low pressure section at supersonic speed compressing and heating the gas. This shock tube is a prototype of all modern shock tubes. In the 1940s, the properties of different driver gases and their influence on post-shock conditions were examined by Payman and Shepherd.² They used shock tubes to produce high velocity flows. The fact that shock waves heat up gases within ns time scales was discovered by Kantrowitz and Hertzberg.³ Finally it was Schott and

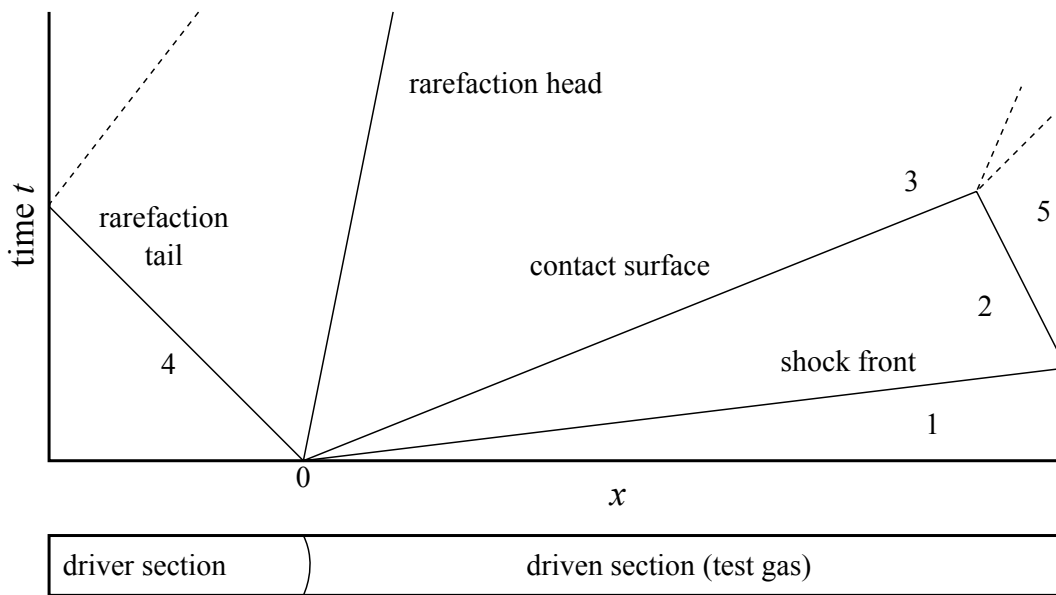


Figure 2.1: $t-x$ diagram of a shock tube experiment. The numbers denote possible states of pressure, temperature and density of the test gas.

Kinsey, who introduced the shock tube technique into chemical kinetics research.⁴

Since then, the shock tube technique has served as a reactor for kinetic experiments in countless studies⁵ because (i) it is ideally suited to vary the experimental temperature and pressure over a wide range (up to $T = 15000$ K, $p = 1000$ bar) and (ii) the heating and compression occurs almost instantaneously. Because of this fast pressure and temperature jump, reactions during the heating period and thus under undefined conditions can be ruled out. A second advantage of shock waves generated in a more or less ideal shock tube is the fact that temperatures and pressures behind the shock waves can be calculated easily and with good accuracy from the well-established theories of shock wave propagation^{6,7} and the initial conditions of the test gas. Only the relatively easy accessible shock wave velocity has to be measured. On the downside, two disadvantages of the shock tube method are the short maximum observation times of some ms and the fact that it is merely impossible to generate exactly identical conditions by two consecutive shock waves. Therefore, averaging procedures as used in many other experiments to enhance the precision cannot be carried out. Shock tube measurements can be considered as single-shot experiments.

2.1.1 Theory of shock wave propagation

The shock wave is caused by the compression of the test gas by the higher pressure driver gas. The shock tube together with all waves that are associated with the burst of the diaphragm is sketched in Figure 2.1. Here, the time t is plotted against the position x in the shock tube. $x = 0$ denotes

2. Experimental

the position of the diaphragm and thus is the starting point of our considerations. The burst of the diaphragm results in compression waves, which are propagating with the speed of sound a ,

$$a = \sqrt{\frac{\gamma RT}{M}}. \quad (2.1)$$

$\gamma = c_p/c_v$ is the heat capacity ratio of the gas, T is the absolute temperature, M the molecular mass of the molecules and R the gas constant. According to equation 2.1 the speed of sound increases after the first compressions have pre-heated the gas such that following compression waves travel at a higher speed. At the same time, the gas starts to flow in the direction of the compression waves. Finally all compression waves coalesce to one single steep shock front, which propagates through the gas with a multiple of the speed of sound (relative to the resting gas in front of the shock front). In a so called over-adiabatic compression it causes large gradients of temperature, pressure and density. The initial state of the test gas before the shock front is denoted 1 in figure 2.1, whereas 2 denotes the test gas region behind the incident shock wave. At the end plate of the shock tube, the shock wave is reflected. It travels back in the opposite direction through the already heated and compressed gas, causing a second pressure and temperature jump (reflected shock region, 5). The reflected shock wave has a lower velocity than the incident wave, corresponding to a lower slope in the $t - x$ diagram. The shock wave is followed by the contact surface; its arrival at the observation point limits the maximum observation period.

The calculation of temperature, pressure and density behind incident and reflected shock waves is based on the conservation equations of mass, momentum and energy (eqs. 2.2, 2.3, 2.4)

$$\rho_1 u_1 = \rho_2 u_2, \quad (2.2)$$

$$p_1 + \rho_1 u_1^2 = p_2 + \rho_2 u_2^2 \quad (2.3)$$

and

$$H_1 + \frac{1}{2}u_1^2 = H_2 + \frac{1}{2}u_2^2. \quad (2.4)$$

in a shock fixed coordinate system (i.e., the shock front is at rest). u is the velocity of the gas entering (u_1) and leaving (u_2) the shock front, ρ is the density, p the pressure and H the specific enthalpy of the gas in front of (index 1) and behind (index 2) the shock wave. With the help of the thermal and caloric equations of state for a perfect gas

$$pV = nRT \quad (2.5)$$

and

$$H_2 - H_1 = c_p \times (T_2 - T_1), \quad (2.6)$$

2. Experimental

the Rankine-Hugoniot equations (2.7, 2.8) can be obtained:

$$\frac{p_2}{p_1} = \frac{1 - \frac{\gamma-1}{\gamma+1} \frac{\rho_1}{\rho_2}}{\frac{\rho_1}{\rho_2} - \frac{\gamma-1}{\gamma+1}} \quad (2.7)$$

$$\frac{\rho_2}{\rho_1} = \frac{\frac{\gamma-1}{\gamma+1} + \frac{p_2}{p_1}}{\frac{\gamma-1}{\gamma+1} \frac{p_2}{p_1} + 1}. \quad (2.8)$$

Introducing the Mach number $M_S = u_1/a_1$, the pressure (eq. 2.9), density (eq. 2.10) and temperature (eq. 2.11) behind the incident shock wave can be derived as follows:^{6,7}

$$\frac{p_2}{p_1} = \frac{2\gamma M_S^2 - (\gamma - 1)}{\gamma + 1} \quad (2.9)$$

$$\frac{\rho_2}{\rho_1} = \frac{(\gamma + 1)M_S^2}{(\gamma - 1)M_S^2 + 2} \quad (2.10)$$

$$\frac{T_2}{T_1} = \frac{\left(\gamma M_S^2 - \frac{\gamma-1}{2}\right) \left(\frac{\gamma-1}{2} \times M_S^2 + 1\right)}{\left(\frac{\gamma+1}{2}\right)^2 \times M_S^2}. \quad (2.11)$$

Based on these equation and the boundary condition of a resting gas behind the reflected shock wave, similar equations for the reflected shock wave region can be derived (eqs. 2.12, 2.13):

$$\frac{p_5}{p_2} = \frac{\frac{\gamma+1}{\gamma-1} + 2 - \frac{p_1}{p_2}}{1 + \frac{\gamma+1}{\gamma-1} \frac{p_1}{p_2}}, \quad (2.12)$$

$$\frac{T_5}{T_2} = \frac{p_5}{p_2} \times \frac{\frac{\gamma+1}{\gamma-1} + \frac{p_5}{p_2}}{1 + \frac{\gamma+1}{\gamma-1} \frac{p_5}{p_2}}. \quad (2.13)$$

Hence, temperatures and pressures for the incident (2) and reflected (5) region can be calculated from the initial conditions and the Mach number M_S of the incident shock wave.

Real gas effects are taken into account by the temperature dependence of the heat capacity c_p . Experimental conditions can be corrected for real gas effects by iterative numerical procedures.⁷ Overall, real gas effects on the pressure were small for the experimental conditions used in this work. Small corrections arose from the necessary excitation of vibrational degrees of freedom at high temperatures resulting in lower temperatures of the gas in the post-shock region.

Additionally, relaxation effects may result from delayed equilibria between translational and vibrational or electronic excitation. Whereas rotation and translation are quickly equilibrated and therefore do not complicate the calculation of post-shock conditions, the slower redistribution of energy into

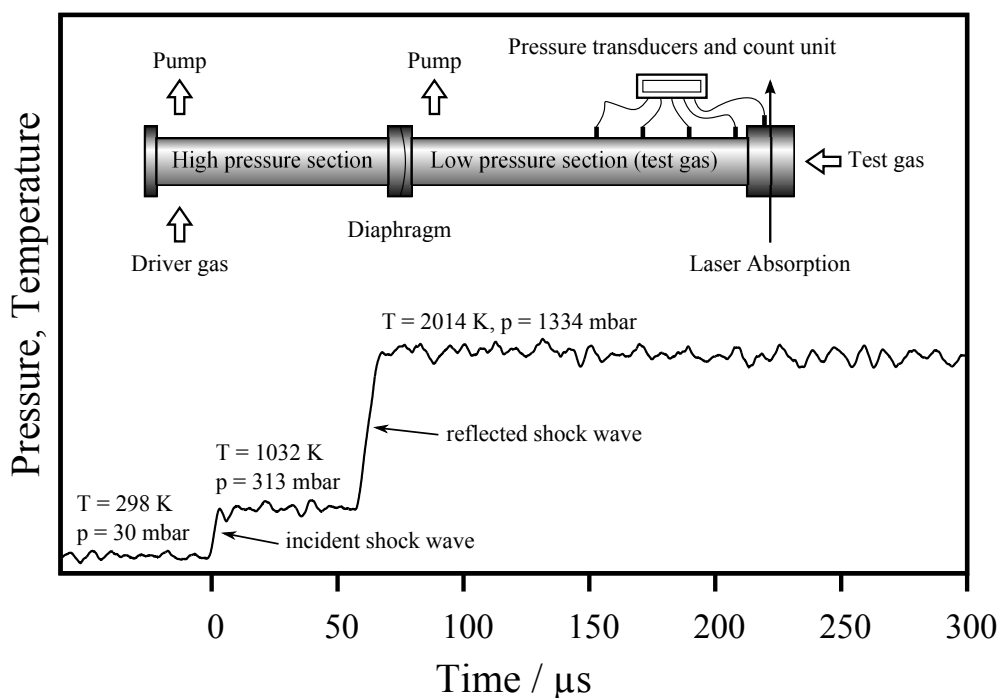


Figure 2.2: Pressure/temperature profile together with a schematic drawing of the Kiel shock tube. Please note that the rise time of the signal is limited by the bandwidth of the pressure transducers.

vibrational degrees of freedom may result in the development of a relaxation zone. In this zone, the temperature (i.e., translational temperature) exponentially decreases starting from the value of a perfect gas until the equilibrium between translation and vibration is reached. On the other hand, the density rises as the temperature decreases. Therefore, a flattening of the shock-front is observed. Since it is difficult to account for these phenomena,⁷ in this work concentrations of polyatomic reactants were kept low such that relaxation effects could be neglected.

2.1.2 The Kiel shock tube

A schematic drawing of the used shock tube^{8,9} together with a typical pressure/temperature-time profile is shown in figure 2.2. The shock tube had an overall length of 8.35 m. The test section of an inner diameter of 81 mm and a length of 4.05 m consisted of electro-polished stainless steel and could be evacuated down to pressures of $p \approx 10^{-7}$ mbar by a combination of oil-free turbomolecular and diaphragm pumps (Pfeiffer Vacuum, TMU261/MVP055-3). The leaking rate of the test section was 3×10^{-6} mbar l s⁻¹.

The temperature and the pressure jump induced by the incident and the reflected shock wave are clearly discernible in Figure 2.2. In this example, only 60 μ s lie between the incident and the re-

2. Experimental

flected shock waves. If needed, longer observation times behind incident shock waves can be realised by extending the distance between observation point and end plate. The real pressure and temperature jumps are much faster than the measured pressure profile suggests. Here, the bandwidth of the pressure transducers limits the rise time to some μs . Four pressure transducers (PCB Piezotronics M113A21) were mounted flush and equidistantly in the shock tube. Another transducer measured the pressure in the observation plane. All pressure transducers were wired to a fast count unit allowing to measure the shock wave velocity. Two quartz windows in the shock tube head allowed for laser diagnostics of the investigated reactants. The spectroscopic setup is shown in more detail in section 2.2.

The shock tube was operated by hydrogen, nitrogen or mixtures of hydrogen and nitrogen as driver gases. The Mach number of a shock wave is affected by the mass of the driver gas molecules according to eq. 2.14⁷

$$\lim_{p_4/p_1 \rightarrow \infty} M_S = \frac{1 + f_1}{2} \times \frac{f_4 a_4}{f_1 a_1} + \sqrt{1 + \left(\frac{1 + f_1}{2} \times \frac{f_4 a_4}{f_1 a_1} \right)^2}. \quad (2.14)$$

$\lim_{p_4/p_1 \rightarrow \infty} M_S$ corresponds to the maximum Mach number at infinite pressure of the driver gas p_4 , f is the number of degrees of freedom of test gas (index 1) and driver gas (index 4) and $a = \sqrt{\gamma RT/M}$ is the speed of sound. The higher the molecular mass of the driver gas, the lower the speed of sound in the driver gas a_4 and thus the Mach number of the shock wave. A high molecular mass of the test gas, however, results in higher Mach numbers. In contrast to the temperature and pressure behind a shock wave, eqs. 2.10 reveals that the density hardly shows any dependence on the actual Mach number. Hence, by using several driver gases with different masses it is possible to vary temperature and pressure, but to keep the total density nearly constant. This is desirable to systematically investigate the density dependence of unimolecular reactions. Since it is not feasible to have a different driver gas for every single temperature, the mass of the driver gas has been varied by using different mixtures of two gases A and B of a different mass M_A and M_B according to

$$M = M_A \frac{p_A}{p_4} + M_B \frac{p_B}{p_4}. \quad (2.15)$$

To generate homogeneous mixtures of the driver gases, a new mixing apparatus has been implemented. The mixing is based on two magnetic valves (Danfoss, BA024A), which are separately opened one after another for defined times between 25 and 475 μs . The driver gases are connected to the valves and thus mixtures between 5% and 95% of A in B can be easily prepared. In this work hydrogen (H_2) was used as the lighter component to which nitrogen (N_2) was added. With this setup, the reproducibility of temperature and pressure with the same mixture of gases was $\pm 2\%$. Moreover, previously observed damping effects resulting from inhomogeneities in the driver gas composition were effectively suppressed by the new quasi-simultaneous mixing procedure.

2. Experimental

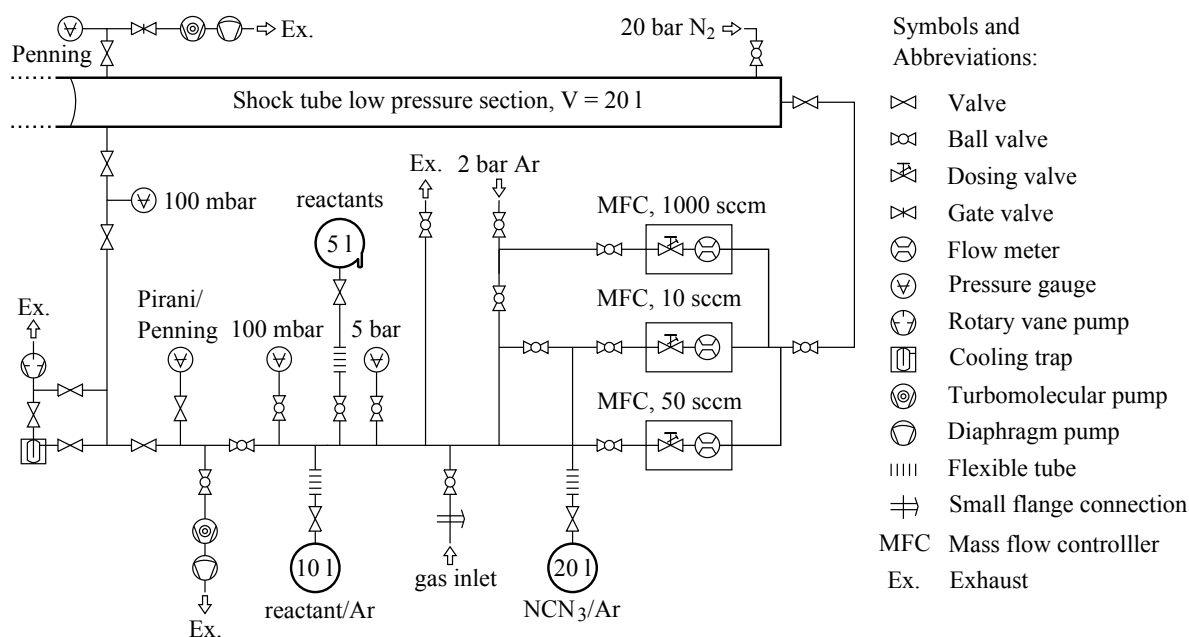


Figure 2.3: Test gas mixing system.

2.1.3 The test gas mixing system

The test gas mixtures entered the shock tube at the shock tube head and could be removed near the diaphragm. In this way, the shock tube was streamed with the particular test gas mixtures to compensate for adsorption effects on the stainless steel walls of the low pressure section. A scheme of the gas mixing and streaming system is shown in figure 2.3. The purpose of the gas mixing system was to purify the reactants, dilute the reactants with inert gas down to the desired concentrations and to fill the low pressure section with variable, but accurately defined mixtures of reactants. Most of the gas mixing system was made of stainless steel with some glass flasks attached to it. A 5 l flask equipped with a cooling finger served to perform freeze-pump-thaw cycles in order to purify NO, NO₂ and N₂O. A 10 l flask held the reactants diluted in argon (usually 1%) and a 20 l storage flask was used for NCN₃ mixtures. NCN₃ was not further purified due to its explosive character upon condensation, but it was immediately diluted with argon down to 0.1%. Three calibrated mass flow controller units (Aera FC-7700C) were used for further mixing and dilution of the test gas directly before entering the shock tube. The gas mixing system could be evacuated by a combination of turbomolecular and diaphragm pump (Pfeiffer Vacuum, TMH071-P/MVP015-2) down to pressures of $\approx 10^{-7}$ mbar. Pressures $p > 1$ mbar were first reduced by a rotary vane pump equipped with a cooling trap to ensure oil free vacuum conditions. To avoid condensation of NCN₃ in the cooling trap, it could be bypassed. For safety reasons, the same setup was also installed at the high pressure section of the shock tube, where the test gas - driver gas mixtures were removed from the shock tube after the experiments. The pressure in the gas mixing system could be measured by three different

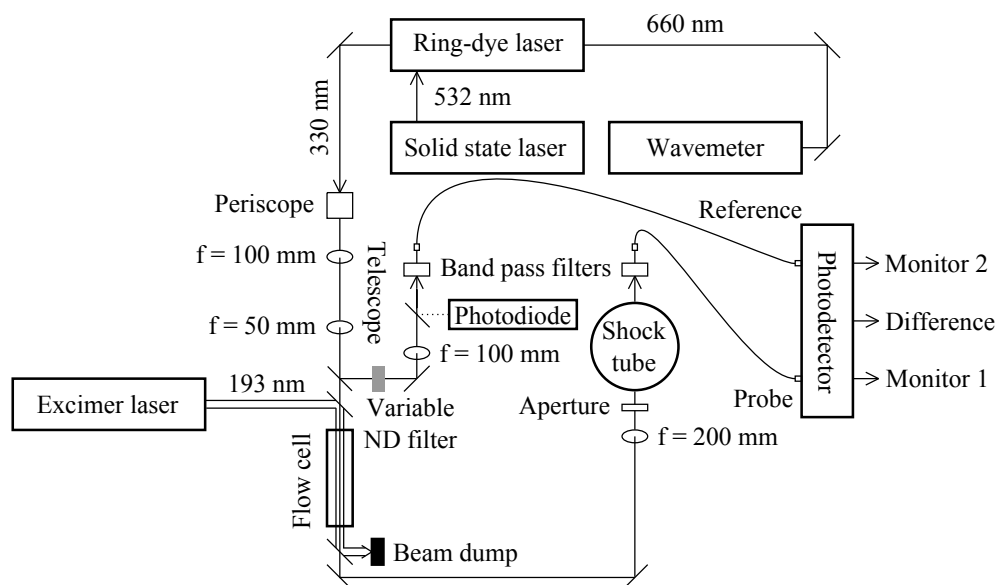


Figure 2.4: The difference amplification laser absorption setup showing the flow cell for room temperature measurements and the shock tube. For high temperature shock wave measurements, the flow cell was removed.

pressure gauges covering the pressure range from 5 bar to 10^{-7} mbar (MKS, 722AMCE2FA; MKS, 622AX12MBE; Pfeiffer Vacuum, PKR 251). The pressure of the test gas prior to shock compression in the test section of the shock tube could be measured by a pressure gauge (MKS, 622AX12MBE).

2.2 Spectroscopic methods

The detection of NCN and HCO was performed using narrow-bandwidth laser absorption spectroscopy. In contrast to emission based methods or mass spectrometry, a quantitative evaluation of the data is straightforward supposing that absorption cross sections of the detected species are known at the respective wavelengths. For the purpose of this work, it was necessary to detect very low reactant concentrations. The very sensitive frequency modulation (FM) spectroscopy was used to detect HCO ($(\alpha cl)_{\min} = 5 \times 10^{-5}$). Unfortunately, the FM set-up cannot be operated at UV wavelengths, such that NCN was detected by difference amplification laser absorption spectroscopy (DLA) ($(\alpha cl)_{\min} = 5 \times 10^{-4}$).

2.2.1 The difference laser absorption setup

A scheme of the newly assembled difference laser absorption setup is shown in figure 2.4. Laser radiation around $\lambda = 330$ nm was generated by intra-cavity frequency doubling of a frequency stabilised

2. Experimental

continuous-wave ring-dye laser (Coherent 899 series). The frequency doubling was performed in a LiIO_4 crystal, which was constantly flushed with boil-off nitrogen to inhibit damage of the hygroscopic material. The dye-laser was pumped by a Nd:YVO_4 solid state laser (Coherent Verdi V10), the pumping power was typically 8 W at 532 nm which resulted in 1.5 mW output power in the UV with DCM Special (Radiant Dyes) as a dye. The UV beam (spectral bandwidth < 10 MHz) was separated from the fundamental and coupled out of the laser by a dichroic mirror and a combination of three prisms.

The accurate wavelength was determined by measuring the wavelength of the fundamental, of which 2 mW were coupled out of the laser cavity through a high reflective mirror. Wavelength measurements were performed by an interferometric type wavemeter (MetroLux WL200) referenced to a HeNe laser. A small offset of $\tilde{\nu} = 0.02 \text{ cm}^{-1}$ was taken into account resulting in an absolute accuracy of 5×10^{-7} corresponding to $\Delta\lambda = 1.65 \times 10^{-4} \text{ nm}$ or $\Delta\tilde{\nu} = 0.015 \text{ cm}^{-1}$. The offset had been determined by measuring the line positions of the ${}^P Q_{1,7}$ rotational transitions of the Σ vibronic sub-band of the $\tilde{A}^2 A_1 \Pi_u(070) - \tilde{X}^2 B_1(000)$ Renner-Teller split electronic doublet absorption feature of NH_2 around $\lambda = 661 \text{ nm}$. Whereas Dressler and Ramsay determined the positions of the peaks to be $\tilde{\nu}_1 = 15114.98 \text{ cm}^{-1}$ and $\tilde{\nu}_2 = 15115.73 \text{ cm}^{-1}$, our measurements resulted in $\tilde{\nu}_1 = 15114.96 \text{ cm}^{-1}$ and $\tilde{\nu}_2 = 15115.71 \text{ cm}^{-1}$, respectively. The position of the maximum is shifted by 0.02 cm^{-1} towards lower wavenumbers compared to the measurement by Dressler and Ramsay.¹⁰ Moreover, by comparison with another recently calibrated wavemeter the same offset has been determined.

The UV output was first lowered to the height of the shock tube windows by a periscope. The beam diameter was reduced ($r = 2 \text{ mm}$) and shaped by a telescope consisting of two biconvex quartz lenses. The beam was then divided into a reference and a probe beam by a 50:50 beam splitter plate. The reference beam was attenuated by a circular variable neutral density filter to level the intensity of both beams. Afterwards the reference beam was focused, band-pass filtered and coupled into a quartz optical fibre (Thorlabs BF H22-550), which was connected to a balanced photodetector and difference amplification unit (Thorlabs PDB 150A-EC). The fibres were custom-made in order to completely illuminate the photodiodes inside the detector. Furthermore, in order to directly monitor laser intensity fluctuations, 10% of the intensity were separated from the main beam by a quartz plate and focused on a fast photodiode (Hamamatsu S5973-2) as an additional reference. This was necessary because the bandwidth of the monitor channels of the photodetector was too low to reliably check the stability of the laser setup. Before passing the shock tube through two wedged quartz windows, the probe beam was focused by a quartz lens with a focal length of $f = 200 \text{ mm}$. An additional aperture ensured a small beam diameter, which turned out to be important for a good temporal resolution and a stable base line of the signals. After band-pass filtering, the reference beam was coupled into a quartz fibre, which was connected to the detector. For room temperature experiments, a flow cell of 45 cm length was introduced into the path of the probe beam. An excimer laser (Radiant Dyes EXC200) was used for the 193 nm photolysis of the precursor molecule NCN_3 at room temperature. The detection beam

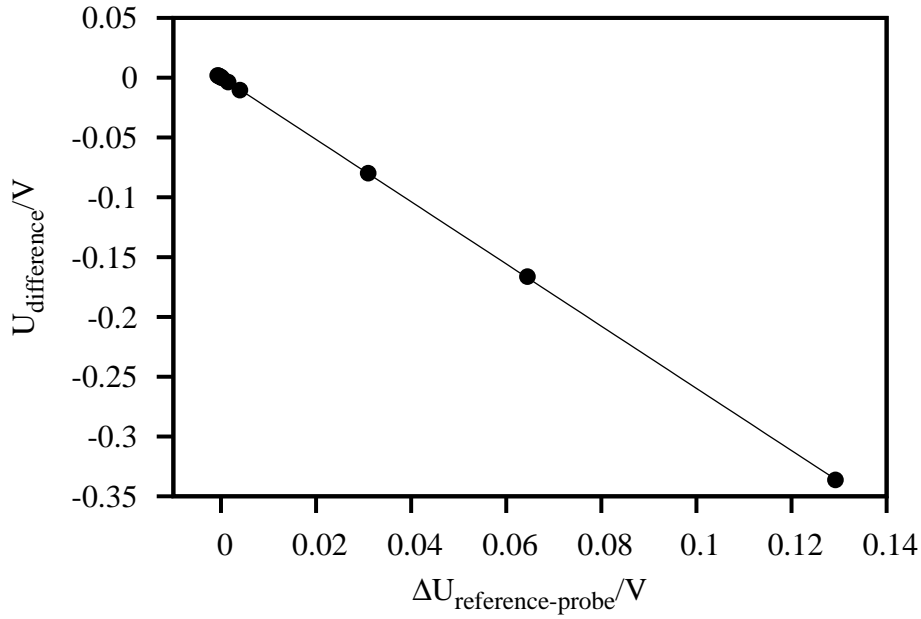


Figure 2.5: Calibration curve of the difference amplifier at level 3, the level used for the experiments performed in this work.

Table 2.1: Gain factors G_d of the difference amplification at different levels.

level	G_d
10^1	0.02615
10^2	0.2643
10^3	2.648
10^4	26.06
10^5	264.1

and the much larger diameter (1 cm) photolysis beam were combined and divided by dichroic mirrors and coupled in and out of the flow cell through quartz windows mounted in Brewster's angle. A slight focusing ($f = 1000$ mm) of the photolysis beam accounted for intensity loss due to absorption in the cell.

To allow for the quantitative detection of species, the gain G_d of the balanced photodetector and amplifier had to be determined. For this purpose, the probe channel was attenuated to different degrees and the difference between the voltage of the two monitor signals was compared to the voltage of the difference channel. This procedure was performed for all five difference amplification levels of the detector. A typical example is shown in figure 2.5. The slope of this straight line corresponds to the gain factor G_d of the detector. The gain factors of all five amplification levels of the detector are summarised in table 2.1. With the help of these gain factors, the absorbance was calculated according to equation 2.16,

$$\ln\left(\frac{I_0}{I}\right) = -\ln\left(1 - \frac{U_{\text{difference}}}{U_0 \times G_d A} - \text{offset}\right). \quad (2.16)$$

$U_{\text{difference}}$ is the voltage of the difference amplified channel, U_0 is the voltage of the the probe monitor channel measured before absorption sets in and A is the gain factor of an additional 18 dB amplifier (Ortec Fast Preamplifier 9305) that amplifies only the difference channel. The gain factor A of this amplifier was determined as $A = 7.667$ by measuring the amplitude of a microwave signal, which was generated by a synthesiser (Marconi Instruments 2023) with and without amplification. The offset had to be introduced to account for a small baseline issue. Due to the high sensitivity of the used set-up, it was not possible to balance the monitor channels completely, such that a very small offset remained. With the absorbance values it was possible to calculate concentrations or (with known concentration) absorption cross sections according to the Beer-Lambert law (2.17):

$$\ln\left(\frac{I_0}{I}\right) = \sigma cl. \quad (2.17)$$

Here, σ is the absorption cross section (unit cm^2/mol), c is the concentration and l is the length of the absorption path. Please note that I_0 is the intensity of the probe beam before absorption occurs and therefore the small offset mentioned above does not affect the precision of the determination of absorption cross-sections.

2.2.2 The Frequency Modulation (FM) setup

HCO concentration-time profiles were measured by means of the very sensitive frequency modulation (FM) spectroscopy. This spectrometer has been developed during the PhD work of Colberg and is based on previous work within the research group.^{11–13}

Briefly, the detection light first passed a Glan-Thompson polariser (New Focus 5524) and an electro optic modulator (EOM) (New Focus 4421). This modulator adds side bands by phase modulation at 1 GHz. The spacing between the side bands and the centre frequency was determined by the modulation frequency of 1 GHz. The spectrum of the modulated light was monitored by a scanning etalon (Coherent SM 240-1, Finesse > 200) to measure the modulation index M . A high value of M corresponds to a larger fraction of the total intensity transferred to the side bands. Typically, in this work a high modulation index of $M \approx 1.6$ was used. After passing another polariser, the modulated light was slightly focused by a lens ($f = 400$ mm), passed the shock tube or the flow cell through two windows and was coupled into an optical fibre (Laser Components HCP 1000). The light was detected by a fast photodiode (Hamamatsu S5973-2, cut-off 1.3 GHz). The signal of the photodiode was split into its AC and DC components by a bias tee (Mini Circuits ZFBT 4R2G). Whereas the DC part was directly recorded by a digital storage oscilloscope, the AC part was band-pass filtered (Trilithic, 5% bandwidth) at 1 GHz, amplified by 40 dB (ZHL 0812 HLN) and finally de-modulated by a frequency mixer (Mini Circuits 5542 ZFM-2000) referenced to the 1 GHz local oscillator (Marconi Instruments 2023) that provided the EOM with the modulation frequency. According to Friedrichs,¹¹ the intensity

of the FM signal is given by equation 2.18,

$$I_{\text{FM}} = I_0 \Delta f \frac{\sigma c l}{2} G_{\text{FM}}, \quad (2.18)$$

where I_0 is the overall intensity (DC signal component), σ , c and l stem from the Beer-Lambert law (equation 2.17), G_{FM} is the gain factor of the FM setup and Δf is the FM factor. The gain factor of the FM-spectrometer had been determined by Colberg,¹² $G = 240 \pm 10$. The FM factor contains all FM specific information (i.e., lineshape of the probed absorption feature, frequency setting of the laser light, modulation index and modulation frequency) and was calculated from a simulated HCO spectrum. Since all parameters of equation 2.18 are known, concentrations could be readily calculated from this equation.

2.3 Numerical methods

2.3.1 Data reduction

Concentration-time profiles were evaluated either by fitting analytical functions to the measured profiles or by systematically varying rate constants in numerically simulated concentration-time profiles using an extensive reaction mechanism.

All fitting procedures were performed by the Gnuplot program.¹⁴ The program uses the non-linear least squares (NLLS) Marquardt-Levenberg algorithm. Rate constants and absorbance levels were used as the fit parameters.

Simulations of concentration-time profiles were carried out by the Chemkin-II program package¹⁵ by numerical integration of the differential equations arising from complex reaction mechanisms. Initial concentrations as well as initial pressures and temperatures were provided by the user, thermodynamic data were included in the form of NASA-polynomials taken from Konnov¹⁶ or Goos *et al.*¹⁷ Rate constants were given in the form of an extended Arrhenius expression

$$k_i = A_i T^{n_i} \exp[-E_{a,i}/RT]. \quad (2.19)$$

In addition to those rate constants included in the tables summarising the most important reactions for the respective parts of this work, the GRI-Mech 3.0¹⁸ has been used as a background mechanism in all simulations. Simulations were performed at a constant volume, variations of the pressure $p(t)$ and the temperature $T(t)$ during the reactions induced by the thermochemistry of the ensuing reactions were included in the simulations. Sensitivity analyses were made possible by the Senkin routine.¹⁵ In this routine, the rate constants of all reactions are varied to examine the influence of the particular reaction on the simulated concentration-time profile. Sensitivity analyses were visualised by plotting the sen-

sitivity coefficients σ over the time. To compare the sensitivity coefficients of different reactions, the coefficients were normalised with respect to the maximum concentrations of the species according to

$$\sigma^\circ(i, j, t) = \sigma(i, j, t) \frac{a_i}{c_{\max}(j)}, \quad (2.20)$$

where $\sigma(i, j, t)$ is the unnormalised sensitivity coefficient depending on the reaction i , the species j and the reaction time t . $c_{\max}(j)$ is the peak concentration of the species j during the simulated time interval. $\sigma(i, j, t)$ is given by

$$\sigma(i, j, t) = \frac{\partial c(i, j, t)}{\partial a_i} \quad (2.21)$$

where a_i is an extra parameter introduced to assure a uniform variation of the rate constants,

$$k_{i,\text{varied}} = a_i \times A_i T^{n_i} \exp[-E_{a,i}/RT]. \quad (2.22)$$

2.3.2 Quantum mechanical and statistical methods

Statistical (RRKM) calculations have been carried out to shed light on the interplay of NCN_3 decomposition and subsequent ^1NCN relaxation.

In RRKM (Rice-Ramsperger-Kassel-Marcus) theory, the specific reaction rate constant of a reactant containing a defined amount of energy E distributed statistically among its degrees of freedom is given by

$$k(E) = \frac{1}{h} \frac{N(E - E_0)}{\rho(E)} \quad (E \geq E_0). \quad (2.23)$$

Here, h is the Planck constant, $N(E - E_0)$ is the number of states of the molecule in the transition state configuration between the energy E and the threshold energy E_0 and $\rho(E)$ is the density of states of the reactant configuration of the molecule at the respective energy E . The temperature dependent thermal rate constant of a unimolecular reaction can be obtained from the time-dependent master equation

$$\frac{\partial x(E, t)}{\partial t} = [\text{M}] \int_0^\infty [R(E, E')x(E', t) - R(E', E)x(E, t)] dE' - k(E)x(E, t). \quad (2.24)$$

$x(E, t)$ is the time-dependent population of reactant molecules of the energy E at time t . $R(E, E')$ are the rate constants of the population gain by collisional energy transfer from all other energy levels with the energy E' , whereas $R(E', E)$ are the rate constants of the corresponding loss processes due to collisional energy transfer to all other energy levels. $k(E)$ is the specific reaction rate constant as given by eq. 2.23. After a short induction time, the population in all levels decays with an overall rate constant that is identical to the macroscopic unimolecular rate constant. The corresponding steady

2. Experimental

state master equation can be written as

$$-k_{\text{uni}}g(E) = [M] \int_0^{\infty} [R(E, E')g(E') - R(E', E)g(E)] dE' - k(E)g(E). \quad (2.25)$$

$g(E')$ and $g(E)$ are the steady state populations of reactant molecules with the energies E' and E , respectively. k_{uni} is the desired overall thermal rate constant, for which eq. 2.26 can be obtained:

$$k_{\text{uni}} = \int_{E_0}^{\infty} k(E)h(E)dE, \quad (2.26)$$

where $h(E)$ is a population distribution function, which gives the probability that a molecule has the energy E .

RRKM calculations were carried out with the help of the ChemRate program.¹⁹ In RRKM calculations, several input parameters need to be specified. (i) For the calculation of the density of states and the sum states in eq. 2.23, vibrational frequencies and rotational constants must be known. Of course, also the threshold energy E_0 must be calculated as accurate as possible. To solve the master equation, a collision model to account for energisation and de-energisation steps is required. In this work, the exponential-down model has been used, which is scaled by the average energy transfer parameter. This parameter corresponds to the efficiency of the collisions in terms of the mean energy transferred per collision $\langle \Delta E \rangle_{\text{all}}$ or the mean energy transferred per downward collision $\langle E \rangle_{\text{down}}$. The ChemRate program package requires the $\langle E \rangle_{\text{down}}$ parameter.

Input parameters were calculated with the Gaussian program package²⁰ using the G3²¹ (threshold energy, 0 K, rotational constants) and MP2 (vibrational frequencies). G3 is a composite method, which calculates molecular structures and vibrational frequencies on the HF/6-31G(d) level of theory and then refines the structure on the MP2/6-31G(d) level. Afterwards a series of single point energies is calculated to account for correlation effects. Finally, empirical parameters are used to correct for known deficiencies of this method. In this way, given that all approximations work well for the system under investigation, the resulting 0 K energies should be similarly accurate as the QCISD(T,FULL)/G3large level of theory. Since the vibrational frequencies are only calculated on the HF level, for the purpose of this work, the MP2/6-31G(d) method was used to obtain more accurate values. MP2 is an *ab initio* (perturbation) method. In contrast to HF, it takes into account electron correlation.

The mean energy transferred per collision $\langle \Delta E \rangle_{\text{all}}$ was calculated using the simplified ergodic collision theory (s-ECT) on intermolecular energy transfer.²² Here,

$$\langle \Delta E \rangle_{\text{all}}(E) = -\frac{2n_{M_{\text{vib}}} + n_{M_{\text{rot}}} + 3}{2n_{A_{\text{vib}}} + 2n_{M_{\text{vib}}} + n_{A_{\text{rot}}} + n_{M_{\text{rot}}} + 3} \times (E - \langle E \rangle_T) \times \beta_E. \quad (2.27)$$

n_{rot} and n_{vib} are the rotational and vibrational degrees of freedom of the reactant A and the collision partner M. $\langle E \rangle_T$ is the mean thermal energy of the reactant molecule ensemble. ECT assumes that the energy is completely statistically distributed among all degrees of freedom of both collision partners during the collision (ergodicity assumption). However the comparison with measurements shows that not all degrees of freedom take part in the redistribution process. To approximately take into account this fact, an energy transfer efficiency parameter β_E has been introduced according to

$$\beta_E = \langle \Delta E \rangle_{\text{measured}} / \langle \Delta E \rangle_{\text{ECT}}. \quad (2.28)$$

Hence, $0 < \beta_E < 1$, but usually $0.1 < \beta_E < 0.8$. The theory is then referred to as partially ergodic collision theory (PECT) and its simplified version (s-PECT), respectively. For the purpose of the ChemRate calculations, the desired parameter was $\langle \Delta E \rangle_{\text{down}}$, the mean energy of the downward collisions. $\langle E \rangle_{\text{all}}$ and $\langle E \rangle_{\text{down}}$ are connected by the relation²³

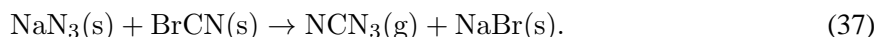
$$\langle E \rangle_{\text{down}} = -\frac{\langle \Delta E \rangle_{\text{all}}}{2} - \sqrt{\frac{\langle \Delta E \rangle_{\text{all}}^2}{4} - kT \langle \Delta E \rangle_{\text{all}}}. \quad (2.29)$$

with k being the Boltzmann constant. For the purpose of this work, temperature dependent $\langle E \rangle_{\text{all}}$ and $\langle E \rangle_{\text{down}}$ were calculated with the help of a very simple C++ routine, which is listed in the supplement. It is based on the s-PECT model and a statistical calculation of rotational, translational and vibrational energies as a measure of $\langle E \rangle_T$. To further simplify the treatment of the collision step, a single $\langle E \rangle_{\text{down}}$ value corresponding to $E = E_0$ was used in the ChemRate program.

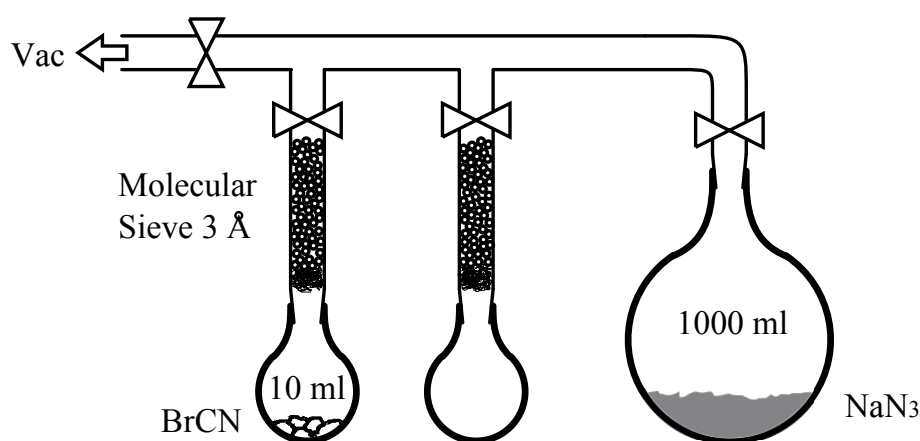
2.4 Precursors

2.4.1 Cyanogen azide (NCN₃) synthesis

The thermal decomposition of cyanogen azide (NCN₃) was used as an NCN radical source. NCN₃ is an extremely explosive and supposedly very toxic substance.²⁴ It holds the potential to explode spontaneously, especially in condensed state. For this reason, no attempt was made to purify NCN₃ after it had been synthesised. Instead, the reactants were prepared such that NCN₃ was obtained in very high purities. Of several different approaches, a variant of the method described by Milligan *et al.*²⁵ lead to the best results. The method is based on the heterogeneous reaction



The synthesis of NCN₃ was performed in the apparatus shown in figure 2.6. The whole apparatus was made of glass, all connections were thoroughly sealed by Halocarbon wax. The synthesis was performed at absolute pressures of ≈ 30 mbar. The apparatus also allowed for the purification of

Figure 2.6: Apparatus for the synthesis of high purity NCN_3 .

the reactants. NaN_3 was activated by re-crystallisation from hot H_2O (reflux, N_2H_4 added to obtain a finer crystals) by pouring the boiling solution into cold (-20°C) acetone. The filter cake was dried *i. vac.* overnight and pestled prior to synthesis. Alternatively to this procedure, a thorough pestling of small portions of not pre-treated NaN_3 was shown to be sufficient to obtain very fine NaN_3 crystals and to reach good purities of NCN_3 . The pestled NaN_3 was degassed *i. vac.* (10^{-4} mbar) overnight to remove H_2O and CO_2 . BrCN was degassed *i. vac.* (10^{-4} mbar) at $T = -78^\circ\text{C}$ for 10 min to remove CO_2 and HCN and was passed through a molecular sieve (3 \AA) to remove H_2O . It was re-sublimated at $T = -78^\circ\text{C}$ in a second flask to repeat the procedure. Then, BrCN was allowed to expand into the flask containing the NaN_3 by removing the cooling. For safety reasons, the amounts of BrCN were chosen such that the pressure of BrCN never exceeded 50 mbar. The vapour pressure of NCN_3 is estimated to be ≈ 100 mbar and condensation of NCN_3 must be avoided to rule out explosions. Furthermore, to maximise the reaction yield, NaN_3 was used in a huge excess. In a typical run, 0.25 g (2.5 mmol, weighed before re-sublimation) reacted with 10 g (170 mmol, weighed after re-crystallisation). After the reactants were brought in contact, the 1000 ml flask was closed. During the 8 h reaction time the flask was boldly, but carefully shaken every 30 min. Directly after the syntheses, the purity of the reaction product was checked by FTIR spectroscopy. Subsequently, the product was immediately diluted with argon to minimise bimolecular reactions. In > 50 syntheses, only one explosion was experienced, when NaN_3 of poor purity was used.

2.4.2 FTIR analysis

A typical FTIR (Bruker, IFS 66V, resolution: 0.25 cm^{-1}) spectrum of NCN_3 is shown in figure 2.7. The vibrational bands have been assigned according to Bak *et al.*²⁶ Three of the nine fundamental vibrations could be observed in the investigated wavelength region, they are denoted ν_{1-3} in the figure. All absorption features, except for the weakest transition around 2655 cm^{-1} have already

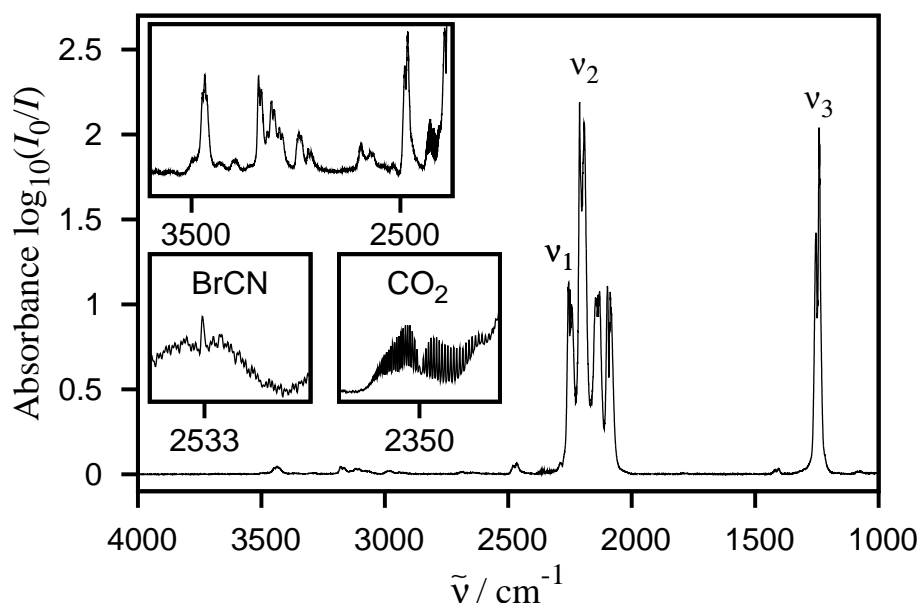


Figure 2.7: IR spectrum of NCN_3 at an NCN_3 pressure of $p = 30.6$ mbar. The insets show magnifications of weak NCN_3 absorption bands and of the two minor impurities BrCN and CO_2 .

been reported by Bak *et al.* and have been assigned to different combination vibrations. Measured IR spectra of possible side products and impurities of the reaction (HN_3 , BrN_3 ²⁷, HCN , $(\text{CN})_2$ ²⁸) showed that neither of them was present in the samples and could thus account for the absorption band at 2650 cm^{-1} . This very weak band was only detected when using a very sensitive liquid nitrogen cooled detector. It was assigned to a combination of the fundamentals $\nu_4 + 2 \times \nu_5$ (see Table 3 in Ref. 26), which add up to 2651 cm^{-1} . Moreover, the separation between P and R branch of this transition is approximately 15 cm^{-1} and thus in good agreement with the other transitions.

Impurities: The mole fraction of the BrCN impurity in the spectrum in Figure 2.7 is 1.8%, CO_2 is present at a mole fraction of $< 0.1\%$, only. Following every synthesis, the BrCN partial pressure has been determined by comparison with BrCN calibration spectra. A spectrum of BrCN is shown in figure 2.8, a plot of BrCN absorbance versus BrCN pressure is provided in figure 2.9. Typically, BrCN impurities were $< 1\%$ and never exceeded 3% in the samples used for kinetic measurements.

NCN_3 partial pressures of samples diluted in argon were determined based on a similar calibration curve. Since the absolute pressure of the diluted samples used for the shock tube experiments is orders of magnitude higher than the pure NCN_3 samples used for the calibration, integral absorption values were used instead of the peak height to avoid errors due to different line broadening behaviour. Integrals of the intense peak at 1250 cm^{-1} (denoted ν_3 in figure 2.7) were used, which does not interfere with any absorption lines of the possible impurities. To minimise base line issues, the integrals were approximated by a sum of two Lorentzian functions. The calibration curve of these data is shown

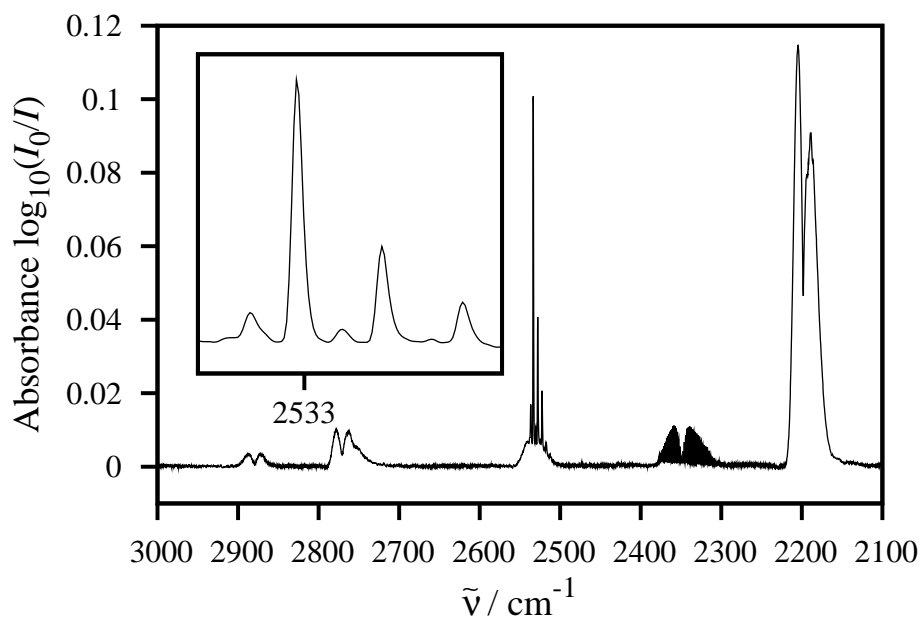


Figure 2.8: IR spectrum of BrCN at $p = 24.8 \text{ mbar}$. The striking feature around 2533 cm^{-1} was used for the calibrating the concentration measurements (see Figure 2.10).

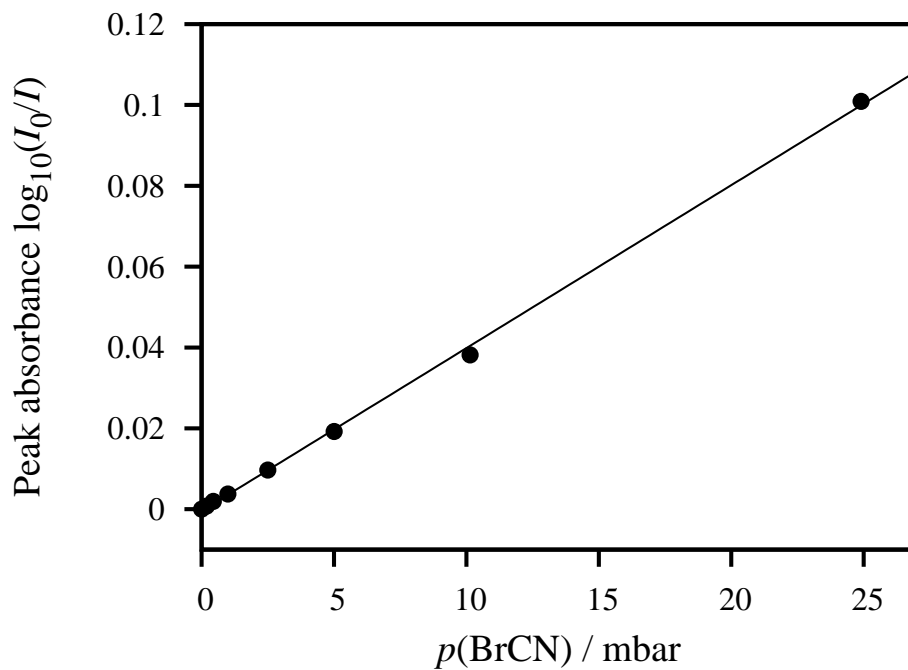


Figure 2.9: BrCN calibration curve. The slope is $4.03 \times 10^{-3} \text{ mbar}^{-1}$.

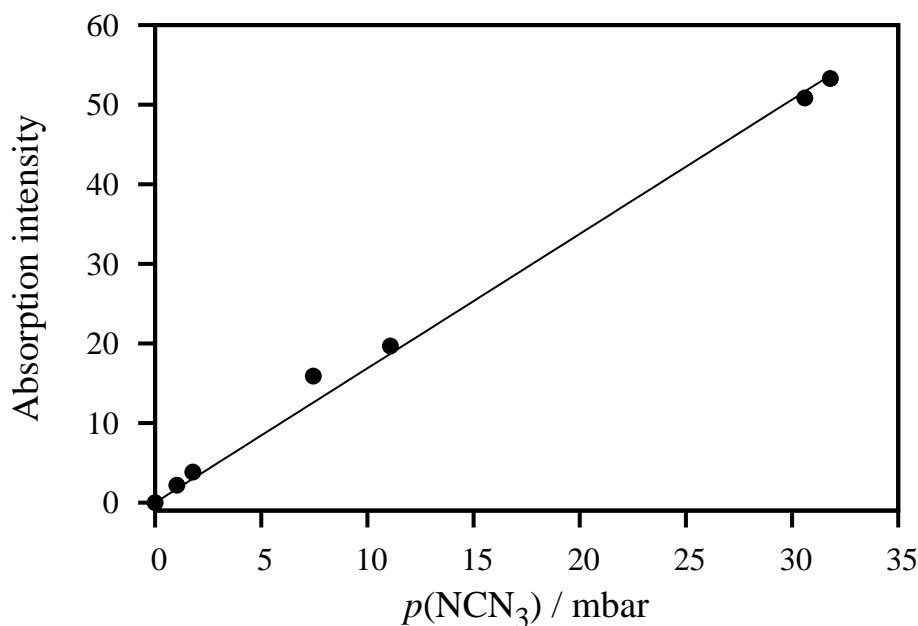


Figure 2.10: NCN_3 calibration curve. Integrated absorption intensities of the $\tilde{\nu}_3$ fundamental band have been used. The slope of the curve is 1.65 mbar^{-1} .

in figure 2.10. It was found that even diluted NCN_3 samples undergo a slow decomposition process (5 – 10% per day). Therefore, for the determination of absolute absorption cross sections (see chapter 3), this FTIR analysis of the diluted samples was performed on a daily basis. Moreover, all NCN_3 mixtures were used within three days after the synthesis.

2.4.3 Glyoxal ((CHO)₂) preparation

Glyoxal ((CHO)₂) was prepared by dehydration of the trimer dehydrate ((CHO₂)₃)·2H₂O.⁹ A mixture of 1 eq. ((CHO₂)₃)·2H₂O, 3 eq. of phosphoric anhydride (P₂O₅) and some silica sand were slowly heated up *i. vac.* to a temperature of $T = 155^\circ \text{C}$. The gaseous reaction products were passed through a cooling trap ($T = 0^\circ \text{C}$) to remove impurities. Yellow crystals were obtained in a second cooling trap ($T = -196^\circ \text{C}$). FTIR analysis showed no impurities of H₂O or CO₂. The monomeric glyoxal was stored in liquid nitrogen. For the preparation of 1% mixtures in argon, the first few mbar of the sublimating (CHO)₂ were discarded. At longer storage times of the monomeric glyoxal, a polymeric substance formed on the walls of the stainless steel storage tank. Therefore, glyoxal/argon mixtures were used within four days after preparation.

Bibliography

- [1] A. P. Vieille, Etude sur le role des discontinuités dans le phénomènes de propagation, *Mém. poudres et salpêtres* **1899**, 10, 117–120.
- [2] W. Payman and W. F. C. Shepherd, The Disturbance Produced by Bursting Diaphragms with Compressed Air, *Proc. Roy. Soc. London Ser. A* **1946**, 186, 293–321.
- [3] A. Hertzberg and A. R. Kantrowitz, Studies with an Aerodynamically Instrumented Shock Tube, *J. Appl. Phys.* **1950**, 21, 874–879.
- [4] G. L. Schott and J. L. Kinsey, Kinetic Studies of Hydroxyl Radicals in Shock Waves II. Induction Times in the Hydrogen Oxygen Reaction, *J. Chem. Phys.* **1958**, 29, 1177–1182.
- [5] K. A. Bhaskaran and P. Roth, The Shock Tube as Wave Reactor for Kinetic Studies and Material Systems, *Progress in Energy and Combustion Science* **2002**, 28, 151–192.
- [6] A. G. Gaydon and I. R. Hurler, *The Shock Tube in High Temperature Chemical Physics*, Chapman and Hall, London, **1963**.
- [7] H. Oertel, *Stossrohre*, Springer-Verlag, Wien, New York, **1966**.
- [8] M. Klatt, *Quantitative Untersuchung der Bildung und des Verbrauchs von H- und O-Atomen sowie OH-Radikalen in verschiedenen Elementarreaktionen bei hohen Temperaturen.*, Ph.D. thesis, Universität Göttingen, **1991**.
- [9] M. Colberg and G. Friedrichs, Room Temperature and Shock Tube Study of the Reaction $\text{HCO} + \text{O}_2$ Using the Photolysis of Glyoxal as an Efficient HCO Source, *J. Phys. Chem A* **2006**, 110, 160–170.
- [10] K. Dressler and D. A. Ramsay, The Electronic Absorption Spectra of NH_2 and ND_2 , *Phil. Trans. Soc. Lond.* **1959**, 251, 553–602.
- [11] G. Friedrichs, *Frequenzmodulierte Spektroskopie zur Untersuchung von Reaktionen des Amino- und Methylenradikals hinter Stoßwellen*, Cuvillier-Verlag, Göttingen, **1999**, ISBN 3-89712-741-5, Ph.D. thesis, Universität Göttingen.
- [12] M. Colberg, *Aufbau und Charakterisierung einer Stoßwellenapparatur zur Untersuchung von Hochtemperaturreaktionen des Formylradikals*, Ph.D. thesis, Christian-Albrechts-Universität zu Kiel, **2006**.
- [13] J. Dammeier, *High Temperature Kinetics of the Reactions $\text{HCO} + \text{NO} \rightarrow \text{HNO} + \text{CO}$ and $\text{HCO} + \text{NO}_2 \rightarrow \text{Products}$ Studied by Frequency Modulation Spectroscopy Behind Shock Waves*, Diploma thesis, **2006**.

- [14] T. Williams, C. Kelley *et al.*, gnuplot, <http://www.gnuplot.info>, **2010**, version 4.4.
- [15] R. J. Kee, F. M. Ruply, and J. A. Miller, Chemkin-II: A Fortran Chemical Kinetics Package for the Analysis of Gas Phase Chemical Kinetics, Sandia report sand89-8009, Sandia National Laboratories, Livermore, CA, **1989**.
- [16] A. A. Konnov, Detailed Reaction Mechanisms for Small Hydrocarbon Combustion, http://homepages.vub.ac.be/akonnov/science/mechanism/version0_5.html, **2007**, release 0.5.
- [17] E. Goos, A. Burcat, and B. Ruscic, Ideal Gas Thermochemical Database with Updates from Active Thermochemical Tables, <ftp://ftp.technion.ac.il/pub/supported/aetdd/thermodynamics>, **2010**.
- [18] G. P. Smith, D. M. Golden, M. Frenklach, N. W. Moriarty, B. Eiteneer, M. Goldenberg, C. T. Bowman, R. K. Hanson, S. Song, W. C. G. Jr., V. V. Lissanski, and Z. Qin, GRI-MECH 3.0, http://www.me.berkeley.edu/gri_mech/.
- [19] V. Mokrushin, V. Bedanov, W. Tsang, M. Zachariah, and V. Knyazev, ChemRate Version 1.5.2, **1996–2006**, National Institute of Standards and Technology, Gaithersburg, USA.
- [20] M. J. Frisch, G. W. Trucks, H. B. Schlegel, G. E. Scuseria, M. A. Robb, J. R. Cheeseman, J. A. Montgomery, Jr., T. Vreven, K. N. Kudin, J. C. Burant, J. M. Millam, S. S. Iyengar, J. Tomasi, V. Barone, B. Mennucci, M. Cossi, G. Scalmani, N. Rega, G. A. Petersson, H. Nakatsuji, M. Hada, M. Ehara, K. Toyota, R. Fukuda, J. Hasegawa, M. Ishida, T. Nakajima, Y. Honda, O. Kitao, H. Nakai, M. Klene, X. Li, J. E. Knox, H. P. Hratchian, J. B. Cross, V. Bakken, C. Adamo, J. Jaramillo, R. Gomperts, R. E. Stratmann, O. Yazyev, A. J. Austin, R. Cammi, C. Pomelli, J. W. Ochterski, P. Y. Ayala, K. Morokuma, G. A. Voth, P. Salvador, J. J. Dannenberg, V. G. Zakrzewski, S. Dapprich, A. D. Daniels, M. C. Strain, O. Farkas, D. K. Malick, A. D. Rabuck, K. Raghavachari, J. B. Foresman, J. V. Ortiz, Q. Cui, A. G. Baboul, S. Clifford, J. Cioslowski, B. B. Stefanov, G. Liu, A. Liashenko, P. Piskorz, I. Komaromi, R. L. Martin, D. J. Fox, T. Keith, M. A. Al-Laham, C. Y. Peng, A. Nanayakkara, M. Challacombe, P. M. W. Gill, B. Johnson, W. Chen, M. W. Wong, C. Gonzalez, and J. A. Pople, Gaussian 03, Revision D.01, Gaussian, Inc., Wallingford, CT, 2004.
- [21] L. A. Curtiss, K. Raghavachari, P. C. Redfern, V. Rassolov, and J. A. Pople, Gaussian-3 (G3) Theory for Molecules Containing First and Second-Row Atoms, *J. Chem. Phys.* **1998**, *109*, 7764–7776.
- [22] D. Nilsson and S. Nordholm, Statistical Model of Energy Transfer in Molecular Collisions: De-Energization of Highly Excited Toluene, *J. Chem. Phys.* **2002**, *116*, 7041–7048.
- [23] M. Quack and J. Troe, *Gas Kinetics and Energy Transfer: Volume 2 (Specialist Periodical Reports), Chapter 5: Unimolecular Reactions and Energy Transfer of Highly Excited Molecules*, P. G. Ashmore and R. J. Donovan, The Chemical Society, London, **1972**.

2. Experimental

- [24] H. Bock and R. Dammel, The Pyrolysis of Azides in the Gas Phase, *Angew. Chem. Int. Ed. Engl.* **1987**, *26*, 504–526.
- [25] D. E. Milligan, M. E. Jacox, and A. M. Bass, Matrix-Isolation Study of the Photolysis of Cyanogen Azide. The Infrared and Ultraviolet Spectra of the Free Radical NCN, *J. Chem. Phys.* **1965**, *43*, 3149–3160.
- [26] B. Bak, F. Nicolaisen, and O. Rump, Assignment of Vibrational Frequencies in the Infrared and Raman Spectra of Cyanogen Azide, *Spectrochim. Acta A* **1971**, *27*, 1865–1871.
- [27] A. Schulz, I. C. Tornieporth-Oetting, and T. M. Klapötke, Experimental and Theoretical Vibrational Studies of Covalent X-N₃ Azides (X = H, F, Cl, Br, I). Application of the Density Functional Theory and Comparison with ab Initio Results, *Inorg. Chem.* **1995**, *34*, 4343–4346.
- [28] P. Linstrom, N. I. o. S. W.G. Mallard, and . Technology, Gaithersburg MD, "Evaluated Infrared Reference Spectra" in NIST Chemistry WebBook, NIST Standard Reference Database Number 69, <http://webbook.nist.gov>.

2.5 Supplement: Program for the calculation of $\langle \Delta E \rangle_{\text{all}}$ and $\langle \Delta E \rangle_{\text{down}}$

```
/* Johannes Dammeier, CAU zu Kiel, 2009
Plan: Berechnung von DeltaE, der mittleren pro Stoss
ausgetauschten Energie fuer NCN3 und Argon nach dem sECT-
Modell, Nordholm et al., Chem Phys 1977,25,433; Nilsson
und Nordholm, JCP 2003,119,7040 */

#include <stdio.h>
#include <float.h>
#include <math.h>
#include <stdlib.h>

const double k=1.3806503E-23;
const double h=6.62606876E-34;
const double c=2.99792458E08;

/* Funktionen zur Berechnung der mittleren Energie ET" */
double mittleretranslationsenergie (double T)
{
    double utrans;

    utrans=3./2.*k*T;
    return utrans;
}
double mittlererotationsenergie (double T)
{
    double urot;
    urot=3./2.*k*T;
    return urot;
}
double mittlereschwingsenergie (double T)
/* Wedler Kapitel Statistische Thermodynamik, S. 641 */
{
    int i=0,j=0;
    double uvib=0,unull=0;
    double nue[100];
    FILE *input;
    input=fopen("Frequenzen.inp","r");
    fscanf(input,"%i",&j);
    /* Einlesen der Schwingungsfrequenzen*/
    for (i=0;i<j;++i)
    {
        fscanf(input,"%lf",&nue[i]);
        nue[i]=nue[i]*100.*c;
        // printf("%lf\n",nue[i]);
    }
    fclose(input);
    /* Berechnung der mittleren Schwingungsenergie uvib inklusive der
    Nullpunktenergie, Naeherung harmonischer Oszillator */
    for (i=0;i<j;++i)
    {
        uvib=uvib+1./2.*h*nue[i]+h*nue[i]/(exp(h*nue[i]/(k*T))-1));
        // printf("%i %e %e\n",i,T);
    }
}
```

2. Experimental

```
    }
    return uvib;
}

double nullpunktsenergie ()
{
    int i,j;
    double unull=0;
    double nue[100];
    FILE *input;
    input=fopen("Frequenzen.inp","r");
    fscanf(input,"%i",&j);
    /* Einlesen der Schwingungsfrequenzen*/
    for (i=0;i<j;++i)
    {
        fscanf(input,"%lf",&nue[i]);
        nue[i]=nue[i]*100.*c;
        // printf("%lf\n",nue[i]);
    }
    fclose(input);
    for (i=0;i<j;++i)
    {
        unull=unull+1./2.*h*nue[i];
        // printf("%i %e\n",i,unull);
    }
    return unull;
}

main()
{
    int AnzahlderRechnungen,i;
    double Tunten,Toben,DeltaT,T;
    double utrans,urot,uvib,unull,uges;
    double E0,E,DeltaE,j,DeltaEdown,E02,rotfrei,schwingfrei;
    printf("untere Temperatur angeben!\n");
    scanf("%lf",&Tunten);
    printf("obere Temperatur angeben!\n");
    scanf("%lf",&Toben);
    printf("Temperaturbereich ist: %lf-%lf K\n",Tunten,Toben);
    printf("Delta T angeben!\n");
    scanf("%lf",&DeltaT);
    printf("Gewuenschte Energie in cm^-1 angeben!\n");
    scanf("%lf",&E02);
    AnzahlderRechnungen=(Toben-Tunten)/DeltaT+1;
    FILE *input;
    input=fopen("Frequenzen.inp","r");
    fscanf(input,"%lf",&j);
    fclose(input);
    FILE *input2;
    input2=fopen("AnzahlFreiheitsgradeStosspartner.inp","r");
    fscanf(input2,"%lf",&rotfrei);
    fscanf(input2,"%lf",&schwingfrei);
    fclose(input2);
    FILE *output;
    output=fopen("mittlereEnergieundDeltaE.out","w+");
    fprintf(output,"T/K uges/cm^-1 DeltaEall/cm^-1 DeltaEdown/cm^-1\n");
```

2. Experimental

```
    for (i=0;i<AnzahlDerRechnungen;++i)
    {
T=Tunten+i*DeltaT;
utrans=mittlereTranslationsenergie(T);
urot=mittlererRotationsenergie(T);
uvib=mittlereschwingungsenergie(T);
unull=nullpunktsenergie();
E0=E02*100.*h*c;
uges=uvib+urot+utrans;
E=E0+unull+urot+utrans;

// printf("Translationsenergie ist: %e J\n",utrans);
// printf("Rotationsenergie ist: %e J\n",urot);
// printf("Schwingungsenergie ist: %e J\n",uvib);
// printf("Gesamtenergie ist: %e J\n\n\n",uges);

//J. Chem. Phys. 119, hier eigentliche Rechnung
DeltaE=-(2.*schwingfrei+rotfrei+1.)
        /(2*j+3.+2.*schwingfrei+rotfrei+1.)*(E-uges);

//empirische Korrektur des simple ECT models, beta-Parameter
DeltaE=DeltaE*0.5;

/* Umrechnung in DeltaEdown, Troe: Gas Kinetics and Energy Transfer -
Volume 2: Ashmore, Donovan, The Chemical Society, London 1972,
neglecting energy dependence of rho(E) */
DeltaEdown=-DeltaE/2.-sqrt(pow(DeltaE,2.)/4.-k*T*DeltaE);

uges=uges/100./c/h;
DeltaE=DeltaE/100./c/h;
DeltaEdown=DeltaEdown/100./c/h;
//printf("%e",unull);

fprintf(output,"%lf.0 %e %e %e\n",T,(uges-unull),DeltaE,DeltaEdown);
    }
    fclose(output);
    printf("\n\nfaeaedisch!\n\n");
    return 0;
}
```

2. Experimental

Example input file

```
9
180
484
508
572
716
924
1252
2410
2465
```

in erste Zeile Anzahl der Schwingungsfreiheitsgrade eingeben,
danach die einzelnen Schwingungsfrequenzen in cm^{-1}

nur fuer Molekuele mit drei Rotationsfreiheitsgraden!

Example output file

```
T/K uges/ $\text{cm}^{-1}$  DeltaEall/ $\text{cm}^{-1}$  DeltaEdown/ $\text{cm}^{-1}$ 
500.000000 7.112731e+03 -1.647801e+02 3.354752e+02
1000.000000 1.094582e+04 -1.013588e+02 3.208948e+02
1500.000000 1.444036e+04 -4.563172e+01 2.421195e+02
2000.000000 1.747782e+04 -2.931271e-01 2.033292e+01
```

3 The Thermal Decomposition of NCN_3 as a High Temperature NCN Radical Source: Singlet-Triplet Relaxation and Absorption Cross Section of $\text{NCN}(^3\Sigma)$

Johannes Dammeier and Gernot Friedrichs*

Institut für Physikalische Chemie,
Christian-Albrechts-Universität zu Kiel

Reprinted with permission from *J. Phys. Chem. A* **2010**, *114*, 12963–12971.
Copyright 2010 American Chemical Society.

Own contributions to this paper:

- NCN_3 : synthesis and characterisation
- Room temperature and shock tube measurements
- Quantum chemical and statistical calculations
- Data analysis and discussion

*friedrichs@phc.uni-kiel.de

Abstract

The potential of the thermal decomposition of cyanogen azide (NCN₃) as a high temperature cyanonitrene (NCN) source has been investigated in shock tube experiments. Electronic ground state NCN($^3\Sigma$) radicals have been detected by narrow-bandwidth laser absorption at overlapping transitions belonging to the Q₁ branch of the vibronic $^3\Sigma^+ - ^3\Pi$ subband of the vibrationally hot $\tilde{A}^3\Pi_u(010) - \tilde{X}^3\Sigma_g^-(010)$ system at $\tilde{\nu} = 30383.11 \text{ cm}^{-1}$ (329.1302 nm). High temperature absorption cross sections σ have been directly measured at total pressures of 0.2-2.5 bar.

$$\log \left(\frac{\sigma}{\text{cm}^2/\text{mol}} \right) = 8.9 - 8.3 \times 10^{-4} \times T/\text{K} \quad (\pm 25\%, 750 \text{ K} < T < 2250 \text{ K})$$

At these high temperatures, NCN($^3\Sigma$) formation is limited by a slow electronic relaxation of the initially formed excited NCN($^1\Delta$) radical rather than thermal decomposition of NCN₃. Measured temperature dependent collision-induced intersystem crossing (CIISC) rate constants are best represented by

$$k_{\text{CIISC}}/(\text{cm}^3 \text{mol}^{-1} \text{s}^{-1}) = (1.3 \pm 0.5) \times 10^{11} \exp[-(21 \pm 4) \text{ kJ/mol}/RT],$$

$$(740 \text{ K} < T < 1260 \text{ K})$$

Nevertheless, stable NCN concentration plateaus have been observed showing that NCN₃ is an ideal precursor for NCN kinetic experiments behind shock waves.

3.1 Introduction

The nitrogen oxides NO and NO₂ (NO_x) are main pollutants of combustion processes and play an important role in tropospheric ozone formation as well as stratospheric ozone depletion by triggering two different chain reaction cycles.¹ Additionally, nitrous oxide (N₂O), a secondary product of NO_x reactions, is of environmental concern due to its high global warming potential.² From several distinct NO formation pathways, especially under rich combustion conditions, *prompt-NO* is generated by reactions of small hydrocarbon radicals with nitrogen stemming from the combustion air. Until recently, it was well accepted that the most important initiation step of prompt-NO formation, according to the Fenimore mechanism,³ is the spin-forbidden reaction



In subsequent reaction steps, N atoms are then transformed into NO.⁴ Assuming that the initially formed energetically excited addition complex undergoes fast intersystem crossing from the doublet to quartet potential energy surface, this only slightly endothermic ($\Delta_r H_{0\text{K}}^\circ = 9 \text{ kJ/mol}$)⁵ reaction

3. High Temperature NCN Radical Source and Absorption Cross Section of NCN($^3\Sigma$)

seemed to be a reasonable candidate for N_2 activation. Moreover, measured activation energies of $E_a \approx 75$ kJ/mol were found to be consistent with a reaction barrier stemming from an elimination step of the postulated quartet intermediate.^{6,7} However, detailed calculations of the intersystem crossing probability led to the conclusion that the overall reaction rate should be much smaller than experimentally measured.⁸ In the year 2000, Moskaleva et al.^{9,10} seemed to have resolved this issue by showing that another spin-allowed, endothermic ($\Delta_r H_{0K}^\circ = 82$ kJ/mol) reaction pathway exists. Based on quantum-chemical exploration of the potential energy surface followed by RRKM and master equation modeling they concluded that the NCN radical forming channel,



dominates the overall reaction. Very recently, another high-temperature reaction channel passing through an alternative intermediate structure (HNNC instead of HCNN) has been discovered.^{5,11} This pathway eventually yields NCN($^3\Sigma$) radicals and H(2S) atoms as well.

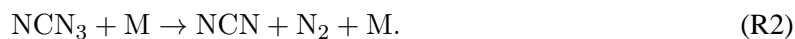
The theoretical predictions of Moskaleva et al. have stimulated much experimental effort in order to clarify the role of NCN radicals in NO formation processes. First experimental evidence for the existence of NCN in flames were provided by LIF detection of NCN reported by Smith¹² and, more recently, by Sutton et al.¹³ and Klein-Douwel et al.¹⁴ In all three studies, NCN concentrations were found to be strongly correlated with the corresponding CH signal. However, it was not until the carefully conducted shock tube experiments of Vasudevan et al.¹⁵ that NCN was shown to be the main product (> 70%) of the reaction $CH + N_2$ at temperatures of $2228 \text{ K} < T < 2905 \text{ K}$. The branching fraction of reaction (R1b) was deduced from detailed modeling of CH concentration profiles measured during the pyrolysis of C_2H_6/Ar mixtures in the presence of N_2 behind shock waves. Vasudevan et al. also detected NCN profiles by laser absorption, which were used to infer NCN absorption cross sections at $\tilde{\nu} = 30383 \text{ cm}^{-1}$ as well as to estimate the high temperature rate constant of the reaction $H + NCN$. So far, to the best of our knowledge, the only other experimental study on NCN high temperature kinetics (i.e., for temperatures $T > 1000 \text{ K}$) was reported by Busch and Olzmann^{16,17} who generated NCN radicals behind shock waves using the fast thermal decomposition of NCN_3 as a NCN radical source. At temperatures of $1800 \text{ K} < T < 2900 \text{ K}$, rate constants of the thermal unimolecular decomposition of NCN were obtained from time-resolved concentration profiles of the reaction products C and N. NCN radicals were not detected.

Other recent work was concerned with the experimental investigation of NCN radical reactions at low temperatures,^{16–22} For example, Baren and Hershberger¹⁸ measured the rate constant of the reaction $NCN + NO$ in the temperature range of $298 \text{ K} < T < 573 \text{ K}$. NCN radicals were generated by 193 nm UV flash photolysis of diazomethane in the presence of cyanogen (CH_2N_2/C_2N_2) and were detected by LIF at a wavenumber of $\tilde{\nu} = 30395 \text{ cm}^{-1}$ ($\lambda \approx 329 \text{ nm}$). Other authors employed 193 nm photolysis of cyanogen azide (NCN_3) as an efficient NCN source,^{19,20,22} in which the initially formed electronically excited $NCN(^1\Delta)$ is subsequently deactivated by collisions to its $NCN(^3\Sigma)$

3. High Temperature NCN Radical Source and Absorption Cross Section of NCN($^3\Sigma$)

ground state.²³ Theoretical work on bimolecular NCN reactions has been mainly performed in the M. C. Lin group. Mostly scaled to fit low temperature experimental rate constant data, high temperature extrapolations were reported for the reactions with NO and NS,^{19,24} NO₂,²⁰ O₂,²⁵ OH,²⁶ and O.²⁷ Finally, first mechanistic studies on NO_x formation by implementing NCN chemistry were conducted by El Bakali et al.,²⁸ Sutton and Fleming,²⁹ Gersen et al.,³⁰ and Konnov.³¹

Although these studies serve as a good starting point for future prompt NO modeling, NCN kinetics model refinements and theoretical predictions should be based on or validated against direct high temperature measurements of NCN rate constants as well. A prerequisite of such direct measurements is the availability of a clean NCN source. In this work, the thermal decomposition of cyanogen azide, NCN₃ has been studied with regard to its potential to serve as such a precursor in shock tube experiments. According to Bock and Dammel³² and Benard et al.³³ the initiating pyrolysis step of NCN₃ can be assumed to yield NCN quantitatively:



We detected NCN, which can be assumed to be initially formed in its first excited electronic singlet state ($^1\Delta$) due to spin conservation, in its electronic $^3\Sigma$ ground state by means of time-resolved laser absorption spectroscopy at wavenumbers around $\tilde{\nu} = 30395 \text{ cm}^{-1}$. NCN($^3\Sigma$) formation rate constants have been extracted from concentration-time profiles measured during pyrolysis experiments of NCN₃ behind incident and reflected shock waves. Moreover, absorption cross sections of NCN($^3\Sigma$) have been directly determined from the observed absorption plateaus at long reaction times. The unimolecular decomposition of NCN₃ was analyzed based on quantum-chemical calculations and statistical rate calculations combined with master equation modeling. A comparison of predicted and experimental temperature dependences revealed that a rather slow collision induced intersystem crossing pathway, $\text{NCN}(^1\Delta) + \text{M} \rightarrow \text{NCN}(^3\Sigma) + \text{M}$ plays a decisive role.

3.2 Experimental

Shock Tube and Slow Flow Photolysis Reactor

High temperature experiments were carried out in an electro-polished stainless steel shock tube of 8 m overall length.³⁴ The 4.4 m long test section with an inner diameter of 81 mm could be evacuated by a combination of oil free turbomolecular drag and diaphragm pumps down to pressures of $p \approx 10^{-7}$ mbar. The shock tube was operated by hydrogen, nitrogen or hydrogen/nitrogen mixtures as driver gas using 30 or 80 μm thick aluminium diaphragms. Experimental temperatures and pressures were calculated from pre-shock conditions and the shock wave velocity, which was measured by a fast count unit wired to four piezo-electric sensors (PCB Piezotronics M 113A21). The registered damping of the shock wave on the order of 1% per meter as well as real gas effects were taken into account

3. High Temperature NCN Radical Source and Absorption Cross Section of $\text{NCN}(^3\Sigma)$

when calculating the shock wave parameters based on a 1-dimensional, frozen chemistry computer code.

Room temperature spectra were recorded using a 45 cm long slow flow photolysis cell equipped with quartz windows. 193 nm UV photolysis of cyanogen azide in Ar mixtures was performed collinearly with the detection laser beam by combining and dividing the photolysis and detection laser by an optical setup with two dichroic mirrors. Although continuously flushed with pure nitrogen, deposition of polymeric material took place at the quartz windows and therefore regular cleaning of the cell windows was necessary.

NCN₃ Synthesis and Gas Mixtures

Cyanogen azide is an extremely explosive substance; for that reason no attempt was made to condense or to purify the gas after the synthesis. Instead, care was taken to directly synthesize NCN_3 as pure as possible using a variant of a synthesis described by Milligan et al.³⁵ Basically, solid sodium azide (NaN_3) and gaseous cyanogen bromide reacted to form gaseous cyanogen azide and solid sodium bromide (NaBr). Cyanogen bromide was purified by re-sublimation and further dried by passing it through a molecular sieve (3 Å). Sodium azide was pestled and then degassed in vacuo overnight at pressures down to 1×10^{-4} mbar. Small amounts (~ 20 mbar) of gaseous cyanogen bromide were allowed to expand into an evacuated flask, which held a huge excess of sodium azide. After 8 h reaction time and repeated careful shaking of the reaction flask, the gaseous product was let into another pre-evacuated storage flask. Immediate analysis of the gaseous reaction product by means of FTIR spectroscopy showed that no water (indicator for gas leak) and only negligible amounts of carbon dioxide ($\approx 0.01\%$) were present. Levels of remaining cyanogen bromide were always $< 3\%$, but in some syntheses an overall purity of $> 99\%$ NCN_3 was achieved. Subsequently, cyanogen azide was diluted with argon and the 0.1-0.5% NCN_3/Ar mixtures, which were stored in a 10 liter glass flask, were used within 3 days after preparation. Since noticeable decomposition of typically 10% per day was found to take place, NCN_3 concentrations were checked by FT-IR on a daily basis. For shock tube experiments, the supply mixtures were further diluted with argon using calibrated mass flow controllers (Aera FC-7700C). Although no noticeable dependence of the absorption signal on the sample preparation procedure was found, the shock tube was flushed with the particular mixture at a pressure of ≈ 50 mbar to minimize any wall adsorption effects.

Gases and chemicals used were argon (99.999%, hydrogen and nitrogen (99.99%, as driver gas), sodium azide (Merck, 99%), and cyanogen bromide (Acros, 97%).

Laser Absorption Setup

NCN was detected in its triplet ground state at $\tilde{\nu} \approx 30395 \text{ cm}^{-1}$ using difference amplification laser absorption spectroscopy. In order to clarify the role of singlet NCN relaxation, some measurements were also performed at $\tilde{\nu} = 30045.7 \text{ cm}^{-1}$. Tunable narrow-bandwidth ($< 10 \text{ MHz}$) UV laser radiation was provided by internal frequency doubling of a frequency stabilized continuous-wave ring-dye laser (Coherent 899) operated with DCM-Special dye. The dye laser was pumped by 8 W of a frequency-doubled Nd:YVO₄ solid states laser (Coherent Verdi V10) at a wavelength of 532 nm resulting in 1.5 mW UV output. The wavelength of the laser fundamental was measured by means of an interferometric type wavemeter referenced to a HeNe laser beam (MetroLux WL200). The readout of the wavemeter was corrected for a small systematic wavelength offset of 0.02 cm^{-1} at $\tilde{\nu} = 15129 \text{ cm}^{-1}$, which was determined by measuring the known wavelengths of several absorption lines of NH₂, resulting in an overall accuracy of the wavelength determination on the order of 5×10^{-7} corresponding to $\Delta\tilde{\nu} \approx \pm 0.015 \text{ cm}^{-1}$ at $\tilde{\nu} = 30395 \text{ cm}^{-1}$. The UV laser beam was split into detection and reference beam by a 50:50 beam splitter plate, where the intensity of the reference beam could be fine-tuned using a variable neutral density filter. The detection beam was passed through the photolysis cell and the shock tube, respectively. The beams were coupled into two separate optical fibres (Thorlabs BF H22-550), which were connected to a balanced photo detector and amplifier (Thorlabs PDB150A-EC). For shock tube measurements, the resulting difference signal was low-pass filtered (1.4 MHz), further amplified (Ortec Fast Preamp 9305, 18 dB) and finally stored by an analog input board (Measurement Computing PCI-DAS4020/12, 12 bit, 20 MHz). For the measurement of room temperature absorption spectra, the wavelength of the detection laser was slowly scanned (20 GHz mode-hop free scan range) and the measured absorption signals were processed in a boxcar amplifier (Stanford Research Systems, SR250, 235, 280). The differences of the boxcar integrals measured after and before the UV photolysis laser pulse were taken as a measure of absorption and were stored in a digital oscilloscope (LeCroy WaveSurfer 454, 500MHz, 8 bit), which was synchronized with the scanning laser.

Numerical Methods

Spectral simulations of the NCN absorption spectra were performed with the PGOPHER program, which is a general purpose program for simulating and fitting rotational, vibrational and electronic spectra developed by the Bristol laser group.³⁶ The complex electronic spectrum of NCN was calculated based on accurate spectroscopic constants taken from Beaton et al.,^{37,38} which have been recently recast and refitted in the work of Lamoureux et al.³⁹ Using the same spectroscopic parameters as they have been used and explained in the work of Lamoureux et al., it was possible to predict temperature dependent spectral contours in order to select a suitable detection wavelength for high temperature measurements of NCN concentration-time profiles.

Thermal rate constants of the unimolecular decomposition of NCN₃ were modeled within the framework of statistical rate theories. Standard RRKM calculations followed by solution of the energy-grained master equation were performed using the NIST ChemRate program package that enables one to calculate time-dependent and steady-state rate coefficients for thermally or chemically activated unimolecular reactions.⁴⁰ Input parameters for the RRKM model have been obtained from ab initio quantum chemical calculations on the G3 (energies) and MP2/6-311+G(d,p) (rotational constants, vibrational frequencies) level of theory⁴¹ using the program suite Gaussian 03.⁴² The harmonic vibrational wavenumbers were scaled by a factor of 0.9496 according to Scott and Radom.⁴³ The transition state was located using the transient-guided quasi-Newton method (QST3) and was verified by vibration frequency calculations and intrinsic reaction coordinate analysis.

3.3 Results and discussion

3.3.1 Room temperature photolysis

The NCN radical is linear in its ground and first excited triplet electronic state. The electronic spectrum is complicated due to the partial overlap of 27 branches originating from the $\tilde{A}^3\Pi_u(000) - \tilde{X}^3\Sigma_g(000)$ transition. Especially at high temperatures, spectral contributions from the (010)–(010) hot band, which is split into three Renner-Teller components in the excited state, have to be taken into account as well. So far, high temperature detection of NCN in flames^{12,13,39} as well as the shock tube work of Vasudevan et al.¹⁵ has been mostly performed at wavenumbers $\tilde{\nu}$ around 30385 cm⁻¹. Therefore, as a starting point, we recorded a high resolution room temperature spectrum of NCN at 30381 cm⁻¹ < $\tilde{\nu}$ < 30386 cm⁻¹ following the 193 nm photolysis of NCN₃. The spectrum is shown in the upper graph of Fig. 1 and has been pieced together from six successive 20 GHz scans. The individual spectral intensities have been rescaled in order to account for different NCN concentrations associated with variable photolysis intensities caused by the slowly forming deposits at the cell windows. Due to the unknown NCN photolysis quantum yield as well as the variable photolysis intensities in the reactor, it was not feasible to measure absolute room temperature absorption cross sections of NCN. Also note that the initially formed NCN is NCN($^1\Delta$), which is subsequently deactivated to the triplet ground state. From NCN signal rise times as well as NCN($^1\Delta$) decays measured at 30045.72 cm⁻¹ (332.8261 nm) (Q branch band head of the $^1\Pi_u(000) - ^1\Delta_g(000)$ transition),⁴⁴ we inferred a rather slow electronic relaxation time constant of $k_{\text{relax}}(\text{Ar}, 298 \text{ K}) \approx 8 \times 10^8 \text{ cm}^3 \text{ mol}^{-1} \text{ s}^{-1}$ corresponding to $\tau_{\text{relax}} \approx 300 \mu\text{s}$ at $p = 100 \text{ mbar}$.

At room temperature, the triplet spectrum is dominated by the intense, but unresolved $^3\Pi_1$ subband origin of the $\tilde{A}^3\Pi_u(000) - \tilde{X}^3\Sigma_g(000)$ ($^{\text{Q}}\text{P}_{21}$, $^{\text{Q}}\text{Q}_{22}$, and $^{\text{Q}}\text{R}_{23}$ branches) at 30385 cm⁻¹. Other, more isolated lines can be assigned to branches originating from the $^3\Pi_0$ and $^3\Pi_2$ subband, where the assignments indicated in Fig. 1 were adopted from the work of Beaton et al.³⁷ Moreover, Beaton

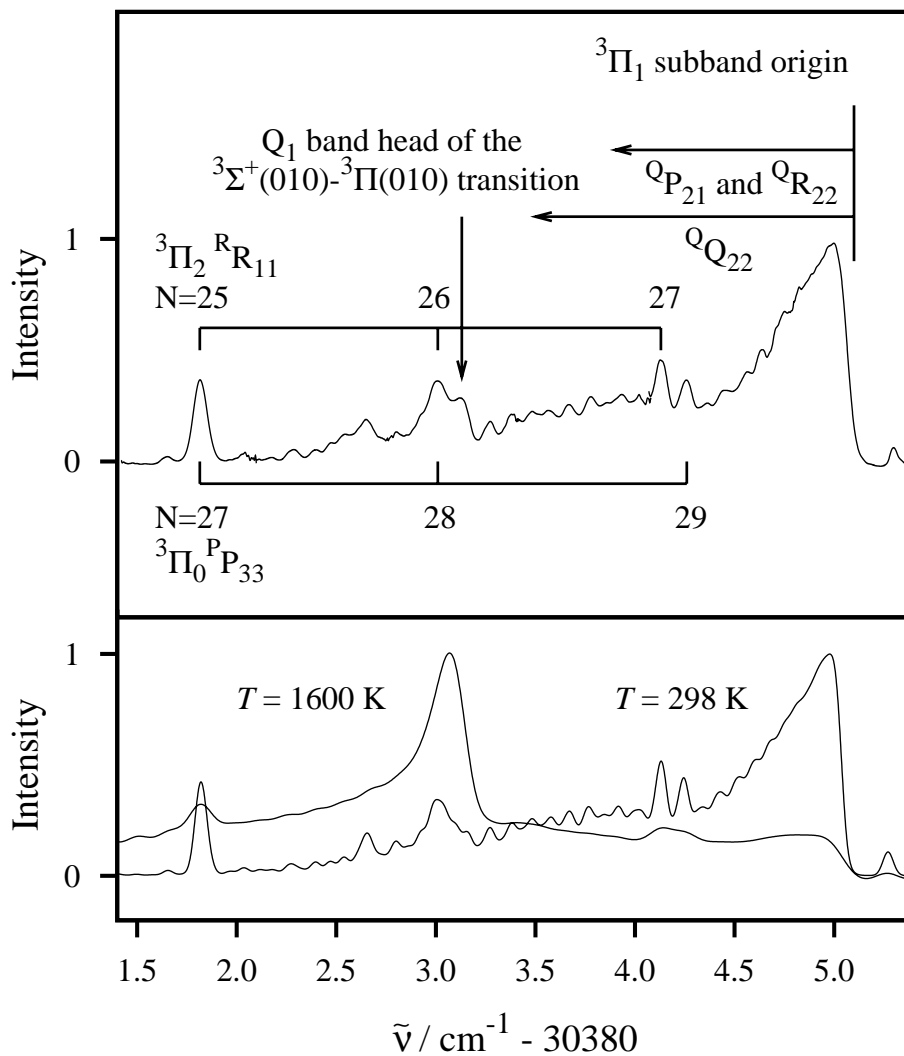


Figure 1: Normalized high resolution spectrum of NCN($^3\Sigma$) around 30383 cm^{-1} . Upper graph: Experimental room temperature spectrum at $p = 25 \text{ mbar}$ in argon. Lower graph: Simulated room ($T = 298 \text{ K}$, $p = 25 \text{ mbar}$) and high temperature ($T = 1600 \text{ K}$, $p = 1000 \text{ mbar}$) spectra. Spectral assignments were taken from Beaton et al.³⁷

and Brown attributed the barely resolved spectral feature at 30383.1 cm^{-1} to the Q_1 branch of the vibronic $^3\Sigma^+ - ^3\Pi$ subband of the vibrationally hot $\tilde{A}^3\Pi_u(010) - \tilde{X}^3\Sigma_g^-(010)$ system of NCN. The lower graph in Fig. 1 illustrates the corresponding PGOPHER simulation of the mainly Doppler broadened room temperature spectrum. A high temperature spectrum calculated for $T = 1600\text{ K}$ at $p = 1.0\text{ bar}$ is shown as well. Allowance was made for a small pressure broadening effect, which was estimated to be identical to that previously measured for the three-atomic radical NH_2 ($2.27 \times (T/295\text{ K})^{-0.78}\text{ GHz/bar}$).⁴⁵ Note that all spectra have been normalized with respect to the highest occurring spectral intensity. Except for minor spectral shifts, the agreement between the experimental and simulated room temperature spectrum is very good and thus it can be concluded that the high temperature extrapolation is reliable as well. As can be seen from a comparison of the two simulated spectra in the lower graph of Fig. 1, at high temperatures the Q_1 band head around 30383.1 cm^{-1} provides much stronger absorption than the congested $^3\Pi_1$ subband transitions around 30385 cm^{-1} , which are strongest at room temperature. This finding is in agreement with the LIF excitation flame spectra reported by Lamoureux et al.,³⁹ which was measured at a lower spectral resolution of 0.15 cm^{-1} . Also Vasudevan et al.¹⁵ observed an absorption maximum 30383.06 cm^{-1} in their shock tube work ($T \approx 2640\text{ K}$), but mistakenly assigned the observed absorption peak to the $^3\Pi_u(000) - ^3\Sigma_g(000)$ band head.

It turns out from the PGOPHER simulation shown in Fig. 1 that the overall spectral shape of the vibrationally hot Q_1 band head remains narrow even at high temperatures. This causes problems because quantitative narrow-bandwidth laser absorption detection of NCN in shock tube experiments relies on a correct, fixed detection wavelength. The laser has to be set to this specific wavelength before the experiment such that the exact band head position has to be accurately known. Unfortunately, as it becomes clear from a comparison of the calculated with the experimental room temperature spectrum, the heavily congested spectral region at wavenumbers around 30383 cm^{-1} is not quantitatively reproduced by the simulation. The remaining discrepancies are small but may indicate a significant offset of the underlying spectral position of the simulated Q_1 band.

3.3.2 High temperature absorption cross section

In order to measure the exact peak position of the Q_1 band head, pyrolysis experiments of NCN_3 have been performed at variable detection laser frequencies with the temperature set to $T = 850 \pm 50\text{ K}$ behind the incident and $T = 1600 \pm 100\text{ K}$ behind the reflected shock waves. Fig. 2 illustrates a typical absorption-time profile measured for a mixture containing 11 ppm NCN_3 in Ar. After the arrival of the incident shock wave, which is indicated by a strong Schlieren signal, a fast rise of the absorption signal is observed that can be attributed to NCN radical formation. During the $160\text{ }\mu\text{s}$ reaction time behind the incident wave, a plateau absorption value is reached indicating almost complete decomposition of NCN_3 . An accurate plateau value was extracted from the absorbance-time profiles by fitting a

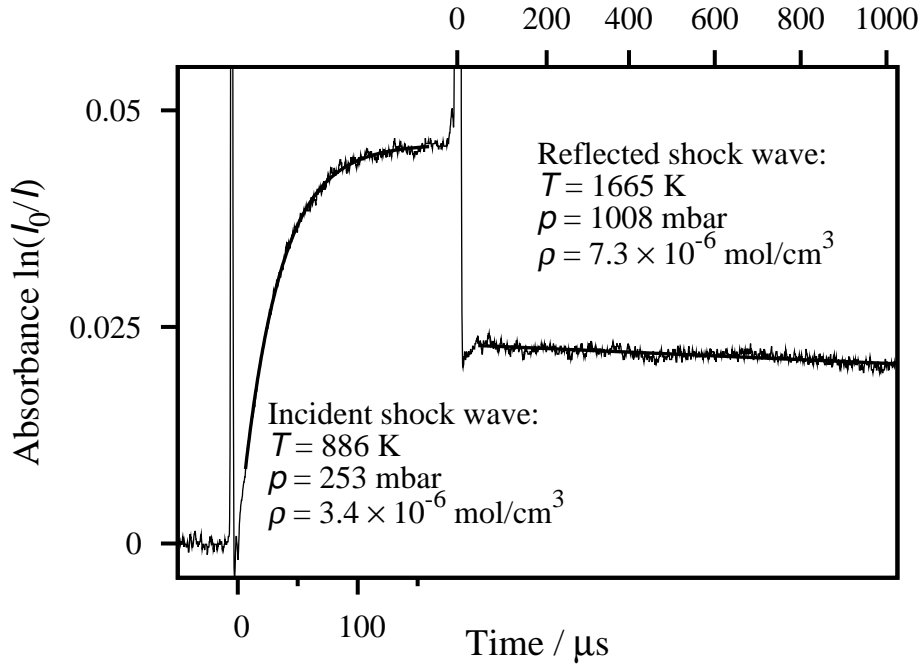


Figure 2: Typical NCN absorption profile measured behind an incident and reflected shock wave. Experimental conditions: 11 ppm NCN_3 , $\tilde{\nu}_{\text{laser}} = 30383.11 \text{ cm}^{-1}$.

first-order production kinetics according to

$$x = x_0(1 - \exp[-k(t - \tau_{\text{Offset}})]) \quad (1)$$

where x denotes NCN absorbance, x_0 the plateau absorbance, and k is the first-order rate constant. At lower experimental temperatures, short induction times were visible in the NCN signals (due to $\text{NCN}(^1\Delta) \rightarrow \text{NCN}(^3\Delta)$ relaxation, see below). These induction times were excluded from the fit by offsetting time zero using a suitable τ_{Offset} in Eq. 1. Following the arrival of the reflected shock wave indicated by the second Schlieren signal, an almost constant NCN absorbance was observed showing that (i) at this high temperature the NCN_3 decomposition is complete within the time-resolution of the experiment and (ii) that secondary chemistry of the NCN radical is almost negligible on the time-scale of the experiment. The slow decay of NCN is most probably due to the onset of the unimolecular decomposition of NCN at these high temperatures. Despite the higher total density behind the reflected wave, the observed NCN absorbance is significantly lower clearly indicating a strong negative temperature dependence of the NCN absorption cross section.

The NCN absorption spectrum has been mapped out via repeated absorbance measurements by setting the laser to different detection wavelengths. The resulting NCN spectrum is plotted in Fig. 3. Measured absorbances have been normalized with respect to initial NCN_3 concentrations and are corrected to average temperatures of $T = 850 \text{ K}$ and $T = 1600 \text{ K}$, respectively, by adopting the temperature dependence of the absorption cross section outlined below. The solid and dashed curves correspond to

PGOPHER simulations, in which the wavenumber scale of the latter has been shifted by 0.04 cm^{-1} . Apart from this obvious wavenumber offset, there is very good agreement between the simulated and experimental band shape. A very slight shift of the band maximum to lower wavenumbers with increasing temperature ($\approx 0.01 \text{ cm}^{-1}/1000 \text{ K}$) is also consistent with our measurements. Note that the necessary wavenumber offset of 0.04 cm^{-1} exceeds the $\pm 0.015 \text{ cm}^{-1}$ precision of our wavemeter. Furthermore, the spectral positions measured for the isolated room temperature lines shown in Fig. 1, which are $\pm 0.01 \text{ cm}^{-1}$ within the corresponding line positions reported by Beaton et al.³⁷ (estimated accuracy $\pm 0.006 \text{ cm}^{-1}$), verify the accuracy of the wavemeter readout. We thus conclude that our measurement of the Q_1 band position are accurate and recommend a high temperature detection wavelength of $\tilde{\nu}_{\text{max}} = 30383.11 \pm 0.01 \text{ cm}^{-1}$ ($329.1302 \pm 0.0001 \text{ nm}$) for future shock tube work.

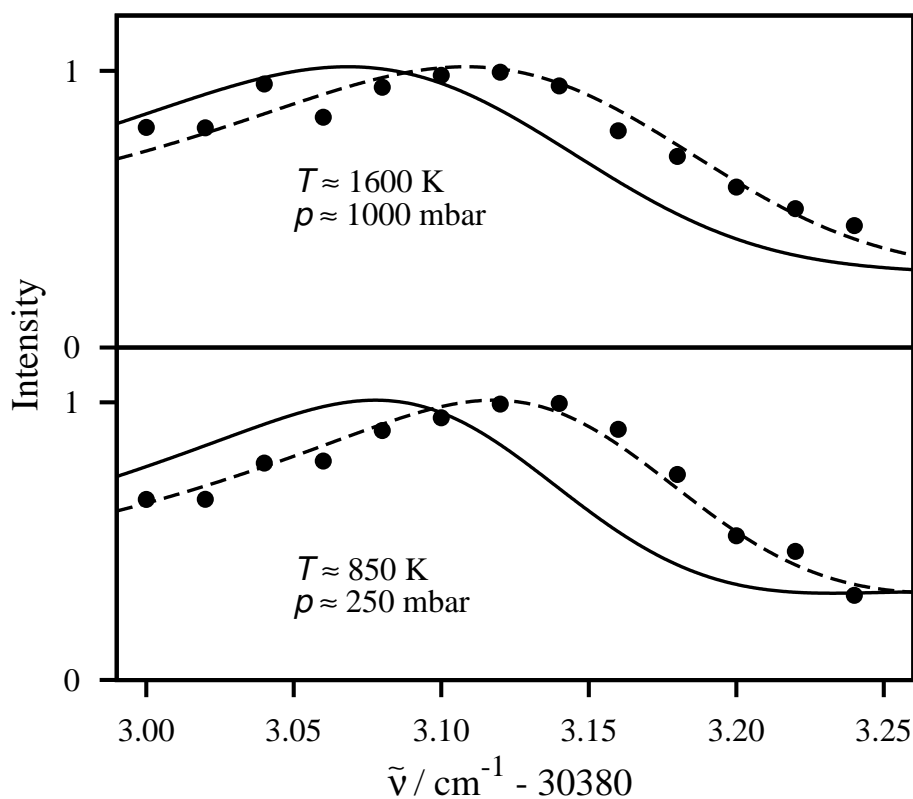


Figure 3: Part of the high temperature NCN absorption spectrum, which is dominated by the Q_1 band head of the $\tilde{A}^3\Pi_u(010) - \tilde{X}^3\Sigma_u(010)$ transition at $\tilde{\nu} = 30383.11 \text{ cm}^{-1}$. Symbols refer to measured absorbances normalized with respect to the band maximum. The solid and dashed curves denote original and slightly shifted PGOPHER simulations, respectively.

Assuming quantitative formation of NCN according to reaction (R2) and relying on a known initial concentration of NCN_3 inferred from the FT-IR measurements, the observed plateau absorptions behind incident and reflected shock waves could be directly converted to high temperature NCN absorption cross sections. Measured temperature dependent values, which were obtained from thermal decomposition experiments of NCN_3 between 766 K and 2241 K are shown as open symbols in Fig. 4

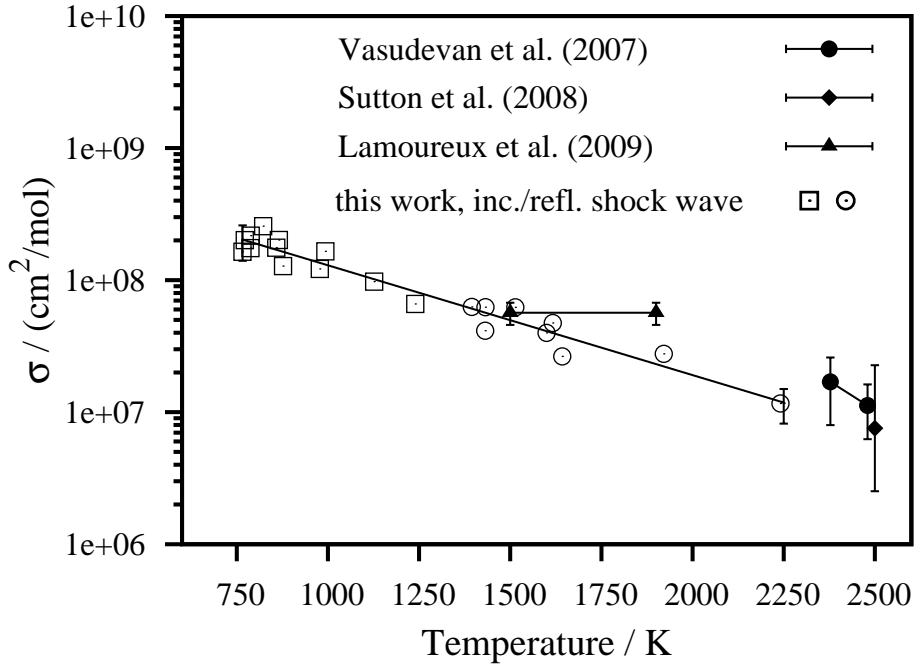


Figure 4: High temperature NCN absorption cross section of the Q_1 band head at $\tilde{\nu} = 30383.11 \pm 0.01 \text{ cm}^{-1}$ ($\lambda = 329.1302 \pm 0.0001 \text{ nm}$) in comparison with literature data.

and are listed in Tab. 1 All measurements have been performed at $\tilde{\nu} = 30383.11 \text{ cm}^{-1}$. The strongly temperature dependent absorption cross section can be approximated by the expression (solid line in Fig. 4)

$$\log\left(\frac{\sigma}{\text{cm}^2/\text{mol}}\right) = 8.9 - 8.4 \times 10^{-4} \times T/\text{K} \quad (\pm 25\%)$$

where the error represents the combined uncertainties related to statistical scatter and initial NCN₃ concentrations. Comparing the data points corresponding to measurements behind the incident wave ($0.2 \text{ bar} < p < 0.8 \text{ bar}$, open squares) with the data points taken from measurements behind the reflected wave ($0.8 \text{ bar} < p < 2.5 \text{ bar}$, open circles) no significant pressure dependence is noticeable within the scatter of the data.

Table 1: Selected experimental data: First-order NCN($^3\Sigma$) formation rate constants k , and high temperature NCN absorption cross sections σ at 30383.11 cm^{-1} .

T / K	p / mbar	$10^6 \times \rho / \text{cm}^3/\text{mol}$	$10^{-4} \times k / \text{s}^{-1}$	$x(\text{NCN}_3) / \text{ppm}$	$10^{-8} \times \sigma / \text{cm}^2/\text{mol}$
incident shock wave: $\rho \approx 3.5 \times 10^{-6} \text{ mol}/\text{cm}^3$					
588	134	2.75	0.07 ¹	≈ 10	₂
593	136	2.76	0.07 ¹	≈ 10	₂
623	148	2.86	0.21 ¹	≈ 10	₂
743	196	3.17	1.82	≈ 10	₂
759	202	3.20	1.88	≈ 5	₂
766	200	3.14	-	7.14	1.60
772	208	3.24	1.96	6.39	1.95

3. High Temperature NCN Radical Source and Absorption Cross Section of NCN($^3\Sigma$)

Table 1, continued:

T / K	p / mbar	$10^6 \times \rho / \text{cm}^3/\text{mol}$	$10^{-4} \times k / \text{s}^{-1}$	$x(\text{NCN}_3) / \text{ppm}$	$10^{-8} \times \sigma / \text{cm}^2/\text{mol}$
788	212	3.23	1.80	6.39	1.71
815	224	3.31	2.41	≈ 5	²
823	225	3.30	2.35	14.9	2.41
859	243	3.40	2.22	6.39	1.71
864	245	3.42	2.14	≈ 10	²
877	250	3.43	2.25	6.39	1.25
916	290	3.81	4.11	≈ 15	⁻²
920	261	3.41	3.34	≈ 30	⁻²
978	291	3.58	3.64	6.39	1.19
1127	351	3.75	6.10	7.14	0.955
1240	395	3.84	8.51	6.39	0.649
incident shock wave: $\rho \approx 7.0 \times 10^{-6} \text{ mol/cm}^3$					
546	236	5.19	0.01 ¹	≈ 10	⁻²
583	264	5.45	0.14 ¹	≈ 10	⁻²
672	335	5.99	1.43 ¹	≈ 10	⁻²
701	358	6.14	1.93 ¹	≈ 10	⁻²
742	391	6.34	2.99	≈ 10	⁻²
764	408	6.42	2.77	≈ 20	⁻²
788	426	6.51	3.03	5.46	2.08
804	438	6.54	4.46	≈ 10	⁻²
816	451	6.66	4.37	≈ 20	⁻²
865	487	6.77	3.28	5.46	1.94
963	570	7.12	6.80	≈ 10	⁻²
993	590	7.15	7.94	11.4	1.55
1073	659	7.39	5.46	≈ 10	⁻²
1153	724	7.55	11.1	≈ 15	⁻²
1155	726	7.56	9.98	≈ 5	⁻²
1257	678	6.49	15.0	≈ 15	⁻²
reflected shock wave					
1395	773	6.66		6.39	0.615
1431	794	6.67		6.39	0.407
1432	1599	13.4		5.46	0.606
1514	866	6.88		14.86	0.601
1600	953	7.17		6.39	0.392
1617	1588	14.3		5.46	0.462
1643	993	7.27		6.39	0.260
1921	2478	15.5		11.4	0.269
2241	1547	8.30		7.14	0.115

¹ Excluded from Arrhenius fit of k , see text.

² Initial mole fraction has not been promptly checked by FT-IR and hence no absorption cross section is specified.

Our absorption cross section data are compared with literature values in Fig. 4. The line marked with solid circles represent the data obtained from shock tube measurements reported by Vasudevan et al.¹⁵

3. High Temperature NCN Radical Source and Absorption Cross Section of NCN($^3\Sigma$)

They performed indirect measurements of the absorption cross section at temperatures between 2378 and 2492 K based on quantitative detection of CH profiles and on the determination of the branching fraction of reaction (R1). The reported values are approximately 60% higher than our extrapolated values, but are consistent within error limits. As a comparison of their flame data with the data of Vasudevan et al., Sutton et al. provided an absorption cross section value of $\sigma = 7.6 \times 10^6 \text{ cm}^2/\text{mol}$ at $T = 2490 \text{ K}$ (solid diamond), which is based on LIF measurements of CH, OH and NCN profiles in low-pressure methane flames.¹³ Given the reported uncertainty estimate of a factor of 3, the nearly perfect agreement with our measurement is fortuitous. Similarly, Lamoureux et al. presented a quantitative determination of NCN radical concentration-time profiles in a low-pressure methane flame, where LIF intensities have been calibrated using cavity-ringdown spectroscopy.³⁹ Laborious spectral simulations – identical to the PGOPHER simulations performed in this work – were used to calculate absolute absorption cross section values starting from the transition dipole moments of the (000) and (010) bands derived from fluorescence lifetime measurements by Smith et al.⁴⁶ Less temperature dependent absorption cross sections have been reported for temperatures between 1500 and 1900 K (line marked with triangles), yielding a factor of 2 higher value at $T = 1700 \text{ K}$. Altogether, keeping in mind the well-known difficulties in determining accurate high temperature absorption cross sections of transient species, the overall good agreement of all above-mentioned indirect studies with our first direct measurement is quite remarkable.

3.3.3 Singlet-triplet relaxation and unimolecular decomposition of NCN₃

Concentration-time profiles of NCN($^3\Sigma$) formation following shock heating of mixtures of 5–20 ppm NCN₃ in Ar have been recorded at temperatures between 546 and 1257 K at two distinct density ranges of $3.0\text{-}4.0 \times 10^{-6} \text{ mol/cm}^3$ ($\rho \approx 3.5 \times 10^{-6} \text{ mol/cm}^3$) and $6.5\text{-}7.5 \times 10^{-6} \text{ mol/cm}^3$ ($\rho \approx 7.0 \times 10^{-6} \text{ mol/cm}^3$). Validation experiments had been performed beforehand in order to exclude interfering absorption or secondary chemistry of CN radicals that may be formed from BrCN impurities. Neither room temperature photolysis experiments of pure BrCN showed visible absorption of CN radicals at the used detection wavelength nor shock tube experiments performed with reaction mixtures containing up to 50% BrCN yielded noticeably different absorption-time traces.

As it is illustrated in Fig. 2, first-order NCN formation rate constants k were determined by fitting Eq. 1 to the time profiles. Short induction times, which have been observed at low temperatures (e.g., $30 \mu\text{s}$ at $T \approx 740 \text{ K}$), were excluded from the fit by slightly offsetting time zero, τ_{Offset} . As a potential chain-accelerated reaction mechanism can be excluded due to the very low reactant concentrations, these induction times have to be attributed to relaxation processes. Possible candidates are the delayed heating of NCN₃ behind the shock wave and, probably more important, the relaxation of the initially formed NCN($^1\Delta$) radicals into the $^3\Pi(010)$ vibronic state of NCN($^3\Sigma$) via intersystem crossing and vibrational cooling. A kinetic simulation assuming the simple consecutive reaction scheme

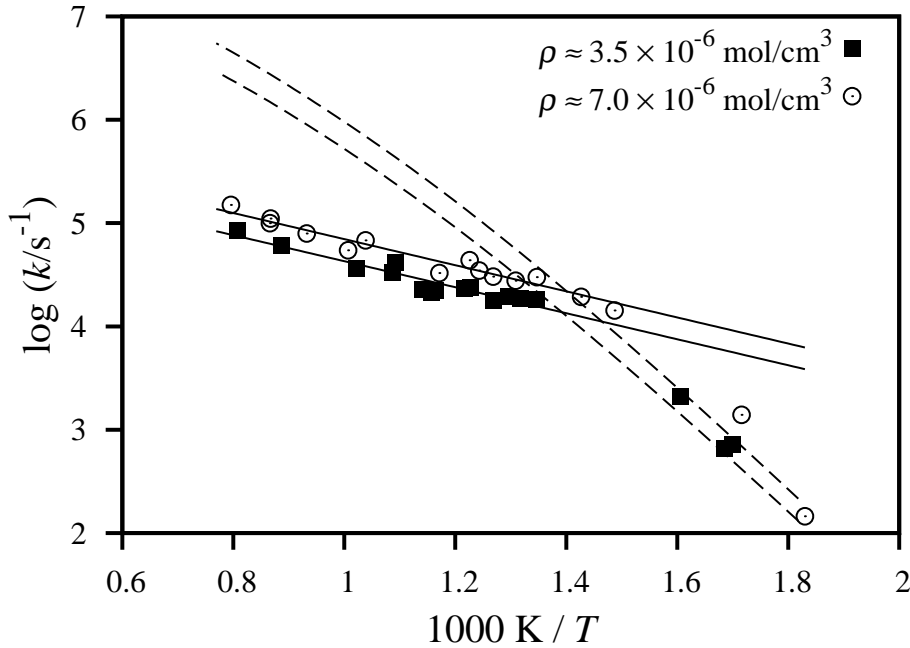


Figure 5: Experimental rate constant data measured at two different total density ranges (symbols), fitted Arrhenius expressions (solid lines), and RRKM/ME prediction of NCN₃ unimolecular decomposition.

NCN₃ (+M) → NCN($^1\Delta$) + N₂ (+M) → NCN($^3\Sigma$) + N₂ (+M) smoothly reproduced the signals. For example, at $T \approx 820$ K, a ratio of $k_{\text{fast}}/k_{\text{slow}} \approx 5$ was obtained for the two rate constants describing the two-step process. At not too high temperatures, good agreement was found between the rate constant of the rate limiting step described by k_{slow} and the corresponding rate constant k obtained by fitting Eq. 1. However, a systematic evaluation of the observed induction times turned out to be imprecise because the observed delays were short and the rate constants of the two consecutive steps were found to be strongly anti-correlated. Moreover, as a consequence of the simple consecutive mechanism, the extracted rate constants were interchangeable in the simulations and thus it was not possible to assign their values unambiguously to the NCN₃ unimolecular decomposition or the relaxation step, respectively. Obtained temperature dependent first-order rate constants are listed in Table 1 and are summarized in Figure 5 as filled ($\rho \approx 3.5 \times 10^{-6}$ mol/cm³) and open ($\rho \approx 7.0 \times 10^{-6}$ mol/cm³) symbols. Data points between $740 \text{ K} < T < 1260 \text{ K}$ can be approximated by the following Arrhenius expressions (solid lines):

$$k(\rho \approx 3.5 \times 10^{-6} \text{ mol/cm}^3)/\text{s}^{-1} = (7.8 \pm 2) \times 10^5 \exp[-(24 \pm 2) \text{ kJ/mol}/RT]$$

$$k(\rho \approx 7.0 \times 10^{-6} \text{ mol/cm}^3)/\text{s}^{-1} = (1.3 \pm 0.3) \times 10^6 \exp[-(24 \pm 2) \text{ kJ/mol}/RT]$$

A clear density dependence of k has been observed, $k(\rho \approx 7.0 \times 10^{-6} \text{ mol/cm}^3)/k(\rho \approx 3.5 \times 10^{-6} \text{ mol/cm}^3) \approx 1.6$, which is consistent with both a unimolecular decomposition close to its low pressure regime and a collision induced relaxation process. Note that the measured rate constants

Table 2: Input parameters for RRKM/ME model of NCN₃ unimolecular decomposition.

	NCN ₃	NCN ₃ [‡]
$\Delta_f H_{T=0}^\circ$	511 kJ/mol	620 kJ/mol
vibrations, $\tilde{\nu}/\text{cm}^{-1}$	155	71
	394	107
	431	235
	433	471
	633	531
	876	1056
	1256	1973
	2079	2032
	2193	
rotational constants/ cm^{-1}	0.0956	0.0798
	0.1030	0.0870
	1.3339	0.9557
critical energy, E_0		9138 cm^{-1}
energy transfer efficiency, β_E		0.8
energy transfer, $\langle\Delta E\rangle_{\text{all}}$		-160 cm^{-1}
$\Delta_f H_{T=0}^\circ(\text{NCN}(^3\Sigma))$		444 kJ/mol
$\Delta_f H_{T=0}^\circ(\text{NCN}(^1\Delta))$		565 kJ/mol

nearly collapse at temperatures $T < 700$ K causing a distinct kink in the Arrhenius plot. Obviously, at a temperature of 700 K, the NCN formation rate changes from being singlet-triplet relaxation rate limited at high temperatures to being rate limited by the thermal decomposition of NCN₃ at lower temperatures. Hence, in order to further support this conclusion, the unimolecular decomposition rate constant of NCN₃ in Ar was estimated based on statistical rate theory. Based on quantum-chemical input structures and energies, specific rate constants were calculated using standard RRKM procedures followed by modeling of the energy transfer step by solving the energy-grained master equation. Input parameters are summarized in Table 2. A reasonable value for the average energy transferred per collision, $\langle\Delta E\rangle_{\text{all}} = -160 \text{ cm}^{-1}$ at $E_0 = 109 \text{ kJ/mol}$, was based on the simplified ergodic collision theory on intermolecular energy transfer (ECT).⁴⁷ The energy transfer efficiency parameter β_E for argon was set to a reasonable value of 0.8,⁴⁸ thus assuming that the energy is almost completely freely distributed among all degrees of freedom of both collision partners. Modeling results are shown in Fig. 5 as dashed curves.

The calculated activation energy of $E_a = 93 \text{ kJ/mol}$, which is significantly lower than E_0 , and the pronounced density dependence (factor 1.8 for twice the density) indicate a unimolecular decomposition close to the low pressure limit. Good agreement is found between the calculated unimolecular decomposition rate constants and the few experimental data points at $T < 700$ K. Of course, the absolute values of the predicted rate constants are critically dependent on the exact values of the estimated

3. High Temperature NCN Radical Source and Absorption Cross Section of NCN($^3\Sigma$)

collision efficiency β_E and the G3 energy barrier height. However, as the low temperature experimental data are also less accurate due to the observed slow NCN formation rates, no attempt was made to further improve the agreement between calculation and experiment. Clearly, at $T < 700$ K, the rate limiting step is the decomposition of NCN₃. In this spirit, the experimental data at $T > 700$ K reflect the rate of the collision-induced intersystem crossing (CIISC) step and can be subsumed in a bimolecular rate constant expression according to:

$$k_{\text{CIISC}}/(\text{cm}^3\text{mol}^{-1}\text{s}^{-1}) = (1.3 \pm 0.5) \times 10^{11} \exp[-(21 \pm 4) \text{ kJ/mol}/RT]$$

Of course, the data points close to the intercept point at $T \approx 700$ K are influenced by both thermal decomposition and relaxation. Therefore, true CIISC rate constants at these temperatures can be expected to be slightly higher than inferred from our approximate analysis, thus somewhat reducing the overall temperature dependence of the relaxation process. More accurate measurements of the CIISC deactivation process by monitoring NCN($^1\Delta$) concentration-time profiles are underway and will be reported elsewhere.

Depending on the inert collision partner, CIISC rate constants for small molecules can vary over several orders of magnitude. For example, room temperature rate constants for the process $\text{CH}_2(^1\text{A}_1) + \text{M} \rightarrow \text{CH}_2(^3\text{B}_1) + \text{M}$ have been reported to be fast both for Ar ($k = 3.6 \times 10^{12} \text{ cm}^3\text{mol}^{-1}\text{s}^{-1}$) and Xe ($9.6 \times 10^{12} \text{ cm}^3\text{mol}^{-1}\text{s}^{-1}$),⁴⁹ whereas significant different rates have been found for the deactivation of singlet NH, $\text{NH}(^1\Delta) + \text{M} \rightarrow \text{NH}(^1\Sigma^-) + \text{M}$. Here, the CIISC is slow for Ar ($< 6 \times 10^8 \text{ cm}^3\text{mol}^{-1}\text{s}^{-1}$) but very efficient in case of Xe ($7.2 \times 10^{12} \text{ cm}^3\text{mol}^{-1}\text{s}^{-1}$).^{50,51} Quantitative prediction of CIISC probabilities remains challenging and even general trends are difficult to work out. Pertaining to CH₂ deactivation, which has been quite extensively studied due to the importance of singlet CH₂ chemistry in high temperature combustion, CIISC rates have been found to show weak temperature dependences according to $k_{\text{CIISC}} \propto T^n$ with $0.5 < n < 1.0$.⁵² Hence, with $k = 1.0 \times 10^{10} \text{ cm}^3\text{mol}^{-1}\text{s}^{-1}$ at $T = 1000$ K, the NCN relaxation rates found in this work are at the lower bound of the expected range, but exhibit an unusually strong temperature dependence. Additional measurements using different collision bath gases, which would have been beyond the scope of this work, are helpful to further elucidate the nature of the relaxation process.

Finally, the role of a possible but spin-forbidden NCN₃ decomposition path directly yielding NCN($^3\Sigma$) should briefly be discussed. Benard et al.³³ performed quantum-chemical calculations of the ground state singlet and excited triplet potential energy surfaces of NCN₃ at the B3LYP/6-311+G(2df) level of theory. They reported a singlet dissociation barrier for the reaction $\text{NCN}_3(^1\text{A}') \rightarrow \text{NCN}(^1\Delta) + \text{N}_2(^1\Sigma)$ of $E_0 = 114$ kJ/mol, which is in good agreement with our G3 result of $E_0 = 109$ kJ/mol. The triplet manifold, which is repulsive and yields $\text{NCN}(^3\Sigma) + \text{N}_2(^1\Sigma)$, was found to cross the singlet manifold near the maximum of the dissociation barrier. In order to compete with the spin-allowed NCN($^1\Delta$) path, the crossing point would have to be located much below the singlet dissociation barrier because the singlet-triplet crossing of NCN₃ prior to dissociation can be assumed to be slow. Note that also the

observed induction times at low temperatures are less compatible with a markedly direct formation of $\text{NCN}(^3\Sigma)$. Therefore we conclude that non-adiabatic branching to ground state $\text{NCN}(^3\Sigma)$ does not play a significant role.

3.4 Conclusion

Based on quantitative formation of NCN during the thermal decomposition of NCN_3 , we were able to directly measure high temperature absorption cross sections of ground state $\text{NCN}(^3\Sigma)$. At high temperatures, the (010) vibrational level is substantially populated and provides stronger absorption than the corresponding (000)–(000)-transitions. For quantitative absorption detection of NCN behind shock waves and in flames, we recommend the use of the spectral feature centered around 30383.11 cm^{-1} (329.1302 nm) corresponding to the Q_1 branch of the vibronic $^3\Sigma^+ - ^3\Pi$ subband of the vibrationally hot $\tilde{A}^3\Pi_u(010) - \tilde{X}^3\Sigma_g^-(010)$ system. A strongly temperature dependent narrow-bandwidth absorption cross section

$$\log\left(\frac{\sigma}{\text{cm}^2/\text{mol}}\right) = 8.9 - 8.3 \times 10^{-4} \times T/\text{K} \quad (\pm 25\%)$$

is recommended for temperatures between $750 \text{ K} < T < 2250 \text{ K}$. The absorption band shape is dominated by Doppler-broadening of the underlying transitions and no significant pressure broadening effect has been detected at pressures between 0.2 and 2.5 bar.

The stable NCN plateau signals observed behind the reflected shock waves clearly reveal the fact that the thermal decomposition of NCN_3 serves as an almost ideal high temperature source of $\text{NCN}(^3\Sigma)$. As it is illustrated for an experiment with an initial NCN_3 mole fraction of 11 ppm in Fig. 2, on the one hand, excellent signal-to-noise ratios are attainable. On the other hand, the resulting NCN concentrations are still low enough to make possible the investigation of bimolecular NCN reactions by means of simple pseudo first-order kinetics using an excess of the respective reactant. Care should be taken, however, to ensure complete singlet-triplet relaxation of the initially formed $\text{NCN}(^1\Delta)$ radicals, which at temperatures between 740 K and 1260 K is best represented by the expression:

$$k_{\text{CHISC}}/(\text{cm}^3\text{mol}^{-1}\text{s}^{-1}) = (1.3 \pm 0.5) \times 10^{11} \exp[-(21 \pm 4) \text{ kJ/mol}/RT]$$

At $p = 1$ bar, relaxation times of $\tau_{\text{CHISC}} < 10 \mu\text{s}$ are obtained for temperatures $T > 875 \text{ K}$, which should be sufficiently short for most kinetic experiments. A useful upper temperature limit is set by the thermal stability of NCN. From an experiment performed at $T = 2303 \text{ K}$ and $p = 3.2$ bar, which already showed a fast decay of NCN behind the reflected shock wave, we deduced a unimolecular decomposition rate constant for $\text{NCN} + \text{M} \rightarrow \text{C} + \text{N}_2 + \text{M}$ of $k = 2.0 \times 10^9 \text{ cm}^3\text{mol}^{-1}\text{s}^{-1}$. This value is in good agreement with the recent experimental determination of Busch and Olzmann who performed atomic resonance absorption spectroscopy (ARAS) of C and N atoms following the thermal

decomposition of NCN_3 at temperatures above 1800 K.¹⁶ In agreement with the theoretical prediction of Moskaleva and Lin⁵³, C atoms were observed as the main cleavage product. Relying on the reported rate expression of Busch and Olzmann, a feasible upper temperature limit of $T \approx 2350$ K (corresponding to a 100 μs NCN lifetime at $p = 1$ bar) can be specified for studying bimolecular reactions behind shock waves with NCN_3 as the NCN precursor.

Though interfering with kinetic $\text{NCN}(^3\Sigma)$ measurements, a benefit of the rather low CIISC rates and with it the long lifetimes of $\text{NCN}(^1\Delta)$ behind shock waves is that it opens the door for studying singlet NCN chemistry. This is in contrast with singlet CH_2 radical chemistry, for example, which is difficult to assess in shock tube experiments due to the very fast singlet-triplet deactivation and hence thermal equilibration with the triplet ground state.^{54,55} Comparative studies of singlet/triplet reactivity of NCN hold the potential to map out different reaction pathways and peculiarities of the underlying potential energy surfaces. These can result in both completely different reaction products as a result of separated singlet and triplet reactivities (e.g., for the reaction $\text{NCN}(^1\Delta, ^3\Sigma) + \text{O}(^3\text{P})$) as well as variable dynamics for a reaction on a shared potential energy surface (e.g., in case of $\text{NCN}(^1\Delta, ^3\Sigma) + \text{NO}_2(^2\text{A}_1)$).^{20,27} Shock tube measurements of the temperature dependences of both singlet and triplet bimolecular reactions are currently underway and will contribute to an improved understanding of the role of NCN chemistry for NO_x formation in combustion processes. Preliminary data on the formation and decay of $\text{NCN}(^1\Delta)$ during the thermal decomposition of NCN_3 are consistent with the conclusion drawn in this paper, namely, that CIISC is the rate determining step for $\text{NCN}(^3\Sigma)$ formation at high temperatures.

Acknowledgment

This work was supported by the Deutsche Forschungsgemeinschaft. We would like to thank Nancy Faßheber and Benjamin Oden for their active help with careful wavemeter calibration, high resolution NCN absorption spectra acquisition, and preliminary measurement of room temperature NCN relaxation rates. Many thanks to Xavier Mercier and Colin Western for providing their PGOPHER input file for NCN spectral simulations. We further acknowledge Friedrich Temps for helpful discussions and advice.

Bibliography

- [1] J. Warnatz, U. Maas, and R. W. Dibble, *Combustion*, Springer, Berlin/Heidelberg, 3. edition, 2001.
- [2] P. Forster, V. Ramaswamy, P. Artaxo, T. Berntsen, R. Betts, D. Fahey, J. Haywood, J. Lean, D. Lowe, G. Myhre, J. Nganga, R. Prinn, G. Raga, M. Schulz, and R. V. Dorland, Changes in At-

3. High Temperature NCN Radical Source and Absorption Cross Section of NCN($^3\Sigma$)

- mospheric Constituents and in Radiative Forcing, in S. Solomon, D. Qin, M. Manning, Z. Chen, M. M. K. Averyt, M. Tignor, and H. Miller, editors, *Climate Change 2007: The Physical Science Basis. Contribution of Working Group I to the Fourth Assessment Report of the Intergovernmental Panel on Climate Change*, chapter 2, Cambridge University Press, Cambridge, United Kingdom, **2007**.
- [3] C. P. Fenimore, Formation of Nitric Oxide in Premixed Hydrocarbon Flames, *Proc. Combust. Inst.* **1971**, *13*, 373–380.
- [4] J. A. Miller and C. T. Bowman, Mechanism and Modelling of Nitrogen Chemistry in Combustion, *Prog. Energy Combust. Sci.* **1989**, *15*, 287–338.
- [5] L. B. Harding, S. J. Klippenstein, and J. A. Miller, Kinetics of CH + N₂ Revisited with Multireference Methods, *J. Phys. Chem. A* **2008**, *112*, 522–532.
- [6] D. Lindackers, M. Burmeister, and P. Roth, Perturbation Studies of High Temperature C and CH Reactions with N₂ and NO, *Proc. Combust. Inst.* **1991**, *23*, 251–257.
- [7] A. J. Dean, R. K. Hanson, and C. T. Bowman, High Temperature Shock Tube Study of Reactions of CH and C-Atoms with N₂, *Proc. Combust. Inst.* **1990**, *23*, 259–265.
- [8] Q. Cui, K. Morokuma, J. M. Bowman, and S. J. Klippenstein, The Spin-Forbidden Reaction CH($^2\Pi$) + N₂ → HCN + N(4S) Revisited. II. Nonadiabatic Transition State Theory and Application, *J. Chem. Phys.* **1999**, *110*, 9469–9482.
- [9] L. V. Moskaleva and M. C. Lin, The Spin-Conserved Reaction CH + N₂ → H + NCN: A Major Pathway to Prompt NO Studied by Quantum/Statistical Theory Calculations and Kinetic Modeling of Rate Constant, *Proc. Combust. Inst.* **2000**, *28*, 2393–2401.
- [10] L. V. Moskaleva, W. S. Xia, and M. C. Lin, The CH + N₂ Reaction Over the Ground Electronic Doublet Potential Energy Surface: A Detailed Transition State Search, *Chem. Phys. Lett.* **2000**, *331*, 269–277.
- [11] M. R. Berman, T. Tsuchiya, A. Gregusova, A. Perara, and R. J. Bartlett, HNNC Radical and Its Role in the CH + N₂ Reaction, *J. Phys. Chem. A* **2007**, *111*, 6894–6899.
- [12] G. P. Smith, Evidence of NCN as a Flame Intermediate for Prompt NO, *Chem. Phys. Lett.* **2003**, *367*, 541–548.
- [13] J. A. Sutton, B. A. Williams, and J. W. Fleming, Laser-Induced Fluorescence Measurements of NCN in Low-Pressure CH₄/O₂/N₂ Flames and Its Role in Prompt NO Formation, *Combust. Flame* **2008**, *153*, 465–478.
- [14] R. J. H. Klein-Douwel, N. J. Dam, and J. J. ter Meulen, Laser-Induced Fluorescence of NCN in Low and Atmospheric Pressure Flames, *Optics Lett.* **2008**, *33*, 2620–2622.

3. High Temperature NCN Radical Source and Absorption Cross Section of NCN($^3\Sigma$)

- [15] V. Vasudevan, R. K. Hanson, C. T. Bowman, D. M. Golden, and D. F. Davidson, Shock Tube Study of the Reaction of CH with N₂: Overall Rate and Branching Ratio, *J. Phys. Chem. A* **2007**, *111*, 11818–11830.
- [16] A. Busch and M. Olzmann, Shock-Tube Study of the Thermal Decomposition of NCN, Vienna, paper p810138, Proc. European Combust. Meeting, **2009**.
- [17] A. Busch, N. González-García, and M. Olzmann, Thermal Decomposition of NCN: Shock-Tube Study and Master-Equation Modeling, Savonlinna, poster abstract, 30th Int. Symp. on Free Radicals, **2009**.
- [18] R. E. Baren and J. F. Hershberger, Kinetics of the NCN Radical, *J. Phys. Chem. A* **2002**, *106*, 11093–11097.
- [19] C.-L. Huang, S. Y. Tseng, T. Y. Wang, N. S. Wang, Z. F. Xu, and M. C. Lin, Reaction Mechanism and Kinetics of the NCN + NO Reaction: Comparison of Theory and Experiment, *J. Chem. Phys.* **2005**, *122*, 184321.
- [20] T.-J. Yang, N. S. Wang, L. C. Lee, Z. F. Xu, and M. C. Lin, Kinetics and Mechanism of the NCN + NO₂ Reaction Studied by Experiment and Theory, *J. Phys. Chem. A* **2008**, *112*, 10185–10192.
- [21] S.-Y. Tzeng, P.-H. Chen, N. S. Wang, L. C. Lee, Z. F. Xu, and M. C. Lin, Kinetics and Mechanism of the CN + NCO → NCN + CO Reaction Studied by Experiment and Theory, *J. Phys. Chem. A* **2009**, *113*, 6314–6325.
- [22] O. Welz and M. Olzmann, An Experimental and Theoretical Study on the Kinetics of the NCN + NO Reaction, Montreal, poster W5P089, 32nd Int. Symp. on Combustion, **2008**.
- [23] H. W. Kroto, T. F. Morgan, and H. H. Sheena, Flash Photolysis of Cyanogen Azide, NCN₃, *Trans. Faraday Soc.* **1970**, *66*, 2237–2243.
- [24] H.-T. Chen and J.-J. Ho, Theoretical Investigation of the Mechanisms of Reaction of NCN with NO and NS, *J. Phys. Chem. A* **2005**, *109*, 2564–2571.
- [25] R. S. Zhu and M. C. Lin, Ab Initio Study on the Oxidation of NCN by O₂, *Int. J. Chem. Kinet.* **2005**, *37*, 593–598.
- [26] R. S. Zhu, M. T. Nguyen, and M. C. Lin, Ab Initio Study on the Oxidation of NCN by OH: Prediction of the Individual and Total Rate Constants, *J. Phys. Chem. A* **2009**, *113*, 298–304.
- [27] R. S. Zhu and M. C. Lin, Ab Initio Study on the Oxidation of NCN by O(3P): Prediction of the Total Rate Constant and Product Branching Ratios, *J. Phys. Chem. A* **2007**, *111*, 6766–6771.
- [28] A. El Bakali, L. Pillier, P. Desgroux, B. Lefort, L. Gasnot, J. F. Pauwels, and I. da Costa, NO Prediction in Natural Gas Flames Using GDF-Kin 3.0 Mechanism. NCN and HCN Contribution to Prompt-NO Formation, *Fuel* **2006**, *85*, 896–909.

3. High Temperature NCN Radical Source and Absorption Cross Section of NCN($^3\Sigma$)

- [29] J. A. Sutton and J. W. Fleming, Towards Accurate Kinetic Modeling of Prompt NO Formation in Hydrocarbon Flames via the NCN Pathway, *Combust. Flame* **2008**, *154*, 630–636.
- [30] S. Gersen, A. V. Mokhov, and H. B. Levinsky, Diode Laser Absorption Measurement and Analysis of HCN in Atmospheric-Pressure, Fuel-Rich Premixed Methane/Air Flames, *Combust. Flame* **2008**, *155*, 267–276.
- [31] A. A. Konnov, Implementation of the NCN Pathway of Prompt-NO Formation in the Detailed Reaction Mechanism, *Combust. Flame* **2009**, *156*, 2093–2105.
- [32] H. Bock and R. Dammel, The Pyrolysis of Azides in the Gas Phase, *Angew. Chem. Int. Ed. Engl.* **1987**, *26*, 504–526.
- [33] D. J. Benard, C. Linnen, A. Harker, J. J. Michels, J. B. Addison, and R. Ondercin, Dissociation of Cyanogen Azide: An Alternative Route to Synthesis of Carbon Nitride, *J. Phys. Chem. B* **1998**, *102*, 6010–6019.
- [34] M. Colberg and G. Friedrichs, Room Temperature and Shock Tube Study of the Reaction HCO + O₂ Using the Photolysis of Glyoxal as an Efficient HCO Source, *J. Phys. Chem. A* **2006**, *110*, 160–170.
- [35] D. E. Milligan, M. E. Jacox, and A. M. Bass, Matrix-Isolation Study of the Photolysis of Cyanogen Azide. The Infrared and Ultraviolet Spectra of the Free Radical NCN, *J. Chem. Phys.* **1965**, *43*, 3149–3160.
- [36] C. M. Western, PGOPHER, a Program for Simulating Rotational Structure, University of Bristol, available at <http://pgopher.chm.bris.ac.uk>.
- [37] S. A. Beaton, Y. Ito, and J. M. Brown, Laser Excitation Spectroscopy of the $\tilde{A}^3\Pi_u-\tilde{X}^3\Sigma_g^-$ -Transition of the NCN Radical. 1. The (0-0) Band, *J. Mol. Spectrosc.* **1996**, *178*, 99–107.
- [38] S. A. Beaton and J. M. Brown, Laser Excitation Spectroscopy of the $\tilde{A}^3\Pi_u-\tilde{X}^3\Sigma_g^-$ -Transition of the NCN Radical. 2. The ν_2 Hot Band, *J. Mol. Spectrosc.* **1997**, *183*, 347–359.
- [39] N. Lamoureux, X. Mercier, C. Western, J. F. Pauwels, and P. Desgroux, NCN Quantitative Measurement in a Laminar Low Pressure Flame, *Proc. Combust. Inst.* **2009**, *32*, 937–944.
- [40] V. Mokrushin, V. Bedanov, W. Tsang, M. Zachariah, and V. Knyazev, ChemRate Version 1.5.2, **1996–2006**, National Institute of Standards and Technology, Gaithersburg, USA.
- [41] L. A. Curtiss, K. Raghavachari, P. C. Redfern, V. Rassolov, and J. A. Pople, Gaussian-3 (G3) Theory for Molecules Containing First and Second-Row Atoms, *J. Chem. Phys.* **1998**, *109*, 7764–7776.

- [42] M. J. Frisch, G. W. Trucks, H. B. Schlegel, G. E. Scuseria, M. A. Robb, J. R. Cheeseman, J. A. Montgomery, Jr., T. Vreven, K. N. Kudin, J. C. Burant, J. M. Millam, S. S. Iyengar, J. Tomasi, V. Barone, B. Mennucci, M. Cossi, G. Scalmani, N. Rega, G. A. Petersson, H. Nakatsuji, M. Hada, M. Ehara, K. Toyota, R. Fukuda, J. Hasegawa, M. Ishida, T. Nakajima, Y. Honda, O. Kitao, H. Nakai, M. Klene, X. Li, J. E. Knox, H. P. Hratchian, J. B. Cross, V. Bakken, C. Adamo, J. Jaramillo, R. Gomperts, R. E. Stratmann, O. Yazyev, A. J. Austin, R. Cammi, C. Pomelli, J. W. Ochterski, P. Y. Ayala, K. Morokuma, G. A. Voth, P. Salvador, J. J. Dannenberg, V. G. Zakrzewski, S. Dapprich, A. D. Daniels, M. C. Strain, O. Farkas, D. K. Malick, A. D. Rabuck, K. Raghavachari, J. B. Foresman, J. V. Ortiz, Q. Cui, A. G. Baboul, S. Clifford, J. Cioslowski, B. B. Stefanov, G. Liu, A. Liashenko, P. Piskorz, I. Komaromi, R. L. Martin, D. J. Fox, T. Keith, M. A. Al-Laham, C. Y. Peng, A. Nanayakkara, M. Challacombe, P. M. W. Gill, B. Johnson, W. Chen, M. W. Wong, C. Gonzalez, and J. A. Pople, Gaussian 03, Revision D.01, Gaussian, Inc., Wallingford, CT, 2004.
- [43] A. P. Scott and L. Radom, Harmonic Vibrational Frequencies: An Evaluation of Hartree-Fock, Møller-Plesset, Quadratic Configuration Interaction, Density Functional Theory, and Semiempirical Scale Factors, *J. Phys. Chem.* **1996**, *100*, 16502–16513.
- [44] H. W. Kroto, The $^1\Pi_u \leftarrow ^1\Delta_g$ Electronic Spectrum of NCN, *Can. J. Phys.* **1967**, *45*, 1439–1450.
- [45] G. Friedrichs, M. Colberg, M. Fikri, Z. Huang, J. Neumann, and F. Temps, Validation of the Extended Simultaneous Kinetics and Ringdown Model by Measurements of the Reaction $\text{NH}_2 + \text{NO}$, *J. Phys. Chem. A* **2005**, *109*, 4785–4795.
- [46] G. P. Smith, R. A. Coppeland, and D. R. Crosley, Electronic Quenching, Fluorescence Lifetime, and Spectroscopy of the $A^3\Pi_u$ State of NCN, *J. Chem. Phys.* **1989**, *91*, 1987–1993.
- [47] D. Nilsson and S. Nordholm, Statistical Model of Energy Transfer in Molecular Collisions: De-energization of Highly Excited Toluene, *J. Chem. Phys.* **2002**, *116*, 7041–7048.
- [48] D. Nilsson and S. Nordholm, Statistical Theory of Collisional Energy Transfer in Molecular Collisions. *trans*-Stilbene Deactivation by Argon, Carbon Dioxide, and *n*-Heptane, *J. Phys. Chem. A* **2006**, *110*.
- [49] M. N. R. Ashfold, M. A. Fullstone, G. Hancock, and G. W. Ketley, Singlet Methylene Kinetics: Direct Measurements of Removal Rates of \tilde{a}^1A_1 and \tilde{b}^1B_1 CH_2 and CD_2 , *Chem. Phys.* **1981**, *55*, 245–257.
- [50] F. Rohrer and F. Stuhl, $\text{NH}(a^1\Delta \rightarrow X^3\Sigma^-)$ Emission From the Gas-Phase Photolysis of HN_3 , *Chem. Phys. Lett.* **1984**, *111*, 234–237.
- [51] W. Hack and A. Wilms, Elementary Reactions of $\text{NH}(a^1\Delta)$ with Atoms and Diatomic Molecules, *J. Phys. Chem.* **1989**, *93*, 3540–3546.

3. High Temperature NCN Radical Source and Absorption Cross Section of NCN($^3\Sigma$)

- [52] U. Bley, M. Koch, F. Temps, and H. Gg. Wagner, Collision-Induced Intersystem Crossing in $\text{CH}_2(\tilde{\text{a}}^1\text{A}_1)$: A Quantitative Analysis Using the Mixed-State Model, *Ber. Bunsenges. Phys. Chem.* **1989**, *93*, 833–841.
- [53] L. V. Moskaleva and M. C. Lin, Computational Study on the Energetics of NCN Isomers and the Kinetics of the $\text{C} + \text{N}_2 \rightleftharpoons \text{N} + \text{CN}$ Reaction, *J. Phys. Chem. A* **2001**, *105*, 4156–4163.
- [54] G. Friedrichs and H. Gg. Wagner, Quantitative FM Spectroscopy at High Temperatures: The Detection of $^1\text{CH}_2$ Behind Shock Waves, *Z. Phys. Chem.* **2000**, *214*, 1723–1746.
- [55] G. Friedrichs and H. Gg. Wagner, Investigation of the Thermal Decomposition of Ketene and of the Reaction $\text{CH}_2 + \text{H}_2 \rightleftharpoons \text{CH}_3 + \text{H}$, *Z. Phys. Chem.* **2001**, *215*, 1601–1623.

4 A Consistent Model for the Thermal Decomposition of NCN_3 and the Singlet-Triplet Relaxation of NCN

Johannes Dammeier, Benjamin Oden, and Gernot Friedrichs*

Institut für Physikalische Chemie,
Christian-Albrechts-Universität zu Kiel

Submitted to *Int. J. Chem. Kinet.*
Copyright granted by John Wiley & Sons, Inc.

Own contributions to this paper:

- Room temperature measurements
(together with Benjamin Oden, State Exam thesis)
- High temperature shock tube measurements
- Data analysis and discussion

*friedrichs@phc.uni-kiel.de

Abstract

The thermal decomposition of cyanogen azide (NCN_3) and the subsequent collision induced intersystem crossing (CIISC) process of cyanonitrene (NCN) have been investigated by monitoring excited electronic state ^1NCN and ground state ^3NCN radicals. NCN was generated by the pyrolysis of cyanogen azide (NCN_3) behind shock waves and by the photolysis of NCN_3 at room temperature. Fall-off rate constants of the thermal unimolecular decomposition of NCN_3 in argon have been extracted from ^1NCN concentration-time profiles in the temperature range $617 \text{ K} < T < 927 \text{ K}$ and at two different total densities: $k(\rho \approx 3 \times 10^{-6} \text{ mol/cm}^3)/\text{s}^{-1} = 4.9 \times 10^9 \times \exp(-71 \text{ kJ mol}^{-1}/RT) (\pm 30\%)$; $k(\rho \approx 6 \times 10^{-6} \text{ mol/cm}^3)/\text{s}^{-1} = 7.5 \times 10^9 \times \exp(-71 \text{ kJ mol}^{-1}/RT) (\pm 30\%)$; $\Delta E_a = \pm 14 \text{ kJ/mol}$. In addition, high-temperature ^1NCN absorption cross sections have been determined in the temperature range $618 \text{ K} < T < 1231 \text{ K}$ and can be expressed by $\sigma/(\text{cm}^2/\text{mol}) = 1.0 \times 10^8 - 6.3 \times 10^4 \text{ K}^{-1} \times T (\pm 50\%)$. Rate constants for the CIISC process have been measured by monitoring ^3NCN in the temperature range $701 \text{ K} < T < 1256 \text{ K}$ resulting in $k_{\text{CIISC}}(\rho \approx 1.8 \times 10^{-6} \text{ mol/cm}^3)/\text{s}^{-1} = 2.6 \times 10^6 \times \exp(-36 \text{ kJ mol}^{-1}/RT) (\pm 20\%)$, $k_{\text{CIISC}}(\rho \approx 3.5 \times 10^{-6} \text{ mol/cm}^3)/\text{s}^{-1} = 2.0 \times 10^6 \times \exp(-31 \text{ kJ mol}^{-1}/RT) (\pm 20\%)$; $k_{\text{CIISC}}(\rho \approx 7.0 \times 10^{-6} \text{ mol/cm}^3)/\text{s}^{-1} = 1.4 \times 10^6 \times \exp(-25 \text{ kJ mol}^{-1}/RT) (\pm 20\%)$, and $\Delta E_a \approx \pm 10 \text{ kJ/mol}$. These values are in good agreement with CIISC rate constants extracted from corresponding ^1NCN measurements. The observed non-linear pressure dependences reveal a pressure saturation effect of the CIISC process.

4.1 Introduction

The cyanonitrene radical ^3NCN has been detected in plasma flames as early as 1960 by Jennings and Linett who added several hydrocarbons to nitrogen atom containing flames.¹ They assigned a complex pattern of absorption bands at wavelengths around $\lambda = 329 \text{ nm}$ to the presence of NCN . A renewed interest in the reaction kinetics of ^3NCN stems from its significance in combustion processes. Ten years ago, Moskaleva and Lin^{2,3} proposed a new initiating step for the mechanism of the prompt NO formation in flames. According to Fenimore,⁴ small hydrocarbon radicals react with atmospheric nitrogen and eventually form NO and NO_2 (NO_x) as major pollutants of combustion processes.⁵ Instead of the formerly assumed spin-forbidden initiation reaction



Moskaleva and Lin proposed an alternative route via the spin-allowed pathway



Meanwhile, reaction 1b has been experimentally proven to be the main product channel of reaction (1).⁶⁻¹⁰ Simultaneously, experimental work on NCN reactions has been carried out.¹¹⁻¹⁷ Besides the photolysis of diazomethane (CH_2N_2) in the presence of cyanogen (C_2N_2), the photolysis or pyrolysis of cyanogen azide (NCN_3) served as a source of NCN radicals. The decomposition of cyanogen azide in a microwave discharge has also been used for the synthesis of carbon nitride (C_3N_4),¹⁸ a very hard material. The mechanism of this synthesis is also believed to proceed via NCN radicals.

Since the NCN precursor molecules yield NCN in its electronically excited single state, ^1NCN , the formation of the combustion relevant ^3NCN requires subsequent relaxation to the triplet ground state. In thermal systems, noticeable equilibrium concentrations of the singlet species can be ruled out due to a large singlet-triplet splitting of about 121 kJ/mol.¹⁵ Both from a theoretical and a practical point of view the question arises how fast the singlet triplet relaxation occurs. Whereas Baren and Hershberger¹¹ noticed unusually long rise times of the ^3NCN signal on the order of some 10 μs in their laser induced fluorescence (LIF) experiments performed at pressures between 50 and 1000 mbar, Huang *et al.*¹² and Yang *et al.*¹³, despite using the same detection technique, did not report any delay of the signals. However, the fact that ^1NCN undergoes a relatively slow spin-forbidden relaxation to the triplet ground state is known for a long time. In 1969, Kroto *et al.*¹⁹ not only measured singlet and triplet spectra of NCN , but also noted that the spin-forbidden relaxation is caused by collisions. In fact, this research article seems to be one of the first descriptions of a so-called collision-induced intersystem crossing (CIISC) process.

In order to provide much needed high temperature ^3NCN rate constant data, we have recently investigated the suitability of the thermal decomposition of NCN_3 as a ^3NCN radical source in shock tube experiments.¹⁵ Measured ^3NCN concentration-time profiles at temperatures $T < 1200$ K clearly revealed induction times for ^3NCN formation on the order of 10-200 μs . In a straightforward evaluation, these were explained by a sequence of the unimolecular decomposition of NCN_3 forming ^1NCN ,



and the collision induced intersystem crossing (CIISC) process converting ^1NCN to the corresponding triplet species



Unfortunately, it was not possible to fully separate the strongly correlated thermal decomposition and relaxation processes. At temperatures $T > 700$ K, an Arrhenius plot of the overall rate constants determined from the rise times of the ^3NCN concentration-time profiles yielded an activation energy of $E_A = 21$ kJ/mol, which is significantly lower than the activation energy expected for the thermal

4. Thermal Decomposition of NCN_3 and Singlet-Triplet Relaxation of NCN

decomposition of NCN_3 . This discrepancy together with the fact that the rate constants seemed to collapse at temperatures of $T < 700$ K led us to the conclusion that at temperatures of $T > 700$ K the measured ^3NCN appearance rate reflects the surprisingly slow relaxation process (3). Statistical rate constant calculations of the unimolecular NCN_3 decomposition were found to be consistent with the observed low rate constants at $T < 700$ K thus confirming that reaction (3) becomes the rate limiting step at temperatures of $T > 700$ K. The experimentally observed density dependence of the high temperature rate constants was rationalized in terms of a collision induced intersystem crossing mechanism. However, an experimental proof of these assumptions, which should be based on time resolved detection of the intermediate ^1NCN rather than the final product ^3NCN , is still pending.

Collision induced intersystem crossing processes have been discovered in the 1970s.²⁰ Typically, they are observed for small polyatomic molecules, for which the density of states of the triplet ground state is too low to drive an efficient intersystem crossing process from the singlet to the triplet state.²⁰ Temperature dependent studies of CIISC rates are scarce, but the CIISC processes of ^1NH and $^1\text{CH}_2$ have been found to exhibit weak positive temperature dependences. ^1NH relaxation has been observed at temperatures up to $T = 596$ K. For N_2 as a collision partner, Nelson *et al.*²¹ as well as Hack *et al.*²² measured overall ^1NH lifetimes on the order of $1 \mu\text{s}$ at $p \approx 100$ mbar and $T = 500$ K and low activation energies around $5 - 6$ kJ/mol. Biggs *et al.*²³ measured the temperature dependence of the singlet-triplet relaxation of CH_2 and reported lifetimes of $\tau \approx 50$ ns at $p = 50$ mbar and $T = 400$ K. The room temperature lifetimes are 50% longer, again indicating a slightly positive activation energy. In an attempt to provide a quantitative mechanistic description of the CIISC process, Bley and Temps²⁴ calculated temperature dependent CIISC rate coefficients for CH_2 by applying a mixed state model. So-called “gate states” were identified, which couple the singlet and the triplet potential energy surfaces. Their results nicely reproduce the measured data by Biggs *et al.* and thus laid a theoretical groundwork to explain such processes. Recently, Gannon *et al.*²⁵ further investigated the $^1\text{CH}_2$ relaxation at temperatures of $200 \text{ K} < T < 800 \text{ K}$ and essentially confirmed the gateway model of Bley and Temps. Some deviations from the theoretical predictions were found for larger colliders, which could be traced back to the existence of alternative gate states.

The pressure dependence of CIISC processes can be complicated.²⁰ Often, at low enough pressures (< 1 mbar for SO_2 ²⁶), Stern-Volmer behavior of the relaxation rates is observed. Toward higher pressures, similar to the fall-off behavior of unimolecular reactions, a saturation is found and the dependence of rate constants on the pressure gets weaker. Overall, the pressure dependence of CIISC processes is difficult to predict. Moreover, the CIISC rates can strongly depend on the nature of the collision partner. In the case of ^1NH , collision with Xe lead to rate constants three orders of magnitude higher than for collisions with Ar.²⁷ Apart from these complications, the mere presence of a pressure dependence can still be taken as a strong indication that collisional processes are involved in the overall singlet-triplet relaxation process.

Behind shock waves, in almost all cases only the electronic ground state of radicals can be detected.

As an exception, the excited singlet state of methylene, $^1\text{CH}_2$, has been detected by Friedrichs and Wagner^{28,29} at temperatures around $T = 2000$ K. Because of the very short lifetimes of singlet methylene, they were not able to observe the CIISC process. Instead, it was implicitly assumed that a fast equilibrium between the two electronic states takes place yielding detectable amounts of $^1\text{CH}_2$. In contrast to NCN , small equilibrium fractions of $^1\text{CH}_2$ are present at high temperatures due to the small singlet-triplet splitting of about 38 kJ/mol. To the best of our knowledge, no direct measurements of CIISC a process behind shock waves is available in the literature, yet. As far as NCN is concerned, our previous shock tube measurements clearly indicate that the role of the spin-forbidden electronic relaxation is important. In this work, concentration-time profiles of both ^1NCN and ^3NCN are reported for high temperatures as well as for room temperature. ^1NCN has been detected behind shock waves for the first time. These measurements shed light on the high temperature characteristics of the CIISC process and allow us to directly measure the NCN_3 decomposition and to reliably predict ^3NCN formation rates as needed for future kinetic measurements.

4.2 Experimental

A detailed description of the experimental set-up can be found elsewhere.^{15,30} Briefly, high-temperature experiments have been carried out behind incident shock waves in an 8 m long electro-polished stainless steel shock tube with a 4.4 m long test section and an inner diameter of 81 mm. A combination of oil free turbomolecular and diaphragm pump served to evacuate the test section down to pressures of $p \approx 10^{-7}$ mbar. The shock tube was operated by mixtures of hydrogen and nitrogen using 30 and 80 μm thick aluminum diaphragms. The shock wave velocity was measured by a fast count unit, which was connected to four pressure transducers (PCB Piezotronics M113A21). Post-shock temperature and pressure were calculated from pre-shock conditions and the shock wave velocity. A frozen chemistry code was used, real gas effects and the shock wave damping on the order of 1% have been taken into account. Room temperature measurements were performed in a 45 cm long slow flow cell made of glass. Two quartz windows were mounted in Brewster's angle at the ends of the flow cell to allow for excimer laser photolysis (193 nm, Radiant Dyes Exc 200) and collinear detection. The detection laser beam ($\varnothing = 1$ mm) and the photolysis laser beam ($\varnothing = 1.5$ cm) were combined and divided by dichroic mirrors.

NCN_3 is an extremely explosive substance. It was directly synthesized without further purification using a variant¹⁵ of the method of Milligan *et al.*³¹ The initial product was analyzed by means of FTIR spectroscopy and immediately diluted by argon down to a concentration of 0.1% to avoid secondary reactions. Since NCN_3 undergoes a slow decomposition process in the storage flask, an NCN_3 loss of 5% per day has been assumed for calculating the NCN_3 mixing ratios.¹⁵ Typically, levels of residual BrCN were $< 1\%$ and never exceeded 3%.

Room temperature ^1NCN measurements have been performed at $\tilde{\nu} = 30045.68 \text{ cm}^{-1}$, corresponding to an absorption plateau of the broad $^1\Pi_u(000) - ^1\Delta_g(000)$ transition with a band head at ($\tilde{\nu} = 30045.76 \text{ cm}^{-1}$).^{19,32} At high temperatures behind shock waves, ^1NCN has been detected at $\tilde{\nu} = 30045.46 \text{ cm}^{-1}$. The slight shift of the detection wavelength in comparison with the room temperature measurements was necessary due to an effective 0.1 cm^{-1} shift of the band head at the investigated high temperatures (see Section 4.3.2). As in our previous work,¹⁵ ^3NCN has been detected at $\tilde{\nu} = 30383.11 \text{ cm}^{-1}$. The absorption feature at this wavelength stems from a superposition of the $^3\Pi_1$ sub band of the $\tilde{A}^3\Pi_u(000) - \tilde{X}^3\Sigma_g(000)$ and the Q_1 band head of the $^3\Sigma^+(010) - ^3\Pi(010)$ transition.³³⁻³⁵

Narrow bandwidth laser radiation ($< 10 \text{ MHz}$) was generated by intra-cavity frequency doubling (LiIO_4 crystal) of the output of an electronically stabilized continuous-wave ring-dye laser (Coherent 899, DCM Special dye) pumped by an Nd:YVO_4 solid state laser (Coherent Verdi V10, $\lambda = 532 \text{ nm}$). The wavelength of the fundamental was measured by an interferometric wavemeter (MetroLux 200), which was referenced to a HeNe laser. Time-resolved absorption measurements have been performed by means of difference amplification using a well-balanced photo detector (Thorlabs PDB 150A-EC). The UV output of the ring-dye laser was split into detection and reference beam by a 50:50 beam splitter plate. The detection beam was passed through the shock tube or the flow cell, the reference beam could be attenuated by a variable neutral density filter to level the intensities of both beams.

Data processing was carried out by fitting selected parameters of the appropriate first-order analytical expressions to the measured absorbance-time profiles using the gnuplot³⁶ program. For some measurements, rate constants were obtained by fitting numerical simulations to concentration-time profiles. These simulations were performed by the Chemkin-II program package.³⁷ Required thermodynamic data for reverse rate constant calculations were taken from Konnov,³⁸ except for NCN , for which the data were taken from Goos *et al.*³⁹ Sensitivity analyses were performed by the Senkin routine; normalized sensitivity coefficients $\sigma(^{1,3}\text{NCN})$ were obtained by referencing with respect to the maximum of the NCN concentration-time profile.

4.3 Results and discussion

4.3.1 Room temperature measurements

Typical concentration-time profiles of the singlet and triplet species of cyanonitrene are shown in Fig. 1. Note that the intense photolysis laser pulse causes a constant offset in the absorption signals, which can be attributed to thermal effects. It is already discernible in the first μs before the actual initial rise of the signals takes place and causes an absorption plateau at longer reaction times. This offset has also been observed, if to a lesser extent, in experiments in pure argon and was dependent on the adjustment of the optical set-up. Following the photolysis of NCN_3 , the singlet signal exhibits

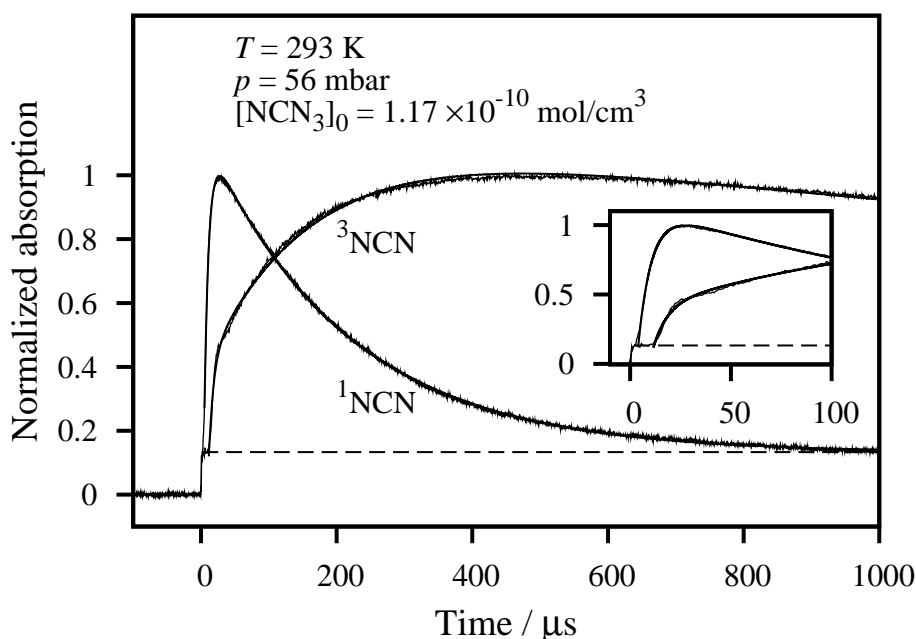


Figure 1: Comparison of ^1NCN and ^3NCN concentration-time profiles and the corresponding fits at room temperature and $p = 56 \text{ mbar}$. $t = 0$ corresponds to the excimer laser photolysis pulse. Note the pronounced offset (dashed line), which affects both singlet and triplet signals.

a fast rise and subsequently a slower decay. The ^3NCN profile is a little bit more complex. As can be seen in the inset of Fig. 1, a pronounced induction period on the order of $10 \mu\text{s}$ is followed by a steep rise of absorption, which then continues with a slower rate. At long reaction times the signal starts to decay slowly.

A simple model describes the singlet measurements: Vibrationally and electronically excited ^1NCN radicals, denoted $^1\text{NCN}^*$, are generated by the laser photolysis of NCN_3 . According to Bise *et al.*⁴⁰, a rich variety of six ^1NCN electronic states is accessible following the 193 nm photolysis of NCN_3 . This excited $^1\text{NCN}^*$ is collisionally deactivated to its lowest electronic singlet state ($^1\Delta_g$), in which ^1NCN is detected. This deactivation process is reflected by the fast increase of the signal. The slower decay of the signal can be attributed to several processes. Next to singlet-triplet relaxation via CIISC, ^1NCN may also disappear through fast bimolecular reactions. Next to a self reaction, $^1\text{NCN} + ^1\text{NCN}$, the reactions with CN radicals and N atoms, which are also formed in the photolysis, are conceivable. Also radiative contributions cannot be completely ruled out. In contrast, diffusional loss can be assumed to be of minor importance since the decay of the ^3NCN signal is much slower than that of the ^1NCN signal and diffusion rates can be supposed to be similar for both species.

Apart from the instrumental offset, the ^3NCN signal indicates three phases: The first phase comprises the initial induction time followed by the steep increase of the signal. We attribute this first phase to the direct relaxation of initially formed highly excited NCN radicals. For example, according to

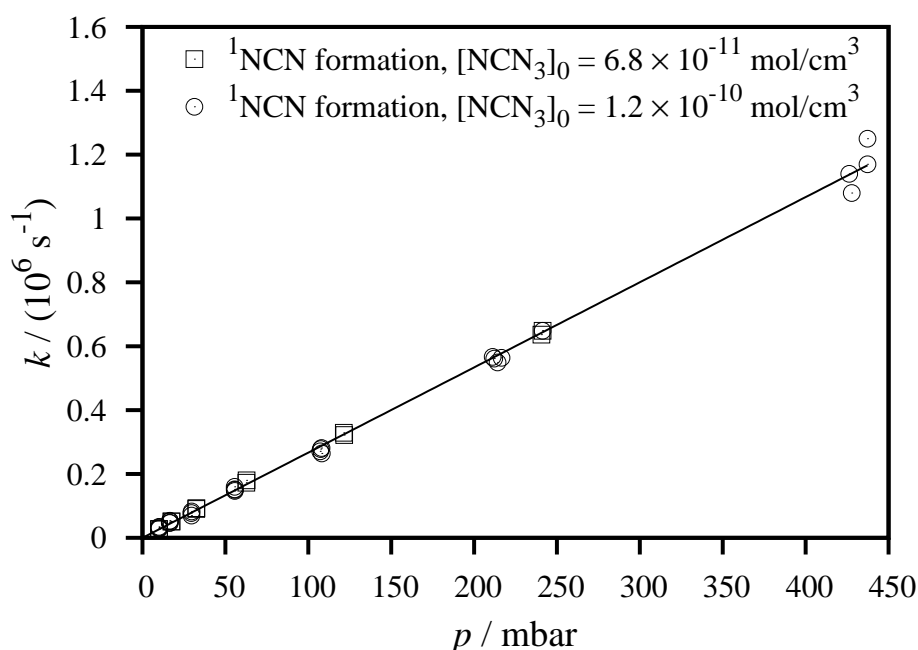
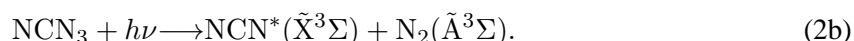


Figure 2: Pressure dependence of the ^1NCN formation rate constants following the 193 nm photolysis of NCN_3 at room temperature.

Baumgärtel *et al.*,⁴¹ even vibrationally excited $^3\text{NCN}^*$ can be directly generated in the spin-allowed photolysis process



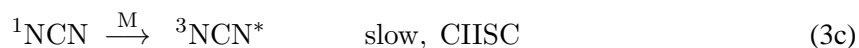
The reported threshold energy of 190 nm is close to the used photolysis wavelength of 193 nm, thus a direct formation of ^3NCN in the 193 nm photolysis via the spin-allowed reaction (2b) cannot be ruled out. It is also feasible that fast intersystem crossing (ISC) processes of electronically and/or vibrationally highly excited $^1\text{NCN}^*$ radicals yield significant amounts of $^3\text{NCN}^*$.

The second phase of the triplet signal comprises the slower rise taking place on the same time scale as the ^1NCN decay. This part of the signal can be attributed to the formation of ^3NCN following the CIISC process of vibrationally thermalized ^1NCN radicals in their lowest electronic singlet state. From this point of view, the corresponding ^3NCN formation should approximately match the ^1NCN decay rate; in accordance with the signals shown in Fig. 1.

Finally, the third phase comprises the slow decay of the ^3NCN signal at longer reaction times. It subsumes all NCN consuming processes such as self-reactions, reactions with other photodissociation or secondary products, and diffusion.

4. Thermal Decomposition of NCN₃ and Singlet-Triplet Relaxation of NCN

Overall, the NCN formation mechanism can be summarized in the following simplified scheme:



In this scheme, processes denoted “fast” represent the fast relaxation of the excited species reflecting the fast increase of the singlet and the triplet signals. The only process generating ³NCN on a slower time scale is the CIISC process (3c). The last two reactions (4,5) reflect possible secondary chemistry and diffusional processes of NCN and are treated in an appropriate manner as simple first-order processes.

¹NCN concentration-time profiles have been evaluated by fitting a simple analytical function to the measured profiles assuming consecutive first order processes. The measured instrumental offset was added as a constant.

$$\frac{\ln(I_0/I)}{\sigma l} = [{}^1\text{NCN}] = \frac{k_{\text{app}} [{}^1\text{NCN}^*]_0}{k_{\text{con}} - k_{\text{app}}} \times (\exp[-k_{\text{app}}(t - t_0)] - \exp[-k_{\text{con}}(t - t_0)]) + \text{Offset}$$

The appearance rate constant k_{app} reflects k_{3b} and the consumption rate constant k_{con} corresponds to the sum of k_{3c} and k_4 . Here, $[{}^1\text{NCN}^*]_0$ denotes the initial concentration of vibrationally excited ¹NCN* that is formed in the photolysis and is thermalized to ¹NCN(¹Δ_g) through reaction (3b). Note that an additional fraction of ¹NCN* that may have been directly transformed to ³NCN* escapes from our ¹NCN detection scheme. t_0 has been introduced to account for the small pressure dependent induction times on the order of 1-10 μs. More sophisticated models intended to extract an additional rate constant to fit these induction times turned out to be numerically unstable.

A plot of the determined ¹NCN formation rate constants is shown in Fig. 2. The experimental conditions and results are listed in the Supplementary Information. The fact that the rate linearly depends on the total pressure and does not show any dependence on the initial NCN₃ concentration reveals a simple collisional deactivation process. The slope of the regression line yields a bimolecular room

4. Thermal Decomposition of NCN_3 and Singlet-Triplet Relaxation of NCN

temperature rate constant of

$$k_{3b} = (6.6 \pm 1.3) \times 10^{10} \text{ cm}^3/\text{mol s.}$$

Actually, this rate constant value is untypically low for a simple vibrational relaxation process, which often proceeds close to the collisional limit. As already outlined above, several electronic states are involved in the 193 nm photolysis of NCN_3 . Consequently, it is feasible that rather slow electronic deactivation steps are subsumed in the measured overall relaxation rate constant.

The decay of the ^1NCN signal is assumed to reflect the sum of the ^1NCN consuming processes, presumably dominated by CIISC. The corresponding rate constants k_{con} are shown in Fig. 3 and will be discussed below together with the results from the triplet measurements.

For fitting the triplet signals, the fast and slow components were treated as two independent processes with the rate constants k_{fastapp} and k_{slowapp} . According to the presented reaction scheme, the triplet species concentration-time profile is given by

$$\begin{aligned} \frac{\ln(I_0/I)}{\sigma l} = [^3\text{NCN}] = & \frac{k_{\text{fastapp}} [^{1,3}\text{NCN}^*]_0}{k_{\text{con}} - k_{\text{fastapp}}} \times (\exp[-k_{\text{fastapp}}(t - t_0)] - \exp[-k_{\text{con}}(t - t_0)]) \\ & + \frac{k_{\text{slowapp}} [^1\text{NCN}]_0}{k_{\text{con}} - k_{\text{slowapp}}} \times (\exp[-k_{\text{slowapp}}(t - t_0)] - \exp[-k_{\text{con}}(t - t_0)]) \\ & + \text{Offset.} \end{aligned}$$

Here, $[^{1,3}\text{NCN}^*]_0$ refers to the fraction of initially formed highly excited singlet and triplet NCN^* that directly forms ^3NCN through reactions (2b), (3a), and (3d). Hence, it does not include initial $^1\text{NCN}^*$ that is thermalized within the singlet system. This latter fraction is termed $[^1\text{NCN}]_0$ and is further deactivated to the triplet ground state via CIISC. Though the experimental induction times are not necessarily equal for the fast and the slow processes, only one t_0 value was used in the fits. Again, k_{con} subsumes secondary NCN reactions and diffusion.

The extracted rate constants of the slow component of the ^3NCN appearance are summarized together with the ^1NCN decay rate constants in Fig. 3. Data of the experimental conditions and results are listed in the Supplementary Information. Overall, the singlet and triplet data show reasonable agreement with respect to absolute rate constant values as well as the observed pressure dependence. Thus, both rate constants can be assumed to represent the same process, namely CIISC. A simple linear fit of the ^3NCN experiments at $p > 20$ mbar roughly represents the overall pressure dependence of all data. It yields a high intercept value of $k = 4.5 \times 10^3 \text{ s}^{-1}$ at $p = 0$ mbar. However, this intercept cannot be attributed to radiative processes in terms of a simple Stern-Volmer plot. Instead, as it is discernible from the ^3NCN data at pressures $p < 20$ mbar, the rate constants indicate a downward trend, which is not reflected by the simple linear fit. To guide the eye, the dashed curve in Fig. 3 represents this low pressure behavior of the triplet data (circles). Unfortunately, due to experimental constraints, we

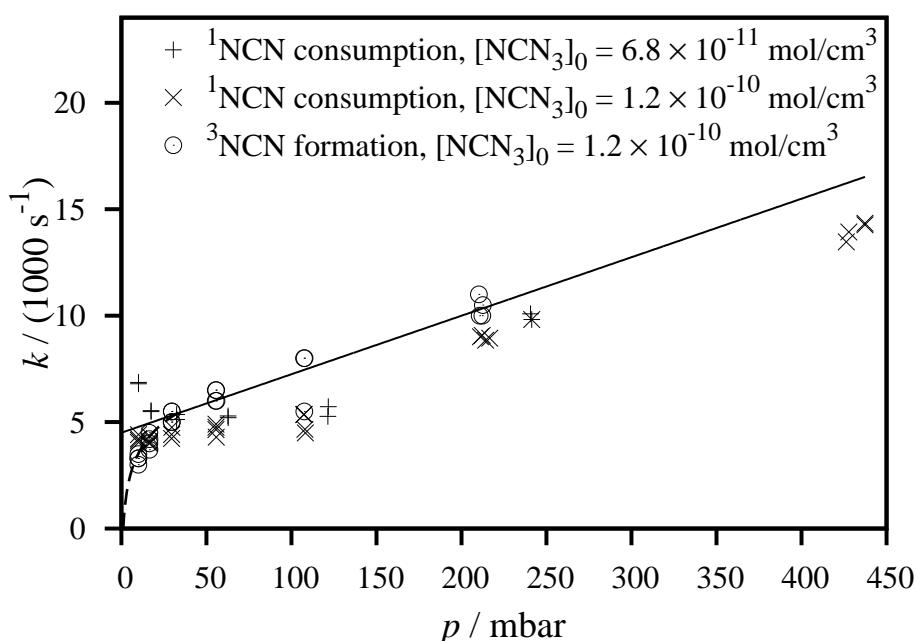


Figure 3: Pressure dependences of the rate constants associated with the CIISC process. The data represent the room temperature singlet decay rates as well as the slow component of the ^3NCN formation following the 193 nm photolysis of NCN_3 . The solid line corresponds to a linear fit of the ^3NCN data at $p > 20$ mbar, the dashed curve indicates the fall-off-like low pressure behavior.

were not able to perform measurements at even lower pressures to further verify this low pressure trend. However, the depicted dashed curve is in agreement with the expected pressure dependence of a CIISC process. As outlined in Section 4.1, the pressure dependence often changes its nature from a Stern-Volmer like behavior at low pressures to a weaker pressure dependence at higher pressures. A more detailed analysis of similar data has been presented by Strickler and Rudolph for the quenching of the $^3\text{B}_1$ state of SO_2 .²⁶ In their work, radiative and non-radiative pressure independent relaxation processes as well as the pressure dependent CIISC have been analyzed. For SO_2 diluted in CO_2 or N_2 , the CIISC process has been found to govern the relaxation and could be rationalized with a simple kinetic model similar to the well established models for unimolecular reactions. Low pressure and high pressure regimes were identified resulting in a pressure saturation effect of the relaxation rate constants toward higher pressures. Qualitatively spoken, the triplet data shown in Fig. 3 are consistent with such a model. Of course, the details of the “fall-off”-like behavior strongly depend on the nature of the collider gas and the particular system under study.

Note that the overall pressure dependence of the data extracted from the ^1NCN concentration-time profiles does not satisfy the discussed fall-off-like trend. As already mentioned above, high electronic states are involved in NCN_3 photodissociation at 193 nm. Relaxation processes of these states may have interfered with our simplified data analysis and therefore the ^1NCN data are less reliable. More

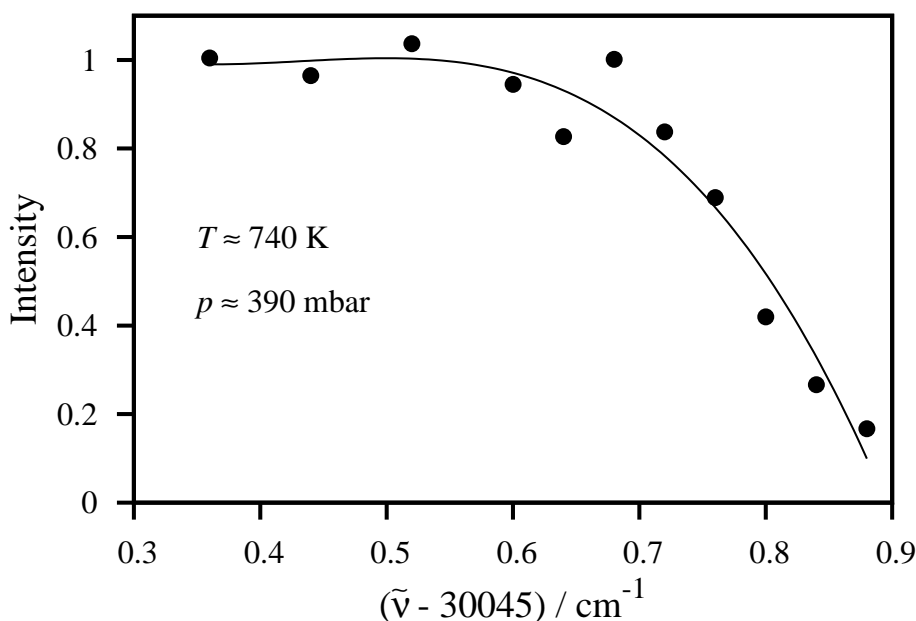


Figure 4: Part of the high temperature spectrum of ^1NCN . Shown is the band head of the $^1\Pi_u(000) - ^1\Delta_g(000)$ transition.

sophisticated experiments with variable photolysis wavelengths and state resolved detection schemes would have been needed to gain further insight into the complicated dynamics of the initially formed highly excited species. Clearly, such measurements would have been beyond the scope of this study.

4.3.2 High temperature measurements

^1NCN high temperature cross section

^1NCN has been detected at high temperatures behind shock waves for the first time. The thermal decomposition of NCN_3 behind shock waves was used as a source of ^1NCN . Since the high temperature detection of ^1NCN is new and absorption cross sections are unknown, a part of the high temperature spectrum of ^1NCN has been measured behind incident shock waves at a temperature of $T \approx 740$ K and a pressure of $p \approx 390$ mbar, beforehand. The resulting spectrum is shown in Fig. 4. Each single data point is based on a separate shock tube experiment with the detection laser tuned to the respective wavelength. The spectrum is dominated by the band head of the $^1\Pi_u - ^1\Delta_g$ transition of the $(000) - (000)$ vibrational ground state. Compared to the room temperature spectrum,^{19,32} the band head is slightly shifted by $\approx 0.1 \text{ cm}^{-1}$ toward lower wavenumbers. All high temperature kinetic measurements have been performed in the region of the absorption plateau at a wavenumber of 30045.46 cm^{-1} . Based on absolute ^1NCN concentrations derived from the kinetic simulations outlined in the next section, temperature dependent ^1NCN absorption cross sections could be determined in the temperature range $618 \text{ K} < T < 1231 \text{ K}$. A plot of the absorption cross sections versus temper-

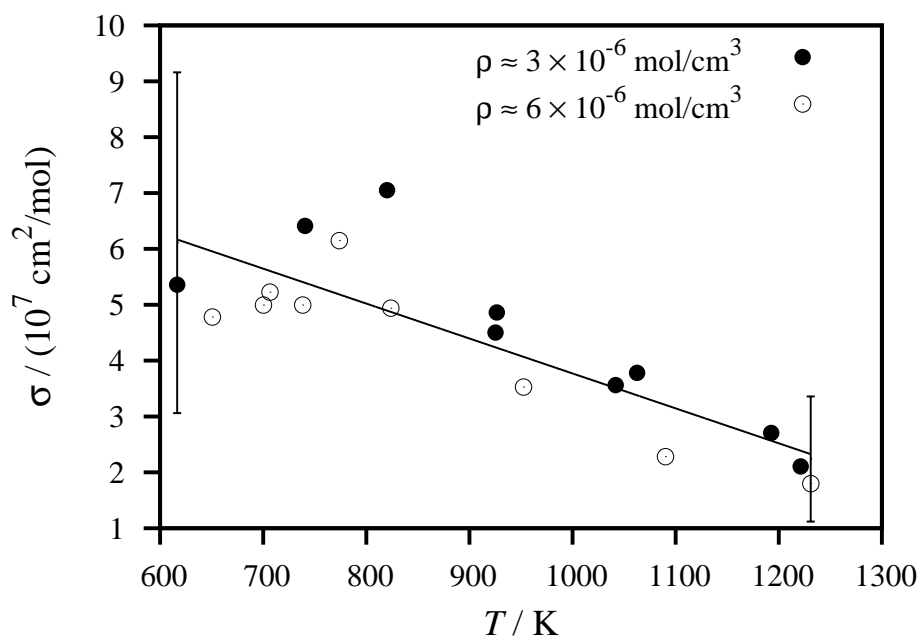


Figure 5: Temperature dependence of the ^1NCN absorption cross sections. σ (base e) at $\tilde{\nu} = 30045.46 \text{ cm}^{-1}$.

ature is shown in Fig. 5. Experiments have been performed at two different total densities. Though the lower density data points seem to be systematically higher by approximately 25%, in the light of the uncertainties of the mechanistic model, this pressure dependence is not significant. The data can be best represented by

$$\sigma / (\text{cm}^2/\text{mol}) = 1.0 \times 10^8 - 6.3 \times 10^4 \text{ K}^{-1} \times T \quad (\pm 50\%).$$

The stated error results from uncertainties in the initial NCN_3 concentrations, the modeled intermediate ^1NCN concentrations, and the statistical error of the fit.

Owing to the broad absorption feature stemming from the overlap of many rovibrational lines, ^1NCN absorption cross sections exhibit a rather weak temperature dependence. Both the absorption cross sections of ^1NCN and of ^3NCN are on the same order of magnitude. At $T = 1000 \text{ K}$, $\sigma(^3\text{NCN}) = 1 \times 10^8 \text{ cm}^2/\text{mol}$, and $\sigma(^1\text{NCN}) = 3 \times 10^7 \text{ cm}^2/\text{mol}$. Therefore, the unusual situation arises that both the electronic ground state and the excited state of a radical can be detected behind shock waves with comparable sensitivities. Performing kinetic measurements at similar experimental conditions simplifies the data evaluation and enhances the reliability of the derived models.

^1NCN measurements

A typical ^1NCN concentration-time profile is shown in Fig. 6. Time zero is set by the Schlieren signal,

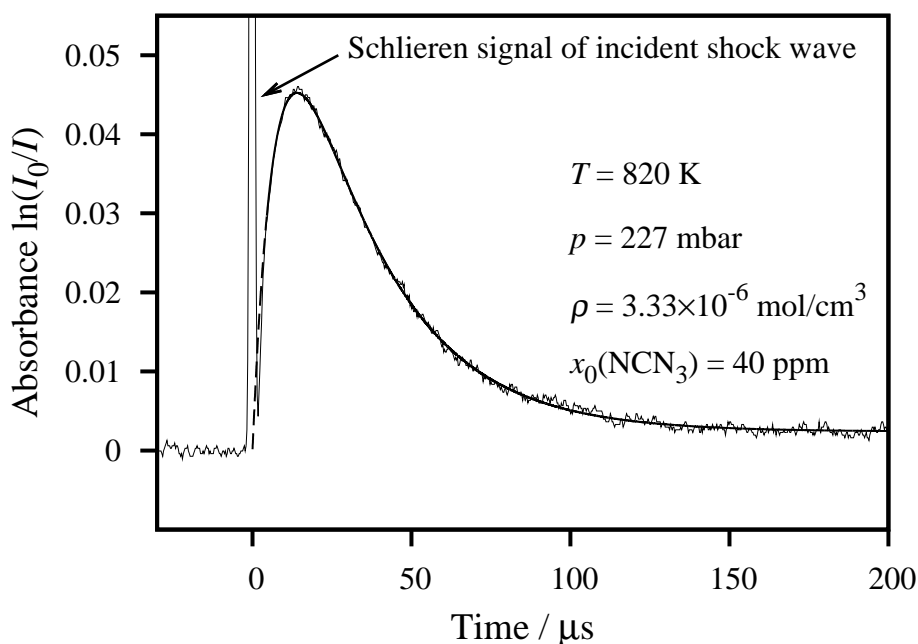


Figure 6: ^1NCN concentration-time profile measured behind an incident shock wave.

which indicates the arrival of the incident shock wave. The width of the Schlieren signal roughly defines the time resolution of the experiments, in this work $\Delta t \approx 4 \mu\text{s}$. The formation of ^1NCN is determined by the thermal decomposition of the precursor molecule NCN_3 . In contrast to the room temperature photolysis experiments, the thermal generation of ^1NCN does not require relaxation of highly excited $^1\text{NCN}^*$ species. Within the time resolution of the experiments no induction times have been observed. The ^1NCN decay can be directly attributed to the CIISC process. Alternative loss processes such as secondary chemistry should not play a role due to the low concentration levels present in the experiments. For example, a simulation assuming a very high rate constant of $k = 1 \times 10^{14}$ for the potential reaction $^1\text{NCN} + ^1\text{NCN}$ resulted in an only 10% lower value for the CIISC rate coefficient. Furthermore, the single exponential decays revealed a dominating (pseudo) first-order process such that there is only little room for a significant contribution of any second-order reaction.

At longer reaction times, a small background absorption signal remains, which can be attributed to interfering ^3NCN absorption. A slow decay of this weak background signal observed in validation experiments with much higher NCN_3 mole fractions is consistent with NCN loss from the bimolecular reaction $^3\text{NCN} + ^3\text{NCN}$. The concentration-time profiles were analyzed based on a simple consecutive first-order kinetics scheme according to



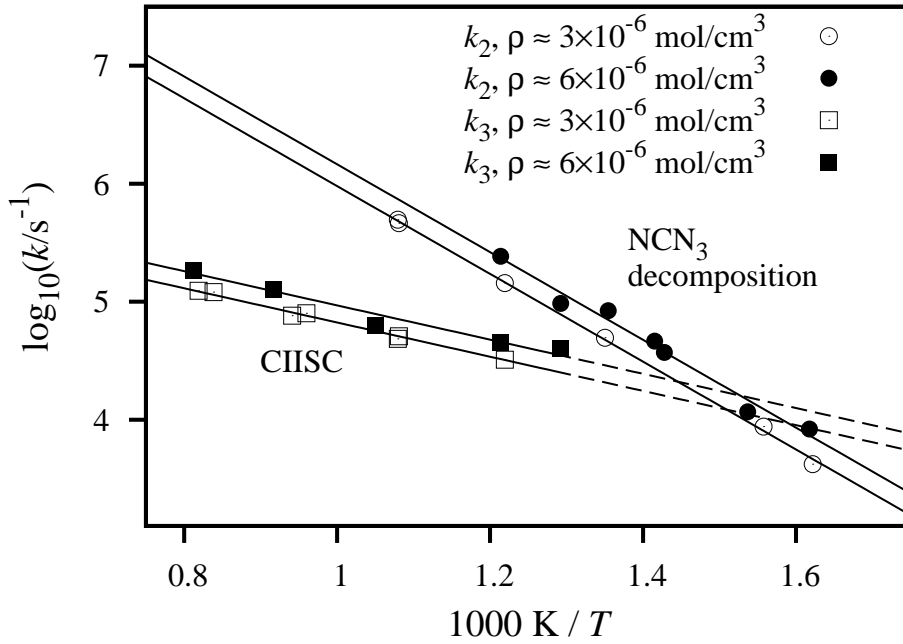


Figure 7: Arrhenius plot of the rate constants of the NCN_3 decomposition and the CIISC process at two different total densities ρ . The dashed lines denote the extrapolation of the rate constants to lower temperatures.

The function

$$\frac{\ln(I_0/I)}{\sigma l} = [^1\text{NCN}] = \frac{k_2 [\text{NCN}_3]_0}{k_3 - k_2} \left(e^{-k_2 t} - e^{-k_3 t} \right) + f \times [\text{NCN}_3]_0 \left(1 - \frac{k_3}{k_3 - k_2} e^{-k_2 t} + \frac{k_2}{k_3 - k_2} e^{-k_3 t} \right)$$

was fitted to the profiles by adjusting the rate constants of reactions (2), $\text{NCN}_3 \rightarrow \text{NCN} + \text{N}_2$, reaction (3), $^1\text{NCN} \rightarrow ^3\text{NCN}$, and the amplitude of the function, which is determined by $[\text{NCN}_3]_0$. The second term the equation takes into account the interfering background absorption of the formed ^3NCN , where $f \approx \sigma(^3\text{NCN})/\sigma(^1\text{NCN})$.

A complication arose from the strong correlation between the two rate constants k_2 and k_3 , which precluded their reliable determination at temperatures of $T < 770$ K. Therefore, k_3 has been extracted only from experiments at temperatures $T > 770$ K, where the two processes were clearly separable. Then, by using extrapolated k_3 values at lower temperatures, it was possible to extract reliable values for k_2 at $T < 770$ K, as well.

An Arrhenius plot of the obtained rate constants is shown in Fig. 7. Experiments have been performed in the temperature range $617 \text{ K} < T < 1239 \text{ K}$ at two different total densities: $\rho_{\text{low}} \approx 3 \times 10^{-6} \text{ mol/cm}^3$ and $\rho_{\text{high}} \approx 6 \times 10^{-6} \text{ mol/cm}^3$. Data of the experimental conditions and results are listed in the Supplementary Information. The rate constants are best represented by the following

expressions (solid lines):

$$\begin{aligned} k_2(\rho_{\text{low}})/\text{s}^{-1} &= 4.9 \times 10^9 \times \exp(-71 \text{ kJ mol}^{-1}/RT), \\ k_2(\rho_{\text{high}})/\text{s}^{-1} &= 7.5 \times 10^9 \times \exp(-71 \text{ kJ mol}^{-1}/RT), \\ k_3(\rho_{\text{low}})/\text{s}^{-1} &= 1.9 \times 10^6 \times \exp(-28 \text{ kJ mol}^{-1}/RT), \\ k_3(\rho_{\text{high}})/\text{s}^{-1} &= 2.7 \times 10^6 \times \exp(-28 \text{ kJ mol}^{-1}/RT). \end{aligned}$$

An error estimate of $\pm 30\%$ holds for all expressions. It is based on a combination of statistical errors and a consideration of systematic errors of temperature, total density and initial NCN_3 concentration. The errors of the Arrhenius activation energies are ± 14 kJ/mol for reaction (2) and ± 7 kJ/mol for reaction (3). The rate constants k_2 of the thermal decomposition of NCN_3 have been determined up to temperatures of $T = 867$ K. At higher temperatures, the too fast increase of the signal could not be resolved. With an activation energy of $E_a = 71$ kJ/mol, the temperature dependence of the unimolecular decomposition of NCN_3 is much stronger than the temperature dependence of the CIISC process. Consequently, at a temperature of $T \approx 650$ K, the dominant reaction for the ^3NCN formation switches from the NCN_3 decomposition at low to CIISC at high temperatures. Regarding the density dependence, with 1.5 times higher rate constants at a doubled total density, the unimolecular decomposition process takes place in the fall-off region. With a factor of 1.4, the CIISC process exhibits a similar pressure dependence. Keeping in mind the elevated pressures behind shock waves, this is in agreement with the pressure saturation effect already discussed in connection with the room temperature experiments.

In our recent paper,¹⁵ we reported an activation energy of $E_a = 93$ kJ/mol for the thermal decomposition of NCN_3 . This value was based on a combination of quantum-chemical (G3) and statistical (RRKM) calculations. Although with 22 kJ/mol the difference between our previous value and the value reported in this work is not extensive, the reason for this deviation remains unclear. We suspect inaccuracies in our calculated threshold energy E_0 , which had been determined by the composite method G3. This method includes empirical scaling factors that might not be perfectly matched for the molecules NCN_3 and NCN . Therefore, we recommend the experimentally based expressions reported in this work for future use.

^3NCN measurements

^3NCN concentration-time profiles have been measured behind incident shock waves in the temperature range $582 \text{ K} < T < 1257 \text{ K}$ at three different total densities. Some of these measurements have already been discussed in our recent publication.¹⁵ In this work, we further extended the database and re-evaluated all data by taking into account the newly determined decomposition rates of NCN_3 from the ^1NCN experiments. A typical ^3NCN signal together with a numerical simulation and the

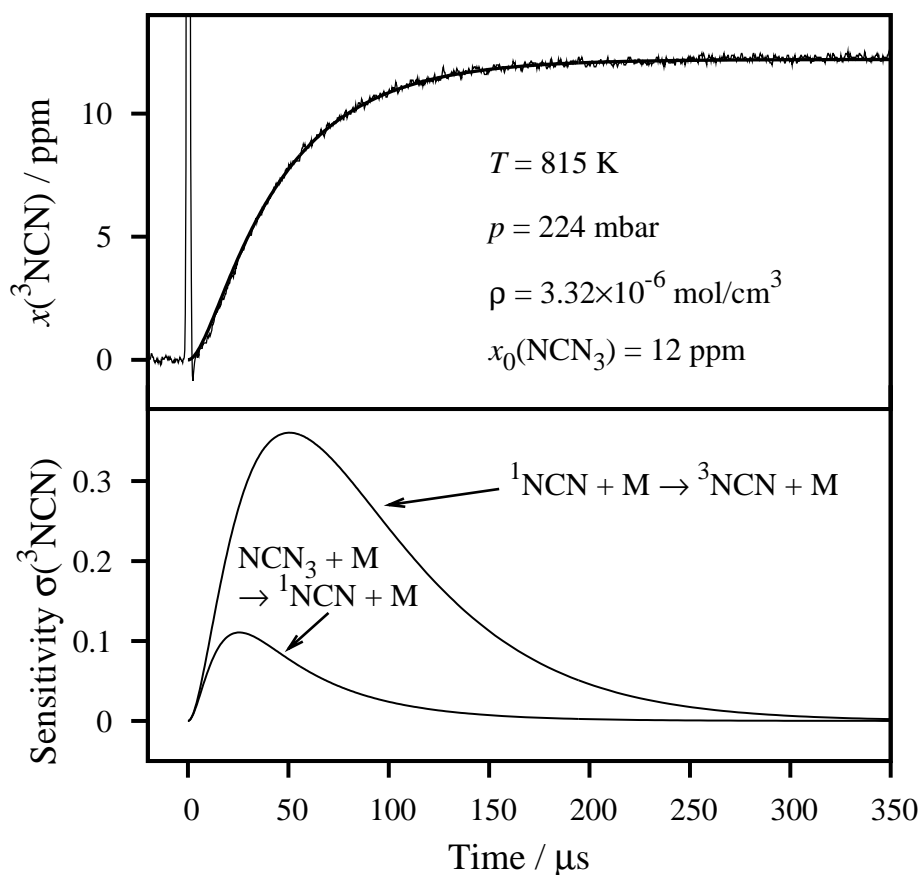


Figure 8: Upper: Typical ^3NCN signal at experimental conditions similar to the conditions of the ^1NCN experiment shown in Fig. 6. The NCN_3 decomposition process is discernible as a short induction time. The solid curve represents the numerical simulation of the reaction system. Lower: Corresponding sensitivity analysis.

corresponding sensitivity analysis is shown in Fig. 8. In addition to the two reactions shown in the sensitivity analysis, our recent NCN mechanism¹⁶ comprising many potentially interfering reactions and the GRI-Mech. 3.0⁴² natural gas mechanism have been used as a background chemistry. After a short induction period, which can be attributed to the pyrolysis of the precursor molecule, the signal increases until it reaches a constant plateau value. The fact that a stable ^3NCN concentration plateau is reached reveals that interfering secondary chemistry does not play a role for the experiment shown in Fig. 8. The sensitivity analysis illustrates that both the assumed rate constants for the NCN_3 decomposition (2) and the CIISC process (3) are important at short reaction times. However, being able to keep k_2 fixed as determined from the ^1NCN measurements, k_3 values could be reliably extracted by fitting the overall ^3NCN formation rate. Data of the experimental conditions and results are listed in the Supplementary Information. In Fig. 9, determined rate constant data are compared to the results of the singlet experiments. The singlet results have been adopted from Fig. 7 and are shown as dashed lines. The solid lines represent the Arrhenius expressions ($701 \text{ K} < T < 1256 \text{ K}$) of the triplet data measured at three different total densities of $\rho_1 \approx 1.8 \times 10^{-6} \text{ mol/cm}^3$, $\rho_2 \approx 3.5 \times 10^{-6} \text{ mol/cm}^3$,

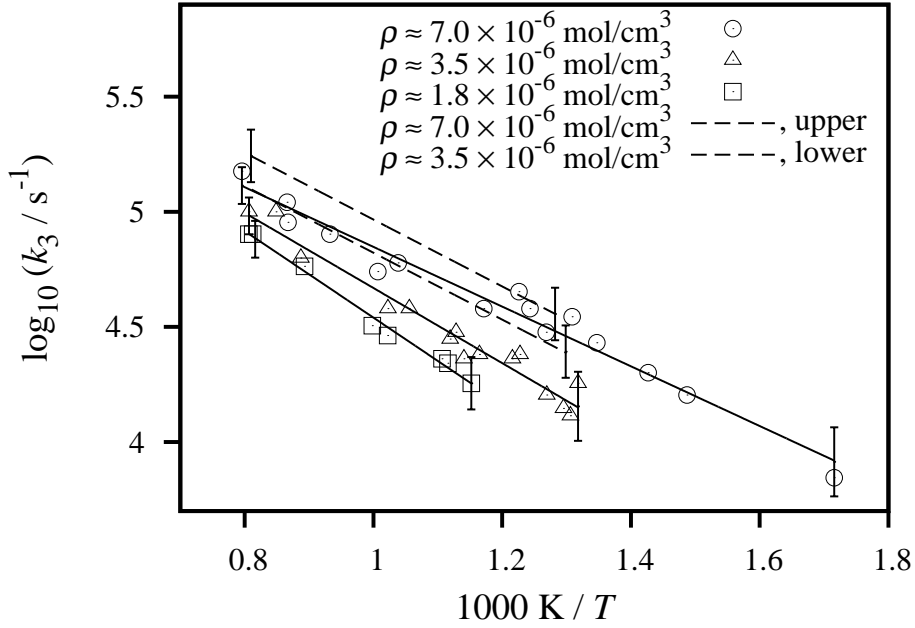


Figure 9: Arrhenius plot of CIISC rate constants extracted from the triplet concentration-time profiles. Solid lines: Arrhenius fit of the measured data points. Dashed lines depict the results from the ^1NCN measurements as shown in Fig. 7.

and $\rho_3 \approx 7.0 \times 10^{-6} \text{ mol/cm}^3$:

$$\begin{aligned} k_3(\rho_1) / \text{s}^{-1} &= 2.6 \times 10^6 \times \exp(-36 \text{ kJ mol}^{-1} / RT), \\ k_3(\rho_2) / \text{s}^{-1} &= 2.0 \times 10^6 \times \exp(-31 \text{ kJ mol}^{-1} / RT), \\ k_3(\rho_3) / \text{s}^{-1} &= 1.4 \times 10^6 \times \exp(-25 \text{ kJ mol}^{-1} / RT). \end{aligned}$$

An error estimate of $\pm 20\%$ holds for all expressions. It is based on combined uncertainties of k_2 and statistical errors. The Arrhenius activation energies are accurate to $\pm 10 \text{ kJ/mol}$. This rather large error results from the fact that only the low temperature data points are systematically affected by the uncertainty of k_2 . At higher temperatures, the NCN_3 decomposition becomes very fast and the signal directly reflects the CIISC relaxation rate constant.

In contrast to the ^1NCN data, the activation energies seem to depend on the total density ρ . However, given the rather large error margin of the Arrhenius activation energies, all data can be assumed to yield essentially the same temperature dependence with an average activation energy of $E_a = 30 \text{ kJ/mol}$. Although there seems to be a significant offset between the ^1NCN and the ^3NCN data, especially at $\rho = 3.5 \text{ mol/cm}^3$, the remaining discrepancies are $< 35\%$ and thus within the combined error limits of the two measurements. As outlined above, a significant influence of ^1NCN secondary chemistry that might have caused an overestimation of the relaxation rate in the ^1NCN measurements

is unlikely. Instead, we ascribe the offset to a numerical effect stemming from the fitting procedures used to separate the strongly correlated k_2 and k_3 values. Overall, the good agreement between the singlet and triplet data sets underlines our initial assumption that both the decay of the ^1NCN and the increase of the ^3NCN profiles directly reflect the CIISC process.

4.4 Conclusion

The pyrolysis and the photolysis of NCN_3 yields electronically excited ^1NCN thus making possible the investigation of the collision induced intersystem crossing (CIISC) process starting from highly excited (photolysis experiments) as well as thermalized (shock tube experiments) cyanonitrene radicals. The CIISC process has been monitored by detecting both ^1NCN and ^3NCN concentration-time profiles. To the best of our knowledge, these data represent the first quantitative measurement of a CIISC process behind shock waves. Consistent data sets have been obtained clearly showing that the CIISC process dominated the ^1NCN and ^3NCN concentration-time profiles. For future work, we recommend the rate constant expressions extracted from the more reliable ^3NCN measurements.

Due to the formation of highly excited $^1\text{NCN}^*$ (and possibly $^3\text{NCN}^*$) in the photolysis experiments, the concentration-time profiles reflect a quite complex superposition of several possible relaxation pathways. Nevertheless, it was possible to extract the overall pressure dependence of the CIISC process. At room temperature and pressures $p > 20$ mbar, a pressure saturation was observed showing that the CIISC process cannot be described as a simple bimolecular reaction step. This finding has been confirmed by the high temperature measurements yielding an approximate density dependence of $k \propto \rho^{0.6}$ instead of $k \propto \rho^1$ as expected for a simple collisional process. Overall, a weak positive temperature dependence has been observed. For example, at a density of $\rho = 3.5 \times 10^{-6}$ mol/cm³, the CIISC rate constant increases from $k_3 = 7.0 \times 10^3$ s⁻¹ at room temperature to $k_3 = 4.8 \times 10^4$ s⁻¹ at $T = 1000$ K.

High temperature measurements of the thermal decomposition of NCN_3 revealed a unimolecular reaction in the fall-off regime. The recommended rate constant expressions, which are based on the first ^1NCN measurements behind shock waves, supersede our previously reported rate constant estimate. Moreover, near UV high temperature absorption cross sections of ^1NCN have been reported. It turns out that both ^3NCN and ^1NCN can be detected with comparable sensitivities. In combination with the unusually long lifetime of the electronically excited ^1NCN radical, this opens the door to perform comparative studies of ^1NCN and ^3NCN reactivity at high temperatures.

Acknowledgment

We would like to thank the German Science Foundation (DFG - FR 1529/4), the cluster of excellence "The Future Ocean" (DFG - EC 80), and Friedrich Temps for financial and scientific support.

Bibliography

- [1] K. R. Jennings and J. W. Linett, Emission Spectra of Flames Supported by Active Nitrogen, *Trans. Faraday Soc.* **1960**, *56*, 1737–1741.
- [2] L. V. Moskaleva and M. C. Lin, The Spin-Conserved Reaction $\text{CH} + \text{N}_2 \rightarrow \text{H} + \text{NCN}$: A Major Pathway to Prompt NO Studied by Quantum/Statistical Theory Calculations and Kinetic Modeling of Rate Constant, *Proc. Combust. Inst.* **2000**, *28*, 2393–2401.
- [3] L. V. Moskaleva, W. S. Xia, and M. C. Lin, The $\text{CH} + \text{N}_2$ Reaction Over the Ground Electronic Doublet Potential Energy Surface: A Detailed Transition State Search, *Chem. Phys. Lett.* **2000**, *331*, 269–277.
- [4] C. P. Fenimore, Formation of Nitric Oxide in Premixed Hydrocarbon Flames, *Proc. Combust. Inst.* **1971**, *13*, 373–380.
- [5] J. Warnatz, U. Maas, and R. W. Dibble, *Combustion*, Springer, Berlin/Heidelberg, 3. edition, **2001**.
- [6] G. P. Smith, Evidence of NCN as a Flame Intermediate for Prompt NO, *Chem. Phys. Lett.* **2003**, *367*, 541–548.
- [7] V. Vasudevan, R. K. Hanson, C. T. Bowman, D. M. Golden, and D. F. Davidson, Shock Tube Study of the Reaction of CH with N_2 : Overall Rate and Branching Ratio, *J. Phys. Chem. A* **2007**, *111*, 11818–11830.
- [8] J. A. Sutton, B. A. Williams, and J. W. Fleming, Laser-Induced Fluorescence Measurements of NCN in Low-Pressure $\text{CH}_4/\text{O}_2/\text{N}_2$ Flames and Its Role in Prompt NO Formation, *Combust. Flame* **2008**, *153*, 465–478.
- [9] R. J. H. Klein-Douwel, N. J. Dam, and J. J. ter Meulen, Laser-Induced Fluorescence of NCN in Low and Atmospheric Pressure Flames, *Optics Lett.* **2008**, *33*, 2620–2622.
- [10] Z. W. Sun, N. J. Dam, and M. Aldn, NCN Detection in Atmospheric Flames, *Combust. Flame* **2010**, *157*, 834–836.
- [11] R. E. Baren and J. F. Hershberger, Kinetics of the NCN Radical, *J. Phys. Chem. A* **2002**, *106*, 11093–11097.

4. Thermal Decomposition of NCN_3 and Singlet-Triplet Relaxation of NCN

- [12] C.-L. Huang, S. Y. Tseng, T. Y. Wang, N. S. Wang, Z. F. Xu, and M. C. Lin, Reaction Mechanism and Kinetics of the $\text{NCN} + \text{NO}$ Reaction: Comparison of Theory and Experiment, *J. Chem. Phys.* **2005**, *122*, 184321.
- [13] T.-J. Yang, N. S. Wang, L. C. Lee, Z. F. Xu, and M. C. Lin, Kinetics and Mechanism of the $\text{NCN} + \text{NO}_2$ Reaction Studied by Experiment and Theory, *J. Phys. Chem. A* **2008**, *112*, 10185–10192.
- [14] A. Busch and M. Olzmann, Shock-Tube Study of the Thermal Decomposition of NCN , Vienna, paper p810138, Proc. European Combust. Meeting, **2009**.
- [15] J. Dammeier and G. Friedrichs, Thermal Decomposition of NCN_3 as a High-Temperature NCN Radical Source: Singlet-Triplet Relaxation and Absorption Cross Section of $\text{NCN}(^3\Sigma)$, *J. Phys. Chem. A* **2010**, *114*, 12963–12971.
- [16] J. Dammeier, N. Faßheber, and G. Friedrichs, Direct Measurements of the High Temperature Rate Constants of the Reactions $\text{NCN} + \text{O}$, $\text{NCN} + \text{NCN}$, and $\text{NCN} + \text{M}$, *Phys. Chem. Chem. Phys.* **2011**, DOI: 10.1039/C1CP22123J.
- [17] J. Dammeier and G. Friedrichs, Direct Measurements of the Rate Constants of the Reactions $\text{NCN} + \text{NO}$ and $\text{NCN} + \text{NO}_2$ Behind Shock Waves, *J. Phys. Chem. A* **2011**, submitted.
- [18] D. J. Benard, C. Linnen, A. Harker, J. J. Michels, J. B. Addison, and R. Ondercin, Dissociation of Cyanogen Azide: An Alternative Route to Synthesis of Carbon Nitride, *J. Phys. Chem. B* **1998**, *102*, 6010–6019.
- [19] H. W. Kroto, T. F. Morgan, and H. H. Sheena, Flash Photolysis of Cyanogen Azide, NCN_3 , *Trans. Faraday Soc.* **1970**, *66*, 2237–2243.
- [20] K. F. Freed, Collision-Induced Intersystem Crossing, *Adv. Chem. Phys.* **1981**, *47*, 291–336.
- [21] H. H. Nelson, J. R. McDonald, and M. H. Alexander, Temperature Dependence of the Collisional Quenching of Imidogen ($a^1\Delta$) by Nitrogen, Oxygen, Carbon Monoxide, and Xenon, *J. Phys. Chem.* **1990**, *94*, 3291–3294.
- [22] W. Hack and K. Rathmann, Collision-Induced Intersystem Crossing of $\text{NH}(a^1\Delta, v'' = 0, 1)$ by N_2 and Xe : Temperature Dependence (N_2 and Product States (N_2, Xe)), *J. Phys. Chem.* **1992**, *96*, 47–52.
- [23] P. Biggs, G. Hancock, M. R. Heal, D. J. McGarvey, and A. D. Parr, Temperature Dependences of $\text{CH}_2(\tilde{a}A_1)$ Removal Rates by Ar , NO and H_2 , *Chem. Phys. Lett.* **1991**, *180*, 533–540.
- [24] U. Bley and F. Temps, Collision-Induced Intersystem Crossing fo CH_2 from \tilde{a}^1A_1 to \tilde{X}^3B_1 : A Case Study of the Mixed State Model, *J. Chem. Phys.* **1993**, *98*, 1058–1072.

4. Thermal Decomposition of NCN_3 and Singlet-Triplet Relaxation of NCN

- [25] K. L. Gannon, M. A. Blitz, T. Kovcs, and P. W. Seakins, State Resolved Measurements of a $^1\text{CH}_2$ Removal Confirm Predictions of the Gateway Model for Electronic Quenching, *J. Chem. Phys.* **2010**, *132*, 024302–8.
- [26] S. J. Strickler and R. N. Rudolph, Pressure Saturation of the Collisional Quenching of the $13B_1$ State of SO_2 , *J. Am. Chem. Soc.* **1978**, *100*, 3326–3331.
- [27] W. Hack and A. Wilms, Elementary Reactions of $\text{NH}(a^1\Delta)$ with Atoms and Diatomic Molecules, *J. Phys. Chem.* **1989**, *93*, 3540–3546.
- [28] G. Friedrichs and H. Gg. Wagner, Quantitative FM Spectroscopy at High Temperatures: The Detection of $^1\text{CH}_2$ Behind Shock Waves, *Z. Phys. Chem.* **2000**, *214*, 1723–1746.
- [29] G. Friedrichs and H. Gg. Wagner, Investigation of the Thermal Decomposition of Ketene and of the Reaction $\text{CH}_2 + \text{H}_2 = \text{CH}_3 + \text{H}$, *Z. Phys. Chem.* **2001**, *251*, 1601–1623.
- [30] M. Colberg and G. Friedrichs, Room Temperature and Shock Tube Study of the Reaction $\text{HCO} + \text{O}_2$ Using the Photolysis of Glyoxal as an Efficient HCO Source, *J. Phys. Chem A* **2006**, *110*, 160–170.
- [31] D. E. Milligan, M. E. Jacox, and A. M. Bass, Matrix-Isolation Study of the Photolysis of Cyanogen Azide. The Infrared and Ultraviolet Spectra of the Free Radical NCN , *J. Chem. Phys.* **1965**, *43*, 3149–3160.
- [32] H. W. Kroto, The $^1\Pi_u \leftarrow ^1\Delta_g$ Electronic Spectrum of NCN , *Can. J. Phys.* **1967**, *45*, 1439–1450.
- [33] N. Lamoureux, X. Mercier, C. Western, J. F. Pauwels, and P. Desgroux, NCN Quantitative Measurement in a Laminar Low Pressure Flame, *Proc. Combust. Inst.* **2009**, *32*, 937–944.
- [34] N. Lamoureux, P. Desgroux, A. El Bakali, and J. F. Pauwels, Experimental and Numerical Study of the Role of NCN in Prompt- NO Formation in Low-Pressure $\text{CH}_4\text{-O}_2\text{-N}_2$ and $\text{C}_2\text{H}_2\text{-O}_2\text{-N}_2$ Flames, *Combust. Flame* **2010**, *157*, 1923–1941.
- [35] S. A. Beaton and J. M. Brown, Laser Excitation Spectroscopy of the $\tilde{A}^3\Pi_u - \tilde{X}^3\Sigma_g^-$ -Transition of the NCN Radical. 2. The ν_2 Hot Band, *J. Mol. Spectrosc.* **1997**, *183*, 347–359.
- [36] T. Williams, C. Kelley *et al.*, gnuplot, <http://www.gnuplot.info>, **2010**, version 4.4.
- [37] R. J. Kee, F. M. Ruply, and J. A. Miller, Chemkin-II: A Fortran Chemical Kinetics Package for the Analysis of Gas Phase Chemical Kinetics, Sandia report sand89-8009, Sandia National Laboratories, Livermore, CA, **1989**.
- [38] A. A. Konnov, Detailed Reaction Mechanisms for Small Hydrocarbon Combustion, http://homepages.vub.ac.be/akonnov/science/mechanism/version0_5.html, **2007**, release 0.5.

4. Thermal Decomposition of NCN_3 and Singlet-Triplet Relaxation of NCN

- [39] E. Goos, A. Burcat, and B. Ruscic, Ideal Gas Thermochemical Database with Updates from Active Thermochemical Tables, <ftp://ftp.technion.ac.il/pub/supported/aetdd/thermodynamics>, **2010**.
- [40] R. T. Bise, H. Choi, and D. M. Neumark, Photodissociation Dynamics of the Singlet and Triplet States fo the NCN Radical, *J. Chem. Phys.* **1999**, 4923–4932.
- [41] S. Baumgärtel, K.-H. Gericke, and F. J. Comes, Characterisation of CN in the Photodissociationh of Cyanogen Azide at 193 nm, *Ber. Bunsenges. Phys. Chem.* **1994**, 98, 1009–1014.
- [42] G. P. Smith, D. M. Golden, M. Frenklach, N. W. Moriarty, B. Eiteneer, M. Goldenberg, C. T. Bowman, R. K. Hanson, S. Song, W. C. G. Jr., V. V. Lissanski, and Z. Qin, GRI-MECH 3.0, http://www.me.berkeley.edu/gri_mech/.

4.5 Supporting information

Table 1: Room temperature ^1NCN measurements: Experimental conditions and results.

$p/$ mbar	$x_0(\text{NCN}_3)/$ ppm	$k_{\text{app}}/$ s^{-1}	$k_{\text{con}}/$ s^{-1}	$p/$ mbar	$x_0(\text{NCN}_3)/$ ppm	$k_{\text{app}}/$ s^{-1}	$k_{\text{con}}/$ s^{-1}
<u>NCN₃/Ar mixture 1</u>				<u>NCN₃/Ar mixture 2</u>			
10.0	166	2.8×10^4	6.8×10^3	10.0	283	3.0×10^4	4.1×10^3
10.0	166	2.6×10^4	6.9×10^3	10.0	283	3.5×10^4	4.2×10^3
17.5	95	5.1×10^4	5.5×10^3	10.0	283	2.8×10^4	4.4×10^3
17.5	95	5.1×10^4	5.5×10^3	10.0	283	3.2×10^4	4.0×10^3
32.5	51	9.0×10^4	5.4×10^3	16.5	171	5.2×10^4	4.0×10^3
32.5	51	9.3×10^4	5.1×10^3	16.6	171	5.3×10^4	4.4×10^3
62.7	27	1.7×10^5	5.3×10^3	16.5	171	4.6×10^4	4.0×10^3
62.8	27	1.8×10^5	5.2×10^3	16.5	171	4.8×10^4	4.1×10^3
121.7	14	3.2×10^5	5.7×10^3	29.7	96	8.2×10^4	4.8×10^3
121.4	14	3.3×10^5	5.3×10^3	29.5	96	7.8×10^4	4.2×10^3
240.6	6.8	6.4×10^5	1.0×10^4	29.5	96	7.0×10^4	4.4×10^3
241.3	6.8	6.5×10^5	9.8×10^3	55.6	51	1.6×10^5	4.9×10^3
				55.6	51	1.5×10^5	4.8×10^3
				55.7	51	1.5×10^5	4.6×10^3
				55.8	51	1.5×10^5	4.3×10^3
				107.5	26	2.8×10^5	5.4×10^3
				107.2	26	2.7×10^5	5.3×10^3
				108.2	26	2.6×10^5	4.5×10^3
				108.0	26	2.8×10^5	4.7×10^3
				212.2	13	5.6×10^5	9.1×10^3
				211.2	13	5.7×10^5	9.0×10^3
				216.6	13	5.6×10^5	8.9×10^3
				214.2	13	5.5×10^5	8.9×10^3
				437.3	6.6	1.3×10^6	1.4×10^4
				437.3	6.6	1.2×10^6	1.4×10^4
				427.8	6.6	1.1×10^6	1.4×10^4
				426.3	6.6	1.1×10^6	1.3×10^4

4. Thermal Decomposition of NCN_3 and Singlet-Triplet Relaxation of NCN

Table 2: Room temperature ^3NCN measurements: Experimental conditions and results.

p/mbar	$x_0(\text{NCN}_3)/\text{ppm}$	$k_{\text{slowapp}}/\text{s}^{-1}$	$k_{\text{fastapp}}/\text{s}^{-1}$	$k_{\text{con}}/\text{s}^{-1}$
10.0	283	3.3×10^3	5.9×10^4	291
10.0	283	3.3×10^3	6.5×10^4	320
10.0	283	3.5×10^3	4.6×10^4	326
10.0	283	3.0×10^3	4.1×10^4	453
16.4	171	4.5×10^3	9.0×10^4	342
16.4	171	4.0×10^3	7.5×10^4	296
16.5	171	4.2×10^3	5.1×10^4	323
16.5	171	3.7×10^3	5.2×10^4	215
29.7	96	5.0×10^3	8.0×10^4	179
29.7	96	5.5×10^3	7.6×10^4	242
29.6	96	5.0×10^3	1.6×10^5	244
29.6	96	5.5×10^3	1.9×10^5	247
55.5	51	6.0×10^3	9.7×10^4	247
55.5	51	6.5×10^3	1.2×10^5	219
55.8	51	6.5×10^3	1.4×10^5	255
55.9	51	6.0×10^3	1.2×10^5	291
107.6	26	5.5×10^3	1.2×10^5	170
107.4	26	8.0×10^3	2.5×10^5	232
107.7	26	8.0×10^3	5.7×10^5	239
212.6	13	1.1×10^4	3.6×10^5	232
212.3	13	1.0×10^4	2.9×10^5	204
210.7	13	1.0×10^4	4.0×10^5	329
210.2	13	1.1×10^4	3.3×10^5	316

4. Thermal Decomposition of NCN_3 and Singlet-Triplet Relaxation of NCN

Table 3: High temperature ^1NCN measurements: Experimental conditions and results.

T/K	p/mbar	$\rho/(\text{mol}/\text{cm}^3)$	$x_0(\text{NCN}_3)/\text{ppm}$	k_2/s^{-1}	k_3/s^{-1}
$\rho \approx 3.5 \times 10^{-6} \text{ mol}/\text{cm}^3$					
617	146	2.84×10^{-6}	37	4.2×10^3	—
741	195	3.17×10^{-6}	37	5.0×10^4	—
820	227	3.33×10^{-6}	37	1.4×10^5	3.2×10^4
925	269	3.50×10^{-6}	37	4.6×10^5	5.1×10^4
927	270	3.50×10^{-6}	37	4.9×10^5	4.8×10^4
1042	317	3.65×10^{-6}	37	—	8.0×10^4
1063	325	3.68×10^{-6}	37	—	7.6×10^4
1193	374	3.77×10^{-6}	37	—	1.2×10^5
1221	389	3.83×10^{-6}	37	—	1.2×10^5
$\rho \approx 7.0 \times 10^{-6} \text{ mol}/\text{cm}^3$					
618	292	5.69×10^{-6}	18	8.4×10^3	—
651	318	5.87×10^{-6}	20	1.2×10^4	—
700	357	6.13×10^{-6}	20	3.7×10^4	—
707	362	6.16×10^{-6}	20	4.6×10^4	—
738	389	6.32×10^{-6}	18	8.4×10^4	—
774	415	6.45×10^{-6}	19	9.7×10^4	4.0×10^4
824	456	6.66×10^{-6}	19	2.4×10^5	4.5×10^4
953	561	7.08×10^{-6}	19	—	6.3×10^4
1090	672	7.42×10^{-6}	18	—	1.3×10^5
1231	787	7.69×10^{-6}	18	—	1.9×10^5

4. Thermal Decomposition of NCN_3 and Singlet-Triplet Relaxation of NCN

Table 4: High temperature ^3NCN measurements: Experimental conditions and results.

T/K	p/mbar	$\rho/(\text{mol}/\text{cm}^3)$	$x_0(\text{NCN}_3)/\text{ppm}$	k_2/s^{-1}	k_3/s^{-1}	
1.8×10^{-6}	868	123	1.71×10^{-6}	13	1.8×10^4	
	896	128	1.72×10^{-6}	14	2.2×10^4	
	904	131	1.74×10^{-6}	14	2.3×10^4	
	978	145	1.79×10^{-6}	14	2.9×10^4	
	1002	150	1.81×10^{-6}	14	3.2×10^4	
	1120	175	1.87×10^{-6}	14	5.8×10^4	
	1231	196	1.92×10^{-6}	14	8.0×10^4	
	1240	198	1.92×10^{-6}	15	8.0×10^4	
	1528	258	2.03×10^{-6}	14	2.0×10^5	
	3.5×10^{-6}	759	202	3.20×10^{-6}	13	1.8×10^4
766		200	3.14×10^{-6}	4.0	1.3×10^4	
772		208	3.24×10^{-6}	7.0	1.4×10^4	
788		212	3.40×10^{-6}	6.5	1.6×10^4	
815		225	3.32×10^{-6}	12	2.4×10^4	
823		225	3.30×10^{-6}	23	2.3×10^4	
859		243	3.43×10^{-6}	7.0	2.4×10^4	
877		250	3.58×10^{-6}	5.6	2.3×10^4	
886		254	3.44×10^{-6}	5.8	3.0×10^4	
894		256	3.44×10^{-6}	6.0	2.8×10^4	
947		274	3.51×10^{-6}	6.3	3.8×10^4	
978		291	2.90×10^{-6}	5.8	3.8×10^4	
1127		351	3.37×10^{-6}	7.4	6.3×10^4	
1178		372	3.80×10^{-6}	5.9	1.0×10^5	
1240		395	3.13×10^{-6}	5.3	1.0×10^5	
7.0×10^{-6}		583	264	5.45×10^{-6}	4.7	7.0×10^3
		674	335	5.99×10^{-6}	4.7	1.6×10^4
	701	358	6.14×10^{-6}	5.1	2.0×10^4	
	742	391	6.34×10^{-6}	5.1	2.7×10^4	
	764	408	6.42×10^{-6}	21	3.5×10^4	
	788	426	6.50×10^{-6}	6.7	3.0×10^4	
	804	438	6.55×10^{-6}	4.9	3.8×10^4	
	816	451	6.66×10^{-6}	21	4.5×10^4	
	854	490	6.82×10^{-6}	6.9	3.8×10^4	
	963	570	7.12×10^{-6}	5.1	6.0×10^4	
	993	590	7.15×10^{-6}	16	5.5×10^4	
	1073	659	7.39×10^{-6}	1.8	8.0×10^4	
	1153	724	7.55×10^{-6}	11	9.0×10^4	
	1155	723	7.56×10^{-6}	2.2	1.1×10^5	
	1257	679	6.49×10^{-6}	11	1.5×10^5	

5 Direct Measurements of the High Temperature Rate Constants of the Reactions $\text{NCN} + \text{O}$, $\text{NCN} + \text{NCN}$, and $\text{NCN} + \text{M}$

Johannes Dammeier, Nancy Faßheber, and Gernot Friedrichs*

Institut für Physikalische Chemie,
Christian-Albrechts-Universität zu Kiel

Phys. Chem. Chem. Phys. **2011**, DOI: 10.1039/C1CP22123J.

- Reproduced by permission of the PCCP Owner Societies.

<http://dx.doi.org/10.1039/C1CP22123J>.

Own contributions to this paper:

- Shock tube experiments using mixtures of NCN_3 and N_2O , together with Nancy Faßheber
- Shock tube experiments using pure NCN_3
- Data analysis and discussion

*friedrichs@phc.uni-kiel.de

Abstract

The rate constant of the reaction $\text{NCN} + \text{O}$ has been directly measured for the first time. According to the revised Fenimore mechanism, which is initiated by the NCN forming reaction $\text{CH} + \text{N}_2 \rightarrow \text{NCN} + \text{H}$, this reaction plays a key role for prompt NO_x formation in flames. NCN radicals and O atoms have been quantitatively generated by the pyrolysis of NCN_3 and N_2O , respectively. NCN concentration-time profiles have been monitored behind shock waves using narrow-bandwidth laser absorption at a wavelength of $\lambda = 329.1302$ nm. Whereas no pressure dependence was discernible at pressures between $709 \text{ mbar} < p < 1861 \text{ mbar}$, a barely significant temperature dependence corresponding to an activation energy of $5.8 \pm 6.0 \text{ kJ/mol}$ was found. Overall, at temperatures of $1826 \text{ K} < T < 2783 \text{ K}$, the rate constant can be expressed as $k_{\text{NCN}+\text{O}} = 9.6 \times 10^{13} \times \exp(-5.8 \text{ kJ mol}^{-1} / RT) \text{ cm}^3 \text{ mol}^{-1} \text{ s}^{-1}$ ($\pm 40\%$). As a requirement for accurate high temperature rate constant measurements, a consistent NCN background mechanism has been derived from pyrolysis experiments of pure NCN_3/Ar gas mixtures, beforehand. Presumably, the bimolecular secondary reaction $\text{NCN} + \text{NCN}$ yields CN radicals hence triggering a chain reaction cycle that efficiently removes NCN . A temperature independent value of $k_{\text{NCN}+\text{NCN}} = (3.7 \pm 1.5) \times 10^{12} \text{ cm}^3 \text{ mol}^{-1} \text{ s}^{-1}$ has been determined from measurements at pressures ranging from 143 mbar to 1884 mbar and temperatures ranging from 966 K to 1900 K . At higher temperatures, the unimolecular decomposition of NCN , $\text{NCN} + \text{M} \rightarrow \text{C} + \text{N}_2 + \text{M}$, prevails. Measurements at temperatures of $2012 \text{ K} < T < 3248 \text{ K}$ and at total pressures of $703 \text{ mbar} < p < 2204 \text{ mbar}$ reveal a unimolecular decomposition close to its low pressure limit. The corresponding rate constants can be expressed as $k_{\text{NCN}+\text{M}} = 8.9 \times 10^{14} \times \exp(-260 \text{ kJ mol}^{-1} / RT) \text{ cm}^3 \text{ mol}^{-1} \text{ s}^{-1}$ ($\pm 20\%$).

5.1 Introduction

The nitrogen oxides NO and NO_2 (NO_x) are main pollutants in combustion processes.¹ They play an important role for ozone formation in the troposphere and contribute to ozone depletion in the stratosphere. Furthermore, as a secondary product of NO_x reactions, the effective green house gas N_2O contributes to global warming.²

Especially under rich combustion conditions, prompt NO formation is a significant pathway to NO_x . Stimulated by the two seminal papers of Moskaleva *et al.*^{3,4} highlighting the until then overlooked role of NCN radicals, the prompt NO formation mechanism had to be revised. Briefly, according to Fenimore,⁵ NO_x formation is initiated by the reaction of small hydrocarbon radicals with molecular nitrogen, which is present in the combustion air. During the last ten years it has been proved that the

initiation step yields NCN radicals in the triplet ground state,^{3,4,6-11}



thus replacing the previously assumed spin-forbidden formation of HCN ,



The reaction takes place on a complex potential energy surface involving HCNN as an intermediate species. In the meantime, another pathway to prompt NO involving intermediate HNNC is being discussed,^{6,12} but it yields the reaction products $\text{NCN} + \text{H}$, as well. Despite this crucial role of NCN for NO_x formation, many aspects of its high temperature chemistry remain unclear and call for a more comprehensive experimental investigation.

Until now, direct measurements of bimolecular NCN reactions are limited to low temperatures.¹³⁻¹⁵ In 2002, Baren and Hershberger¹³ measured the rate constant of the reaction $\text{NCN} + \text{NO}$ at temperatures $T < 573$ K and, additionally, stated upper limits for the reactions $\text{NCN} + \text{O}_2$, C_2H_4 , and NO_2 . NCN was generated by 193 nm photolysis of diazomethane (CH_2N_2) in the presence of cyanogen (C_2N_2) and was detected by laser induced fluorescence. Similar studies have been performed by Huang *et al.*¹⁴ for the reaction $\text{NCN} + \text{NO}$ at temperatures $T < 353$ K in 2005. Another work on NCN reactions using NCN_3 photolysis as a precursor was concerned with the pressure dependence of the reaction $\text{NCN} + \text{NO}_2$, again studied at rather low temperatures of $T < 349$ K.¹⁵

Only two direct measurements of high temperature ($T > 1000$ K) NCN reaction rate constants are available yet, both performed using the shock tube technique.^{8,16} Vasudevan *et al.*⁸ determined the rate constant of the reaction $\text{NCN} + \text{H}$ in the temperature range of $2228 \text{ K} < T < 2905 \text{ K}$ by measuring absorption-time profiles of NCN following the pyrolysis of mixtures of ethane in N_2 . The pyrolysis of ethane yielded CH radicals, which subsequently reacted with N_2 to generate NCN radicals and H atoms. The rate constant of the reaction $\text{NCN} + \text{H}$ was extracted from the experiments by fitting the decay of the measured NCN profiles. Very recently, Busch and Olzmann^{16,17} investigated the unimolecular decomposition of NCN by generating NCN via the pyrolysis of highly diluted mixtures of NCN_3 at temperatures ranging from 1800 K to 2950 K. By means of monitoring C atom concentration-time profiles and in agreement with theoretical work,¹⁸ the reaction was found to yield almost exclusively C atoms and molecular nitrogen, $\text{NCN} + \text{M} \rightarrow \text{C} + \text{N}_2 + \text{M}$.

In addition to the rather scarce experimental work, bimolecular NCN reactions have been exploited by theoretical methods, mostly by the M.C. Lin group.^{4,14,15,19-22} Rate constants have been reported for the reactants NO , NS , NO_2 , O_2 , O , OH , and H . In contrast to the rather fast $\text{NCN} + \text{NO}/\text{NO}_2$ reactions ($k > 10^{10} \text{ cm}^3\text{mol}^{-1}\text{s}^{-1}$),^{14,15} even at a temperature of 2000 K a comparably low rate constant value of $k \approx 5 \times 10^8 \text{ cm}^3\text{mol}^{-1}\text{s}^{-1}$ has been predicted for O_2 , which is caused by substantial reaction barriers yielding an activation energy of $E_a \approx 110 \text{ kJ/mol}$.²⁰ As expected, the radical-radical

and radical-atom reactions $\text{NCN} + \text{OH}$, H , and O are considerably faster and less temperature dependent. Rate constants of $k > 10^{13} \text{ cm}^3\text{mol}^{-1}\text{s}^{-1}$ have been predicted.^{3,21,22} Although high-level computational methods as well as sophisticated kinetic modelling schemes have been used to ensure reliable results, the accuracy of these rate constant estimates is difficult to assess and thus has to await experimental verification.

For the title reaction, Zhu and Lin derived (V)RRKM rate constant estimates including feasible reaction products deduced from potential surface diagrams calculated with G2M compound as well as CASPT3 and MRCI+Q ab initio methods.²¹ According to their work, with a branching fraction of $> 99\%$ in the temperature range of 2000-3000 K, the formation of CN and NO is dominant,



and the overall reaction is predicted to be independent of pressure up to 100 bar.

Relying on the fragmentary experimental and theoretical results, several modelling groups have started to improve combustion mechanisms by implementing NCN high temperature chemistry.²³⁻²⁸ For example, El Bakali *et al.*²³ compared HCN and NCN contributions to prompt NO formation in methane-air combustion by assuming NCN formation according to reaction 1a. Consecutive NCN reactions were adopted from an early estimate of Glarborg *et al.*²⁹ Sensitivity analyses showed that for accurate modelling of NO concentration profiles in flames, the rate constants of the reactions $\text{NCN} + \text{O}_2$, $\text{NCN} + \text{OH}$, and $\text{NCN} + \text{O}$ have to be known. With respect to NCN consumption, the most sensitive reaction were $\text{NCN} + \text{H}$, followed by $\text{NCN} + \text{O}_2$, $\text{NCN} + \text{O}$ and $\text{NCN} + \text{OH}$. Especially at leaner combustion conditions, the reaction $\text{NCN} + \text{O}$ gained importance. More recently, Gersen *et al.*²⁴ published a modelling study based on an implementation of NCN chemistry into the well-known GRI-Mech 3.0 natural gas mechanism³⁰ in order to model experimentally measured HCN profiles. Similarly, Sutton and Fleming²⁵ included an alternative set of rate constant parameters relying largely on the theoretical work of Lin and coworkers. Actually, the two different sets of parameters lead to the modelling of significantly different NO concentration levels. However, taking into consideration the most recent modelling work of Konnov²⁶ and the extensive measurements of NO , CH , and NCN in methane and ethylene flames by Lamoureux *et al.*,²⁷ by now there seems to be consensus that the Lin and coworker's set of rate constants yield the more reliable results. Other open issues remain, for instance, the role of the reaction $\text{C}_2\text{O} + \text{N}_2$ yielding additional NCN as proposed by Konnov. Of course, the sensitivities of the bimolecular NCN reactions depend on the fuel-air ratio and the nature of the fuel. Whereas in rich methane flames the reaction $\text{NCN} + \text{H}$ is most important both for NCN and NO modelling, in leaner mixtures, rich ethylene flames, and higher molecular weight combustibles the reaction $\text{NCN} + \text{O}$ becomes equally or even most sensitive. Nevertheless, to the best of our knowledge, experimental work on the rate of reaction 2 neither at high nor low temperatures has been published yet.

Clearly, measurements of the high temperature rate constant of the reaction $\text{NCN} + \text{O}$ are highly desirable. In this context, we have shown in a recent paper that NCN_3 pyrolysis is a suitable, quantitative source of NCN radicals at high temperatures, $\text{NCN}_3 + \text{M} \rightarrow \text{NCN} + \text{N}_2 + \text{M}$.³¹ Moreover, consistent high temperature absorption cross sections of NCN have been determined both experimentally^{8,31} and theoretically^{27,32} thus making it possible to investigate bimolecular NCN reactions. In this paper, the first direct measurement of the rate constant of the reaction $\text{NCN} + \text{O}$ using NCN_3 as a precursor molecule for NCN radicals and N_2O as an O atom source is presented. Laser absorption spectroscopy at a wavelength of $\lambda = 329.1302$ nm (corresponding to $\tilde{\nu} = 30383.11$ cm^{-1}) has been applied to sensitively and quantitatively monitor NCN concentration-time profiles behind shock waves. Furthermore, a detailed NCN sub-mechanism has been worked out from experiments without addition of N_2O allowing us to account for background NCN chemistry. High temperature rate constants for the reactions $\text{NCN} + \text{NCN}$ and $\text{NCN} + \text{M}$ will be reported.

5.2 Experimental section

All experiments have been performed using a shock tube apparatus that has been described in more detail elsewhere.^{33,34} Briefly, NCN concentration-time profiles have been recorded behind reflected shock waves in an 8 m long electro-polished stainless steel shock tube. The test section of 4.4 m length and with an inner diameter of 81 mm could be evacuated down to pressures of $p \approx 10^{-7}$ mbar by an oil-free combination of turbomolecular drag and diaphragm pump. The shock tube was operated by different mixtures of hydrogen and nitrogen and 30, 80 or 100 μm thick aluminium diaphragms. Temperatures and pressures behind shock waves were calculated from pre-shock conditions and the shock wave velocity, which was measured by a fast count unit wired to four piezoelectric pressure transducers. For the calculation of the experimental shock wave parameters, a frozen chemistry code was applied taking into account real gas effects and the measured shock wave damping, which was on the order of 1% per meter.

The NCN precursor molecule cyanogen azide (NCN_3) is an extremely explosive and presumably very toxic chemical; thus great care should be taken while handling this substance. No attempt was made to purify NCN_3 by freeze-pump cycles. Instead, high purity NCN_3 was directly synthesised using a variant of a method originally described by Milligan *et al.*³⁵ Solid sodium azide NaN_3 had been pestled and degassed *in vacuo* (10^{-4} mbar) overnight and cyanogen bromide (BrCN) had been re-sublimated and passed through a molecular sieve (3 Å) to remove CO_2 and H_2O , respectively. For synthesis, small amounts of BrCN were allowed to expand into the reaction flask, which held the sodium azide in great excess. During the 8 h of reaction time, the flask was carefully shaken several times. The purity of the fresh products was analysed by FTIR spectroscopy showing that the NCN_3 content was typically $> 99\%$, hence, residual amounts of BrCN were $< 1\%$. Diluted mixtures of 0.1% NCN_3 in argon were used within 2–3 days since repeated FTIR analysis revealed a

slow decomposition of NCN_3 . Commercial nitrous oxide was purified by repeated freeze-pump-thaw cycles and was stored in a glass flask (10 L) as a 2% mixture in argon. For shock tube experiments, the supply mixtures were further diluted with argon using calibrated mass flow controllers and the shock tube was flushed with the particular reaction mixture for 5 min to prevent any wall adsorption effects. Gases and chemicals used were argon (Air Liquide, 99.999%), nitrous oxide (Air Liquide, 99%), nitrogen and helium (Air Liquide, 99.99% as the driver gases), sodium azide (Merck, 99%), and cyanogen bromide (Acros, 97%).

NCN was detected in its electronic triplet ground state by UV narrow-bandwidth laser absorption spectroscopy at a wavelength of $\lambda = 329.1302 \text{ nm}$ ($\tilde{\nu} = 30383.11 \text{ cm}^{-1}$). The intense absorption band is a superposition of the ${}^3\Pi_1$ sub-band of the $\tilde{A}{}^3\Pi_u(000) - \tilde{X}{}^3\Sigma_g(000)$ transition and the Q_1 band head of the vibrationally excited Renner-Teller split ${}^3\Sigma^+(010) - {}^3\Pi(010)$ transition.^{32,36} Temperature dependent absorption cross sections were adopted from previous work,³¹ $\log(\sigma/(\text{cm}^2/\text{mol})) = 8.9 - 8.3 \times 10^{-4} \times T/\text{K}$ ($\pm 25\%$, $750 \text{ K} < T < 2250 \text{ K}$, $0.2 \text{ bar} < p < 2.5 \text{ bar}$). Laser radiation of the respective wavelength was generated by intra-cavity frequency doubling (LiIO_4 crystal) of a frequency-stabilised (bandwidth $< 10 \text{ MHz}$) continuous-wave ring-dye laser (Coherent 899) operated by DCM Special dye (Radiant Dyes) and pumped by a Nd:YVO_4 solid state Laser (Coherent Verdi V10) at $\lambda = 532 \text{ nm}$. The wavelength of the UV output of the ring-dye laser was determined by measuring the wavelength of the fundamental by an interferometric wavemeter (MetroLux WL200) with an accuracy of $1.6 \times 10^{-4} \text{ nm}$ at $\lambda = 329 \text{ nm}$.³¹ The laser beam was split into the detection and the reference beam by a 50:50 beam splitter plate. The detection beam passed the shock tube through two flush-mounted quartz windows, whereas the reference beam intensity could be adjusted by a variable neutral density filter. The light beams were coupled into two optical fibres (Thorlabs BF H22-550), which were connected to a balanced photo-detector and amplifier (Thorlabs PDB 150A-EC). The resulting difference signal (ΔI) as well as the monitor signal (I_0) were stored by an analog input board (Measurement Computing PCI-DAS4020/12, 12 bit, 20 MHz).

Numerical simulations of concentration-time profiles were carried out by the Chemkin-II program package.³⁷ Where applicable, rate constants of reverse reactions were calculated based on thermodynamic data taken from Konnov³⁸ except for NCN , for which the data were adopted from Goos *et al.*³⁹ ($\Delta_f H_{298}^\circ = 465.9 \text{ kJ/mol}$). For sensitivity analyses, the sensitivity coefficient $\sigma(i, j)$ of the i^{th} reaction of species j was normalised with respect to the maximum concentration of the species j occurring during the recorded time interval.

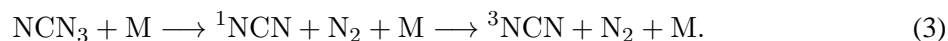
5.3 Results and discussion

5.3.1 NCN mechanism

As a requirement for the accurate determination of NCN high temperature rate constants, a consistent NCN background mechanism including bimolecular NCN reactions and its thermal decomposition has to be known. In order to provide such a mechanistic model, pyrolysis experiments of mixtures of NCN_3 in argon have been performed under experimental conditions similar to those applied for the measurements of the rate constants of the reaction $\text{NCN} + \text{O}$.

NCN + NCN.

Figure 1 shows a typical NCN concentration-time profile measured behind the incident ($T = 915 \text{ K}$, $\rho = 1.74 \times 10^{-6} \text{ mol/cm}^3$) and reflected shock wave ($T = 1734 \text{ K}$, $\rho = 3.72 \times 10^{-6} \text{ mol/cm}^3$). The two signal spikes correspond to Schlieren signals indicating the arrival of the incident and reflected shock wave, respectively. Behind the incident wave, cyanogen azide (NCN_3) undergoes a fast unimolecular decomposition forming ^1NCN and N_2 ,



Initially formed electronically excited ^1NCN is transformed to the ^3NCN ground state by a collision-induced intersystem crossing (CIISC) process. As was shown in our previous work,³¹ at temperatures above $T \approx 700 \text{ K}$ the formation rate of ^3NCN is limited by the CIISC process rather than the thermal decomposition of cyanogen azide. In any case, under the experimental conditions of this work the ^3NCN formation was fast enough to ensure stable ^3NCN plateau concentrations before the arrival of the reflected shock wave such that only ^3NCN (denoted NCN in the following) is present in the reaction system. Measured plateau absorption signals behind the incident wave as well as the observed absorption levels directly behind the reflected wave were used to determine the actual NCN_3 concentration and with it the $[\text{NCN}]_0$ value based on the known absorption cross section of NCN. Within error limits, agreement was found between initial NCN concentrations and the metered NCN_3 content in the reaction gas mixture. Note that as a result of the strongly temperature dependent cross section, the lower NCN concentrations behind the incident shock waves actually yielded significantly higher absorption signals. With a half-lifetime of approximately $400 \mu\text{s}$ for the experiment shown in Figure 1, NCN radicals were slowly consumed by several secondary reactions behind the reflected wave. The half-lifetimes of the signal were found to strongly depend on the initial NCN_3 concentration showing that bimolecular reactions play a significant role.

The three curves shown in Figure 1 correspond to numerically simulated NCN concentration-time profiles assuming different reaction models. The GRI-Mech 3.0 served as a base mechanism and

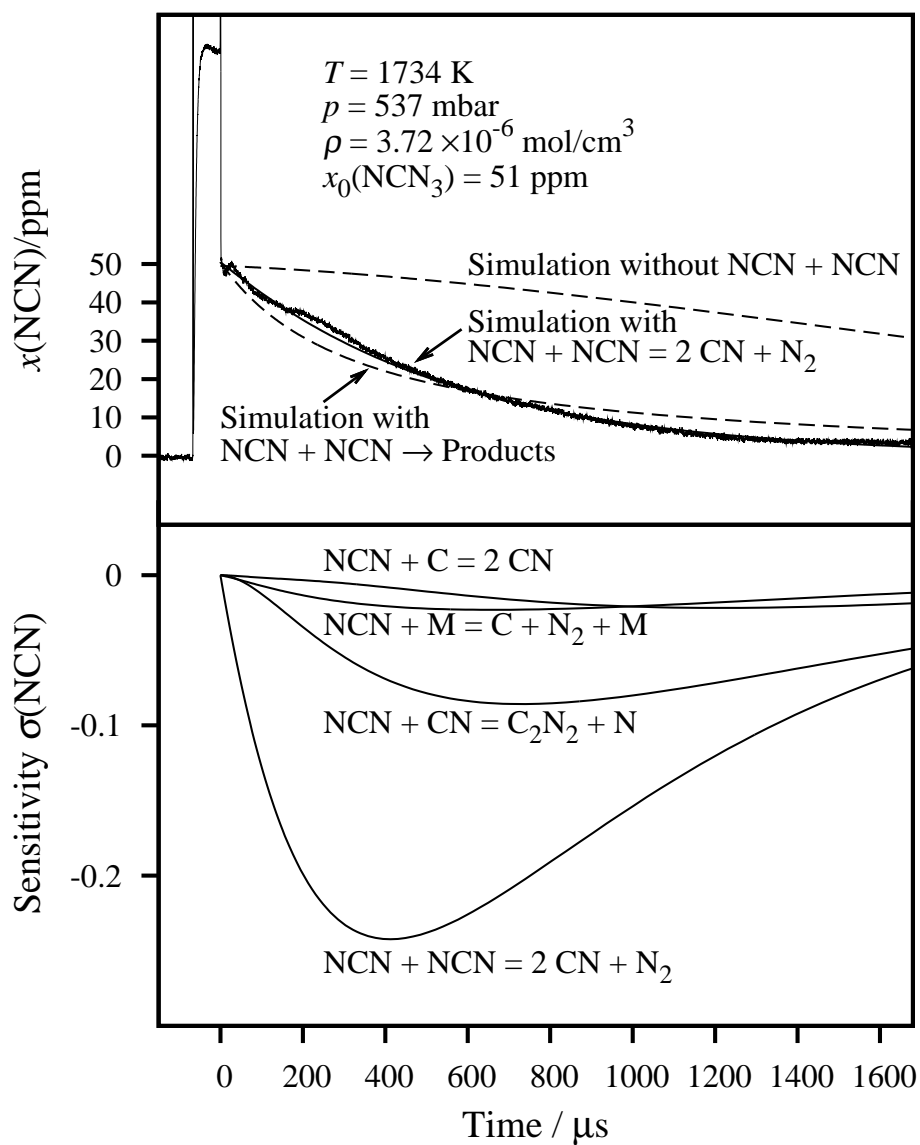


Figure 1: Rate constant measurement of the reaction $\text{NCN} + \text{NCN} \rightarrow 2 \text{ CN} + \text{N}_2$. NCN concentration-time profile and numerical simulations (upper frame); corresponding sensitivity analysis (lower frame). Only NCN_3 and Ar were present in the reaction gas mixture.

5. High Temperature Rate Constants of the Reactions $\text{NCN} + \text{O}$, $\text{NCN} + \text{NCN}$, and $\text{NCN} + \text{M}$

Table 1: Supplemental high temperature NCN/CN reaction mechanism. The GRI-Mech 3.0 has been used as a base mechanism. Rate constants are given as $k_i = AT^n \exp(-E_a/RT)$; units are cm, mol, s, K, and kJ.

No.	Reaction	A	n	E_a	Ref.
4	$\text{NCN} + \text{NCN} \rightleftharpoons 2 \text{CN} + \text{N}_2$	3.70×10^{12}			this work
5	$\text{NCN} + \text{M} \rightleftharpoons \text{C} + \text{N}_2 + \text{M}$	8.90×10^{14}		260	this work
		2.68×10^{14}		233	¹⁶
6	$\text{NCN} + \text{C} \rightleftharpoons 2 \text{CN}$	1.00×10^{14}			¹⁶ , this work
7	$\text{NCN} + \text{CN} \rightleftharpoons \text{C}_2\text{N}_2 + \text{N}$	1.25×10^{14}		33.5	³
8	$\text{NCN} + \text{N} \rightleftharpoons \text{CN} + \text{N}_2$	1.00×10^{13}			³
9	$\text{CN} + \text{M} \rightleftharpoons \text{C} + \text{N} + \text{M}$	1.89×10^{14}		589	⁴⁰
10	$\text{CN} + \text{C} \rightleftharpoons \text{C}_2 + \text{N}$	3.00×10^{14}		150	⁴⁰
11	$\text{C}_2 + \text{M} \rightleftharpoons 2 \text{C} + \text{M}$	1.50×10^{16}		595	⁴¹
12	$\text{C}_2\text{N}_2 + \text{M} \rightleftharpoons 2 \text{CN} + \text{M}$	1.07×10^{34}	-4.32	545	⁴¹

has been complemented by several NCN and CN reactions. Added reactions are listed together with corresponding rate constant expressions in Table 1. A similar mechanism has been used by Sutton⁹ and Konnov²⁶ for flame modelling studies. The upper dashed curve in Figure 1 corresponds to a simulation excluding the reaction $\text{NCN} + \text{NCN}$, thus assuming the usual flame modelling chemistry. Obviously, the experimentally observed NCN decay is dramatically underestimated showing that the bimolecular $\text{NCN} + \text{NCN}$ reaction is important under the present experimental conditions. Including and fitting the rate of this reaction with unspecified stable products, $\text{NCN} + \text{NCN} \rightarrow \text{products}$, fails to reproduce the overall decay profile (lower dashed curve). In fact, the experimental profile seems to resemble a first-order rather than the expected bimolecular decay characteristic. A possible explanation is that the observed profile results from a chain accelerated reaction sequence triggered by reactive products of the $\text{NCN} + \text{NCN}$ reaction. Whereas the potential reaction products $2 \text{C} + 2 \text{N}_2$ ($\Delta_r H_{298}^\circ = +501 \text{ kJ/mol}$) and $\text{C}_2 + 2 \text{N}_2$ ($\Delta_r H_{298}^\circ = -101 \text{ kJ/mol}$) can be excluded by thermodynamic and/or mechanistic reasoning, the most feasible product set is $2 \text{CN} + \text{N}_2$ ($\Delta_r H_{298}^\circ = -56 \text{ kJ/mol}$).



Presumably, the reaction proceeds via vibrationally highly excited C_2N_2 , which instantly dissociates forming two CN radicals. Subsequently, CN radicals can react with NCN yielding $\text{C}_2\text{N}_2 + \text{N}$ followed by the reaction $\text{N} + \text{NCN} \rightarrow \text{CN} + \text{N}_2$. Assuming the reactive products of reaction 4, the experimental NCN profiles could be nicely reproduced (solid curve). Moreover, the sensitivity analysis of the experiment shown in Figure 1 reveals that the rate of the reaction $\text{NCN} + \text{NCN}$ dominates the decay profile rendering possible a direct rate constant determination. Note that the sensitivity of the unimolecular NCN decomposition reaction 5, $\text{NCN} + \text{M} \rightarrow \text{C} + \text{N}_2 + \text{M}$, is rather low at temperatures $T < 2000 \text{ K}$.^{16,17} However, C atoms formed in this reaction are rapidly transformed to CN radicals via the reaction 6, $\text{NCN} + \text{C} \rightarrow 2 \text{CN}$, as well.

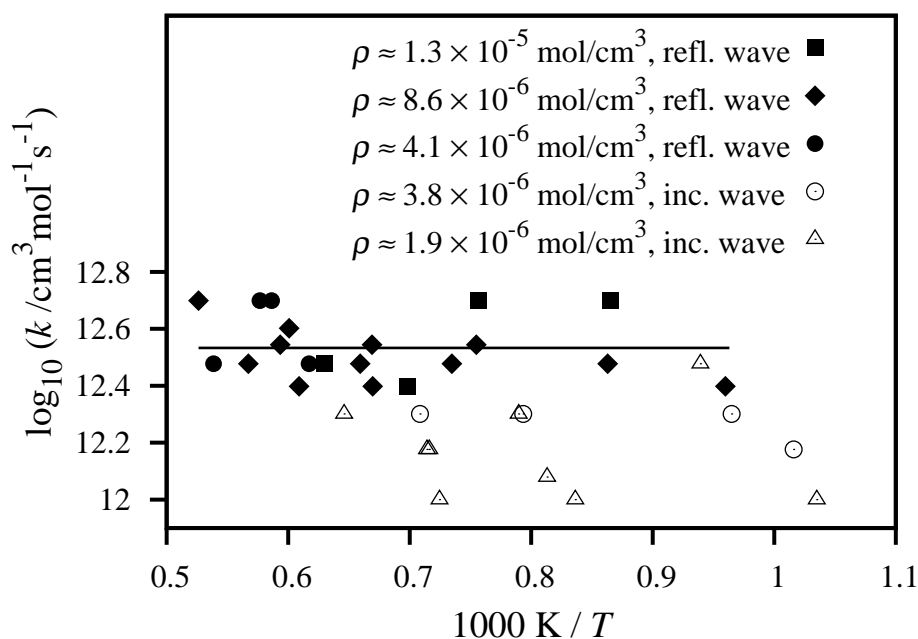


Figure 2: Arrhenius plot of the rate constants of the reaction $\text{NCN} + \text{NCN} \rightarrow 2\text{CN} + \text{N}_2$. Filled symbols refer to measurements behind reflected, open symbols to measurements behind incident shock waves. The solid line represents the recommended temperature and density independent rate constant $k_4 = 3.7 \times 10^{12} \text{ cm}^3 \text{ mol}^{-1} \text{ s}^{-1}$.

Determined k_4 values from experiments performed at temperatures of $965 \text{ K} < T < 1900 \text{ K}$, at total pressures of $140 \text{ mbar} < p < 1900 \text{ mbar}$, and with initial NCN mole fractions ranging from 4 ppm to 130 ppm are plotted in Arrhenius form in Figure 2. Details on the experimental conditions are given in the Supplementary Information. Within the scatter of the data, the experiments behind reflected shock waves performed at total densities of $\rho = (3.6 - 14) \times 10^{-6} \text{ mol/cm}^3$ (filled symbols) reveal no discernible temperature or density dependence of the rate constant. The solid line represents the recommended average value of the rate constant of the reaction $\text{NCN} + \text{NCN}$,

$$k_4 = 3.7 \times 10^{12} \text{ cm}^3 \text{ mol}^{-1} \text{ s}^{-1} \quad (\Delta \log k = \pm 0.2)$$

The stated error estimate accounts for the uncertainty of the absolute NCN concentration and the scatter of the data. In some experiments, the observed NCN concentration-time-profiles already begun to decay behind the incident shock wave allowing us to extract rate constant values at overall lower densities, $\rho = (1.8 - 4.0) \times 10^{-6} \text{ mol/cm}^3$. In comparison with the reflected shock wave data, the evaluation of these short signals yielded approximately a factor of 2 lower k_4 values (open symbols in Figure 2). Instead of indicating a slight density dependence of the $\text{NCN} + \text{NCN}$ reaction, we attribute this systematic effect to an imperfect modelling of the superimposed, yet incomplete ^1NCN relaxation supplying additional ^3NCN . Consequently, in the light of the more approximate nature of these experiments, the incident shock wave data were excluded from the recommended rate constant

fit.

The only other mentioning of the rate constant of the reaction $\text{NCN} + \text{NCN}$ so far is found in the experimental shock tube work of Busch.¹⁶ From measured C atom concentration-time profiles following NCN_3 decomposition, Busch was able to deduce the sum of the rate constants of reactions 6 and 4. A value of $k_4 + k_6 = 1 \times 10^{14} \text{ cm}^3\text{mol}^{-1}\text{s}^{-1}$ was reported to be consistent with the observed C atom decays at long reaction times. Since the rate constant of reaction 4 has been determined above to be $3.7 \times 10^{12} \text{ cm}^3\text{mol}^{-1}\text{s}^{-1}$, the value of $k = 1 \times 10^{14} \text{ cm}^3\text{mol}^{-1}\text{s}^{-1}$ can now be attributed to the reaction 6 alone and has been included in Table 1 accordingly.

NCN + M.

Toward higher temperatures and at lower NCN concentrations the unimolecular decomposition of the NCN radical according to



gains importance and eventually prevails the observed NCN decay. Figure 3 illustrates a typical experiment at a temperature of 2406 K that has been used to determine k_5 . Due to low absorption cross section at high temperatures, a rather low signal level arose behind the reflected wave. However, as indicated by the high sensitivity coefficients of reaction 5 depicted in the lower frame of Figure 3, k_5 could still be sensitively extracted from such an experiment. Rate constants have been determined at temperatures of $2012 \text{ K} < T < 3248 \text{ K}$, at total pressures of $703 \text{ mbar} < p < 2204 \text{ mbar}$, and with initial NCN mole fractions ranging from 19 ppm to 130 ppm. The results are plotted in Arrhenius form in Figure 4. Details on the experimental conditions are given in the Supplementary Information. Within the scatter of the data, no density dependence of the second-order rate constant is discernible at densities of $\rho = (4.0 - 9.1) \times 10^{-6} \text{ mol/cm}^3$ showing that the unimolecular decomposition takes place close to its low pressure limit. The data can be represented by the following Arrhenius expression:

$$k_5 = 8.9 \times 10^{14} \times \exp(-260 \text{ kJ mol}^{-1}/RT) \text{ cm}^3\text{mol}^{-1}\text{s}^{-1} \quad (\pm 20\%).$$

The stated combined error estimate results from the statistical error of the Arrhenius fit and the uncertainty associated with the rate constant of the second most sensitive reaction 4, $\text{NCN} + \text{NCN}$. The comparison of our data with the recent shock tube data of Busch,¹⁶ which are based on C atom concentration-time profile measurements following NCN_3 pyrolysis at similar total densities, reveals excellent agreement within 50% over the whole overlapping temperature range. Our slightly higher value for the activation energy, $E_a = 260 \text{ kJ/mol}$ instead of 233 kJ/mol , is further supported by the theoretical (V)RRKM prediction of Moskaleva and Lin¹⁸ (dashed curve). The excellent agreement of experimental and theoretical results shows that the rate constant of the unimolecular decomposition of the NCN radical is surprisingly well constrained.

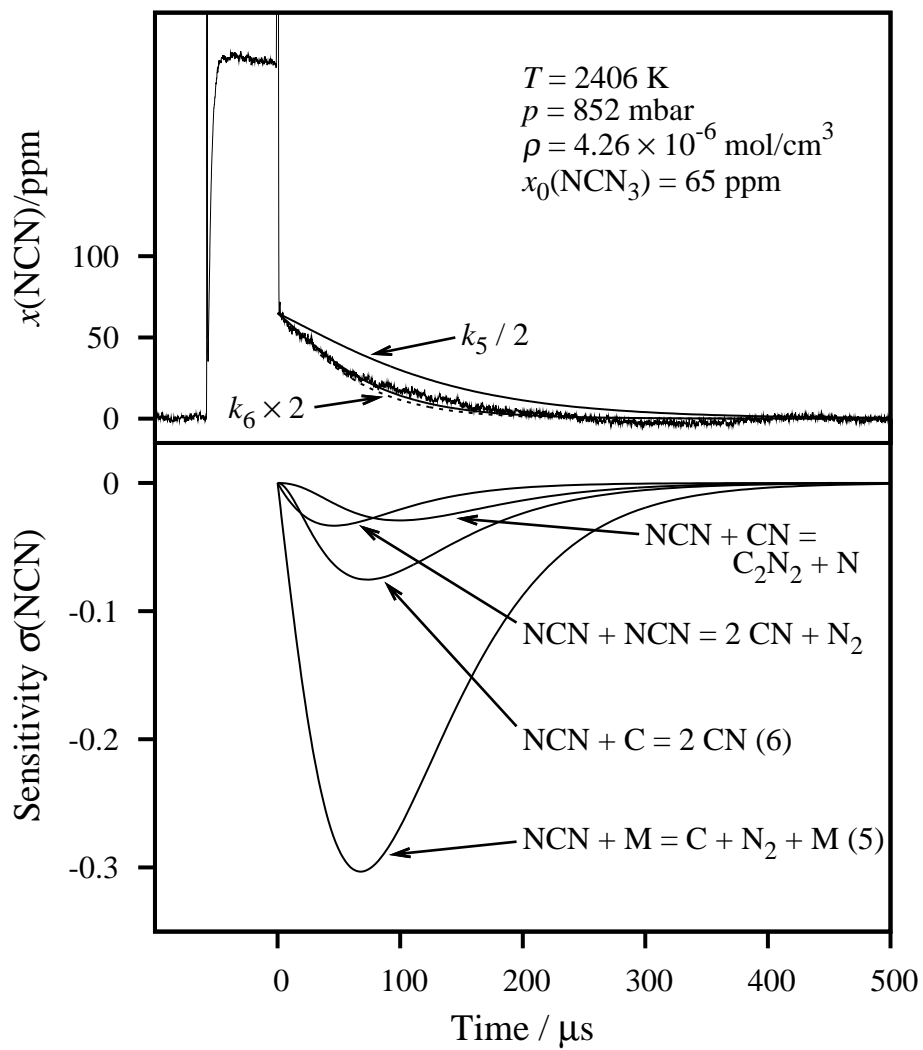


Figure 3: Upper frame: Rate constant measurement of the reaction $\text{NCN} + \text{M} \rightarrow \text{C} + \text{N}_2 + \text{M}$. NCN concentration-time profile and numerical simulations (best fit and two simulations illustrating the influence of reactions 5 and 6); Lower frame: Corresponding sensitivity analysis. Only NCN_3 and Ar were present in the reaction gas mixture.

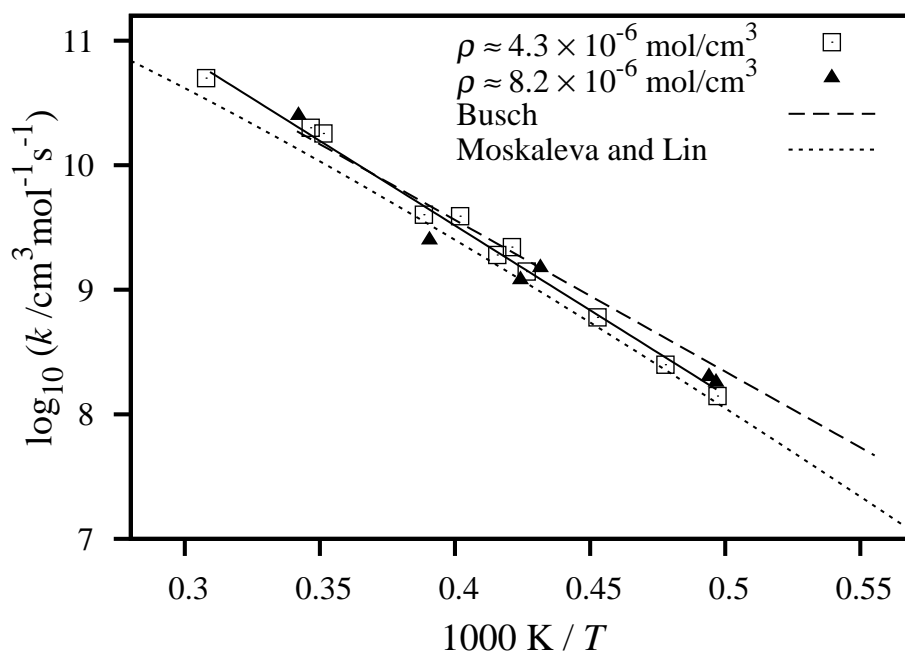


Figure 4: Arrhenius plot of the rate constants of the reaction $\text{NCN} + \text{M} \rightarrow \text{C} + \text{N}_2 + \text{M}$. Symbols and the straight solid line refer to measurements performed in this work, the dashed and dotted curves to literature data from Busch¹⁶ and Moskaleva and Lin¹⁸, respectively.

In summary, with the set of parameters outlined in Table 1 it was possible to model NCN concentration-time profiles in the temperature range of $966 \text{ K} < T < 3248 \text{ K}$, in the pressure range $140 \text{ mbar} < p < 2204 \text{ mbar}$, and for reaction gas mixtures containing 5 – 130 ppm initial mole fractions of NCN.

5.3.2 The reaction $\text{NCN} + \text{O}$

The rate constant of the reaction



has been measured behind reflected shock waves using gas mixtures containing cyanogen azide and nitrous oxide. Whereas NCN_3 served as a clean source of NCN radicals, the well studied thermal decomposition of N_2O was used to generate O atoms according to



In numerous literature studies on this reaction, mostly shock tube experiments, a range of different detection techniques (e.g., O-ARAS, mass spectrometry, IR and UV/Vis absorption and emission) have been applied to determine its rate constant.^{42–57} As shown in the paper of Ross *et al.*,⁵⁷ at

Table 2: Supplemental reactions for reaction mixtures containing N_2O . The GRI-Mech 3.0 mechanism expanded by the reactions listed in table 1 has been used as a base mechanism. Rate constants are given as $k_i = A\exp(-E_a/RT)$; units are cm, mol, s, K, and kJ.

No.	Reaction	A	E_a	Ref.
2	$\text{NCN} + \text{O} \rightleftharpoons \text{CN} + \text{NO}$	9.6×10^{13}	5.8	this work
13	$\text{N}_2\text{O} + \text{M} \rightleftharpoons \text{N}_2 + \text{O} + \text{M}$	3.98×10^{14}	237	⁵⁶
14	$\text{NCN} + \text{NO} \rightleftharpoons \text{CN} + \text{N}_2\text{O}$	1.9×10^{12}	26	Dammeier and Friedrichs*
15	$\text{C}_2\text{N}_2 + \text{O} \rightleftharpoons \text{CN} + \text{NCO}$	4.60×10^{12}	37	⁵⁸

* to be published elsewhere

temperatures of $T > 1800$ K all measured rate constants essentially agree. For the purpose of this work, the rate constant expression reported by Röhrig *et al.*⁵⁶ has been adopted. Their experiments have been performed in a similar temperature and pressure range at comparable initial mole fraction of N_2O and using Ar as the bath gas.

A typical experimental NCN concentration-time profile is shown in Figure 5. Compared to the experiment without N_2O addition (see Figure 1), NCN is consumed much faster due to its reaction with the generated O atoms. At early reaction times, a short induction period is noticeable. Starting from the background NCN_3 mechanism presented above, several reactions were added to the reaction mechanism in order numerically simulate the measured NCN profile (see Table 2). In particular, as NO constitutes a product of reaction 2, allowance was made for the reaction $\text{NCN} + \text{NO}$. The temperature dependent rate constant of this reaction, which eventually turned out to be of minor importance, has been measured separately in our laboratory. Details of these measurements will be published elsewhere. Note that the reactions $\text{NCN} + \text{CN}$, $\text{N}_2\text{O} + \text{CN}$ and $\text{N}_2\text{O} + \text{O}$ are already included in the GRI-Mech 3.0 base mechanism and are not listed in Table 2. In Figure 5, the simulation using the rate of reaction 2 as the sole adjustable parameter nicely reproduces the measured NCN profile. To further elucidate the importance of reaction 2, simulations with $k_2 \times 2$ and $k_2/2$ are displayed in Figure 5 as well.

The corresponding sensitivity analysis is depicted in the lower frame of Figure 5. Next to the target reaction $\text{NCN} + \text{O}$, the assumed rate constant of the N_2O unimolecular decomposition exhibit a very similar sensitivity profile showing that O atom formation (dashed curve in the upper frame of Figure 5) is a limiting factor for the NCN decay rate. Even at the high temperature of $T = 2459$ K, the N_2O decomposition is rather slow such that O atom formation takes place on a comparable time scale as the NCN radical decay. This continuing O atom concentration buildup is the principle reason for the observed induction time of the NCN decay profile. Of course, the interfering sensitivity of reaction 13 is unfavourable for the determination of the rate of reaction 2. The assumed rate constant of reaction 13 directly affects the extracted k_2 value. Unfortunately, it was not possible to fully decouple these two reactions by tuning the reaction conditions. Whereas the N_2O decomposition limits the lower range of accessible temperatures, toward higher temperatures the unimolecular decomposition

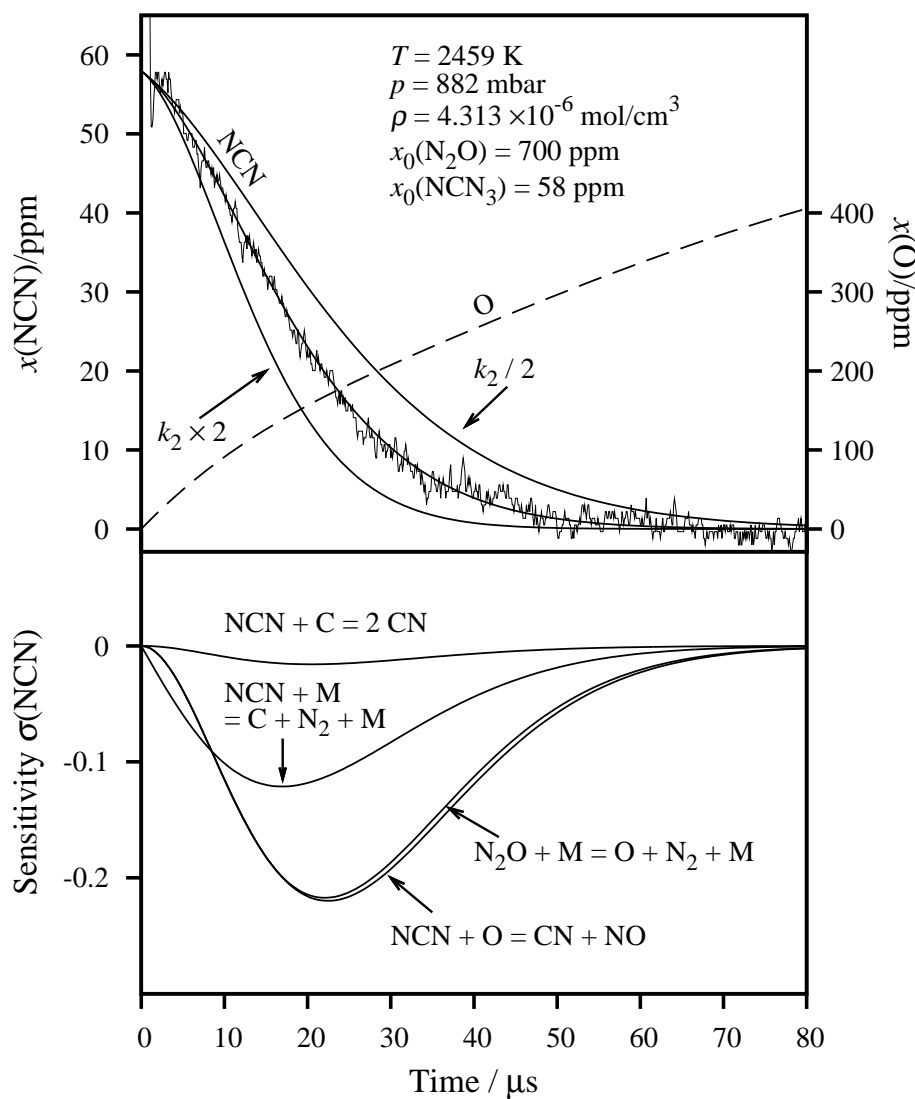


Figure 5: Rate constant measurement of the reaction $\text{NCN} + \text{O} \rightarrow \text{CN} + \text{NO}$. NCN concentration-time profile and numerically simulated NCN and O profiles (upper frame); corresponding sensitivity analysis for NCN (lower frame).

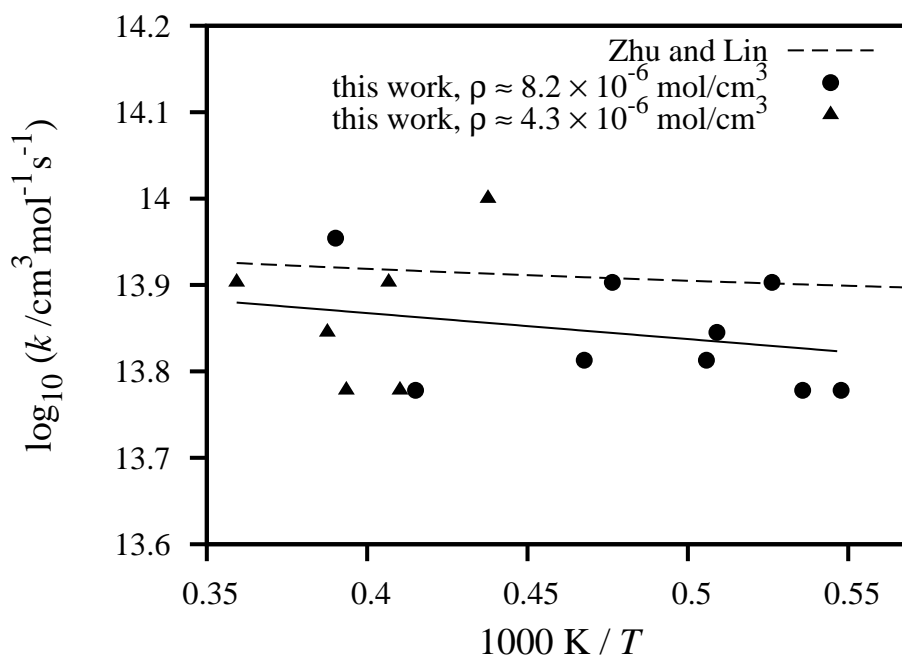


Figure 6: Arrhenius plot of measured rate constants of the reaction $\text{NCN} + \text{O}$ at two different total densities (symbols and solid line) in comparison with the theoretical prediction by Zhu and Lin²¹ (dashed curve).

of NCN sets in. Rate constant values, which were extracted from 16 concentration-time profiles in the rather narrow intermediate temperature range of $1826 \text{ K} < T < 2580 \text{ K}$ at pressures of $709 \text{ mbar} < p < 2334 \text{ mbar}$ are plotted in Figure 6. Details on the experimental conditions are given in the Supplementary Information. Within the scatter of the data, the experiments performed at two different total densities, $4 \times 10^{-6} \text{ mol/cm}^3$ (dots) and $8 \times 10^{-6} \text{ mol/cm}^3$ (triangles), are indistinguishable. The data points are best represented by the Arrhenius expression (solid line)

$$k_2 = 9.6 \times 10^{13} \times \exp(-5.8 \text{ kJ mol}^{-1} / RT) \text{ cm}^3 \text{mol}^{-1} \text{s}^{-1} \quad (\pm 40\%)$$

with a barely significant temperature dependence corresponding to an activation energy of $5.8 \pm 6.0 \text{ kJ/mol}$. The stated error estimate of $\pm 40\%$ was based on a combination of errors arising from the statistical fit ($\pm 15\%$), the absolute NCN and N_2O concentrations ($\pm 5\%$), and the uncertainties of the rate constant expressions used in the reaction mechanism. As already outlined above, the main uncertainty of k_2 is associated with the assumed rate constant of the unimolecular decomposition of N_2O . Whereas Röhrig *et al.*⁵⁶ stated an absolute error of $\pm 30\%$ for this reaction, an error of $\pm 15\%$ has been assumed for k_{13} in this work. This is justified by the very good agreement of all measured N_2O decomposition rate constants found in the literature. However, as the N_2O decomposition is strongly temperature dependent, allowance was made for an additional 5% error stemming from an experimental temperature uncertainty ($\pm 0.5\%$, precision of the shock wave velocity measurement).

Figure 6 also compares the rate constant fit of this work (solid line) with the only other available

literature result taken from the theoretical work of Zhu and Lin²¹ (dashed line). Zhu and Lin calculated singlet and triplet potential energy surfaces with the G2M compound as well as the CASPT3 and MRCI+Q methods. Three different sets of reaction products ($\text{CN} + \text{NO}$, $\text{CO} + \text{N}_2$, $\text{N} + \text{NCO}$) as well as ten different reaction pathways have been mapped out. Rate constants were calculated for a temperature range of $200 \text{ K} < T < 3000 \text{ K}$ using the (V)RRKM method. From a mechanistic point of view, the reaction resembles an association-decomposition process. An NCNO complex is formed that can undergo several isomerisation steps and finally dissociates forming the different products. It turned out from the calculation that both for the initially formed singlet and triplet NCNO intermediates dissociation into $\text{CN} + \text{NO}$ is energetically favourable resulting in a predominance ($> 99\%$) of these products over the entire temperature and pressure range. Overall, the reaction is exothermic, $\Delta_r H_{298}^\circ = -187 \text{ kJ/mol}$. Due to energetically low lying exit barriers, which are well below the entrance energy of the collisional complexes, no collision-induced deactivation of the NCNO intermediate takes place at pressures below 100 bar. As is a common feature of such an association-controlled reaction, the observed rate constant is close to the collision limit and is little temperature dependent. Both the predicted absolute rate constant value as well as the pressure and (more or less) temperature independent rate is consistent with our results. By analysing potential effects of variable entrance profiles as well as calculated ab initio energies on their predicted rate constant, Zhu and Lin quoted that their rate expression may be accurate within $\pm 10\%$. In the light of potential errors associated with the model assumptions and the applied approximate treatment of rotational effects, this narrow error estimate may be somewhat too optimistic, however, the agreement of our experimental result with their theoretical prediction within error limits is intriguing.

5.4 Conclusion

Quantitative generation and detection of NCN radicals behind shock waves by means of NCN_3 pyrolysis and narrow-bandwidth laser UV absorption renders possible direct measurements of high temperature rate constants of bimolecular NCN reactions. As a prerequisite for such measurements, a detailed high temperature NCN background mechanism has been worked out. It is capable of reproducing measured NCN concentration-time profiles at temperatures of $966 \text{ K} < T < 3248 \text{ K}$, at pressures of $140 \text{ mbar} < p < 2204 \text{ mbar}$, and for reaction gas mixtures containing 5 to 130 ppm initial mole fractions of NCN_3 . For the first time, rate constants for the self reaction of NCN radicals have been measured. Presumably, the reaction yields CN radicals according to $\text{NCN} + \text{NCN} \rightarrow 2 \text{CN} + \text{N}_2$. Determined NCN unimolecular decomposition rate constants, $\text{NCN} + \text{M} \rightarrow \text{C} + \text{N}_2 + \text{M}$, have been found to be in excellent agreement with experimental literature data and theoretical predictions. Moreover, using the pyrolysis of N_2O as an additional O atom source, rate constants of the reaction $\text{NCN} + \text{O} \rightarrow \text{CN} + \text{NO}$ could be directly measured in the temperature range of $1826 \text{ K} < T < 2783 \text{ K}$ and at pressures of $709 \text{ mbar} < p < 1861 \text{ mbar}$. These measurements represent the first available experimental

data on this key reaction for NO_x formation modelling in hydrocarbon flames according to the Fenimore mechanism. With a rate constant of $k = 9.6 \times 10^{13} \times \exp(-5.8 \text{ kJ mol}^{-1} / RT) \text{ cm}^3 \text{ mol}^{-1} \text{ s}^{-1}$, the reaction proceeds close to the collision limit, is independent of total pressure, is only slightly temperature dependent, and hence supports the model of an association-controlled reaction as proposed by Zhu and Lin.²¹

Acknowledgement

We would like to thank the German Science Foundation (FR 1529/4) and the cluster of excellence "The Future Ocean" (DFG - EC 80) for financial support. We also thank Anna Busch and Matthias Olzmann (KIT) for lively discussions.

Bibliography

- [1] J. Warnatz, U. Maas, and R. W. Dibble, *Combustion*, Springer, Berlin/Heidelberg, 3. edition, **2001**.
- [2] P. Forster, V. Ramaswamy, P. Artaxo, T. Berntsen, R. Betts, D. Fahey, J. Haywood, J. Lean, D. Lowe, G. Myhre, J. Nganga, R. Prinn, G. Raga, M. Schulz, and R. V. Dorland, Changes in Atmospheric Constituents and in Radiative Forcing, in S. Solomon, D. Qin, M. Manning, Z. Chen, M. M. K. Averyt, M. Tignor, and H. Miller, editors, *Climate Change 2007: The Physical Science Basis. Contribution of Working Group I to the Fourth Assessment Report of the Intergovernmental Panel on Climate Change*, chapter 2, Cambridge University Press, Cambridge, United Kingdom, **2007**.
- [3] L. V. Moskaleva and M. C. Lin, The Spin-Conserved Reaction $\text{CH} + \text{N}_2 \rightarrow \text{H} + \text{NCN}$: A Major Pathway to Prompt NO Studied by Quantum/Statistical Theory Calculations and Kinetic Modeling of Rate Constant, *Proc. Combust. Inst.* **2000**, 28, 2393–2401.
- [4] L. V. Moskaleva, W. S. Xia, and M. C. Lin, The $\text{CH} + \text{N}_2$ Reaction Over the Ground Electronic Doublet Potential Energy Surface: A Detailed Transition State Search, *Chem. Phys. Lett.* **2000**, 331, 269–277.
- [5] C. P. Fenimore, Formation of Nitric Oxide in Premixed Hydrocarbon Flames, *Proc. Combust. Inst.* **1971**, 13, 373–380.
- [6] L. B. Harding, S. J. Klippenstein, and J. A. Miller, Kinetics of $\text{CH} + \text{N}_2$ Revisited with Multireference Methods, *J. Phys. Chem. A* **2008**, 112, 522–532.

- [7] G. P. Smith, Evidence of NCN as a Flame Intermediate for Prompt NO, *Chem. Phys. Lett.* **2003**, 367, 541–548.
- [8] V. Vasudevan, R. K. Hanson, C. T. Bowman, D. M. Golden, and D. F. Davidson, Shock Tube Study of the Reaction of CH with N_2 : Overall Rate and Branching Ratio, *J. Phys. Chem. A* **2007**, 111, 11818–11830.
- [9] J. A. Sutton, B. A. Williams, and J. W. Fleming, Laser-Induced Fluorescence Measurements of NCN in Low-Pressure $\text{CH}_4/\text{O}_2/\text{N}_2$ Flames and Its Role in Prompt NO Formation, *Combust. Flame* **2008**, 153, 465–478.
- [10] R. J. H. Klein-Douwel, N. J. Dam, and J. J. ter Meulen, Laser-Induced Fluorescence of NCN in Low and Atmospheric Pressure Flames, *Optics Lett.* **2008**, 33, 2620–2622.
- [11] R. J. H. Klein-Douwel, A. A. Konnov, N. J. Dam, and J. J. ter Meulen, NCN Concentration and Interfering Absorption by CH_2O , NH and OH in Low Pressure Methane/Air Flames With and Without N_2O , *Combust. Flame* **2011**, 158.
- [12] M. R. Berman, T. Tsuchiya, A. Gregusova, A. Perara, and R. J. Bartlett, HNNC Radical and Its Role in the $\text{CH} + \text{N}_2$ Reaction, *J. Phys. Chem. A* **2007**, 111, 6894–6899.
- [13] R. E. Baren and J. F. Hershberger, Kinetics of the NCN Radical, *J. Phys. Chem. A* **2002**, 106, 11093–11097.
- [14] C.-L. Huang, S. Y. Tseng, T. Y. Wang, N. S. Wang, Z. F. Xu, and M. C. Lin, Reaction Mechanism and Kinetics of the $\text{NCN} + \text{NO}$ Reaction: Comparison of Theory and Experiment, *J. Chem. Phys.* **2005**, 122, 184321.
- [15] T.-J. Yang, N. S. Wang, L. C. Lee, Z. F. Xu, and M. C. Lin, Kinetics and Mechanism of the $\text{NCN} + \text{NO}_2$ Reaction Studied by Experiment and Theory, *J. Phys. Chem. A* **2008**, 112, 10185–10192.
- [16] A. Busch, *Stoßwellenuntersuchungen zum Zerfall stickstoffhaltiger Verbindungen mit spektroskopischen Methoden*, Ph.D. thesis, Karlsruher Institut für Technologie, **2010**.
- [17] A. Busch and M. Olzmann, Shock-Tube Study of the Thermal Decomposition of NCN, Vienna, paper p810138, Proc. European Combust. Meeting, **2009**.
- [18] L. V. Moskaleva and M. C. Lin, Computational Study on the Energetics of NCN Isomers and the Kinetics of the $\text{C} + \text{N}_2 \rightleftharpoons \text{N} + \text{CN}$ Reaction, *J. Phys. Chem. A* **2001**, 105, 4156–4163.
- [19] H.-T. Chen and J.-J. Ho, Theoretical Investigation of the Mechanisms of Reaction of NCN with NO and NS, *J. Phys. Chem. A* **2005**, 109, 2564–2571.
- [20] R. S. Zhu and M. C. Lin, Ab Initio Study on the Oxidation of NCN by O_2 , *Int. J. Chem. Kinet.* **2005**, 37, 593–598.

- [21] R. S. Zhu and M. C. Lin, Ab Initio Study on the Oxidation of NCN by $\text{O}(^3\text{P})$: Prediction of the Total Rate Constant and Product Branching Ratios, *J. Phys. Chem. A* **2007**, *111*, 6766–6771.
- [22] R. S. Zhu, M. T. Nguyen, and M. C. Lin, Ab Initio Study on the Oxidation of NCN by OH : Prediction of the Individual and Total Rate Constants, *J. Phys. Chem. A* **2009**, *113*, 298–304.
- [23] A. El Bakali, L. Pillier, P. Desgroux, B. Lefort, L. Gasnot, J. F. Pauwels, and I. da Costa, NO Prediction in Natural Gas Flames Using GDF-Kin 3.0 Mechanism. NCN and HCN Contribution to Prompt-NO Formation, *Fuel* **2006**, *85*, 896–909.
- [24] S. Gersen, A. V. Mokhov, and H. B. Levinsky, Diode Laser Absorption Measurement and Analysis of HCN in Atmospheric-Pressure, Fuel-Rich Premixed Methane/Air Flames, *Combust. Flame* **2008**, *155*, 267–276.
- [25] J. A. Sutton and J. W. Fleming, Towards Accurate Kinetic Modeling of Prompt NO Formation in Hydrocarbon Flames via the NCN Pathway, *Combust. Flame* **2008**, *154*, 630–636.
- [26] A. A. Konnov, Implementation of the NCN Pathway of Prompt-NO Formation in the Detailed Reaction Mechanism, *Combust. Flame* **2009**, *156*, 2093–2105.
- [27] N. Lamoureux, P. Desgroux, A. El Bakali, and J. F. Pauwels, Experimental and Numerical Study of the Role of NCN in Prompt-NO Formation in Low-Pressure $\text{CH}_4\text{-O}_2\text{-N}_2$ and $\text{C}_2\text{H}_2\text{-O}_2\text{-N}_2$ Flames, *Combust. Flame* **2010**, *157*, 1923–1941.
- [28] A. V. Sepman, A. V. Mokhov, and H. B. Levinsky, The Effects of Hydrogen Addition on NO Formation in Atmospheric-Pressure, Fuel-Rich-Premixed, Burner-Stabilized Methane, Ethane and Propane Flames, *Int. J. Hydrogen Energ.* **2011**, *36*, 4474–4481.
- [29] P. Glarborg, M. U. Alzueta, K. Dam-Johansen, and J. A. Miller, Kinetic Modeling of Hydrocarbon/Nitric Oxide Interactions in a Flow Reactor, *Combust. Flame* **1998**, *115*, 1–27.
- [30] G. P. Smith, D. M. Golden, M. Frenklach, N. W. Moriarty, B. Eiteneer, M. Goldenberg, C. T. Bowman, R. K. Hanson, S. Song, W. C. G. Jr., V. V. Lissanski, and Z. Qin, GRI-MECH 3.0, http://www.me.berkeley.edu/gri_mech/.
- [31] J. Dammeier and G. Friedrichs, Thermal Decomposition of NCN_3 as a High-Temperature NCN Radical Source: Singlet-Triplet Relaxation and Absorption Cross Section of $\text{NCN}(^3\Sigma)$, *J. Phys. Chem. A* **2010**, *114*, 12963–12971.
- [32] N. Lamoureux, X. Mercier, C. Western, J. F. Pauwels, and P. Desgroux, NCN Quantitative Measurement in a Laminar Low Pressure Flame, *Proc. Combust. Inst.* **2009**, *32*, 937–944.
- [33] M. Klatt, *Quantitative Untersuchung der Bildung und des Verbrauchs von H- und O-Atomen sowie OH-Radikalen in verschiedenen Elementarreaktionen bei hohen Temperaturen.*, Ph.D. thesis, Universität Göttingen, **1991**.

- [34] M. Colberg and G. Friedrichs, Room Temperature and Shock Tube Study of the Reaction $\text{HCO} + \text{O}_2$ Using the Photolysis of Glyoxal as an Efficient HCO Source, *J. Phys. Chem. A* **2006**, *110*, 160–170.
- [35] D. E. Milligan, M. E. Jacox, and A. M. Bass, Matrix-Isolation Study of the Photolysis of Cyanogen Azide. The Infrared and Ultraviolet Spectra of the Free Radical NCN, *J. Chem. Phys.* **1965**, *43*, 3149–3160.
- [36] S. A. Beaton and J. M. Brown, Laser Excitation Spectroscopy of the $\tilde{\text{A}}^3\Pi_u - \tilde{\text{X}}^3\Sigma_g^-$ -Transition of the NCN Radical. 2. The ν_2 Hot Band, *J. Mol. Spectrosc.* **1997**, *183*, 347–359.
- [37] R. J. Kee, F. M. Ruply, and J. A. Miller, Chemkin-II: A Fortran Chemical Kinetics Package for the Analysis of Gas Phase Chemical Kinetics, Sandia report sand89-8009, Sandia National Laboratories, Livermore, CA, **1989**.
- [38] A. A. Konnov, Detailed Reaction Mechanisms for Small Hydrocarbon Combustion, http://homepages.vub.ac.be/akonnov/science/mechanism/version0_5.html, **2007**, release 0.5.
- [39] E. Goos, A. Burcat, and B. Ruscic, Ideal Gas Thermochemical Database with Updates from Active Thermochemical Tables, <ftp://ftp.technion.ac.il/pub/supported/aetdd/thermodynamics>, **2010**.
- [40] M. W. Slack, Kinetics and Thermodynamics of the CN Molecule. III. Shock Tube Measurements of CN Dissociation Rates, *J. Chem. Phys.* **1975**, *64*, 228–236.
- [41] K. Natarajan, K. Thielen, H. D. Hermanns, and P. Roth, Thermal Decomposition of Cyanogen Measured in $\text{C}_2\text{N}_2/\text{O}_2$ and $\text{C}_2\text{N}_2/\text{H}_2$ Reaction Systems by Atomic Resonance Absorption, *Ber. Bunsenges. Phys. Chem.* **1986**, *90*, 533–539.
- [42] W. Jost, K. W. Michel, J. Troe, and H. Gg. Wagner, Untersuchung des thermischen Zerfalls von N_2O in Stoßwellen, *Z. Naturforsch. A Phys. Sci.* **1964**, *19*, 59–64.
- [43] A. Martinengo, J. Troe, and H. Gg. Wagner, Untersuchung von Zerfallsreaktionen mit der Methode der adiabatischen Kompression, *Z. Phys. Chem.* **1966**, *51*, 104–107.
- [44] H. A. Olschewski, J. Troe, and H. G. Wagner, Niederdruckbereich und Hochdruckbereich des unimolekularen N_2O -Zerfalls, *Ber. Bunsenges. Phys. Chem.* **1966**, *70*, 450.
- [45] S. C. Baber and A. M. Dean, N_2O Dissociation Behind Reflected Shock Waves, *Int. J. Chem. Kinet.* **1975**, *7*, 381–398.
- [46] J. E. Dove, W. S. Nip, and H. Teitelbaum, The Vibrational Relaxation and Pyrolysis of Shock Heated Nitrous Oxide, *Proc. Combust. Inst.* **1975**, *15*, 903–916.

5. High Temperature Rate Constants of the Reactions $\text{NCN} + \text{O}$, $\text{NCN} + \text{NCN}$, and $\text{NCN} + \text{M}$

- [47] A. M. Dean, Shock Tube Studie of the $\text{N}_2\text{O}/\text{Ar}$ and $\text{N}_2\text{O}/\text{H}_2/\text{Ar}$ Systems, *Int. J. Chem. Kinet.* **1976**, 8, 459–474.
- [48] A. M. Dean and D. C. Steiner, A Shock Tube Study of the Recombination of Carbon Monoxide and Oxygen Atoms, *J. Chem. Phys.* **1977**, 66, 598–604.
- [49] K. M. Pamidimukkala, A. Lifshitz, G. B. Skinner, and D. R. Wood, Resonance Absorption Measurements of Atom Concentrations in Reacting Gas Mixtures. VI. Shapes of the Vacuum Ultraviolet Oxygen ($^3S - ^3P$) Resonance Triplet from Microwave Sources and Empirical Calibration in a Shock Tube, *J. Chem. Phys.* **1981**, 75, 1116–1122.
- [50] P. Roth and T. Just, Kinetics of the High Temperature, Low Concentration CH_4 Oxidation Verified by H and O Atom Measurements, *Proc. Combust. Inst.* **1985**, 20, 807–818.
- [51] P. Frank and T. Just, High Temperature Reaction Rate for $\text{H} + \text{O}_2 = \text{Oh} + \text{O}$ and $\text{OH} + \text{H}_2 = \text{H}_2\text{O} + \text{H}$, *Ber. Bunsenges. Phys. Chem.* **1985**, 89, 181–187.
- [52] N. Fujii, S. Sagawai, T. Sato, Y. Nosaka, and H. Miyama, Study of the Thermal Dissociation of N_2O and CO_2 Using $\text{O}(^3\text{P})$ Atomic Resonance Absorption Spectroscopy, *J. Phys. Chem.* **1989**, 5474–5478.
- [53] W. Tsang and J. T. Herron, Chemical Kinetic Data Base for Propellant Combustion I. Reactions Involving NO , NO_2 , HNO , HNO_2 , HCN and N_2O , *J. Phys. Chem. Ref. Data* **1991**, 20, 609–664.
- [54] J. V. Michael and K. P. Lim, Rate Constants for the N_2O Reaction System: Thermal Decomposition of N_2O ; $\text{N} + \text{NO} \rightarrow \text{N}_2 + \text{O}$; and Implications for $\text{O} + \text{N}_2 \rightarrow \text{NO} + \text{N}$, *J. Chem. Phys.* **1992**, 97, 3228.
- [55] W. D. Breshears, Falloff Behavior in the Thermal Dissociation Rate of N_2O , *J. Phys. Chem.* **1995**, 99, 12529–12535.
- [56] M. Röhrig, E. L. Petersen, D. F. Davidson, and R. K. Hanson, The Pressure Dependence of the Thermal Decomposition of N_2O , *Int. J. Chem. Kinet.* **1996**, 28, 599–608.
- [57] S. K. Ross, J. W. Sutherland, S.-C. Kuo, and R. B. Klemm, Rate Constants for the Thermal Dissociation of N_2O and the $\text{O}(^3\text{P}) + \text{N}_2\text{O}$ Reaction, *J. Phys. Chem. A* **1997**, 1104–1116.
- [58] M. Y. Louge and R. K. Hanson, Shock Tube Study of Cyanogen Oxidation Kinetics, *Int. J. Chem. Kinet.* **1984**, 16, 231–250.

5.5 Supporting information

Table 1: Experimental conditions and results of shock tube experiments without additional reaction partner.

T/K	p/mbar	$\rho/(\text{mol}/\text{cm}^3)$	$x(\text{NCN})/\text{ppm}$	$\frac{k_{\text{NCN}+\text{M}}}{\text{cm}^3/\text{mol s}}$	$\frac{k_{\text{NCN}+\text{NCN}}}{\text{cm}^3/\text{mol s}}$
$\rho \approx 1.9 \times 10^{-6} \text{ mol}/\text{cm}^3$, incident shock wave					
966	143	1.78×10^{-6}	59	-	1.0×10^{12}
1065	163	1.84×10^{-6}	56	-	3.0×10^{12}
1196	190	1.91×10^{-6}	67	-	1.0×10^{12}
1230	197	1.92×10^{-6}	130	-	1.2×10^{12}
1266	204	1.94×10^{-6}	60	-	2.0×10^{12}
1380	227	1.98×10^{-6}	59	-	1.0×10^{12}
1396	231	1.99×10^{-6}	61	-	1.5×10^{12}
1400	231	1.99×10^{-6}	59	-	1.5×10^{12}
1548	261	2.03×10^{-6}	67	-	2.0×10^{12}
$\rho \approx 3.8 \times 10^{-6} \text{ mol}/\text{cm}^3$, incident shock wave					
984	293	3.58×10^{-6}	21	-	1.5×10^{12}
1036	305	3.54×10^{-6}	21	-	2.0×10^{12}
1261	406	3.87×10^{-6}	28	-	2.0×10^{12}
1412	467	3.98×10^{-6}	50	-	2.0×10^{12}
$\rho \approx 4.1 \times 10^{-6} \text{ mol}/\text{cm}^3$, reflected shock wave					
1620	489	3.61×10^{-6}	14	-	3.0×10^{12}
1705	523	3.71×10^{-6}	15	-	5.0×10^{12}
1734	537	3.72×10^{-6}	50	-	5.0×10^{12}
1857	594	3.85×10^{-6}	64	-	3.0×10^{12}
2093	703	4.04×10^{-6}	60	2.5×10^8	-
2209	758	4.13×10^{-6}	65	6.0×10^8	-
2345	823	4.22×10^{-6}	30	1.4×10^9	-
2375	838	4.24×10^{-6}	65	2.2×10^9	-
2406	852	4.26×10^{-6}	65	1.9×10^9	-
2488	892	4.31×10^{-6}	130	3.9×10^9	-
2574	933	4.36×10^{-6}	60	4.0×10^9	-
2847	1066	4.50×10^{-6}	60	1.8×10^{10}	-
2886	1084	4.52×10^{-6}	64	2.0×10^{10}	-
3248	1262	4.61×10^{-6}	65	5.0×10^{10}	-
$\rho \approx 8.6 \times 10^{-6} \text{ mol}/\text{cm}^3$, reflected shock wave					
1042	475	5.48×10^{-6}	9	-	2.5×10^{12}
1159	364	8.41×10^{-6}	19	-	3.0×10^{12}
1325	710	6.45×10^{-6}	9	-	3.5×10^{12}
1361	741	6.55×10^{-6}	14	-	3.0×10^{12}
1494	857	6.90×10^{-6}	13	-	2.5×10^{12}
1495	859	6.91×10^{-6}	4	-	3.5×10^{12}
1517	961	7.62×10^{-6}	12	-	3.0×10^{12}

5. High Temperature Rate Constants of the Reactions $\text{NCN} + \text{O}$, $\text{NCN} + \text{NCN}$, and $\text{NCN} + \text{M}$

Table 1, continued:

T/K	p/mbar	$\rho/(\text{mol}/\text{cm}^3)$	$x(\text{NCN})/\text{ppm}$	$\frac{k_{\text{NCN}+\text{M}}}{\text{cm}^3/\text{mol s}}$	$\frac{k_{\text{NCN}+\text{NCN}}}{\text{cm}^3/\text{mol s}}$
1642	990	7.25×10^{-6}	16	-	2.5×10^{12}
1665	1008	7.28×10^{-6}	12	-	4.0×10^{12}
1685	1020	7.28×10^{-6}	13	-	3.5×10^{12}
1763	1099	7.50×10^{-6}	17	-	3.0×10^{12}
1900	1227	7.77×10^{-6}	20	-	5.0×10^{12}
2012	1331	7.96×10^{-6}	19	1.4×10^8	-
2014	1334	7.97×10^{-6}	31	1.8×10^8	-
2024	1304	7.75×10^{-6}	20	2.0×10^8	-
2317	1619	8.41×10^{-6}	18	1.5×10^9	-
2357	1663	8.49×10^{-6}	22	1.2×10^9	-
2561	1854	8.71×10^{-6}	26	2.5×10^9	-
2924	2204	9.07×10^{-6}	50	2.5×10^{10}	-
$\rho \approx 1.3 \times 10^{-5} \text{ mol}/\text{cm}^3$, reflected shock wave					
1156	1134	1.18×10^{-5}	5	-	5.0×10^{12}
1322	1415	1.29×10^{-5}	5	-	5.0×10^{12}
1432	1599	1.34×10^{-5}	7	-	2.5×10^{12}
1588	1884	1.43×10^{-5}	7	-	3.0×10^{12}

Table 2: Experimental conditions and results of shock tube experiments with N_2O as an O atom precursor.

T/K	p/mbar	$\rho/(\text{mol}/\text{cm}^3)$	$x(\text{NCN})/\text{ppm}$	$x(\text{N}_2\text{O})/\text{ppm}$	$\frac{k_{\text{NCN}+\text{O}}}{\text{cm}^3/\text{mol s}}$
$\rho \approx 4.3 \times 10^{-6} \text{ mol}/\text{cm}^3$					
2099	709	4.06×10^{-6}	63	1052	8.0×10^{13}
2285	797	4.20×10^{-6}	63	1052	1.0×10^{14}
2438	870	4.29×10^{-6}	63	1052	6.0×10^{13}
2459	882	4.31×10^{-6}	58	700	8.0×10^{13}
2541	921	4.36×10^{-6}	63	1052	6.0×10^{13}
2580	939	4.38×10^{-6}	57	1275	7.0×10^{13}
2783	1040	4.50×10^{-6}	55	1948	8.0×10^{13}
$\rho \approx 8.2 \times 10^{-6} \text{ mol}/\text{cm}^3$					
1826	1176	7.75×10^{-6}	17	4280	6.0×10^{13}
1866	1198	7.72×10^{-6}	20	1080	6.0×10^{13}
1900	1232	7.79×10^{-6}	19	1080	8.0×10^{13}
1964	1289	7.89×10^{-6}	22	1080	7.0×10^{13}
1977	1305	7.94×10^{-6}	29	1068	6.5×10^{13}
2138	1454	8.18×10^{-6}	21	1080	6.5×10^{13}
2409	1713	8.55×10^{-6}	55	1046	6.0×10^{13}
2563	1861	8.76×10^{-6}	38	1977	9.0×10^{13}

6 Direct Measurements of the Rate Constants of the Reactions $\text{NCN} + \text{NO}$ and $\text{NCN} + \text{NO}_2$ Behind Shock Waves

Johannes Dammeier and Gernot Friedrichs*

Institut für Physikalische Chemie,
Christian-Albrechts-Universität zu Kiel

Submitted to *J. Phys. Chem. A*.
Copyright granted by the American Chemical Society.

Own contributions to this paper:

- Shock tube measurements
- Data analysis and discussion

*friedrichs@phc.uni-kiel.de

Abstract

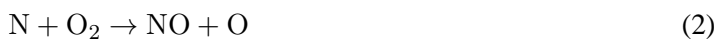
The high temperature rate constants of the reactions $\text{NCN} + \text{NO}$ and $\text{NCN} + \text{NO}_2$ have been directly measured behind shock waves under pseudo-first order conditions. NCN has been generated by the pyrolysis of cyanogen azide (NCN_3) and quantitatively detected by sensitive difference amplification laser absorption spectroscopy at a wavelength of 329.1302 nm. The NCN_3 decomposition initially yields electronically excited ^1NCN radicals, which are subsequently transformed to the triplet ground state by collision induced intersystem crossing (CIISC). CIISC efficiencies were found to increase in the order of $\text{Ar} < \text{NO}_2 < \text{NO}$ as the collision gases. The rate constants of the $\text{NCN} + \text{NO}/\text{NO}_2$ reactions can be expressed as $k_{\text{NCN}+\text{NO}}/(\text{cm}^3\text{mol}^{-1}\text{s}^{-1}) = 1.9 \times 10^{12} \exp[-26.3 (\text{kJ/mol})/RT]$ ($\pm 7\%$, $\Delta E_a = \pm 1.6 \text{ kJ/mol}$, $764 \text{ K} < T < 1944 \text{ K}$) and $k_{\text{NCN}+\text{NO}_2}/(\text{cm}^3\text{mol}^{-1}\text{s}^{-1}) = 4.7 \times 10^{12} \exp[-38.0 (\text{kJ/mol})/RT]$ ($\pm 19\%$, $\Delta E_a = \pm 3.8 \text{ kJ/mol}$, $704 \text{ K} < T < 1659 \text{ K}$). In striking contrast to reported low temperature measurements, which are dominated by recombination processes, both reaction rates show a positive temperature dependence and are independent of the total density ($1.7 \times 10^{-6} \text{ mol/cm}^3 < \rho < 7.6 \times 10^{-6} \text{ mol/cm}^3$). For both reactions, the minima of the total rate constants occur at temperatures below 700 K showing that at combustion relevant temperatures the overall reactions are dominated by abstraction-like pathways according to $\text{NCN} + \text{NO} \rightarrow \text{CN} + \text{N}_2\text{O}$ and $\text{NCN} + \text{NO}_2 \rightarrow \text{NCNO} + \text{NO}$.

6.1 Introduction

Encouraged by the demand for clean energy sources, the efforts to reduce the emissions of hazardous substances from combustion processes continue. Nitrogen oxides NO_x (NO and NO_2) are among the main pollutants, which are generated in the combustion of fossil fuels as well as fuels made from regrowing resources.¹ The hazardous potential of NO_x lies in its contribution to photochemical smog in the troposphere and to ozone depletion in the stratosphere.² Furthermore, nitrous oxide (N_2O), a secondary product of NO_x reactions, is an active atmospheric trace gas with a high global warming potential.³

There are several formation mechanisms and two principal sources of NO_x in combustion processes.¹ Firstly, NO_x stems from nitrogen impurities in the fuel, which are oxidized. This mechanism is referred to as fuel-N-conversion.⁴ Secondly, NO_x can be generated from atmospheric molecular nitrogen. At high temperatures, the primary formation pathway takes place according to the Zeldovich

mechanism,^{5,6}



Thirdly, in low temperature combustion at high pressures, NO_x is yielded via the reaction sequence^{7,8}



Finally, especially under fuel-rich combustion conditions, prompt-NO is generated by the reaction of small hydrocarbon radicals with N_2 . Fenimore⁹ suggested that a key initiating step of the reaction sequence is the spin-forbidden reaction



In fact, it has long been recognized that the intersystem crossing probability from the doublet to the quartet potential energy surface necessary for reaction 6a is low and thus theoretically predicted rate constants were lower than experimentally measured.¹⁰ In the year 2000, the products of this textbook reaction have been revised by Moskaleva *et al.*^{11,12} according to



By quantum chemical and statistical rate calculations they showed that this spin-allowed reaction pathway exists and yields rate constants that are consistent with the experimental data. The pathway generates NCN radicals, a species which had not been discussed in the context of combustion research before. Later, it was experimentally proven by flame and shock tube measurements that the NCN channel (6b) is in fact the dominating reaction channel of reaction 6.¹³⁻¹⁶ Since then, several theoretical^{11,17-22} and experimental^{16-18,23-26} studies have addressed NCN reactions and available rate constants have been introduced into existing combustion models.^{14,26-30}

Objects of previous theoretical work were the reactions $\text{NCN} + \text{O}$ (7),²¹ $\text{NCN} + \text{O}_2$ (8),²⁰ $\text{NCN} + \text{OH}$ (9),²² $\text{NCN} + \text{NO}$ (10),^{17,19} $\text{NCN} + \text{NO}_2$ (11),¹⁸ and $\text{NCN} + \text{H}$ (12).¹¹ Rate constants and product branching ratios have been theoretically predicted over a wide range of temperatures and pressures. In contrast, available experimental results are limited to a few reactions and mainly to temperatures below $T < 600$ K. An exception is the reaction $\text{NCN} + \text{H}$, which has been investigated behind shock waves in the temperature range $2378 \text{ K} < T < 2492 \text{ K}$ by Vasudevan *et al.*¹⁶ NCN was obtained by the pyrolysis of ethane (C_2H_6), which yields CH radicals that subsequently reacted with the bath gas N_2 to form NCN (reaction 6b). Observed NCN decays were attributed to the reaction $\text{NCN} + \text{H}$ (12). An indirect determination of the rate constant of reaction 12 has also been reported by Lamoureux *et*

*al.*²⁶ In a combined modeling and flame diagnostics study they attributed deviations of simulated from measured CH, NCN and NO concentrations to reaction 12. Furthermore, high temperature reaction rates of the unimolecular NCN decomposition $\text{NCN} + \text{M} \rightarrow \text{C} + \text{N}_2 + \text{M}$ (13) have been directly measured (C-ARAS) behind shock waves at temperatures of 1800 – 2950 K.^{31,32}

Recently, in order to provide much needed high temperature rate constant data for bimolecular NCN reactions, we have thoroughly investigated the thermal decomposition of NCN_3 as a quantitative high temperature NCN radical source.³³ NCN formation rates and high temperature absorption cross section have been directly measured showing that NCN can be sensitively detected in the ppm range behind shock waves. At such low concentrations subsequent NCN secondary chemistry is efficiently suppressed turning the thermal NCN_3 decomposition into an ideal NCN radical source. Nevertheless, as a requirement for accurate rate constant measurements, a consistent NCN background mechanism has been derived from pyrolysis experiments reporting rate constants for the reactions $\text{NCN} + \text{M}$ (13) at $2010 \text{ K} < T < 3250 \text{ K}$ and $\text{NCN} + \text{NCN}$ (14) at $965 \text{ K} < T < 1900 \text{ K}$.³⁴ Furthermore, by adding O atoms generated from the N_2O decomposition to the reaction mixtures, we were able to measure the rate constant of the reaction $\text{NCN} + \text{O}$ (7) for the first time ($1825 \text{ K} < T < 2785 \text{ K}$).

Regarding reaction 10, $\text{NCN} + \text{NO}$, the theoretical investigations agree that the reaction proceeds via an NCNNO intermediate.^{17,24} Huang *et al.*¹⁷ performed quantum chemical (G2M/CC5) and statistical rate (VTST/RRKM) calculations. It was found that the overall reaction exhibits negative temperature dependence at $T < 500 \text{ K}$ and a pronounced positive temperature dependence toward higher temperatures. At low temperatures, a recombination reaction according to $\text{NCN} + \text{NO} + \text{M} \rightleftharpoons \text{NCNNO} + \text{M}$ takes place, whereas at high temperatures an abstraction-like channel yields $\text{N}_2\text{O} + \text{CN}$. One of the first experimental works on elementary NCN gas phase reactions was concerned with reaction 10 and has been performed by Baren and Hershberger²³ in 2002. NCN was generated by 193 nm photolysis of diazomethane (CH_2N_2) in the presence of cyanogen (C_2N_2). Rate constants could be determined from NCN concentration-time profiles measured by means of laser induced fluorescence (LIF) in the temperature range $298 \text{ K} < T < 573 \text{ K}$. Both NCN (by LIF) and the possible products N_2O and CO_2 (by IR absorption) were detected. Similarly, Huang *et al.*¹⁷ measured rate constants in the temperature range of $254 \text{ K} < T < 353 \text{ K}$ following the 193 nm photolysis of cyanogen azide (NCN_3) as a source of NCN. In the examined temperature range both studies support the expected negative temperature dependence. Welz²⁴ extended the temperature range to $254 \text{ K} < T < 485 \text{ K}$ and characterized the pressure dependence at pressures ranging from $p = 30 \text{ mbar}$ to $p = 50 \text{ bar}$. Again, NCN was detected by LIF following the photodissociation of NCN_3 at $\lambda = 193 \text{ nm}$ and $\lambda = 248 \text{ nm}$.

Reaction 11, $\text{NCN} + \text{NO}_2$, has been the subject of two combined experimental and theoretical studies. Yang *et al.*¹⁸ measured rate constants in the temperature range $260 \text{ K} < T < 296 \text{ K}$ at pressures between $p = 133 \text{ mbar}$ and $p = 666 \text{ mbar}$. NCN was generated by 193 nm photolysis of NCN_3 and detected by LIF. Additionally, rate constants have been calculated at temperatures of $200 \text{ K} < T < 2000 \text{ K}$ using a combination of quantum mechanical (G2M//B3LYP/6-311+G(d)) and sta-

tistical (RRKM) methods. Based on these calculations, an association reaction is expected for temperatures $T < 700$ K to take place exhibiting a negative temperature dependence, whereas at higher temperatures a positively temperature dependent abstraction channel is predicted to yield $\text{NCNO} + \text{NO}$. In similar experiments, Kappler²⁵ extended the temperature range to $255 \text{ K} < T < 349 \text{ K}$ and measured fall-off curves in the pressure range $155 \text{ mbar} < p < 38 \text{ bar}$. In agreement with Yang *et al.*, a negative temperature and a positive pressure dependence has been noted, which was explained by an association-isomerization mechanism finally yielding NCO and N_2O as the products.

So far, only the low temperature recombination processes of reactions 10 and 11 could be experimentally confirmed. High temperature experiments suitable to assess the dominating $\text{N}_2\text{O} + \text{CN}$ channel for reaction 10 and $\text{NCNO} + \text{NO}$ for reaction 11 are not available. In this spirit, the high temperature measurements presented in this paper provide an opportunity to bring together theory and experiment. Assessing and characterizing the temperature and pressure dependencies of bimolecular reactions of small unpaired species, i.e., the preference of an association complex at low temperatures and the opening of an activation energy controlled abstraction-like reaction channel at high temperatures, remains challenging. Recent examples from our shock tube lab addressing similar problems are the measurements of the rate constants of the reactions $\text{HCO} + \text{NO}/\text{NO}_2$ ³⁵ and $\text{HCO} + \text{O}_2$.³⁶

In this paper, first high temperature measurements on the reactions



will be presented to provide rate constant data at combustion relevant temperatures and to verify the theoretically predicted dominance of the abstraction-like reaction channels.

6.2 Experimental

All experiments have been performed using a shock tube set-up^{36,37} equipped with a narrow bandwidth laser absorption spectrometer³³ to measure NCN concentration-time profiles. Briefly, the 4.4 m long test section of the shock tube could be evacuated down to pressures of 10^{-7} mbar by a combination of oil-free diaphragm and turbomolecular pump (Pfeiffer Vacuum). Hydrogen, nitrogen or mixtures of hydrogen and nitrogen were used as the driver gases; diaphragms were made from 30 or 80 μm thick aluminum foil. Pressures and temperatures behind shock waves were calculated based on pre-shock conditions and the shock wave velocity. Real gas effects and the shock wave damping on the order of 1% were taken into account. The shock wave velocity was measured by a fast count unit wired to four piezoelectric sensors (PCB Piezotronics M 113A21).

NCN has been detected in its triplet ground state at a wavelength of $\lambda = 329.1302 \text{ cm}^{-1}$ (superpo-

sition of the ${}^3\Pi_1$ sub-band of the $\tilde{A}{}^3\Pi_u(000) - \tilde{X}{}^3\Sigma_g(000)$ transition and the Q₁ band head of the ${}^3\Sigma^+(010) - {}^3\Pi(010)$ vibrationally excited Renner-Teller split transition) by a difference amplification laser absorption scheme. 1.5 mW of laser light of the respective wavelength was generated by internal frequency doubling of a stabilized continuous wave ring-dye laser (Coherent 899) with DCM Special (Radiant Dyes) as a dye, which was pumped by a Nd:YVO₄ solid state laser (Coherent Verdi V10) at $\lambda = 532$ nm. The wavelength of the fundamental has been measured by an interferometric type wavemeter (MetroLux WL200) with an accuracy of ± 0.0015 cm⁻¹. Detection and reference beam were divided by a 50:50 beam splitter plate, the detection beam was passed through the shock tube and the reference beam could be attenuated by a variable neutral density filter. Both beams were band pass filtered and coupled into two optical fibers (Thorlabs BF H22-550), which were connected to a balanced photo detector and amplifier (Thorlabs PDB150A-EC). The resulting difference signal was further amplified (Ortec Fast Preamp 9305) low pass filtered by 1.4 MHz and stored by an analog input board (PCI-DAS4020/12, 20 MHz, 12 bit).

The absorption signals were transformed into concentrations using the previously determined NCN absorption cross section ($\log_{10}(\sigma/(\text{cm}^2/\text{mol})) = 8.9 - 8.3 \times 10^{-4} \times T/\text{K}$).³³ The measurements were evaluated by fitting numerical simulations to the measured concentration-time profiles. Numerical simulations were performed using the Chemkin-II³⁸ program package. For sensitivity analyses, the sensitivity coefficient $\sigma(i, j)$ of the i^{th} reaction of species j was normalised with respect to the maximum concentration of the species j occurring during the recorded time interval. The GRI-Mech. 3.0³⁹ natural flame mechanism has been used as a background mechanism and an additional subset of reactions taking into account NCN and CN secondary chemistry has been adopted from our previous paper.³⁴ Rate constants of reverse reactions have been taken into account based on thermodynamic data from Konnov,⁴⁰ except for NCN, for which the data were taken from Goos *et al.*⁴¹

NCN was generated by the thermal decomposition of NCN₃. NCN₃ was synthesized from gaseous BrCN and solid NaN₃ using a variant³³ of the method described by Milligan *et al.*⁴² NCN₃ is an extremely explosive substance, hence, no attempt was made to further purify the initially generated gas. Its purity was checked by means of FTIR spectroscopy. Remaining BrCN impurities were always < 3%, but usually < 1%. CO₂ was on the order of 0.01% and water was not detectable. Freshly prepared NCN₃ was immediately diluted by argon down to mole fractions of 0.1%, nevertheless, a slow decomposition of $\approx 5\%$ per day was found to take place.

Gases and chemicals used were argon (Air Liquide, 99.99%), hydrogen and nitrogen as driver gases (Air Liquide, 99%), NO and NO₂ (Air Liquide, 99.95%), BrCN (Acros, 97%), and NaN₃ (Merck, 99%). Gas mixtures were prepared using the partial pressure method; the NO₂/N₂O₄ equilibrium has been taken into account. NO and NO₂ were purified by repeated freeze-pump-thaw cycles. All gas mixtures were used within 3 days after preparation. Before all shock tube experiments, the shock tube was flushed with the respective test gas mixtures at a pressure of $p \approx 50$ mbar. No dependence of measured signals on the flushing time or the time between sample preparation and experiment could

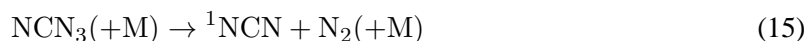
be noticed revealing that wall absorption effects or room temperature reactions of NCN_3 with NO or NO_2 did not perturb the measurements.

6.3 Results and discussion

6.3.1 $\text{NCN} + \text{NO}$

NCN concentration-time profiles of mixtures of NCN_3 and NO behind incident shock waves have been recorded in the temperature range $764 \text{ K} < T < 1944 \text{ K}$ at two different total densities of $\rho \approx 1.8 \times 10^{-6} \text{ mol/cm}^3$ and $\rho \approx 3.5 \times 10^{-6} \text{ mol/cm}^3$ ($123 \text{ mbar} < p < 690 \text{ mbar}$). Mole fractions of NCN_3 were between 5 and 15 ppm and much lower than the mole fractions of the excess component NO , which were 5000 or 10000 ppm. A typical concentration-time profile together with the respective numerical simulation and a sensitivity analysis is shown in Fig. 1. To illustrate the influence of added NO , an experiment without NO is shown as well. Two strong Schlieren signals accompany the incident and reflected shock wave passages and thus define $t = 0$ of the corresponding temperature and pressure jumps.

Without the addition of NO , NCN consuming reactions are negligible. Up to temperatures of $T = 2000 \text{ K}$, stable NCN plateaus were found. At higher temperatures, the decomposition of NCN set in according to $\text{NCN} + \text{M} \rightarrow \text{C} + \text{N}_2$ (13). The initial increase of the NCN absorption signal in Fig. 1 reflects two processes: The decomposition of the precursor molecule NCN_3 yielding ^1NCN and the subsequent relaxation of the electronically excited ^1NCN to its triplet ground state (^3NCN) via collision-induced intersystem crossing (CIISC):



Rate constants for both processes have been reported in our previous publications.³³ Updated rate constant expressions as used in this work rely on recent ^1NCN concentration-time profile measurements, which will be reported elsewhere.⁴³ Upon the addition of 0.5 – 1% NO , the initial increase of the ^3NCN signal gets much faster. Since the unimolecular decomposition process can be expected to be only slightly affected by such small amounts of a different bath gas, this increase is attributed to a much more efficient CIISC process of NO compared to argon. To support this assumption, test experiments have been performed with the detection laser frequency tuned to a strong ^1NCN transition. In the measured ^1NCN concentration-time profiles, the addition of NO did not alter the formation rate of ^1NCN , but had a strong influence on the ^1NCN decays.

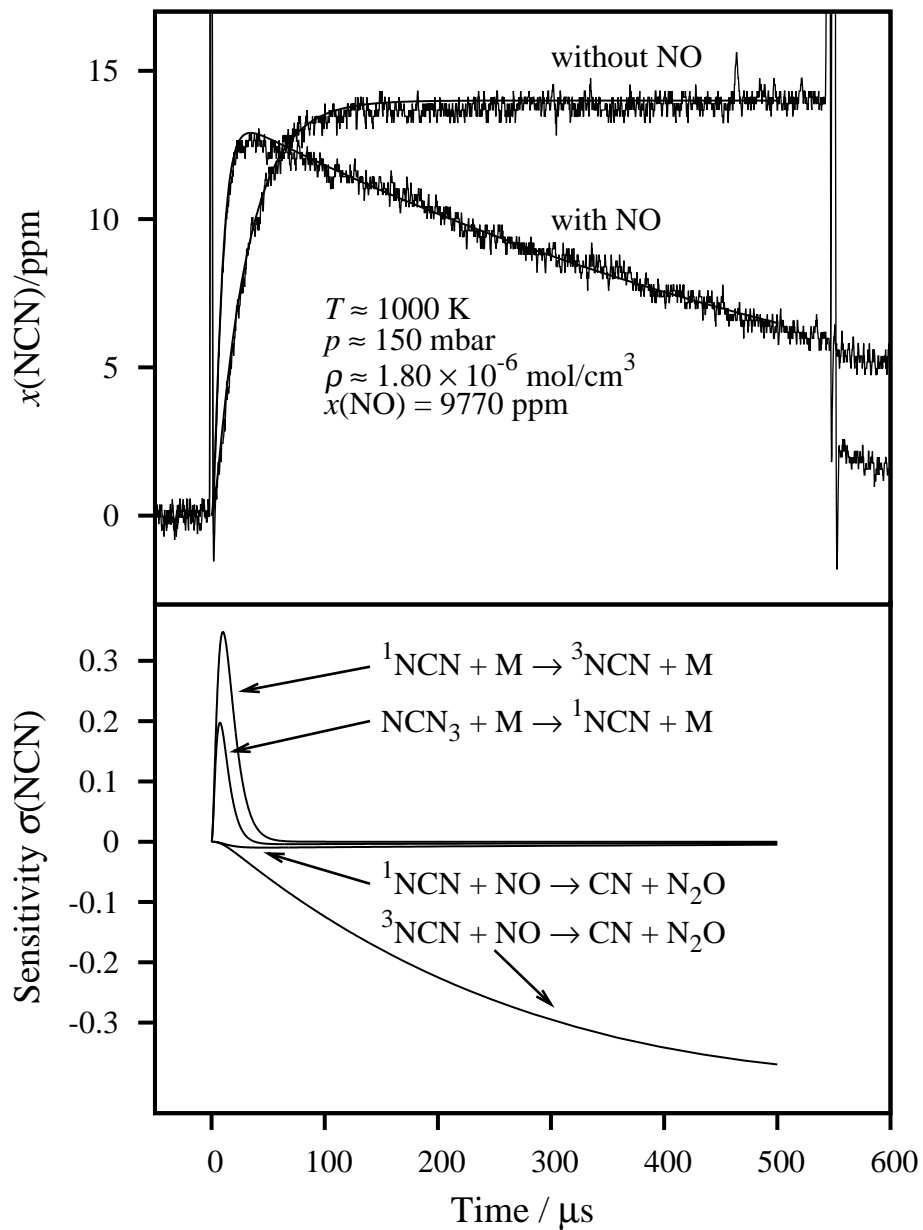


Figure 1: Upper: NCN concentration-time profiles for experiments with and without NO added to the reaction mixtures. With NO: $T = 996 \text{ K}$, $p = 149 \text{ mbar}$, $\rho = 1.80 \times 10^{-6} \text{ mol/cm}^3$, $x(\text{NCN}_3) = 13.4 \text{ ppm}$; without NO: $T = 1002 \text{ K}$, $p = 150 \text{ mbar}$, $\rho = 1.81 \times 10^{-6} \text{ mol/cm}^3$, $x(\text{NCN}_3) = 14.0 \text{ ppm}$. Below: Sensitivity analysis of the experiment with NO.

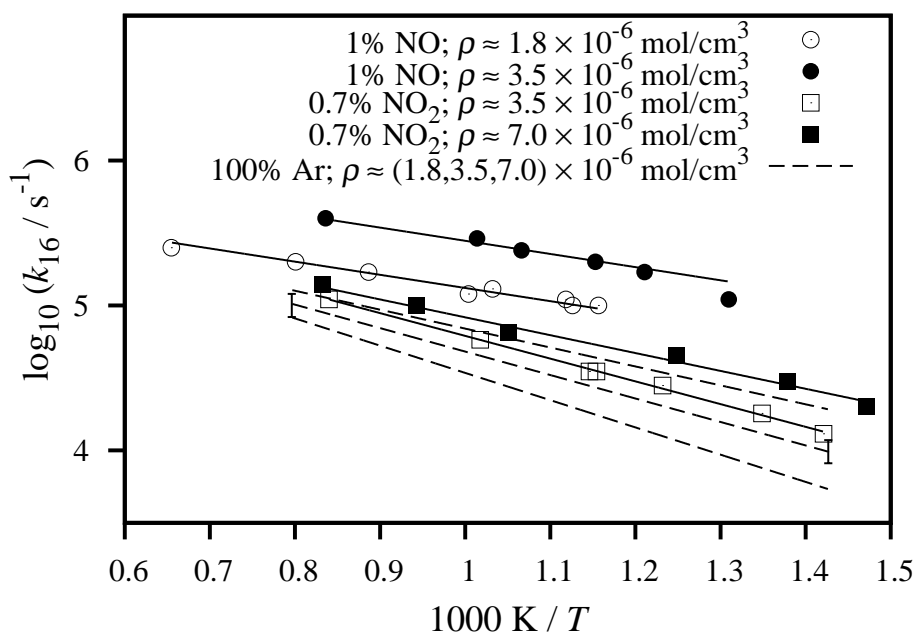


Figure 2: Arrhenius plot of measured first order CIISC rate constants at several total densities with NO or NO_2 added to the gas mixtures. Arrhenius expressions of rate constants in pure Ar have been determined from ^1NCN concentration-time profiles⁴³ and are shown as dashed lines.

With 1% NO added to the mixture, rise times are shortened by a factor of about 5 showing that NO exhibits a CIISC efficiency higher by a factor of 400 compared to argon. Rate constants of the relaxation reaction 16 were extracted from the measured profiles and are shown together with corresponding data for argon⁴³ and NO_2 (see Section 6.3.2) in Fig. 2. Similar values of the apparent activation energies on the order of 20 kJ/mol are found for NO, NO_2 and Ar. The apparent activation energies as well as the observed density dependences ($n \approx 1$ for NO, $n \approx 0.5$ for NO_2 , $n \approx 0.6$ for Ar; according to $k_b = (\frac{\rho_b}{\rho_a})^n k_a$) reflect the complicated underlying physical processes that govern the CIISC probability and are difficult to predict.^{44,45}

As it is discernible in the sensitivity analysis shown in the lower frame of Fig. 1, the CIISC process is completed within 50 μs and thus does not critically interfere with the rate constant measurement of the reaction $\text{NCN} + \text{NO}$. In fact, reaction 10 is the only sensitive NCN consuming reaction showing that the measurements essentially follow pseudo-first order kinetics. Possible secondary chemistry is successfully suppressed by using very low (≈ 10 ppm) mole fractions of NCN_3 . Rate constants were extracted in the temperature range of 764 K $< T$ 1944 K. Toward low temperatures, the accessible temperature range was limited by the rate of the NCN_3 decomposition. It is slower than the ^1NCN relaxation below $T = 750$ K. At high temperatures, NCN absorption cross sections are too low and higher NCN_3 concentrations used to compensate for the lower sensitivity resulted in significant secondary chemistry. Selected rate constants of the reaction used in the mechanism can be found in Table 1.

Table 1: Selected reactions of the mechanism used in the numerical simulations to extract the rate constants of the reaction NCN + NO. Possible secondary chemistry has been taken into account by the GRI-Mech. 3.0³⁹ and a subset of NCN and CN reactions as outlined in our previous paper.³⁴ Rate constants are given as $k_i = AT^n \exp[-E_a/RT]$. Units are cm, mol, s, K and kJ.

No.	Reaction	A	E_a	Ref.	
(10)	³ NCN + NO → CN + N ₂ O	1.9×10^{12}	26.3	this work	
(15)	NCN ₃ → ¹ NCN + N ₂	3.3×10^9	71.2	43	$\rho = 1.8 \times 10^{-6} \text{ mol/cm}^3$
		5.0×10^9	71.2	43	$\rho = 3.5 \times 10^{-6} \text{ mol/cm}^3$
(16)	¹ NCN → ³ NCN	1.1×10^6	17.4	this work	1.0% NO, $\rho = 1.8 \times 10^{-6} \text{ mol/cm}^3$
		2.3×10^6	17.4	this work	1.0% NO, $\rho = 3.5 \times 10^{-6} \text{ mol/cm}^3$
(17)	¹ NCN + NO → CN + N ₂ O	1.9×10^{12}	26.3	this work	set equal to reaction 10
(18)	³ NCN + CN ⇌ C ₂ N ₂ + N	1.3×10^{14}	33.5	11	
(19)	³ NCN + N ⇌ CN + N ₂	1.0×10^{13}		46	

An Arrhenius plot of the rate constant data for k_{10} including selected literature results^{17,23,24} is shown in Fig. 3. Data of the experimental conditions are given in the supplementary information. No dependence of the measured rate constants on the total density is discernible within the scatter of the data. All data points fall within a narrow margin and can be very well represented by the Arrhenius expression:

$$k_{10}/(\text{cm}^3\text{mol}^{-1}\text{s}^{-1}) = 1.89 \times 10^{12} \exp[-26.3 \text{ (kJ/mol)}/RT] \quad (\pm 7\%)$$

The stated error estimate reflects a combination of the statistical error of the Arrhenius fit ($\pm 1\%$, 2σ), uncertainties of the NO mole fraction ($\pm 5\%$), and uncertainties in the ³NCN formation mechanism ($\pm 1\%$). Due to the pseudo-first order reaction conditions, uncertainties of the NCN absorption cross section and thus NCN concentration did not result in an additional error. The uncertainty of the Arrhenius activation energy of ± 1.6 kJ/mol corresponds to the 2σ error of the slope of the Arrhenius fit.

In additional measurements, ¹NCN concentration-time profiles have been recorded to assess potential differences of the reactivities of ¹NCN and ³NCN. However, because of the fast CIISC process, the evaluation of these signals did not yield reliable rate constants for the reaction ¹NCN + NO. Therefore, ¹NCN and ³NCN radical reactions have been assumed to proceed with the same rate. As can be seen from the sensitivity analysis shown in Fig.1, the reaction ¹NCN + NO exerts a minor influence on the ³NCN profile and did not significantly interfere with the measurements of the corresponding ³NCN rate constant.

In contrast to all previous experimental studies, which have been performed at temperatures below $T = 573$ K, a positive temperature dependence has been found at temperatures > 764 K. This positive

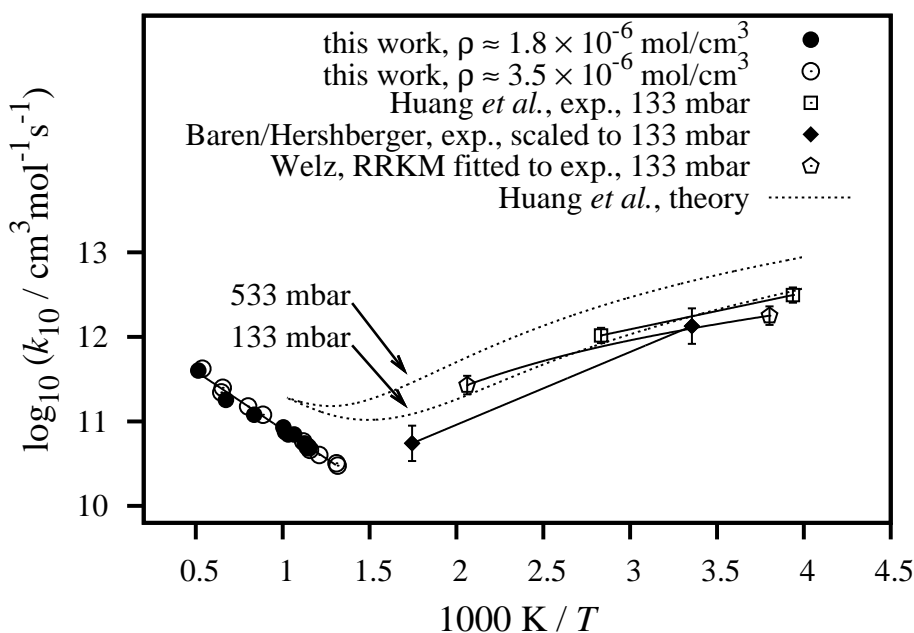


Figure 3: Comparison of measured rate constants of reaction 10, $\text{NCN} + \text{NO}$, with selected literature data.^{17,23,24} The literature values of Baren and Hershberger²³ and Welz²⁴ have been scaled to 133 mbar based on the Troe parameters given in the work of Welz.

temperature dependence has been predicted by Huang *et al.*¹⁷ in their theoretical study. In Fig. 3, theoretically derived rate constant expressions for two different total pressures are shown. At low temperatures, according to a recombination process, the reaction proceeds close to the low pressure limit. The corresponding pressure dependence is also supported by the experimental studies.^{17,23,24} In contrast, at high temperatures we find reaction rates that are independent of the total density. Rate constant values are approximately a factor of two lower than the Huang *et al.*¹⁷ prediction. Although no direct evidence of the postulated minimum of the rate constants is provided by our measurements, all experimental data are consistent with a minimum at a temperature around $T \approx 670$ K.

An explanation of the complex temperature and pressure dependence can be best illustrated on the basis of the characteristics of the underlying potential energy surface. A simplified scheme of the potential energy surface, adopted from the calculations of Huang *et al.*,¹⁷ is outlined in Fig. 4. Other possible reaction channels forming $\text{CNO} + \text{N}_2$ or $\text{NCO} + \text{N}_2$ do not play a role because the barriers on the corresponding minimum energy paths are too high. Two different electronic states are involved. A simple association of NCN and NO leads to the ${}^2\text{A}''$ state (dashed lines) with two different isomers denoted $\text{cis-}{}^2\text{A}''$ and $\text{trans-}{}^2\text{A}''$. The reaction continues by crossing to the ${}^2\text{A}'$ surface through two conical intersections (CI) yielding the local minima $\text{trans-}{}^2\text{A}'$ and $\text{cis-}{}^2\text{A}'$. Further dissociation to the products $\text{CN} + \text{N}_2\text{O}$ involves barriers that are significantly higher in energy than the entrance energy of the initial $\text{NCN} + \text{NO}$ fragments. Therefore, at low temperatures the $\text{trans-}{}^2\text{A}'$ and $\text{cis-}{}^2\text{A}'$ intermediates can be stabilized by collisions. Consequently, the reaction exhibits the typical behavior

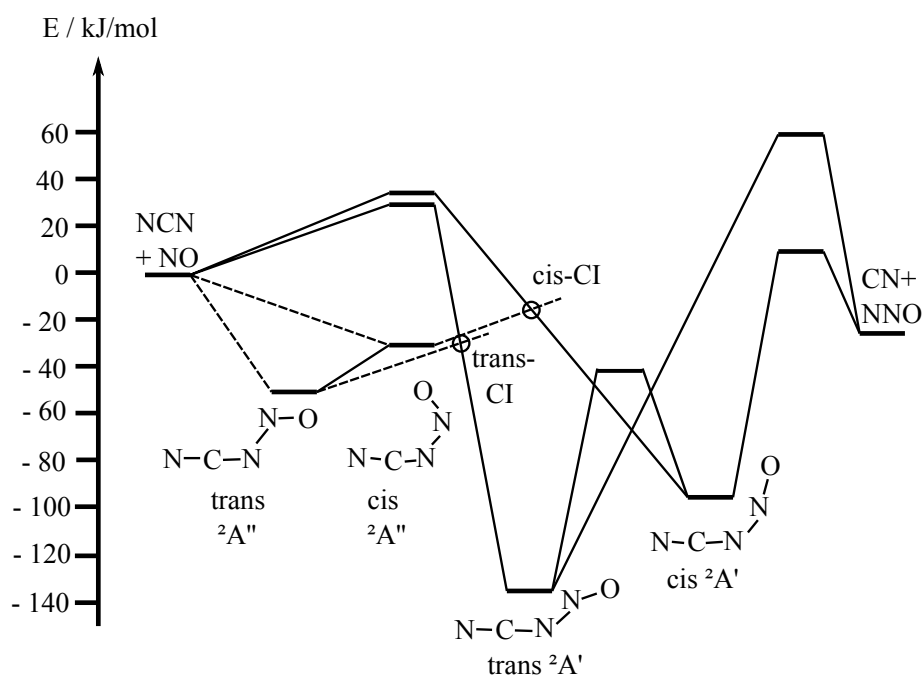


Figure 4: Part of the potential energy surface of the reaction $\text{NCN} + \text{NO}$ (10) (G2M/CC5//B3LYP/6-311+G(d) level of theory), adopted from Huang *et al.*¹⁷

of a recombination reaction, i.e., a negative temperature dependence (faster re-dissociation to the reactants at higher temperature) and a positive pressure dependence (collisional stabilization of the intermediates). Toward high temperatures, however, enough thermal energy is involved to overcome the exit barriers of the cis- and trans- $^2A'$ intermediates. In this case, the forward reaction resembles an abstraction-like mechanism with a positive temperature dependence stemming from the exit barrier and virtually no pressure dependence. The measured activation energy of $E_a = 26$ kJ/mol is between the barriers of the trans- (61 kJ/mol with respect to the reactants) and the cis- $^2A'$ (14 kJ/mol) pathways. The much closer agreement with the cis value reveals that the overall reaction at high temperatures is dominated by the cis pathway.

6.3.2 $\text{NCN} + \text{NO}_2$

The kinetics of the reaction $\text{NCN} + \text{NO}_2 \rightarrow \text{NCNO} + \text{NO}$ (11) have been investigated in the temperature range $704 \text{ K} < T < 1659 \text{ K}$ and at two different total densities of $\rho \approx 3.5 \times 10^{-6} \text{ mol/cm}^3$ and $\rho \approx 7.0 \times 10^{-6} \text{ mol/cm}^3$. Corresponding pressures were $182 \text{ mbar} < p < 654 \text{ mbar}$. Initial mole fractions of NCN_3 in Ar were between 3 and 14 ppm, mole fractions of the excess component NO_2 were 7000 ppm or, for a validation experiment, 19000 ppm. Fig. 5 shows a typical absorbance-time profile. Absorbance of NCN has been used instead of NCN mole fractions to illustrate the effect of interfering NO_2 background absorption stemming from its broad $\tilde{A}^2B_2 - \tilde{X}^2A_1$ transition.⁴⁷ Already before the

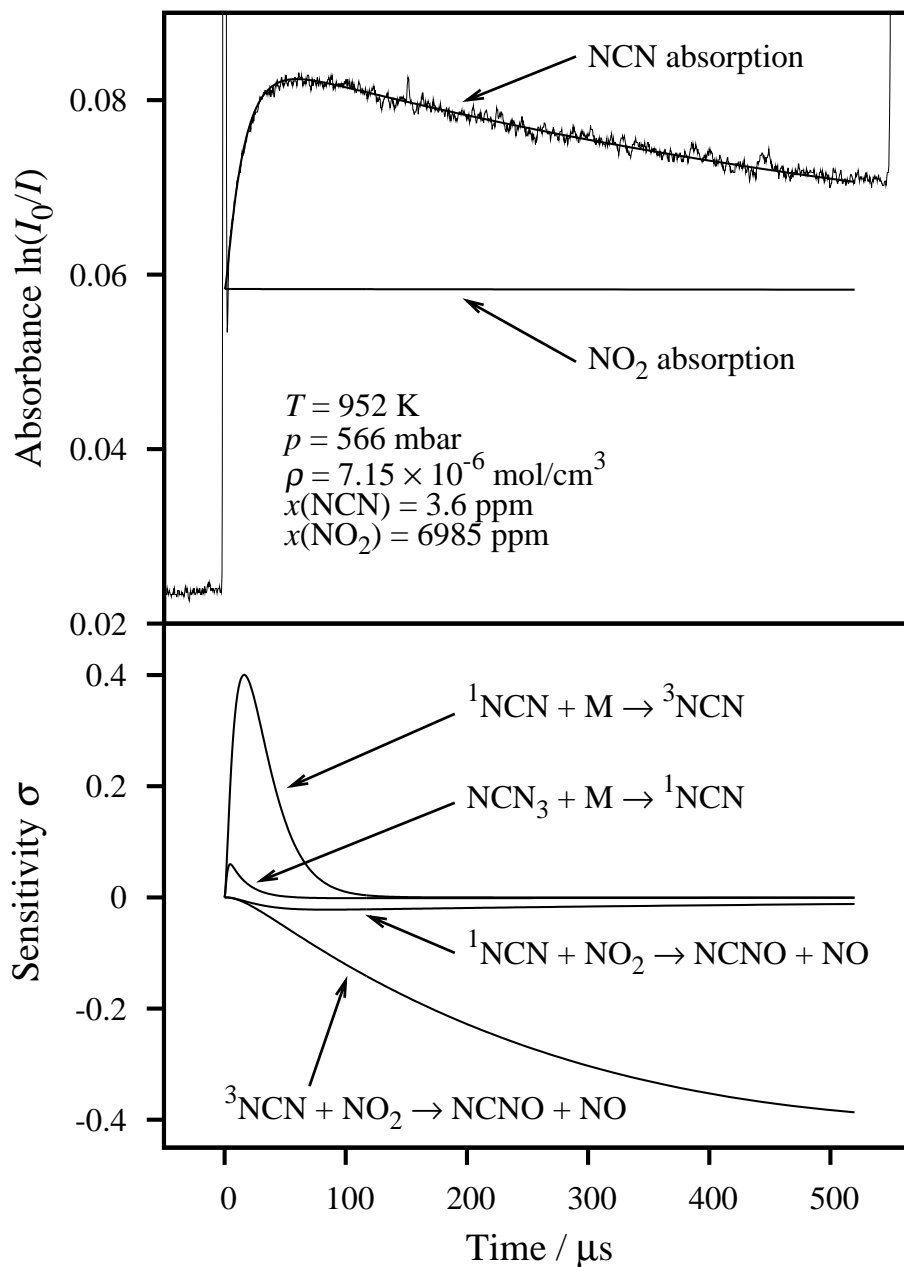


Figure 5: Upper: Absorbance-time profile of an NO_2 experiment behind an incident shock wave. Both NO_2 absorbance and NCN absorbance are shown. Due to the interfering NO_2 background absorption, the baseline is not zero. Lower: NCN sensitivity analysis indicating pseudo-first order conditions after 100 μs .

arrival of the shock wave, significant NO_2 absorption is discernible. Due to the higher density, higher background absorption values are observed behind the incident shock wave. Superimposed to this background absorption, the NCN absorbance profile indicates the thermal decomposition of NCN_3 followed by CIISC and ^3NCN formation. The decay at longer times can be attributed to reaction 11, $\text{NCN} + \text{NO}_2$.

In order to take into account NO_2 background absorption, temperature dependent NO_2 absorption cross sections at $\tilde{\nu} = 30383.11 \text{ cm}^{-1}$ had been measured, beforehand in experiments without NCN_3 . NO_2 absorption coefficients are best represented by the expression

$$\log_{10}(\sigma/\text{cm}^2\text{mol}^{-1}) = 5.28 - 1.21 \times 10^{-4} \times T/\text{K}$$

An extrapolation to room temperature yields a value of $1.8 \times 10^5 \text{ cm}^2/\text{mol}$, thus in very good agreement with a value of $1.9 \times 10^5 \text{ cm}^2/\text{mol}$ reported by Bogumil *et al.*⁴⁸ A plot of the measured cross sections can be found in the supplemental information. NO_2 concentration-time profiles were simulated based on the initial NO_2 concentrations and the reaction mechanism summarized in Table 2. Corresponding absorbance values are denoted “ NO_2 absorption” in Figs. 5 and 6. Remaining absorbances have been attributed to NCN absorption, which could be extracted from the profiles with high precision.

CIISC rate constants extracted from the resulting NCN concentration-time profiles are included in Fig. 2. The relaxation process mediated by collisions with NO_2 is less efficient than with NO , but still a factor of approximately 40 more efficient than with argon. After 100 μs , the ^3NCN formation is completed and a decay of the absorption can be observed in Fig. 5. The sensitivity analysis reveals that reaction 11 is the only important reaction for the consumption of NCN . In this regard, the experimental conditions are close to pseudo-first order conditions and thus enabled an accurate determination of k_{11} . However, at temperatures of $> 1400 \text{ K}$ more reactions gain importance. Such an experiment is shown in Fig. 6. The unimolecular decomposition of NO_2 , $\text{NO}_2 + \text{M} \rightarrow \text{NO} + \text{O} + \text{M}$ (20) sets in and thus the consecutive reaction $\text{NCN} + \text{O}$ (7) plays a role. This interfering secondary chemistry constitutes a high temperature limit for k_{11} measurements of about $T \approx 1700 \text{ K}$. Again, the low temperature limit was set by the decomposition rate of NCN_3 .

Measured rate constant values are compared to selected literature data in Fig. 7. All data points can be nicely represented by a straight Arrhenius fit, thus supporting the reliability of the applied evaluation procedure:

$$k_{11}/(\text{cm}^3\text{mol}^{-1}\text{s}^{-1}) = 4.7 \times 10^{12} \exp[-38.0 \text{ (kJ/mol)}/RT] \quad (\pm 19\%).$$

At temperatures $704 \text{ K} < T < 1659 \text{ K}$, the rate constants were found to be independent of the total density. The stated error results from a 5% uncertainty of the NO_2 concentration, a 7% statistical error (2σ), and 2% uncertainty attributable to the precursor molecule decomposition and the singlet cyanonitrene relaxation mechanism. Although uncertainties resulting from possible inaccuracies of the NO_2

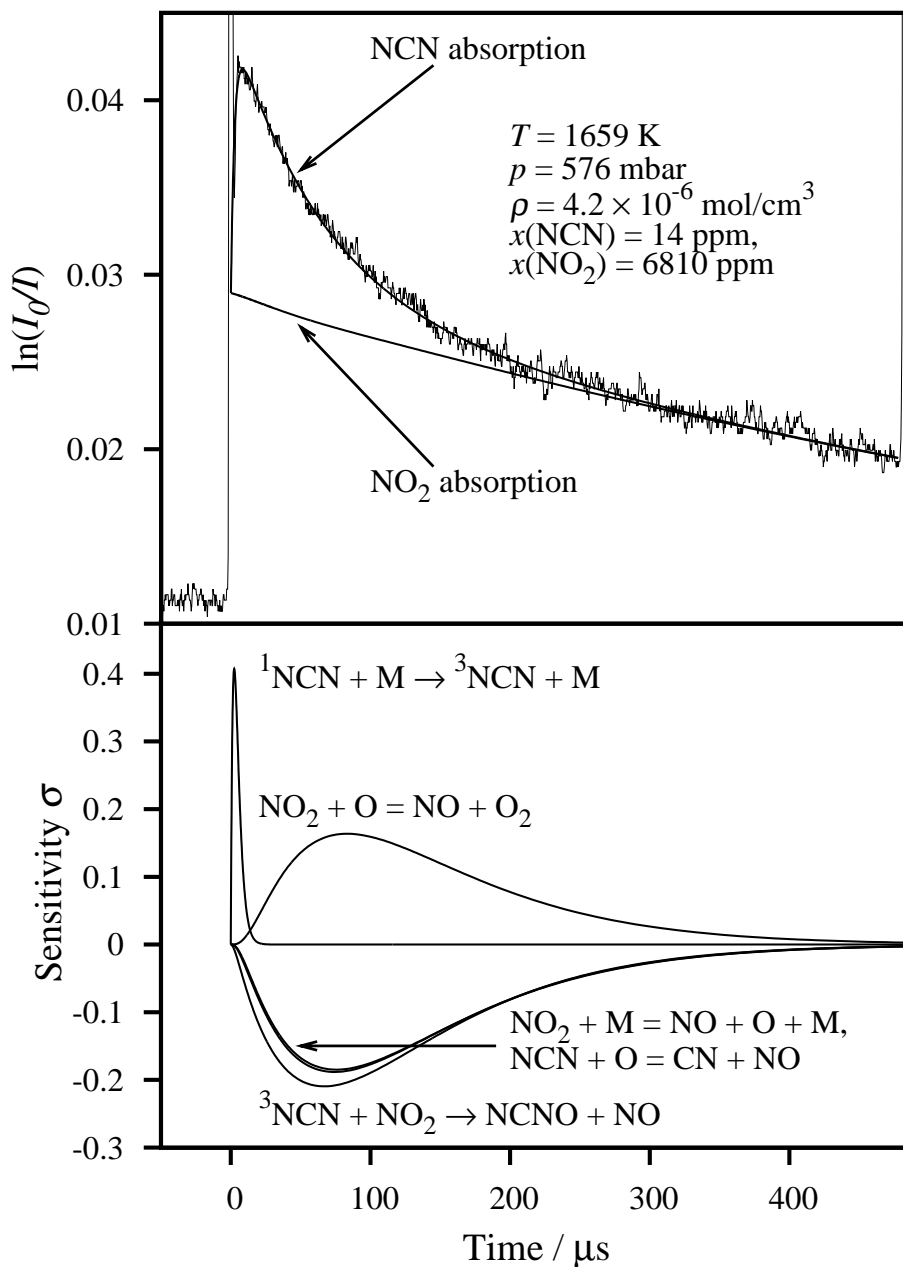


Figure 6: High temperature NO_2 experiment and corresponding NCN sensitivity analysis.

6. Rate Constants of the Reactions NCN + NO and NCN + NO₂

Table 2: Selected reactions of the mechanism used in the numerical simulations to extract the rate constants of the reaction NCN + NO₂. Possible secondary chemistry has been taken into account by the GRI-Mech. 3.0³⁹ and a subset of NCN and CN reactions as outlined in our previous paper.³⁴ Rate constants are given in terms of $k = A \exp[-E_a/RT]$. Units are cm, s, mol and kJ.

No.	Reaction	A	E_a	Ref.	
(7)	NCN + O \rightleftharpoons CN + NO	9.6×10^{13}	5.8	34	set equal for ¹ NCN and ³ NCN
(11)	NCN + NO ₂ \rightarrow NCNO + NO	4.7×10^{12}	38.0	this work	set equal for ¹ NCN and ³ NCN
(15)	NCN ₃ \rightarrow ¹ NCN + N ₂	5.0×10^9	71.2	43	$\rho = 3.5 \times 10^{-6}$ mol/cm ³
		7.7×10^9	71.2	43	$\rho = 7.0 \times 10^{-6}$ mol/cm ³
(16)	¹ NCN \rightarrow ³ NCN	2.3×10^6	30.1	this work	0.7% NO ₂ , $\rho = 3.5 \times 10^{-6}$ mol/cm ³
		1.7×10^6	24.8	this work	0.7% NO ₂ , $\rho = 7.0 \times 10^{-6}$ mol/cm ³
(20)	NO ₂ + M \rightleftharpoons NO + O + M	4.0×10^{15}	251	49	
(21)	NO ₂ + NO ₂ \rightleftharpoons 2 NO + O ₂	2.0×10^{12}	105	49	
(22)	NO ₂ + NO ₂ \rightleftharpoons NO ₃ + NO	1.0×10^{13}	108	49	
(23)	NO ₂ + O \rightleftharpoons NO + O ₂	3.9×10^{12}	-1	50	
(24)	NO ₃ + M \rightleftharpoons NO ₂ + O + M	4.0×10^{17}	200	49	
(25)	NO ₃ + O \rightleftharpoons NO ₂ + O ₂	1.0×10^{13}		50	

decomposition mechanism are only relevant at the high temperature limit, based on simulations with varied k_{20} , allowance was made for an additional 5% error for k_{11} . The Arrhenius activation energy is accurate to $\Delta E_a = \pm 3.8$ kJ/mol. This estimate already includes the potential uncertainty of the high temperature data points resulting from the NO₂ decomposition mechanism.

Selected results from the literature^{18,23,25} are also included in Fig. 7. At room temperature all results are in very good agreement, but toward higher temperatures differences become apparent. The rate constant data by Kappler²⁵ exhibit a significantly stronger temperature dependence than those measured by Yang *et al.*¹⁸ In both studies, rate constants have been determined assuming pseudo-first order conditions, thus excluding secondary chemistry. However, as Kappler already discussed in her work, the used excimer laser photolysis at $\lambda = 248$ nm next to NCN radicals also generates NO and O atoms from NO₂ photolysis, $\text{NO}_2 \xrightarrow{h\nu} \text{NO} + \text{O}$ (26). The possible overestimation of the determined rate constants due to the very fast subsequent reaction 7, NCN + O, was estimated by Kappler to be $< 5\%$. Yang *et al.* used 193 nm instead of 248 nm photolysis. At this wavelength, NO₂ absorption cross sections are much larger and O atom yields can be expected to be higher. Although Yang *et al.* argued that O atom formation did not interfere in their experiments due to subtle diffusion effects, the neglected O atom chemistry via reaction 7 may account for the differences and the data of Kappler can therefore be assumed to be more reliable. The dashed curves in Fig. 7 represent the theoretical fit of Yang *et al.* Clearly, a strong pressure dependence emerges. However, due to the mentioned effect,

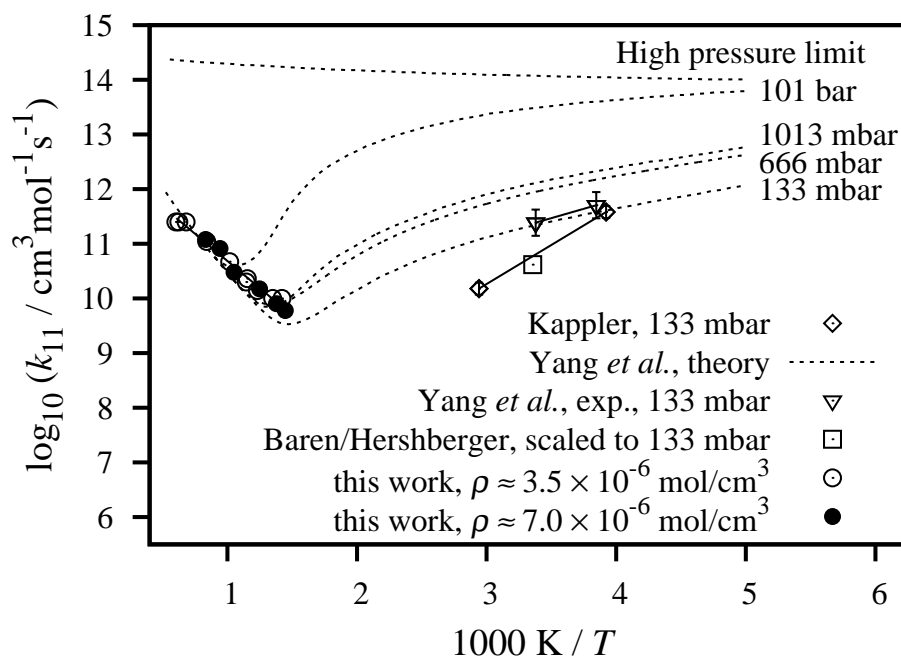


Figure 7: Arrhenius plot of the measured rate constants for the reaction $\text{NCN} + \text{NO}_2$ at two different total densities. For comparison, low temperature experimental data^{18,23,25} as well as theoretical predictions of Yang *et al.*¹⁸ are also shown. The original 4 mbar value of Baren and Hershberger²³ has been scaled to a pressure of 133 mbar based on the Troe parameters reported by Kappler.²⁵

the low temperature rate constants may be somewhat over predicted.

Our data represent the first high temperature measurements and can only be compared with the theoretical prediction of Yang *et al.*¹⁸ In agreement with their work and similar to the reaction $\text{NCN} + \text{NO}$, a positive temperature dependence is found at high temperatures. Note that for the temperature and pressure range of this work ($182 \text{ mbar} < p < 654 \text{ mbar}$), the overall reaction is predicted to be almost independent of the experimental pressure. The predicted absolute values of k_{11} and the absence of pressure dependence is in very good agreement with our data. Only at the lowest experimental temperatures, deviations of about a factor of two are observed. These remaining discrepancies can be easily explained by a slightly over predicted temperature dependence. Unfortunately, the expected inversion of the temperature dependence could not be observed in the experiments. Obviously, at pressures below $p < 1 \text{ bar}$ the rate constant minimum arise at temperatures $T < 700 \text{ K}$. Combining the low temperature data of Kappler and the high temperature rate constants determined in this work, a rough estimate of $T \approx 500 \text{ K}$ can be made for $p = 133 \text{ mbar}$, hence $\approx 150 \text{ K}$ lower than calculated by Yang *et al.*

The switch from a negative to a positive temperature dependence can be explained by the competition of an association and an abstraction reaction mechanism. The dominating reaction channels of the

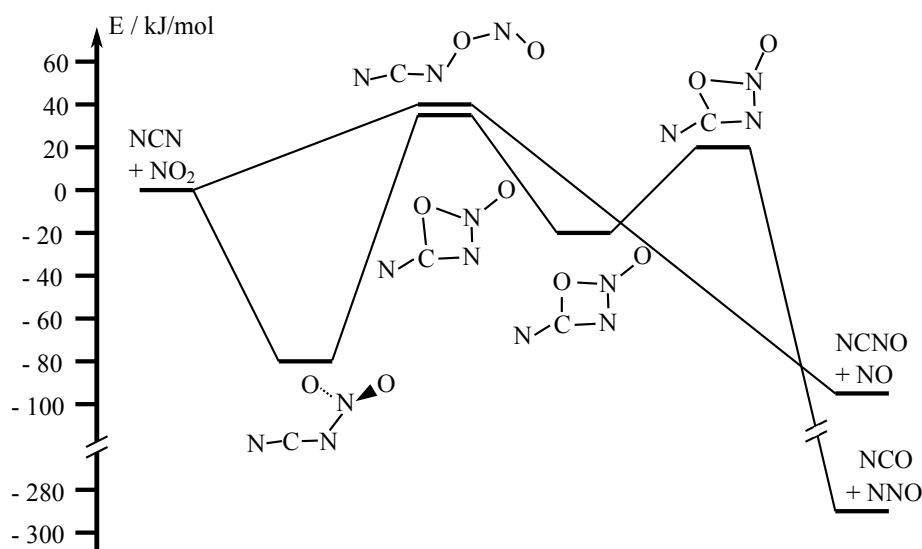


Figure 8: Part of the potential energy surface of the reaction $\text{NCN} + \text{NO}_2$ (11) (G2M//B3LYP/6-311+G(d) level of theory), adopted from Yang *et al.*¹⁸

potential energy surface as it has been explored by Yang *et al.*¹⁸ are reproduced in Fig. 8. Additional reaction channels leading to $\text{CNO} + \text{N}_2\text{O}$ or $\text{CN} + \text{N}_2\text{O}_2$ do not play a role due to very high associated barriers.

As for the reaction $\text{NCN} + \text{NO}$, at low temperatures the reaction is a typical example of an association reaction forming the collisionally stabilized recombination product NCNNO_2 . The sequential transition state lies energetically too high, (116 kJ/mol above the minimum, 34 kJ/mol above the entrance energy) such that the thermodynamically most stable products NCO and N_2O are not formed. At high temperatures, with a threshold energy of $E_0 = 41$ kJ/mol, a direct abstraction reaction channel becomes accessible. Here, an O atom is abstracted from NO_2 yielding the high temperature reaction products NCNO and NO . According to Yang *et al.*, even at high temperatures the contribution of the reaction channel forming $\text{NCO} + \text{N}_2\text{O}$ remains negligible. Corresponding rate constants are predicted to be several orders of magnitude lower than for the $\text{NCNO} + \text{NO}$ channel.

The positive temperature dependence of the overall reaction, which has been determined in this work, supports the proposed reaction mechanism. The measured Arrhenius activation energy of $E_a = 38.0$ kJ/mol is in close agreement with the calculated threshold energy of $E_0 = 41$ kJ/mol corresponding to the direct $\text{NCNO} + \text{NO}$ abstraction channel.

6.4 Conclusion

For the first time, high temperature rate constants of the reactions $\text{NCN} + \text{NO} \rightarrow \text{N}_2\text{O} + \text{CN}$ (10) and $\text{NCN} + \text{NO}_2 \rightarrow \text{NCNO} + \text{NO}$ (11) have been measured. For reaction 10, rate constants are represented by the Arrhenius expression $k_{10}/(\text{cm}^3\text{mol}^{-1}\text{s}^{-1}) = 1.9 \times 10^{12} \exp[-26.3 (\text{kJ/mol})/RT]$ in the temperature range $764 \text{ K} < T < 1944 \text{ K}$. The experimentally accessible temperature range was limited by the decomposition rate of the NCN precursor NCN_3 at the lower bound and too small NCN absorption cross sections at high temperatures. Regarding reaction 11, the expression $k_{11}/(\text{cm}^3\text{mol}^{-1}\text{s}^{-1}) = 4.7 \times 10^{12} \exp[-38.0 (\text{kJ/mol})/RT]$ accounts for the measured data points in the temperature range $691 \text{ K} < T < 1659 \text{ K}$. Here, the temperature range was limited by the onset of the NO_2 decomposition and interfering secondary chemistry. In striking contrast to previous low temperature studies, at high temperatures no pressure but a pronounced positive temperature dependence has been determined. For reaction 10, $E_a = (26.3 \pm 1.6) \text{ kJ/mol}$ and for reaction 11 $E_a = (38.0 \pm 3.8) \text{ kJ/mol}$. These values are in agreement with theoretical predictions and prove the postulated change of the overall reaction from a recombination to an abstraction-like pathway. Together with the low temperature data taken from the literature, the position of the minimum of the overall reaction rate constant has been estimated to be around $T \approx 670 \text{ K}$ for reaction 10 and $T \approx 500 \text{ K}$ for reaction 11. Additionally, the influence of NO and NO_2 on the CIISC process, which transfers electronically excited ^1NCN to the ^3NCN ground state, has been investigated. With respect to CIISC probability, NO and NO_2 are 400 and 40 times more efficient collision partners than argon, respectively.

Acknowledgment

We would like to thank the German Science Foundation (FR 1529/4), the cluster of excellence "The Future Ocean" (DFG - EC 80), and Friedrich Temps for financial and scientific support. Thanks to Anna Busch, Claudia Kappler, Matthias Olzmann, and Oliver Welz (Karlsruher Institut für Technologie, KIT) for sharing data prior to publication.

Bibliography

- [1] J. Warnatz, U. Maas, and R. W. Dibble, *Combustion*, Springer, Berlin/Heidelberg, 3. edition, **2001**.
- [2] R. M. Harrison, editor, *Principles of Environmental Chemistry*, RSC Publishing, Cambridge, **2007**.
- [3] P. Forster, V. Ramaswamy, P. Artaxo, T. Berntsen, R. Betts, D. Fahey, J. Haywood, J. Lean,

- D. Lowe, G. Myhre, J. Nganga, R. Prinn, G. Raga, M. Schulz, and R. V. Dorland, Changes in Atmospheric Constituents and in Radiative Forcing, in S. Solomon, D. Qin, M. Manning, Z. Chen, M. M. K. Averyt, M. Tignor, and H. Miller, editors, *Climate Change 2007: The Physical Science Basis. Contribution of Working Group I to the Fourth Assessment Report of the Intergovernmental Panel on Climate Change*, chapter 2, Cambridge University Press, Cambridge, United Kingdom, **2007**.
- [4] P. Glarborg, M. U. Alzueta, K. Dam-Johansen, and J. A. Miller, Kinetic Modeling of Hydrocarbon/Nitric Oxide Interactions in a Flow Reactor, *Combust. Flame* **1998**, *115*, 1–27.
- [5] Y. B. Zeldovich, The Oxidation of Nitrogen in Combustion and Explosions, *Acta Physicochim. USSR* **1946**, *21*, 577–628.
- [6] D. L. Baulch, C. J. Cobos, A. M. Cox, P. Frank, G. Hayman, Th. Just, J. A. Kerr, T. Murrels, M. J. Pilling, J. Troe, R. W. Walker, and J. Warnatz, Evaluated Kinetic Data for Combustion Modelling Supplement I, *Int. J. Phys. Chem. Ref. Data* **1994**, *23*, 847–1033.
- [7] J. Wolfrum, Bildung von Stickstoffoxiden bei der Verbrennung, *Chemieingenieurtechnik* **1972**, *44*, 656–659.
- [8] P. C. Malte and D. T. Pratt, Measurement of Atomic Oxygen and Nitrogen Oxides in Jet-Stirred Combustion, *Proc. Comb. Inst.* **1974**, *15*, 1061.
- [9] C. P. Fenimore, Formation of Nitric Oxide in Premixed Hydrocarbon Flames, *Proc. Combust. Inst.* **1971**, *13*, 373–380.
- [10] Q. Cui, K. Morokuma, J. M. Bowman, and S. J. Klippenstein, The Spin-Forbidden Reaction $\text{CH}({}^2\Pi) + \text{N}_2 \rightarrow \text{HCN} + \text{N}({}^4\text{S})$ Revisited. II. Nonadiabatic Transition State Theory and Application, *J. Chem. Phys.* **1999**, *110*, 9469–9482.
- [11] L. V. Moskaleva and M. C. Lin, The Spin-Conserved Reaction $\text{CH} + \text{N}_2 \rightarrow \text{H} + \text{NCN}$: A Major Pathway to Prompt NO Studied by Quantum/Statistical Theory Calculations and Kinetic Modeling of Rate Constant, *Proc. Combust. Inst.* **2000**, *28*, 2393–2401.
- [12] L. V. Moskaleva, W. S. Xia, and M. C. Lin, The $\text{CH} + \text{N}_2$ Reaction Over the Ground Electronic Doublet Potential Energy Surface: A Detailed Transition State Search, *Chem. Phys. Lett.* **2000**, *331*, 269–277.
- [13] G. P. Smith, Evidence of NCN as a Flame Intermediate for Prompt NO, *Chem. Phys. Lett.* **2003**, *367*, 541–548.
- [14] J. A. Sutton, B. A. Williams, and J. W. Fleming, Laser-Induced Fluorescence Measurements of NCN in Low-Pressure $\text{CH}_4/\text{O}_2/\text{N}_2$ Flames and Its Role in Prompt NO Formation, *Combust. Flame* **2008**, *153*, 465–478.

- [15] R. J. H. Klein-Douwel, N. J. Dam, and J. J. ter Meulen, Laser-Induced Fluorescence of NCN in Low and Atmospheric Pressure Flames, *Optics Lett.* **2008**, *33*, 2620–2622.
- [16] V. Vasudevan, R. K. Hanson, C. T. Bowman, D. M. Golden, and D. F. Davidson, Shock Tube Study of the Reaction of CH with N_2 : Overall Rate and Branching Ratio, *J. Phys. Chem. A* **2007**, *111*, 11818–11830.
- [17] C.-L. Huang, S. Y. Tseng, T. Y. Wang, N. S. Wang, Z. F. Xu, and M. C. Lin, Reaction Mechanism and Kinetics of the $\text{NCN} + \text{NO}$ Reaction: Comparison of Theory and Experiment, *J. Chem. Phys.* **2005**, *122*, 184321.
- [18] T.-J. Yang, N. S. Wang, L. C. Lee, Z. F. Xu, and M. C. Lin, Kinetics and Mechanism of the $\text{NCN} + \text{NO}_2$ Reaction Studied by Experiment and Theory, *J. Phys. Chem. A* **2008**, *112*, 10185–10192.
- [19] H.-T. Chen and J.-J. Ho, Theoretical Investigation of the Mechanisms of Reaction of NCN with NO and NS, *J. Phys. Chem. A* **2005**, *109*, 2564–2571.
- [20] R. S. Zhu and M. C. Lin, Ab Initio Study on the Oxidation of NCN by O_2 , *Int. J. Chem. Kinet.* **2005**, *37*, 593–598.
- [21] R. S. Zhu and M. C. Lin, Ab Initio Study on the Oxidation of NCN by $\text{O}(^3\text{P})$: Prediction of the Total Rate Constant and Product Branching Ratios, *J. Phys. Chem. A* **2007**, *111*, 6766–6771.
- [22] R. S. Zhu, M. T. Nguyen, and M. C. Lin, Ab Initio Study on the Oxidation of NCN by OH: Prediction of the Individual and Total Rate Constants, *J. Phys. Chem. A* **2009**, *113*, 298–304.
- [23] R. E. Baren and J. F. Hershberger, Kinetics of the NCN Radical, *J. Phys. Chem. A* **2002**, *106*, 11093–11097.
- [24] O. Welz, *Laserspektroskopische Untersuchungen und molekularkinetische Modellierung der Kinetik von Radikalreaktionen in der Gasphase*, Ph.D. thesis, Universität Karlsruhe (TH), **2009**.
- [25] C. Kappler, *Untersuchungen komplexbildender bimolekularer Reaktionen in der Gasphase mit laserspektroskopischen Methoden und statistischer Reaktionstheorie*, Ph.D. thesis, Karlsruher Institut für Technologie, **2010**.
- [26] N. Lamoureux, P. Desgroux, A. El Bakali, and J. F. Pauwels, Experimental and Numerical Study of the Role of NCN in Prompt-NO Formation in Low-Pressure $\text{CH}_4\text{-O}_2\text{-N}_2$ and $\text{C}_2\text{H}_2\text{-O}_2\text{-N}_2$ Flames, *Combust. Flame* **2010**, *157*, 1923–1941.
- [27] A. El Bakali, L. Pillier, P. Desgroux, B. Lefort, L. Gasnot, J. F. Pauwels, and I. da Costa, NO Prediction in Natural Gas Flames Using GDF-Kin 3.0 Mechanism. NCN and HCN Contribution to Prompt-NO Formation, *Fuel* **2006**, *85*, 896–909.

- [28] S. Gersen, A. V. Mokhov, and H. B. Levinsky, Diode Laser Absorption Measurement and Analysis of HCN in Atmospheric-Pressure, Fuel-Rich Premixed Methane/Air Flames, *Combust. Flame* **2008**, *155*, 267–276.
- [29] A. A. Konnov, Implementation of the NCN Pathway of Prompt-NO Formation in the Detailed Reaction Mechanism, *Combust. Flame* **2009**, *156*, 2093–2105.
- [30] A. V. Sepman, A. V. Mokhov, and H. B. Levinsky, The Effects of Hydrogen Addition on NO Formation in Atmospheric-Pressure, Fuel-Rich-Premixed, Burner-Stabilized Methane, Ethane and Propane Flames, *Int. J. Hydrogen Energ.* **2011**, *36*, 4474–4481.
- [31] A. Busch and M. Olzmann, Shock-Tube Study of the Thermal Decomposition of NCN, Vienna, paper p810138, Proc. European Combust. Meeting, **2009**.
- [32] A. Busch, *Stoßwellenuntersuchungen zum Zerfall stickstoffhaltiger Verbindungen mit spektroskopischen Methoden*, Ph.D. thesis, Karlsruher Institut für Technologie, **2010**.
- [33] J. Dammeier and G. Friedrichs, Thermal Decomposition of NCN_3 as a High-Temperature NCN Radical Source: Singlet-Triplet Relaxation and Absorption Cross Section of $\text{NCN}(^3\Sigma)$, *J. Phys. Chem. A* **2010**, *114*, 12963–12971.
- [34] J. Dammeier, N. Faßheber, and G. Friedrichs, Direct Measurements of the High Temperature Rate Constants of the Reactions $\text{NCN} + \text{O}$, $\text{NCN} + \text{NCN}$, and $\text{NCN} + \text{M}$, *Phys. Chem. Chem. Phys.* **2011**, DOI: 10.1039/C1CP22123J.
- [35] J. Dammeier, M. Colberg, and G. Friedrichs, Wide temperature range ($T = 295 \text{ K}$ and $770 - 1305 \text{ K}$) study of the kinetics of the reactions $\text{HCO} + \text{NO}$ and $\text{HCO} + \text{NO}_2$ using frequency modulation spectroscopy, *Phys. Chem. Chem. Phys.* **2007**, *9*, 41774188.
- [36] M. Colberg and G. Friedrichs, Room Temperature and Shock Tube Study of the Reaction $\text{HCO} + \text{O}_2$ Using the Photolysis of Glyoxal as an Efficient HCO Source, *J. Phys. Chem A* **2006**, *110*, 160–170.
- [37] M. Klatt, *Quantitative Untersuchung der Bildung und des Verbrauchs von H- und O-Atomen sowie OH-Radikalen in verschiedenen Elementarreaktionen bei hohen Temperaturen.*, Ph.D. thesis, Universität Göttingen, **1991**.
- [38] R. J. Kee, F. M. Ruply, and J. A. Miller, Chemkin-II: A Fortran Chemical Kinetics Package for the Analysis of Gas Phase Chemical Kinetics, Sandia report sand89-8009, Sandia National Laboratories, Livermore, CA, **1989**.
- [39] G. P. Smith, D. M. Golden, M. Frenklach, N. W. Moriarty, B. Eiteneer, M. Goldenberg, C. T. Bowman, R. K. Hanson, S. Song, W. C. G. Jr., V. V. Lissanski, and Z. Qin, GRI-MECH 3.0, http://www.me.berkeley.edu/gri_mech/.

- [40] A. A. Konnov, Detailed Reaction Mechanisms for Small Hydrocarbon Combustion, http://homepages.vub.ac.be/akonnov/science/mechanism/version0_5.html, **2007**, release 0.5.
- [41] E. Goos, A. Burcat, and B. Ruscic, Ideal Gas Thermochemical Database with Updates from Active Thermochemical Tables, <ftp://ftp.technion.ac.il/pub/supported/aetdd/thermodynamics>, **2010**.
- [42] D. E. Milligan, M. E. Jacox, and A. M. Bass, Matrix-Isolation Study of the Photolysis of Cyanogen Azide. The Infrared and Ultraviolet Spectra of the Free Radical NCN, *J. Chem. Phys.* **1965**, *43*, 3149–3160.
- [43] J. Dammeier, B. Oden, and G. Friedrichs, A Consistent Model for the Thermal Decomposition of NCN_3 and the Singlet-Triplet Relaxation of NCN, *Int. J. Chem. Kinet.* **2011**, submitted.
- [44] K. F. Freed, Collision-Induced Intersystem Crossing, *Adv. Chem. Phys.* **1981**, *47*, 291–336.
- [45] U. Bley and F. Temps, Collision-Induced Intersystem Crossing for CH_2 from \tilde{a}^1A_1 to \tilde{X}^3B_1 : A Case Study of the Mixed State Model, *J. Chem. Phys.* **1993**, *98*, 1058–1072.
- [46] M. W. Slack, Kinetics and Thermodynamics of the CN Molecule. III. Shock Tube Measurements of CN Dissociation Rates, *J. Chem. Phys.* **1975**, *64*, 228–236.
- [47] A. Delon, R. Georges, B. Kirmse, and R. Jost, Fourier-Transform Analysis of the NO_2 Spectrum, *Faraday Discuss.* **1995**, *102*, 117–128.
- [48] K. Bogumil, J. Orphal, T. Homann, S. Voigt, P. Spietz, O. Fleischmann, A. Vogel, M. Hartmann, H. Kromminga, H. Bovensmann, J. Frerick, and J. Burrows, Measurements of Molecular Absorption Spectra with the SCIAMACHY Pre-Flight Model: Instrument Characterization and Reference Data for Atmospheric Remote-Sensing in the 2302380 nm Region, *J. Photochem. Photobiol. A* **2003**, *157*, 167–184.
- [49] M. Röhrig, E. L. Petersen, D. F. Davidson, and R. K. Hanson, The Pressure Dependence of the Thermal Decomposition of N_2O , *Int. J. Chem. Kinet.* **1996**, *28*, 599–608.
- [50] R. Atkinson, D. L. Baulch, R. A. Cox, R. F. Hampson, J. A. Kerr, and J. Troe, Evaluated Photochemical Data for Atmospheric Chemistry: Supplement III, *J. Phys. Chem. Ref. Data* **1989**, *18*, 881–1108.

6.5 Supporting information

Table 1: Experimental conditions and results of measurements of the kinetics of the reaction NCN + NO.

T/K	p/mbar	$\rho/\text{mol}/\text{cm}^3$	$x(\text{NCN})/\text{ppm}$	$x(\text{NO})/\text{ppm}$	k_{16}/s^{-1}	$k_{10}/\text{cm}^3/\text{mol s}$
$\rho \approx 1.8 \times 10^{-6} \text{ mol}/\text{cm}^3$						
865	123	1.71×10^{-6}	12.6	9853	1.0×10^5	4.6×10^{10}
888	127	1.73×10^{-6}	13.8	9765	1.0×10^5	5.5×10^{10}
894	130	1.74×10^{-6}	12.8	9853	1.1×10^5	5.8×10^{10}
969	145	1.81×10^{-6}	14.0	9765	1.3×10^5	7.0×10^{10}
996	149	1.80×10^{-6}	13.4	9765	1.2×10^5	8.5×10^{10}
1128	176	1.88×10^{-6}	13.3	9853	1.7×10^5	1.2×10^{11}
1249	202	1.95×10^{-6}	13.7	9853	2.0×10^5	1.5×10^{11}
1527	258	2.03×10^{-6}	14.0	9853	2.5×10^5	2.5×10^{11}
1861	329	2.13×10^{-6}	15.0	9853	-	4.2×10^{11}
$\rho \approx 3.5 \times 10^{-6} \text{ mol}/\text{cm}^3$						
760	203	3.22×10^{-6}	5.2	5222	8.0×10^4	2.5×10^{10}
764	204	3.22×10^{-6}	12.6	9853	1.1×10^5	3.2×10^{10}
826	229	3.34×10^{-6}	12.7	9853	1.7×10^5	4.3×10^{10}
867	246	3.41×10^{-6}	6.3	10398	2.0×10^5	4.8×10^{10}
875	250	3.43×10^{-6}	5.0	5222	1.2×10^5	5.0×10^{10}
938	277	3.55×10^{-6}	5.8	10398	2.4×10^5	7.0×10^{10}
986	295	3.60×10^{-6}	5.8	10398	2.9×10^5	7.5×10^{10}
1196	380	3.82×10^{-6}	5.9	10398	4.0×10^5	1.2×10^{11}
1485	501	4.06×10^{-6}	5.3	10002	-	1.8×10^{11}
1547	525	4.09×10^{-6}	6.0	5222	-	2.2×10^{11}
1944	690	4.27×10^{-6}	5.6	10002	-	4.0×10^{11}

Table 2: Experimental conditions and results of measurements of the reaction NCN + NO₂.

T/K	p/mbar	$\rho/\text{mol}/\text{cm}^3$	$x(\text{NCN})/\text{ppm}$	$x(\text{NO}_2)/\text{ppm}$	k_{16}/s^{-1}	$k_{11}/\text{cm}^3/\text{mol s}$
704	182	3.10×10^{-6}	12.7	7143	1.3×10^4	1.0×10^{10}
741	197	3.20×10^{-6}	12.8	7143	1.8×10^4	1.0×10^{10}
812	226	3.34×10^{-6}	13.5	7143	2.8×10^4	1.4×10^{10}
866	247	3.43×10^{-6}	12.4	6807	3.5×10^4	2.3×10^{10}
873	250	3.44×10^{-6}	13.3	7143	3.5×10^4	2.0×10^{10}
983	295	3.62×10^{-6}	14.0	6807	5.8×10^4	4.7×10^{10}
1191	381	3.85×10^{-6}	13.8	6807	1.1×10^5	1.1×10^{11}
1467	494	4.05×10^{-6}	13.8	6807	2.5×10^5	2.5×10^{11}
1600	550	4.14×10^{-6}	14.0	6807	4.0×10^5	2.5×10^{11}
1659	576	4.17×10^{-6}	14.1	6807	4.0×10^5	2.5×10^{11}
$\rho \approx 7.0 \times 10^{-6} \text{ mol}/\text{cm}^3$						
691	358	6.23×10^{-6}	3.8	18709	2.0×10^4	6.0×10^9
726	381	6.31×10^{-6}	3.2	6985	3.0×10^4	8.0×10^9
801	442	6.64×10^{-6}	3.1	6985	4.5×10^4	1.5×10^{10}
952	566	7.15×10^{-6}	3.6	6985	6.5×10^4	3.0×10^{10}

6. Rate Constants of the Reactions $\text{NCN} + \text{NO}$ and $\text{NCN} + \text{NO}_2$

Table 2, continued:

T/K	p/mbar	$\rho/\text{mol}/\text{cm}^3$	$x(\text{NCN})/\text{ppm}$	$x(\text{NO}_2)/\text{ppm}$	k_{16}/s^{-1}	$k_{11}/\text{cm}^3/\text{mol s}$
1060	654	7.43×10^{-6}	3.2	6985	1.0×10^5	8.2×10^{10}
1202	764	7.64×10^{-6}	3.8	6990	1.0×10^5	1.2×10^{11}

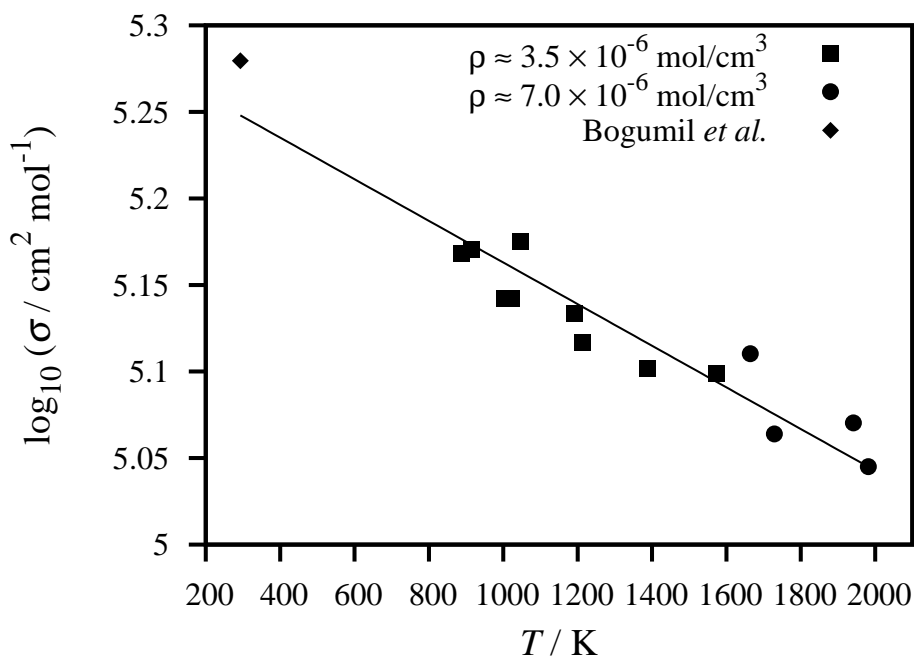


Figure 1: Temperature dependent NO_2 absorption cross sections and comparison to room temperature value reported by Bogumil *et al.*⁴⁸

7 Wide Temperature Range ($T = 295$ K and 770-1305 K) Study of the Kinetics of the Reactions $\text{HCO} + \text{NO}$ and $\text{HCO} + \text{NO}_2$ using Frequency Modulation Spectroscopy

Johannes Dammeier, Mark Colberg and Gernot Friedrichs*

Institut für Physikalische Chemie,
Christian-Albrechts-Universität zu Kiel

Phys. Chem. Chem. Phys. **2007**, 9, 4177 – 4188. - Reproduced by permission of the PCCP Owner Societies.
<http://dx.doi.org/10.1039/B704197G>.

Own contributions to this paper:

Prior to dissertation:

- Shock tube measurements of $(\text{CHO})_2/\text{NO}$ and $(\text{CHO})_2/\text{NO}_2$ mixtures using FM detection of HCO, together with Mark Colberg
- Room temperature measurements of $(\text{CHO})_2/\text{NO}$ mixtures
- Data analysis

During dissertation:

- Room temperature measurements of $(\text{CHO})_2/\text{NO}_2$ mixtures
- Re-evaluation of all high temperature and room temperature NO_2 measurements to extract product branching ratios

*friedrichs@phc.uni-kiel.de

Abstract

The rate constants for reaction (1), $\text{HCO} + \text{NO} \rightarrow \text{HNO} + \text{CO}$, and reaction (2), $\text{HCO} + \text{NO}_2 \rightarrow \text{products}$, have been measured at temperatures between $770 \text{ K} < T < 1305 \text{ K}$ behind reflected shock waves and, for the purpose of a consistency check, in a slow flow reactor at room temperature. HCO radicals were generated by 193 nm excimer laser photolysis of diluted gas mixtures containing glyoxal, $(\text{CHO})_2$, and NO or NO₂ in argon and were monitored using frequency modulation (FM) absorption spectroscopy. Kinetic simulations based on a comprehensive reaction mechanism showed that the rate constants for the title reactions could be sensitively extracted from the measured HCO profiles. The determined high temperature rate constants are $k_1(295 \text{ K}) = (8.1 \pm 0.2) \times 10^{12} \text{ cm}^3 \text{ mol}^{-1} \text{ s}^{-1}$, $k_1(769-1307 \text{ K}) = (7.1 \pm 2.7) \times 10^{12} \text{ cm}^3 \text{ mol}^{-1} \text{ s}^{-1}$ and $k_2(804-1186 \text{ K}) = (3.3 \pm 1.8) \times 10^{13} \text{ cm}^3 \text{ mol}^{-1} \text{ s}^{-1}$. The room temperature values were found to be in very good agreement with existing literature data and show that both reactions are essentially temperature independent. The weak temperature dependence of reaction (1) can be explained by the interplay of a dominating direct abstraction pathway and a complex-forming mechanism. Both pathways yield the products HNO + CO. In contrast to reaction (1), no evidence for a significant contribution of a direct high temperature abstraction channel was found for reaction (2). Here, the observed temperature independent overall rate constant can be described by a complex-forming mechanism with several product channels. Detailed information on the strongly temperature dependent channel branching ratios is provided. Moreover, the high temperature rate constant of reaction (7), $\text{OH} + (\text{CHO})_2$, has been determined to be $k_7 \approx 1.1 \times 10^{13} \text{ cm}^3 \text{ mol}^{-1} \text{ s}^{-1}$.

7.1 Introduction

The formyl radical, HCO, is a key intermediate for the mechanistic description of combustion processes. HCO lies on the main oxidation pathway of hydrocarbons and is mainly formed by the reactions of O, OH, H, and CH₃ with formaldehyde. The most important HCO removal reactions are its thermal decomposition and several other bimolecular reactions, e.g. with H, OH, and O₂. In spite of the importance of HCO reactions, large uncertainties exist in high temperature rate data for oxidation and NO_x reactions of HCO. Most direct determinations of high temperature rate constants ($T > 1000 \text{ K}$) rely on measurements behind shock waves, because of the unique potential of the shock tube method to provide well defined high temperature reaction conditions.¹ Detecting HCO behind shock waves is difficult due to the high reactivity and thermal instability of HCO, which causes its lifetime to be short and the observable concentrations to be low. Quite recently, using the very sensitive absorption based frequency modulation (FM) spectroscopy, the detection of HCO behind shock

waves became feasible.² In combination with efficient HCO generation by UV photolysis of suitable precursor molecules such as formaldehyde (CH₂O) or glyoxal ((CHO)₂), the uncertainty range of several important HCO reaction rate constants, e.g. H + HCO, HCO + M, and HCO + O₂, could be considerably narrowed.²⁻⁴ Moreover, sensitive absorption measurements of OH, CH₂O, and (CHO)₂ behind shock waves were performed in order to characterise several HCO forming reactions, e.g. H + CH₂O,⁵ H + (CHO)₂,⁴ CH₂O + M,^{3,6} CH₂O + O₂,⁶ and OH + CH₂O.⁷ As a result of these studies, consistent mechanisms were developed that allow one to quantitatively model formaldehyde pyrolysis/photolysis³ and glyoxal photolysis⁴ behind shock waves.

The quantitative modelling of NO_x formation and control in combustion processes is a long-standing challenge for combustion research. Several well-known NO_x formation pathways have been established⁸⁻¹³ that enable reliable predictions of NO_x levels over a wide range of experimental temperatures and pressures. The rate constants of the title reactions



which are especially important in the post flame region,¹⁴ have to be known in order to model the overall NO_x production. Until now, direct measurements of the rate constants are limited to temperatures $T < 623$ K for reaction (1) and $T < 713$ K for reaction (2).^{15,16}

According to theoretical studies, which will be discussed in more detail in this paper below, the rate constants of both reactions are expected to be more or less temperature independent up to temperatures of $T = 1000$ K, but the proposed mechanisms are quite different. Xu et al.¹⁷ treated the overall rate of reaction (1) as a competition of a quasi-direct abstraction channel and a pressure dependent association-fragmentation mechanism. Both pathways yield the products HNO + CO. They concluded that even at room temperature the reaction is dominated by the abstraction process that proceeds through a loose hydrogen-bonding molecular complex with only 12 kJ/mol binding energy and a very small decomposition barrier (8 kJ/mol). In contrast to reaction (1), *ab initio*/RRKM computations of Guo et al.¹⁸ showed that a temperature independent overall rate constant for reaction (2) is consistent with an association-fragmentation mechanism exhibiting several feasible product channels with strongly temperature dependent channel branching ratios. A possible contribution of a direct abstraction pathway with the products HONO + CO, which should gain importance at increasingly high temperatures, was not addressed. Experimental high temperature rate data for both reactions are needed to improve the reliability of rate constant extrapolations to combustion relevant temperatures. Furthermore, these data can serve as a critical test of the theoretical predictions, i.e. (i) a dominant abstraction channel in case of reaction (1) and (ii) a negligible contribution of a direct abstraction channel even at high temperatures in case of reaction (2).

In this work, the 193 nm laser photolysis of glyoxal was used as an efficient high temperature HCO

source. The observed HCO concentration-time profiles were described by a comprehensive mechanism based on a our previous study on glyoxal photolysis.⁴ Subsequently, the high temperature and, for the purpose of a consistency check with previous low temperature studies, also the room temperature rate constants of the title reactions have been measured by a perturbation approach. Observed differences between HCO profiles measured with and without NO/NO₂ added to the reaction mixtures could be attributed almost exclusively to reaction (1) and reaction (2), respectively.

7.2 Experimental section

7.2.1 Shock tube and slow flow reactor

High temperature experiments were carried out in an electro-polished stainless steel shock tube.^{4,19} The 4.4 m long test section with an inner diameter of 81 mm could be evacuated by a combination of a turbomolecular drag pump and an oil free diaphragm pump down to pressures of $p \approx 10^{-7}$ mbar. The shock tube was pressure driven with hydrogen or hydrogen/nitrogen mixtures as driver gases using 30 μm thick aluminium diaphragms. Experimental temperature, pressure and density behind the reflected shock waves were obtained from the initial conditions of the test gas and the shock wave velocity. The shock wave velocity was measured by a fast count unit wired to four fast piezoelectric sensors (PCB Piezotronics M113A21) mounted flush to the tube wall at distances of 400 mm each. Typically, a slight damping of the shock wave of $\sim 1.5\%$ per meter was registered. In order to monitor the experimental pressure profiles, at a distance of 19 mm from the end plate, a fifth piezo sensor (Kistler type 603B) was installed together with two optical ports. Shock wave parameters were calculated from a 1-dimensional, frozen chemistry code taking into account real gas effects. A small independent correction has been applied to allow for boundary layer effects.^{4,20,21} Typically, these corrections yielded 1% higher temperatures and 2% higher pressures compared to the ideal shock tube code.

Experiments at $T = 295$ K were performed in a slow flow reactor of 45 cm length.²² Two quartz windows mounted at Brewster's angle at both ends of the flow cell served as entrance and exit ports for the detection and photolysis laser beams.

An ArF excimer laser (Radiant Dyes Exc 200 or Lambda Physik Compex 102) was used for the UV photolysis of the reaction mixtures at a wavelength of $\lambda = 193$ nm. The excimer and the dye laser beams were combined and divided by the use of two dichroic mirrors in front of and behind the shock tube (side-on photolysis) or flow cell. In the shock tube experiments, the photolysis laser beam was slightly focussed by a lens to compensate for intensity loss by absorption of glyoxal. In this way, a uniform radical yield across the shock tube was achieved.⁴ Moreover, the diameter of the photolysis laser (8 mm) was set much larger than the diameter of the detection laser (1.5 mm) in order to ensure

negligible radial diffusion effects.

7.2.2 Gas mixtures

Gas mixtures were prepared using a gas mixing system consisting of a 24 liter stainless steel tank for the storage of glyoxal/argon mixtures, a 5 liter glass flask for the storage and purification of NO and NO₂, and a 20 liter glass flask for the storage of NO/argon and NO₂/argon mixtures. The whole system could be evacuated by a combination of turbomolecular drag and diaphragm pump to pressures as low as $p \approx 10^{-6}$ mbar. Gas mixtures of typically 1-2% glyoxal in argon and 1-2% NO/NO₂ in argon were prepared by the partial pressure method and were used within 3 days after preparation. No noticeable change in the experimental HCO signals was discernible with increasing reaction mixture age. A flow system with calibrated mass flow controllers was used to prepare the final test gas mixtures, which were slowly pumped through the shock tube for 2 minutes to eliminate any wall adsorption effects.

Gases and chemicals used were Ar (99.999%), N₂/H₂ (99.99%, as driver gas), NO (99.95%), and NO₂ (99.95%). Both NO and NO₂ were purified before mixture preparation by repeated fractional distillation and several freeze-pump-thaw cycles. For a quantitative preparation of NO₂ gas mixtures, the N₂O₄/NO₂ equilibrium was taken into account. At high temperatures, with a lifetime $\tau < 1$ ns at $T = 1000$ K and $p = 1$ bar,²³ an instantaneous thermal decomposition of N₂O₄ \rightarrow 2 NO₂ could be assumed.

Glyoxal was prepared by dehydration of the trimer dihydrate. A mixture of 15 g (1 eq.) ((CHO)₂)₃·2H₂O, 30 g (3 eq.) of phosphoric anhydride (P₂O₅) and some silica sand was slowly heated up under vacuum to a temperature of 155°C. Gaseous products were passed through an ice water cooled trap to remove impurities. The product was obtained as yellow crystals in a dry ice/isopropanol cooled trap and was stored at liquid nitrogen temperature. No impurities of H₂O or CO₂ could be detected by means of FTIR spectroscopy.

7.2.3 Quantitative detection of HCO radicals

HCO was detected by means of frequency modulation (FM) spectroscopy. A detailed description of the FM setup can be found elsewhere.^{2,4} Briefly, the wavelength of a Nd:YVO₄ solid-state laser (Coherent Verdi-V10) pumped *cw* ring-dye laser (Coherent 899-21) was measured by a wavemeter (MetroLux WL200) with an absolute accuracy of 200 MHz. The laser light was modulated at a frequency of 1.0 GHz using a resonant electro-optic modulator (New Focus 4421). The frequency spectrum of the modulated laser light was monitored by a scanning etalon and the modulation depth was set to a modulation index $M = 1.6$. The slightly focussed laser beam passed through the shock tube, was coupled into an optical fibre and was detected with a fast silicon photodiode (Hamamatsu

S5973-2). The FM signal was demodulated using a double balanced frequency mixer. A voltage controlled phase shifter (Lorch) was used in combination with a two polarizer setup to set the phase angle of demodulation to zero, resulting in purely absorption induced signal. Finally, the signal was low-pass filtered resulting in an electronic time response of ≈ 400 ns and was stored in a digital oscilloscope (LeCroy WaveSurfer 454, 500 MHz, 8 bit).

The demodulated FM signal, I_{FM} , is proportional to the concentration c of the absorbing species according to^{2,24}

$$I_{\text{FM}} = \frac{I_0}{2} \times \Delta f \times \sigma c l \times G$$

Here, I_0 is the total light intensity, σ the narrow-bandwidth absorption cross section, l the absorption path length and G the electronic gain of the FM spectrometer. Whereas Δf , the FM factor, was calculated from linewidth data, the gain factor G was determined experimentally.⁴

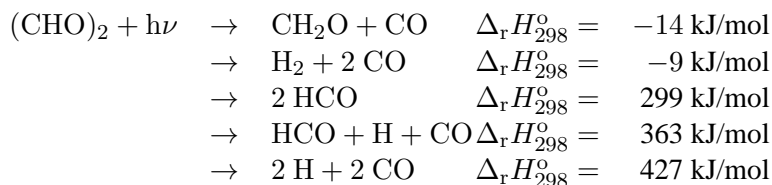
The HCO radicals were detected at a wavelength of $\lambda = 614.752$ nm, corresponding to the overlapping Q(6)P(1) line of the $\tilde{A}^2A''(0, 9^0, 0) \leftarrow \tilde{X}^2A'(0, 0^1, 0)$ transition. Absolute concentrations were calculated based on the accurate line shape data and differential absorption cross sections determined previously for the Q(9)P(2) line at $\lambda = 614.872$ nm.² Allowance was made for a small pressure broadening effect according to an assumed pressure broadening coefficient $\Delta\nu_p = 2.0 \times (T/298 \text{ K})^{-0.75}$ GHz/bar. Recently, Flad et al.,²⁵ based on sensitive cavity ringdown spectroscopic detection and photochemical calibration of HCO, found agreement within $\pm 2\%$ with our room temperature cross section. In the light of this excellent agreement, the uncertainty of the calculated HCO concentrations including errors of temperature dependent absorption cross section, the FM factor, and the gain factor can be estimated to be $\leq 20\%$.

For all numerical simulations the Chemkin-II package²⁶ was used. Where applicable, rate constants for reverse reactions were calculated automatically on the basis of thermodynamic data taken from Konnov,²⁷ except for glyoxal.²⁸ Starting with the experimental conditions calculated from the shock tube code, simulations were performed under the constraint of a constant volume such that the experimental pressure and temperature were allowed to slightly increase over the reaction time up to 1%. For sensitivity analysis the sensitivity coefficient $\sigma(i, j)$ of the i -th reaction of species j was normalized with respect to the maximum concentration of the species j over the time history.

7.3 Glyoxal photolysis

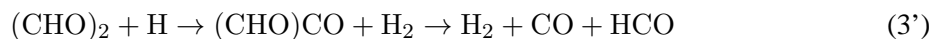
The photolysis of glyoxal was used as an efficient high temperature HCO source. Based on the absorption cross section,²⁹ $\sigma_{193\text{nm}} = 4.8 \times 10^{-19}$ cm²/molecule, about 2 % of the glyoxal were photodissociated in a typical shock tube experiment. The following photodissociation pathways of

glyoxal are thermodynamically accessible:



According to Zhu et al.,²⁹ the HCO quantum yield is $\phi = (0.42 \pm 0.21)$. Next to other stable species, H atoms are also generated in high yields. Initial $[\text{H}]_0/[\text{HCO}]_0$ ratios were taken from a preceding study of Colberg and Friedrichs (Fig. 3 in Ref.⁴). They found that the initial ratio increases with increasing total density. Typically, under the experimental conditions behind shock waves, $[\text{H}]_0/[\text{HCO}]_0 \approx 2.9$.

Through the reaction sequence



additional HCO is formed from the H atom abstraction reaction with excess glyoxal. Even at room temperature, (CHO)CO decomposes within the time resolution of the experiment³⁰ and reaction (3') can be rewritten as



At high temperatures, with a lifetime of $\tau \approx 4 \mu\text{s}$ ($T = 1000 \text{ K}$, $p = 1 \text{ bar}$), HCO radicals also rapidly decompose forming H atoms,



which will subsequently lead to a regeneration of HCO radicals via reaction (3). It is this HCO regeneration chain mechanism with reactions (3) and (4) as the propagation steps that steadily converts glyoxal into HCO radicals and makes HCO detection behind shock waves feasible in the first place. Based on room temperature and high temperature mechanisms reported in Ref.² and as they are included in Tables 1 and 2, experimentally observed HCO profiles can be quantitatively modelled. Note that the room temperature mechanism also takes into account the chemistry of initially formed excited HCO* radicals,^{2,4} e.g. the fast relaxation process



At high temperatures and using Ar as bath gas, this relaxation process can be assumed to be complete within less than $1 \mu\text{s}$ and HCO* chemistry can be neglected.³¹ Also at high temperatures, next to the reaction shown in Table 2, the GRI-Mech 3.0 mechanism³² was used as a detailed base mechanism in order to identify important additional reactions.

7.4 The reaction HCO + NO

7.4.1 Room temperature measurements

HCO concentration-time profiles were recorded following the 193 nm photolysis of mixtures of 0.54% glyoxal in argon at a total pressure of $p = 51$ mbar. Due to the small absorption cross section of NO ($\sigma_{\text{NO}} < 1 \times 10^{-22}$ cm²/molecule),³³ NO photolysis is negligible. NO mole fractions were 533, 1058, and 2128 ppm. The total gas flow was chosen such that the gas volume in the flow cell was replaced every 6 photolysis laser shots.

Fig. 1a illustrates three HCO concentration-time profiles measured with and without NO added to the gas mixture. Without NO, the long term consumption of HCO is quite slow. The initial increase of the HCO signal following the photolysis is due to collision-induced relaxation of vibrationally excited HCO*, which is transparent at the detection wavelength used. The effect of added NO is clearly visible. Lower maximum HCO concentrations and significantly shorter overall lifetimes are observed. The solid curves in Fig. 1a correspond to numerical simulations based on the mechanism outlined in Table 1. By fitting the onset, the initial increase and the maxima of the observed HCO profiles, an average HCO* relaxation rate constant $k_5 = 1.6 \times 10^{11}$ cm³mol⁻¹s⁻¹ and an average initial ratio of $[\text{HCO}^*]_0/[\text{HCO}]_0 = 2.3$ was obtained. The rate constant of reaction (1) was fitted in order to reproduce the decay of the HCO profiles.

The sensitivity analysis for the 533 ppm NO experiment shown in Fig. 1b reveals the influence of the most sensitive reactions on the simulated HCO concentration-time profile. Reaction (5), the HCO* relaxation process, dominates during the first few μs . However, the key reaction for the HCO radical decay is reaction (1). Moreover, since the rate constant set chosen for other HCO removal reactions nicely reproduces the observed HCO decay for the experiment without NO, the differences between the profiles measured with and without NO can be almost exclusively attributed to reaction (1). As an average of five measurements with three different NO concentrations, $k_1 = 8.1 \times 10^{12}$ cm³mol⁻¹s⁻¹ was obtained. At high NO concentrations, however, the simulations with k_1 chosen such that the calculated profiles fitted the observed HCO decays at short reaction times deviate from the experimental profiles at long reaction times (see 1058 ppm experiment in Fig.1, solid curve). This deviation is probably due to a further unidentified HCO producing reaction not included in the mechanism or to an interfering absorbing product species. Note that a potential reaction sequence according to $\text{HNO} + (\text{CHO})_2 \rightarrow \text{H}_2\text{NO} + (\text{CHO})\text{CO} \rightarrow \text{H}_2\text{NO} + \text{HCO} + \text{CO}$ is endothermic by $\Delta_r H_{298}^\circ \approx 95$ kJ/mol and thus cannot play a significant role. In contrast, due to the very rich $\tilde{\text{A}}^1\text{A}'' - \tilde{\text{X}}^1\text{A}'$ absorption band system, weak HNO absorption might have interfered (asymmetry splitted ^RQ₂(6) line of the 003 – 000 3 – 2 subband at $\lambda = 614.757$ nm).^{34–36} Therefore, in another analysis, allowance was made for a time-dependent HNO background absorption. The corresponding simulations (see 1058 ppm experiment in Fig. 1, dashed curve) gave a better but not perfect agreement for the high

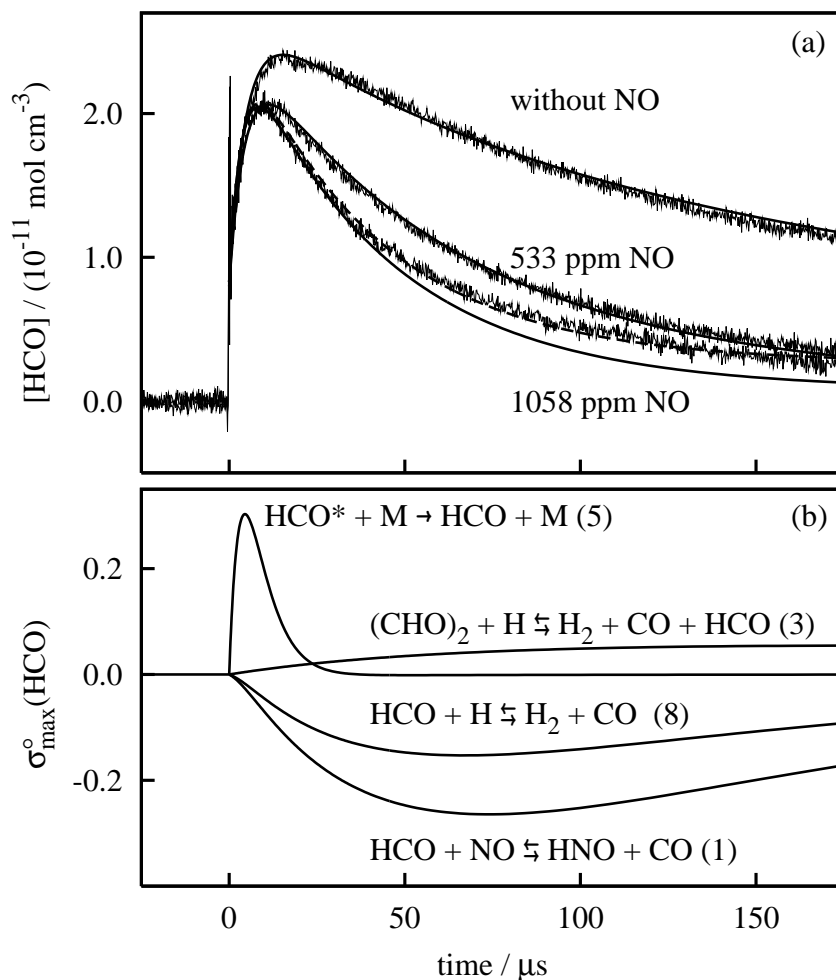


Figure 1: Room temperature determination of the rate constant of reaction (1), $\text{HCO} + \text{NO}$. (a) 32 times averaged HCO concentration-time profiles and corresponding numerical simulations (solid curves) for experiments at $T = 295 \text{ K}$, $p = 51 \text{ mbar}$, an initial glyoxal mole fraction of 0.54%, and different amounts of NO added. The dashed curve corresponds to a simulation taking into account a possibly interfering background absorption (see text). (b) Sensitivity analysis for the 533 ppm NO experiment.

Table 1: Room temperature mechanism. Units are cm, mol, and s.

no.	reaction	k	ref.
a) glyoxal photolysis mechanism:			
(5)	HCO* + M → HCO + M	1.6×10^{11}	1
(3)	H + (CHO) ₂ ⇌ H ₂ + HCO + CO	3.6×10^{10}	37
(8) ²	HCO + H ⇌ H ₂ + CO	1.1×10^{14}	2,3
(9) ²	HCO + HCO ⇌ CH ₂ O + CO	2.7×10^{13}	3,38
(10)	H + CH ₂ O ⇌ H ₂ + HCO	2.4×10^{10}	39
b) additional NO/HNO reactions:			
(1) ²	HCO + NO ⇌ HNO + CO	8.1×10^{12}	1
(11)	H + NO + M ⇌ HNO + M	1.4×10^{16}	40
(12)	H + HNO ⇌ H ₂ + NO	3.4×10^{12}	40
(13) ²	HCO + HNO → HNOH + CO	1.9×10^{12}	3
c) additional NO ₂ /OH reactions:			
(2) ²	HCO + NO ₂ ⇌ products	3.1×10^{13}	1
(2a)	⇌ H + CO ₂ + NO	$\phi = 0.35$	1
(2b)	⇌ HNO + CO ₂	$\phi = 0.00$	1
(2c)	⇌ HONO + CO	$\phi = 0.25$	1
(2d)	⇌ OH + NO + CO	$\phi = 0.40$	1
(6)	H + NO ₂ ⇌ OH + NO	8.4×10^{13}	40
(7)	OH + (CHO) ₂ ⇌ H ₂ O + HCO + CO	6.4×10^{12}	42
(14a)	OH + NO ₂ ⇌ HNO ₃	6.8×10^{11}	43 ⁴
(15) ²	OH + HCO ⇌ H ₂ O + CO	1.1×10^{14}	44

¹ this work.² reactions of the vibrationally excited HCO* were taken into account in an approximate manner by assuming the same rate constant as for the thermally equilibrated HCO.³ estimated based on Ref. 41⁴ measured at $p = 39$ mbar.

concentration experiments and resulted in < 10 % higher k_1 values.

Throughout this paper, for a final error assessment, next to the 2σ standard error of the mean and the fit inaccuracies, also systematic errors arising from uncertainties of the calculated absolute HCO concentration ($\pm 20\%$) and the assumed $[H]_0/[HCO]_0$ ratio ($\pm 25\%$ at room temperature, $\pm 17\%$ at high temperatures) were taken into account. The total error, which was derived from simulations with a combined variation of the error sources, can be taken as a reasonable estimate of the absolute uncertainty of k_1 ,

$$k_1(295 \text{ K}) = 8.1_{-1.3}^{+2.0} \times 10^{12} \text{ cm}^3 \text{ mol}^{-1} \text{ s}^{-1}.$$

Experimental data and conditions are listed in the Electronic Supplementary Information.

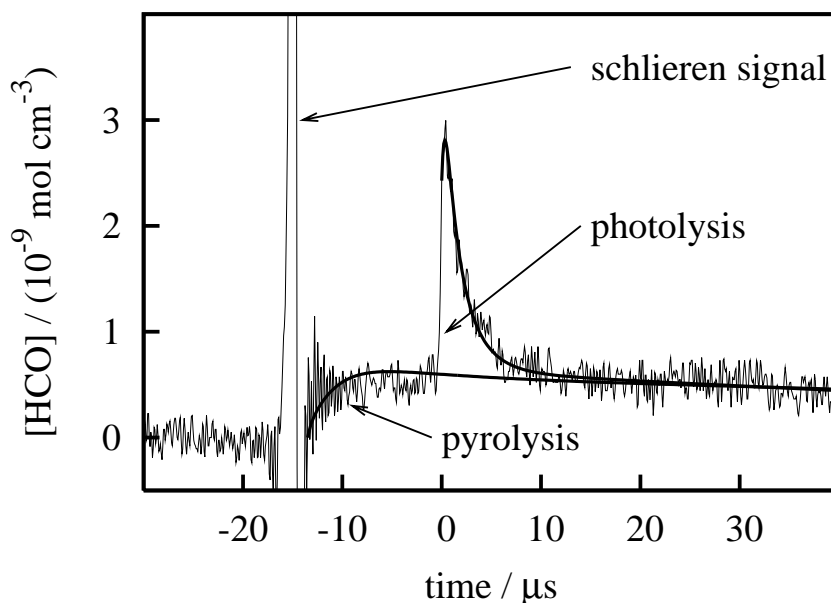


Figure 2: High temperature HCO profile following the shock heating and photolysis of a mixture containing 0.97% glyoxal and 0.46% NO in argon at $T = 1272 \text{ K}$, $p = 1.43 \text{ bar}$. Thick solid curves correspond to numerical simulations taking into account glyoxal pyrolysis and photolysis.

7.4.2 High temperature measurements

Shock tube experiments were carried out at temperatures between $769 \text{ K} < T < 1307 \text{ K}$ and pressures of $851 \text{ mbar} < p < 1307 \text{ mbar}$ using initial test gas mixtures containing 0.25-1.0% glyoxal and 1230 - 6150 ppm NO in argon. The photolysis was initiated 15 μs after the arrival of the reflected shock waves. For experiments at temperatures $T > 1050 \text{ K}$, the thermal decomposition of glyoxal could not be neglected. Therefore, numerical simulations were carried out beforehand to take the pyrolysis of glyoxal into account. In contrast to previous literature reports,⁴⁵ the thermal decomposition of glyoxal generates HCO radicals in high yields. A detailed study of the thermal glyoxal decomposition is currently underway and will be published elsewhere.⁴⁶

Fig. 2 shows an experimental HCO profile obtained at a temperature of $T = 1272 \text{ K}$. The arrival of the reflected shock wave is indicated by a strong schlieren signal followed by the onset of HCO formation due to glyoxal pyrolysis. The UV photolysis initiates a quasi-instantaneous formation of HCO, which is superimposed on the thermal HCO background. The complete signal can be reproduced by taking into account glyoxal pyrolysis and photolysis (solid curves). In the experiment shown in Fig. 2, 18% of the glyoxal had been thermally decomposed prior to photolysis.

An experimental HCO profile obtained at a temperature of $T = 1013$ K is shown in Fig. 3 together with a numerical simulation and sensitivity analysis, which is based on the reaction mechanism outlined in Table 2. In contrast to the experiment shown in Fig. 2, no thermal HCO background is discernible. Moreover, no indication was found for an interfering HNO background absorption. With a lifetime of $\sim 3 \mu\text{s}$, the HCO decay is very fast, but still can be resolved. The rate constant k_1 was fitted as adjustable parameter. Again, the initial $[\text{H}]_0/[\text{HCO}]_0$ ratio was taken from the paper of Colberg and Friedrichs.⁴ As becomes clear from the sensitivity analysis (Fig. 3b), the initial increase of the HCO profile at very short reaction times is due to the fast formation of additional HCO by reaction (3), $\text{H} + (\text{CHO})_2$. The rate of reaction (1) is the most sensitive reaction at longer reaction times and its importance is further emphasized by a direct comparison of the experiment with a simulation of the unperturbed system. The curve in Fig. 3a corresponding to a simulation with the mole fraction of NO set to zero strongly differs from the experimental data with NO.

An Arrhenius plot of the determined 35 k_1 values (dots) is shown in Fig. 4. Experimental data and conditions are listed in the Electronic Supplementary Information. In the temperature range investigated, the rate constant is almost temperature independent. A simple linear fit of the data yields $k_1 = 1.3 \times 10^{13} \exp(-5.0 \text{ kJ mol}^{-1}/RT) \text{ cm}^3 \text{ mol}^{-1} \text{ s}^{-1}$. However, with a probability value of $p = 0.03$ for the linear fit, it is clear that the small temperature dependence of k_1 is barely significant. Moreover, keeping in mind that the values at high temperatures are affected by the thermal decomposition of glyoxal and are less accurate, the data are well represented by a temperature independent average (solid line with error bars in Fig. 4). The logarithmic mean value of all measurements is

$$k_1 = (7.1 \pm 2.7) \times 10^{12} \text{ cm}^3 \text{ mol}^{-1} \text{ s}^{-1}.$$

The stated total error, next to the 2σ standard error of the mean, also includes several systematic errors and was derived from simulations with a combined variation of all error sources (see discussion of errors in Section 7.4.1).

7.4.3 Discussion

The determined room temperature and high temperature rate constants of reaction (1) are compared with theoretical predictions of Xu et al.¹⁷ and experimental literature data in Fig. 4. Measurements at room temperature were reported by Ninomiya et al.⁵¹ (cavity ringdown spectroscopy), Langford and Moore⁵² (laser absorption spectroscopy), Sarkisov et al.⁵³ (intra-cavity laser absorption spectroscopy), Reilly et al.⁵⁴ (intra-cavity laser absorption spectroscopy), and Shibuya et al.⁵⁵ (absorption spectroscopy with Ar-discharge lamp). Recently, DeSain et al.¹⁵ published temperature dependent results for temperatures between $196 \text{ K} < T < 623 \text{ K}$ obtained by *cw* laser-induced fluorescence experiments using a slow flow reactor setup. The only other temperature dependent study was performed by Veyret and Lesclaux.⁵⁶ They determined the rate constant at temperatures of $298 \text{ K} < T < 503 \text{ K}$

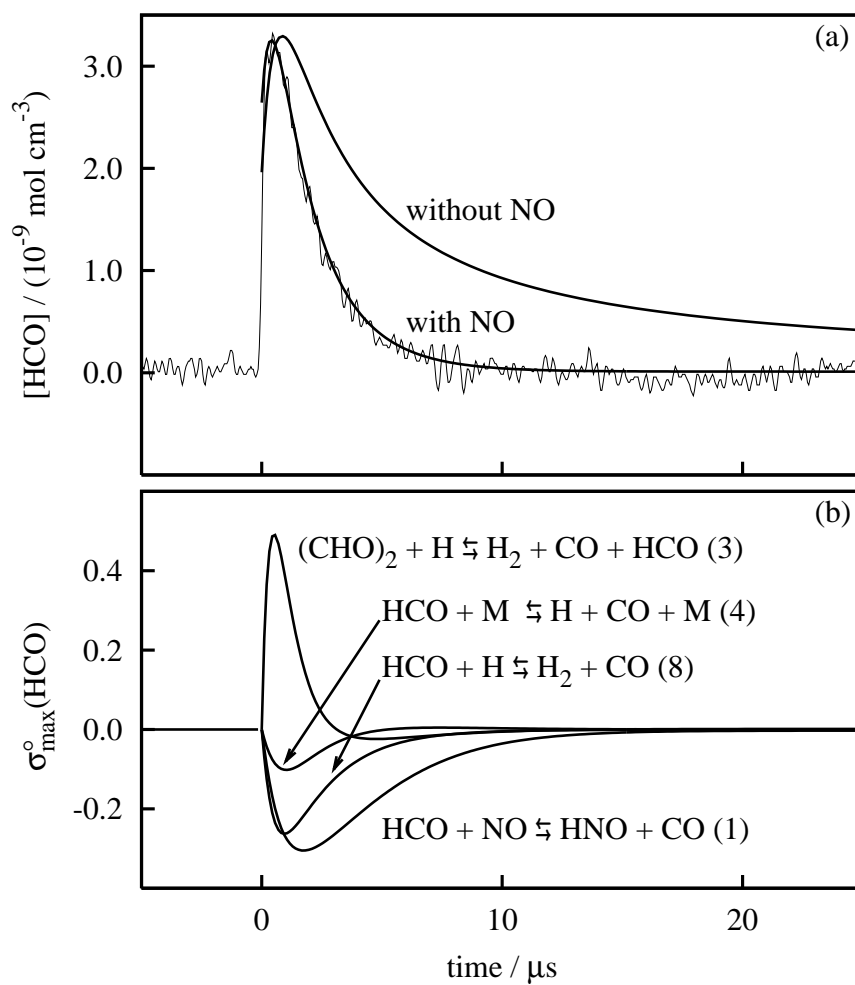


Figure 3: High temperature determination of the rate constant of reaction (1), $\text{HCO} + \text{NO}$. (a) HCO concentration-time profile and corresponding numerical simulations for an experiment at $T = 1013 \text{ K}$, $p = 1.44 \text{ bar}$, 1.03% glyoxal, and 0.51% NO. (b) Sensitivity analysis.

Table 2: High temperature reaction mechanism. Rate constants are given as $k_i = AT^n \exp(-E_a/RT)$ (units are cm, mol, K, s and kJ). Additionally, the GRI Mech 3.0³² mechanism has been used as a base mechanism in order to include potential secondary chemistry.

no.	reaction	A	n	E_a	ref.
a) glyoxal mechanism:					
(3)	$\text{H} + (\text{CHO})_2 \rightleftharpoons \text{H}_2 + \text{HCO}$	5.4×10^{13}		18	37
(4)	$\text{HCO} + \text{M} \rightleftharpoons \text{H} + \text{CO} + \text{M}$	4.0×10^{13}		65	2
(8)	$\text{HCO} + \text{H} \rightleftharpoons \text{H}_2 + \text{CO}$	1.1×10^{14}			3
(9)	$\text{HCO} + \text{HCO} \rightleftharpoons \text{CH}_2\text{O} + \text{CO}$	2.7×10^{13}			3,38
(10)	$\text{H} + \text{CH}_2\text{O} \rightleftharpoons \text{H}_2 + \text{HCO} + \text{CO}$	5.7×10^7	1.9	11.5	5,39
b) additional NO/HNO reactions:					
(1)	$\text{HCO} + \text{NO} \rightleftharpoons \text{HNO} + \text{CO}$	7.1×10^{12}			1
(11)	$\text{H} + \text{NO} + \text{M} \rightleftharpoons \text{HNO} + \text{M}$	9.0×10^{19}	-1.32	3.08	40
(12)	$\text{H} + \text{HNO} \rightleftharpoons \text{NO} + \text{H}_2$	1.8×10^{13}		4.15	40
(13a)	$\text{HCO} + \text{HNO} \rightarrow \text{HNOH} + \text{OH}$	6.0×10^{11}			3
(13b)	$\rightarrow \text{CH}_2\text{O} + \text{NO}$	5.8×10^{-1}	3.84	0.48	41
(13c)	$\rightarrow \text{H}_2\text{NO} + \text{CO}$	4.9×10^1	3.27	7.34	41
(16)	$\text{NO} + \text{HNO} \rightleftharpoons \text{N}_2\text{O} + \text{OH}$	8.5×10^{12}		124	47
(17)	$\text{NO} + \text{H} \rightleftharpoons \text{OH} + \text{N}$	1.7×10^{14}		204	40
c) additional NO ₂ /OH reactions:					
(2)	$\text{HCO} + \text{NO}_2 \rightleftharpoons \text{products}$	3.3×10^{13}			1
(2a)	$\rightleftharpoons \text{H} + \text{CO}_2 + \text{NO}$	$\phi = 0.70$			1
(2b)	$\rightleftharpoons \text{HNO} + \text{CO}_2$	$\phi = 0.00$			1
(2c)	$\rightleftharpoons \text{HONO} + \text{CO}$	$\phi = 0.15$			1
(2d)	$\rightleftharpoons \text{OH} + \text{NO} + \text{CO}$	$\phi = 0.15$			1
(6)	$\text{H} + \text{NO}_2 \rightleftharpoons \text{OH} + \text{NO}$	1.3×10^{14}		1.5	48
(7)	$\text{OH} + (\text{CHO})_2 \rightleftharpoons \text{H}_2\text{O} + \text{HCO} + \text{CO}$	1.1×10^{13}			1
(14b)	$\text{OH} + \text{NO}_2 \rightleftharpoons \text{HO}_2 + \text{NO}$	1.8×10^{13}		27.9	49
(15)	$\text{OH} + \text{HCO} \rightleftharpoons \text{H}_2\text{O} + \text{CO}$	1.1×10^{14}			44
(18)	$\text{HONO} + \text{M} \rightleftharpoons \text{OH} + \text{NO} + \text{M}$	3.0×10^{30}	-3.8	211	40
(19)	$\text{NO}_2 + (\text{CHO})_2 \rightleftharpoons \text{HONO} + \text{HCO} + \text{CO}$	8.0×10^2	2.77	57.5	4

¹ this work

³ estimated based on Ref. 41

⁴ set equal to rate constant of reaction $\text{NO}_2 + \text{CH}_2\text{O}$ given in Ref. 50

using a flash photolysis-laser resonance absorption technique. The present work, however, presents the first measurements of k_1 at combustion relevant temperatures of about 1000 K.

Overall, the room temperature rate constant determined in this work is in excellent agreement with literature data. Therefore it can be concluded that the measurement strategy (perturbation approach) and also the mechanism used are suitable for an accurate rate constant determination.

Both the weak negative temperature dependence reported in the literature for the intermediate temperature range and the absolute high temperature rate constant determined in this work are well reproduced by the theoretical predictions of Xu et al. At first glance, the overall small temperature dependence of k_1 seems to be consistent with a simple capture rate controlled complex-forming mechanism. However, as has been concluded from RRKM calculations by Xu et al.¹⁷ and earlier by Kulkarni and Koga,⁵⁷ this is not the case. Fig. 5 illustrates a simplified sketch of the singlet state potential energy surface (PES) as calculated by Xu et al. using Gaussian-2 theory. For a more complete scheme we refer to the original literature.¹⁷ The association-fragmentation pathway to the products $\text{HNO} + \text{CO}$ via the energetically favoured association complex ON-CHO (LM1 in Fig. 5) exhibits a pronounced exit barrier of 28 kJ/mol (relative to the reactants, TS1). This barrier causes the forward dissociation rate constant to be much lower (dash-dotted curve in Fig. 4) and its temperature dependence to be inconsistent with the experimental measurements. At $T = 1000$ K and $p = 1$ bar the predicted association-elimination rate constant is three orders of magnitude smaller than the experimental results. Kulkarni and Koga discussed an alternative direct abstraction process with a downhill path (indicated by the dashed line in Fig. 5) and, based on a calculation using simple transition state theory, concluded that this channel also cannot contribute significantly to the total reaction rate. Xu et al. came to a different conclusion, which is further illustrated in Fig. 5. Here, the abstraction channel was found to exhibit a local minimum structure ON-HCO (LM2) followed by a small barrier that is lower than the reactant energy (TS2). A variational transition state treatment showed that this channel is nearly temperature independent up to temperatures of $T = 1000$ K (dashed curve in Fig. 4) and is the dominating pathway. According to their calculations, even at room temperature this quasi-direct abstraction channel contributes 70% ($p = 1$ bar) or $> 99\%$ (1 mbar) to the total rate constant.

The total rate of Xu et al. (long solid curve in Fig. 4, $p = 1$ bar) and our room and high temperature data match. Therefore, in particular when keeping in mind the predicted strongly negative temperature dependence for the association-elimination pathway, our data clearly support the high temperature dominance of a direct abstraction pathway.

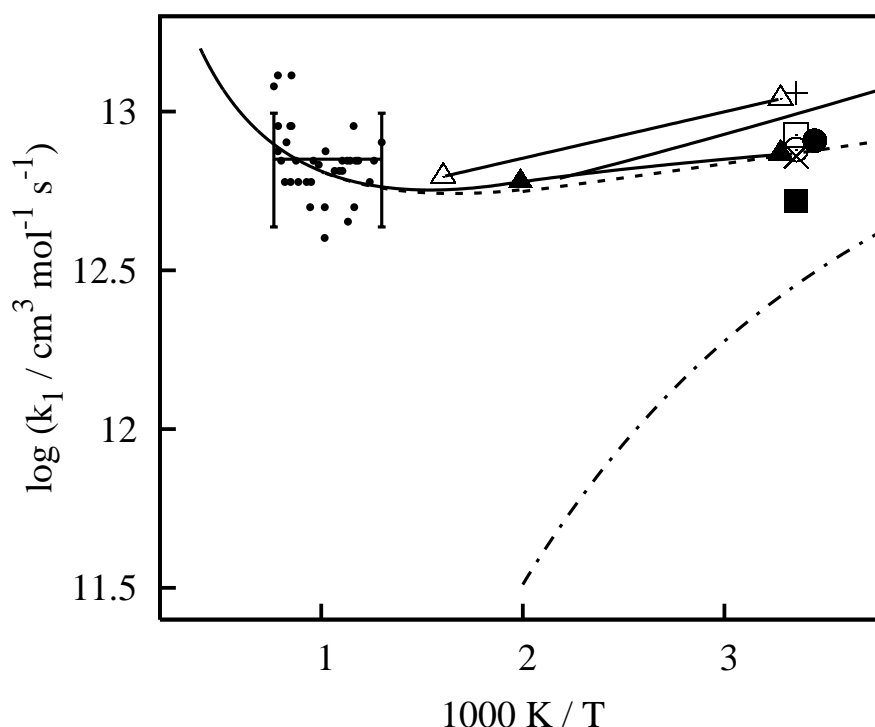


Figure 4: Comparison of the determined room and high temperature rate constants of reaction (1), HCO + NO, with literature data. Solid line marked with error bars, ●: this work. (△) DeSain et al.¹⁵, (+) Ninomiya et al.⁵¹, (○) Langford and Moore⁵², (×) Sarkisov et al.⁵³, (▲) Veyret and Lesclaux⁵⁶, (□) Reilly et al.⁵⁴, (■) Shibuya et al.⁵⁵ Solid curve: total rate constant, dashed curve: direct abstraction channel, and dash-dotted curve: association-elimination channel ($p = 1$ bar) as calculated by Xu et al.¹⁷ (RRKM/VTST, see text).

7.5 The reaction HCO + NO₂

Since the early papers of Morrison and Hecklen^{58,59} it has been long recognised that several product channels contribute to the overall reaction (2), HCO + NO₂ → products, namely^{16,18,50,60–62}



Due to several energetically low-lying exit barriers of the initially formed association-complexes (Fig. 6), the direct recombination products O₂N-CHO and ONO-CHO can play a role only in the high pressure regime, which can be assumed to be well above ambient pressures.

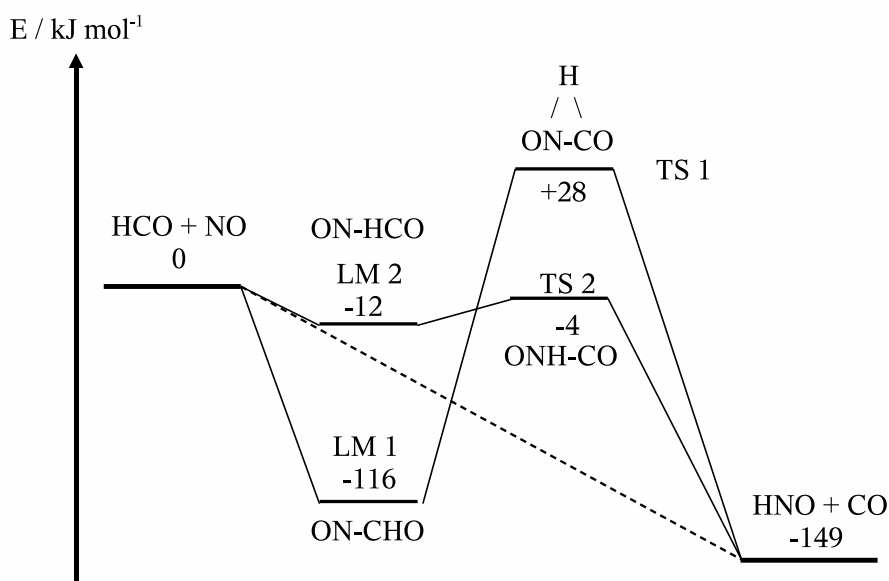


Figure 5: Schematic potential energy diagram of reaction (1) as calculated by Xu et al.¹⁷ (solid lines, G2 method, see text). LM: local minimum, TS: transition state. Dashed line: direct abstraction channel as discussed by Kulkarni et al.⁵⁷

Within this section, measurements of the rate constant k_2 at room temperature and up to temperatures of $T = 1183$ K will be presented. It turned out that the determined overall rate constants depend on the assumed product branching ratio which is still uncertain.

7.5.1 Product branching ratios

Available data on the product branching ratios of reaction (2) are summarised in Table 3. Note that the products of channel (2d) are generated from the decomposition of vibrationally excited HONO* formed in reaction (2c) according to



Hence, channels (2c) and (2d) are not separate channels and, moreover, the relative branching fractions can be assumed to be pressure dependent due to more or less efficient collisional stabilisation of the primary HONO* product. From measured vibrational distributions of CO₂ and CO ($T = 298$ K, $p = 1$ mbar) Butkovskaya and Setser⁶³ concluded that both the HONO channel and the OH + NO channel contribute to the overall rate.

Table 3: Branching ratios $k_{2x}/k_{2,\text{total}}$ (in %) of reaction (2), HCO + NO₂.

ref., method	T/K	p/mbar	2a	2a+2b	2b	2b+2c	2c	2c+2d	2d
Meyer&Temps, ⁶⁰ FTIR spectroscopy	295	570		34 ± 10		28 ± 10		66 ± 10	
Rim&Hershberger, ⁶¹ IR laser absorption	298	2	37 ± 5			< 10			63 ± 5
Butkovskaya&Setser, ⁶³ IR emission	298	1	39		0		> 0	61	> 0
Guo et al., ¹⁸ IR/VIS laser absorption	296	< 960		52 ± 14	< 10			48 ± 14	
based on Guo et al., ¹⁸ calculated ¹	296	0 ²	47		10			43	
based on Guo et al., ¹⁸ calculated ¹	1000	0 ²	72		12			17	
He et al., ⁶² FTIR spectroscopy	425	64	34				66		
Lin et al., ⁵⁰ IR laser absorption	1000	550	88				12		
this work, ¹ VIS laser absorption	295	50	35				25		40
this work, ¹ VIS laser absorption	1000	1250	70				15		15

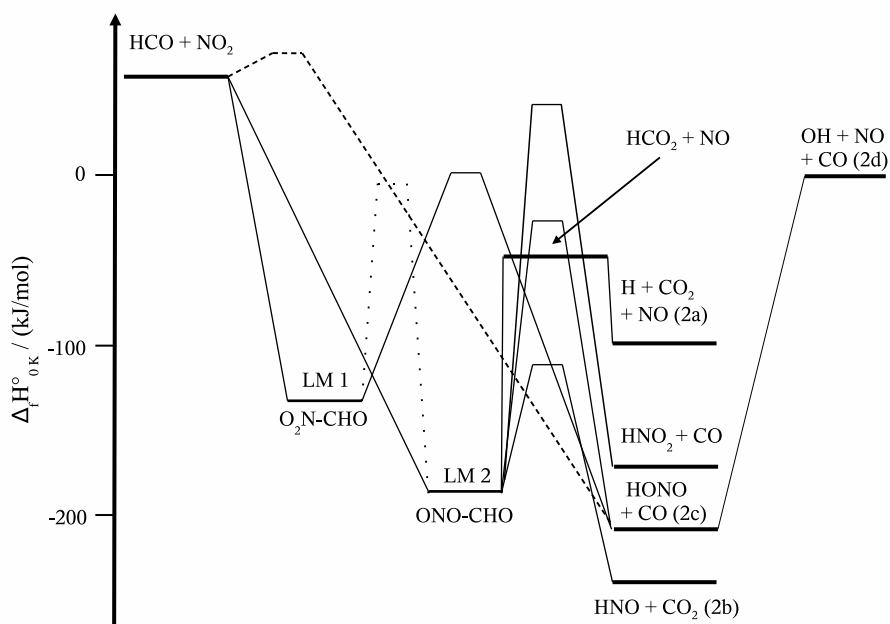


Figure 6: Schematic energy diagram of reaction (2) as calculated by Guo et al.¹⁸ (solid lines, BAC-MP4 method). LM: local minimum. Dashed line: direct abstraction channel (estimated transition state barrier), dotted line: LM1–LM2 interconversion barrier (estimated based on MP2/6-31G(d), see Electronic Supplementary Information).

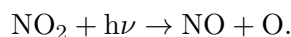
In addition to the experimental data, also theoretically derived branching ratios are given in Table 3. Guo et al. modelled the overall reaction rate constant and the individual product rate constants by using a variational RRKM approach based on structures and energies obtained by the BAC-MP4 method. Fig. 6 illustrates the calculated reaction energy diagram. Two different collisional complexes, $\text{O}_2\text{N-CHO}$ (LM1 in Fig. 6) and ONO-CHO (LM2), and several rearrangement and fragmentation pathways are feasible. LM1 and LM2 are connected by an energy barrier that is lower than the reactant energy and enables an interconversion of both structures. As a first approximation, due to the very constrained *tight* interconversion barrier (3 membered ring structure), the rate of interconversion can be assumed to be negligible compared to the rate of redissociation and forward reaction to $\text{HONO} + \text{CO}$. Whereas $\text{HONO} + \text{CO}$ can be formed from both intermediates, the products $\text{H} + \text{CO}_2 + \text{NO}$ and $\text{HNO} + \text{CO}_2$ can be formed from LM1 only. Besides the association-fragmentation pathways, also a direct abstraction pathway exhibiting a small transition state barrier is feasible giving rise to the products $\text{HONO} + \text{CO}$. This abstraction pathway was not considered in the rate calculations, however, it might become important at high temperatures. Guo et al. specified temperature dependent rate constants for the capture rate, the redissociation, and the forward fragmentation processes (Table 1 in Ref.¹⁸). In these calculations, the two collisional complexes LM1 and LM2 were assumed to react independently. Making the additional assumption that both collisional complexes are formed with equal probability, the data of Guo et al. can be used to estimate the overall branching ratios of

reaction (2) as given in Table 3. Within the framework of this analysis, HONO is exclusively formed by elimination from the collision complex LM1, whereas the fragmentation of LM2 mainly yields H + CO₂ + NO. In the latter case, the preferential formation of the intermediate HCO₂ (\rightarrow H + CO₂) instead of the thermodynamically more stable products HNO + CO₂ can be readily understood in terms of the *loose* structure of the HCO₂ forming transition state (simple bond fission vs. elimination pathway). For the same reason, the formation of HONO + CO and HNO₂ + CO from LM2 does not play a role. A comparison of the predicted branching ratios at $T = 296$ K and $T = 1000$ K reveals that with increasing temperature the importance of reaction channel (2a) increases (47% \rightarrow 72%), that of channel (2c+2d) strongly decreases (43% \rightarrow 17%), and that of channel (2b) remains almost unchanged (10% \rightarrow 12%). Here, the overall temperature dependence can be largely traced back to the fate of LM1. Due to the energetically high lying *tight* transition state barrier of the HONO forming channel (2c), the temperature dependence of the LM1 pathway is dominated by the collisional complex forming step. At high temperatures, a larger fraction of LM1 dissociates back to the reactants such that less HONO is formed. In contrast, due to the lower exit barriers and fast HCO₂ formation, the LM2 pathways are less temperature dependent such that channel (2a) gains importance for the overall reaction at high temperatures. For a more detailed discussion of this complicated interplay of the different reaction channels we refer to the original work of Guo et al.¹⁸ Note that a more sophisticated treatment of the reaction system should be based on a higher level calculation of the potential energy surface and should properly include the interconversion of LM1 and LM2. For the purpose of this paper, however, the presented level of approximation was found to be in good accordance with experimental findings.

Although the reported branching ratios seem to differ, overall and within the reported error limits a consistent picture arises. Based on the studies of He et al., Lin et al., and Guo et al. an increasing importance of channel (2a) with increasing temperature can be expected. At temperatures around $T = 1000$ K as used in this work, channel (2a) should account for approximately 70% of the overall reaction and the remaining 30% can be attributed to channels (2c+2d). Due to the lack of consistent information, 15% were attributed to the HONO channel (2c) and 15% to the OH + NO channel (2d), respectively. As a starting point for our room temperature modelling, based on the studies of Meyer and Temps,⁶⁰ Rim and Hershberger,⁶¹ and Butkovskaya and Setser,⁶³ the branching ratio of channel (2a) was reduced to 35% such that the sum of channels (2c) and (2d) contributed 65%. As will be pointed out below, from the best fit of the experimental room temperature data, a ratio of 25% for channel (2c) and 40% for channel (2d) was obtained. These final values are consistent with the branching ratios reported by Meyer and Temps.⁶⁰ Note that a possible minor contribution of channel (2b), which is presumably $< 10\%$, was neglected in our analysis.

7.5.2 Room temperature measurements

Experimental procedures were the same as for the NO measurements. HCO profiles were recorded following the photolysis of mixtures of 0.50% glyoxal and 259-1024 ppm NO₂ in Ar at a total pressure of $p = 50$ mbar. Due to the high NO₂ concentrations used, a possible interference of NO₂ photolysis has to be considered:



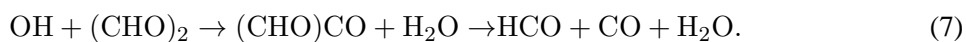
The absorption cross section of NO₂, $\sigma_{193\text{nm}} = 2.9 \times 10^{-19}$ cm²/molecule,⁶⁴ is comparable to the absorption cross section of glyoxal and approximately 0.6% of NO₂ was photodissociated. Detailed simulations taking into account the additional O atom and NO formation showed that the photolysis of NO₂ did not have a significant effect on the simulated HCO profiles and thus could be neglected. Likewise, no indications were found for an interfering NO₂ absorption at the detection laser wavelength. NO₂ shows little absorption at wavelengths around 615 nm ($\sigma_{614.8\text{nm}} = 3.2 \times 10^{-20}$ cm²/molecule),⁶⁵ however, due to the derivative-like nature of FM spectroscopy, a broad background absorption level does not give rise to a signal.

Typical HCO concentration-time profiles measured without NO₂ and with increasing NO₂ concentration levels are shown in Fig. 7a. The thick solid curves correspond to numerical simulations using the mechanism outlined in Table 1. The simulations were fitted to the experimental profiles by varying the overall rate constant k_2 . It turned out that the quality of the fit was dependent on the assumed product branching ratios. Based on a branching ratio of 35% for channel (2a) (see section 7.5.1), an iterative fitting procedure yielded 25% for channel (2c) and 40% for channel (2d). Detailed simulations showed that changing any of these ratios (2a, 2c, or 2d) by only $\pm 5\%$ gave a significantly worse fit of the overall shape of the observed HCO transient.

At a first sight, the profiles in Fig. 7a are somewhat surprising since higher HCO peak concentrations are obtained for test gas mixtures containing NO₂. As can be concluded from the sensitivity analysis of the 508 ppm experiment shown in Fig. 7b, initially generated H atoms from glyoxal photolysis are rapidly converted to OH radicals by the fast reaction



Subsequently, OH radicals are scavenged by glyoxal yielding HCO radicals,



Thus, the comparatively slow HCO forming reaction (3), $\text{H} + (\text{CHO})_2$, that governs the HCO yield in case of pure glyoxal mixtures is replaced by the faster reaction sequence (6) + (7). The used mechanism, which relies on literature data for reactions (3) and (6), nicely reproduces this rather

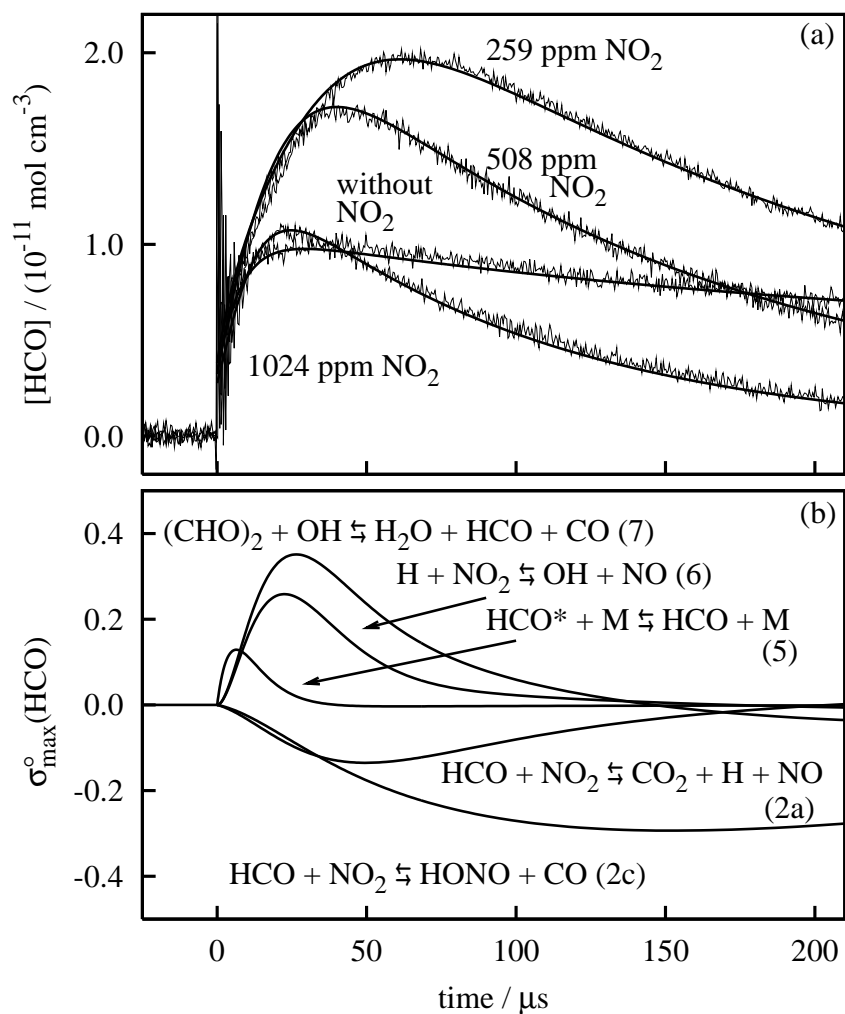


Figure 7: Room temperature determination of the rate constant of reaction (2), $\text{HCO} + \text{NO}_2$. (a) 32 times averaged HCO concentration-time profiles and corresponding numerical simulations for experiments at $T = 295 \text{ K}$, $p = 50 \text{ mbar}$, an initial glyoxal mole fraction of 0.50%, and different amounts of NO_2 added. (b) Sensitivity analysis for the 508 ppm NO_2 experiment.

complex kinetic behaviour.

The observed long-term HCO decay is dominated by the rate of reaction (2c). Again, H atoms and OH radicals generated in reactions (2a) and (2d) are quickly converted to HCO causing these reactions to be less sensitive at long reaction times. In contrast, HONO (as well as HNO) formed by reaction (2c) (or reaction (2b)) is quite unreactive and finally removes HCO. In this regard, reaction channel (2b), which was assumed to be negligible, is indistinguishable from reaction channel (2c) and cannot be ruled out.

The total rate constant has been determined to be

$$k_2(298\text{ K}) = (3.1 \pm 1.2) \times 10^{13} \text{ cm}^3 \text{ mol}^{-1} \text{ s}^{-1}.$$

The stated error, which includes the 2σ standard error of the mean of 6 measurements and several systematic errors, was derived from simulations with a combined variation of several error sources. Next to the error sources outlined in Section 7.4.1, an additional $\pm 5\%$ error was included to allow for uncertainties of the channel branching ratios. Experimental data and conditions are listed in the Electronic Supplementary Information.

7.5.3 High temperature measurements

Shock tube experiments were carried out at temperatures between $804\text{ K} < T < 1183\text{ K}$ and pressures of $925\text{ mbar} < p < 1437\text{ mbar}$ using initial test gas mixtures containing 0.48-1.0% glyoxal and 1060-2440 ppm NO₂ in argon. Fig. 8a illustrates an experiment performed at a temperature of $T = 804\text{ K}$. As already discussed for the room temperature experiments, the HCO regeneration is controlled by the rate constant of reaction (7), which could be roughly determined from the initial increase of the HCO concentration-time profiles. A temperature independent value of

$$k_7 \approx 1.1 \times 10^{13} \text{ cm}^3 \text{ mol}^{-1} \text{ s}^{-1}$$

has been obtained in good agreement with an earlier estimate from Colberg and Friedrichs,⁴ $k_7 = 1.3 \times 10^{13} \text{ cm}^3 \text{ mol}^{-1} \text{ s}^{-1}$, which was based on similar OH abstraction reactions. k_2 values were determined by fitting the HCO decay based on the product branching ratios discussed in section 7.5.1. The pronounced influence of the addition of NO₂ is evident from Fig. 8a. A simulation with the NO₂ concentration set to zero strongly deviates from the best fit curve. The sensitivity plot shown in Fig. 8b reveals that the two reaction channels (2a) and (2c) significantly contribute to the simulated HCO decay. Although the OH radical forming channel (2d) was attributed the same branching ratio as channel (2c), 15%, reaction (2d) is absent in the sensitivity plot. OH radicals are rapidly reconverted to HCO by reaction (7) such that the rate of reaction (2d) could not be determined from the experimental HCO profiles.

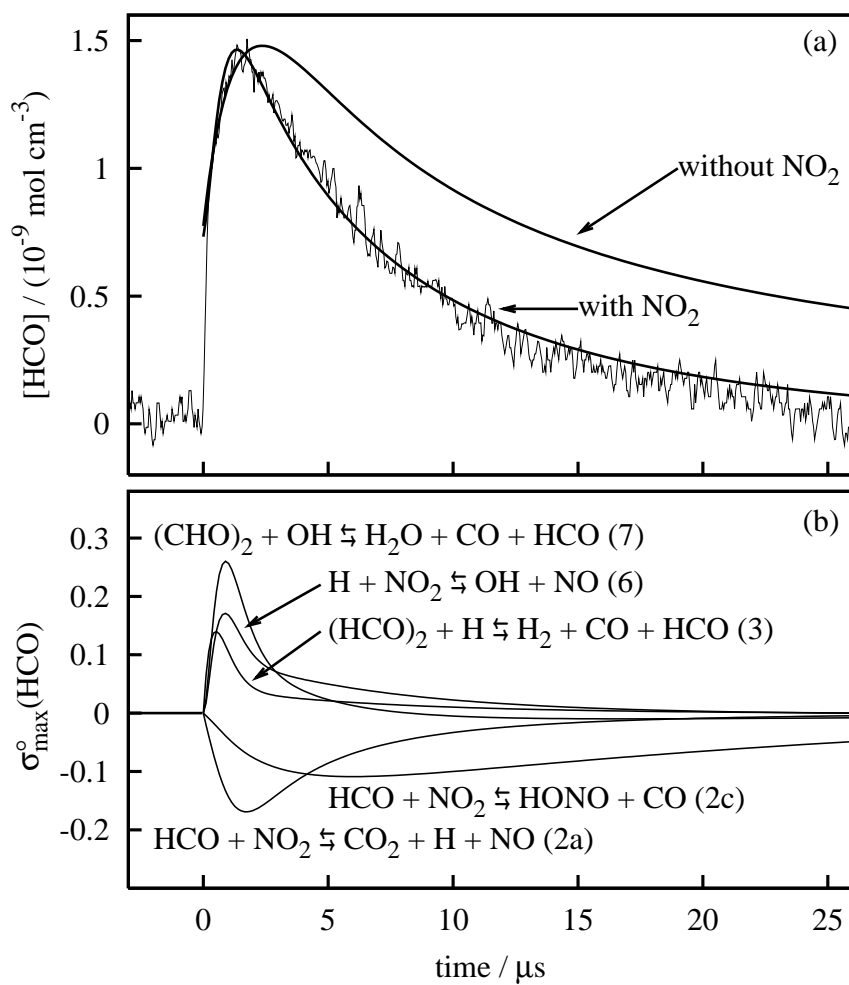


Figure 8: High temperature determination of the rate constant of reaction (2), $\text{HCO} + \text{NO}_2$. (a) HCO concentration-time profile and corresponding numerical simulations for an experiment at $T = 804 \text{ K}$, $p = 0.925 \text{ bar}$, 1.02% glyoxal, and 0.14% NO_2 . (b) Sensitivity analysis.

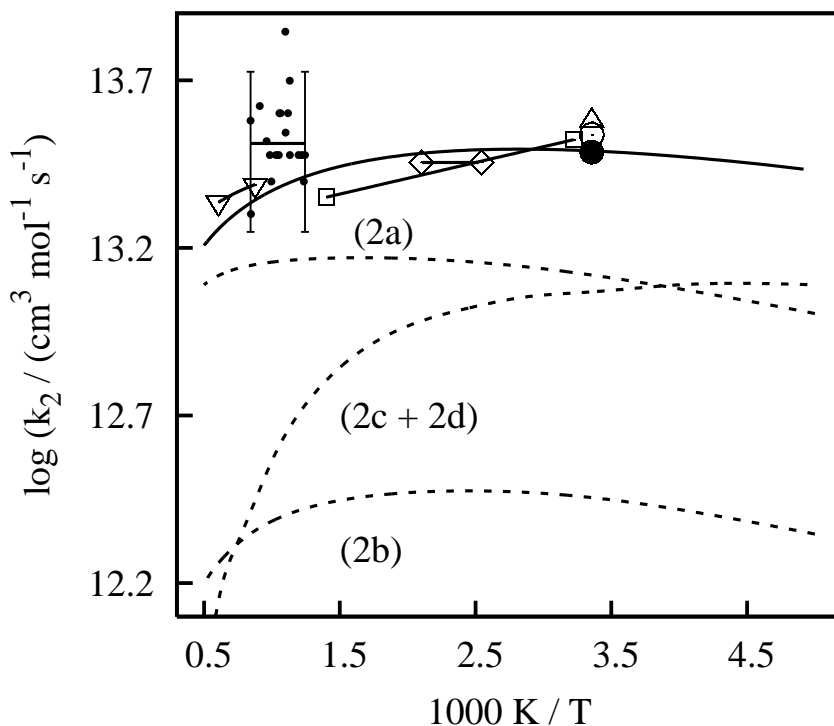


Figure 9: Comparison of the determined room and high temperature rate constants of reaction (2), HCO + NO₂, with literature data. Solid line marked with error bars, ●: this work. (□) Timonen et al.¹⁶, (△) Guo et al.¹⁸, (○) Ninomiya et al.⁵¹, (◇) He et al.⁶², (▽) Lin et al.⁵⁰ Long solid and dashed curves: total rate constant k_2 and individual product rate constants k_{2a} (H + CO₂ + NO), k_{2b} (HNO + CO₂), and k_{2c+2d} (HONO + CO, OH + NO + CO) as calculated based on the theoretical data taken from Guo et al.¹⁸ (RRKM, see text).

The influence of the reactions (2a) and (2c) on the HCO profiles is somewhat decoupled. The rate of reaction (2a) is most important during the initial decay whereas reaction (2c) gains importance at later reaction times. Thus, different overall shapes of the simulated HCO profiles are obtained by changing the ratio of the rate constants k_{2a} and k_{2c} . A fine-tuning of k_{2a} and k_{2c} showed that the profiles are best represented by an average ratio of $k_{2a}/k_{2c} = (5.6 \pm 1.3)$. This value is close to the initially assumed ratio of 4.7 and thus supports the estimated branching of reaction (2).

An Arrhenius plot of the determined 19 k_2 values, $k_2 = k_{2a} + k_{2c} + k_{2d}$, is shown in Fig. 9 (dots) together with the resulting logarithmic mean value (solid line with error bars). Within the scatter of the data, a temperature independent rate constant of

$$k_2 = (3.3 \pm 1.8) \times 10^{13} \text{ cm}^3 \text{ mol}^{-1} \text{ s}^{-1}$$

was obtained. Again, next to the 2σ standard error of the mean, the error estimate is based on a com-

bin variation of several systematic error sources (Section 7.4.1) including the assumed branching ratios for channels (2a) and (2c). Moreover, a $\pm 10\%$ error was added to account for the uncertainty of the branching ratio of the insensitive reaction channel (2d).

7.5.4 Discussion

Fig. 9 draws a comparison of the determined room and high temperature rate constants of reaction (2) with available literature data. The room temperature rate constant is in very good agreement with the available direct measurements^{16,18,51} and thus confirms the accuracy of the applied perturbation approach. Moreover, the nearly perfect modelling of the HCO profiles as shown in Fig. 7 strongly supports the assumed mechanism and channel branching ratios of reaction (2). To the best of our knowledge, the only direct measurement of the temperature dependence of k_2 was performed by Timonen et al.¹⁶ at temperatures between $294 \text{ K} < T < 713 \text{ K}$ (line marked with squares in Fig. 9). HCO profiles were recorded by means of time-resolved mass spectrometry under pseudo-first order conditions using NO₂ as the excess species. Within the scatter of their data, a slightly negative temperature dependence of the HCO disappearance rate could be confirmed. The intermediate and high temperature measurements performed by Lin and coworkers^{50,62} are based on pyrolysis experiments of CH₂O/NO₂ mixtures. The kinetic simulations of the reaction system were less sensitive to the rate of reaction (2), however, the reported rate constant for temperatures between $1140 \text{ K} < T < 1650 \text{ K}$ is in very good agreement with our high temperature results. Despite the scatter and the wide error margin, our much more direct data can be considered to be more reliable.

Also shown in Fig 9 are theoretical estimates that are based on a variational RRKM calculation of Guo et al.¹⁸ as already discussed in more detail in section 7.5.1. The long solid curve represents the calculated total rate constant, whereas the dashed curves illustrate the temperature dependences of the different product channels. Overall, in agreement with all available experimental data, the predicted total rate constant is almost temperature independent. Due to the predicted strongly negative temperature dependence of the HONO (or OH + NO) forming channel (2c+2d), channel (2a) with the products H + NO + CO₂ is the dominating channel at high temperatures. Whereas the exact branching ratios could not be determined from our experiment, the inferred high temperature ratio of $k_{2a}/k_{2c} \approx 5.6$ is consistent with the theoretical estimate.

The average of our high temperature rate constant data is approximately 50% higher than the theoretical value. However, within the error limits of the experimental data and by taking into account the inaccuracies and the assumptions made for the theoretical estimate, the difference is not significant. Based on our data and in very good agreement with the other direct measurements, we recommend the use of a temperature independent rate constant of

$$k_2 = 3.2 \times 10^{13} \text{ cm}^3 \text{ mol}^{-1} \text{ s}^{-1}$$

over the entire investigated temperature range of $295 \text{ K} < T < 1183 \text{ K}$.

Next to the purpose of the present study to provide reliable high temperature rate data for reaction (2), also the question about a possible contribution of a direct abstraction pathway, $\text{NO}_2 + \text{HCO} \rightarrow \text{HONO} + \text{CO}$, should be addressed. Such a pathway, due to a transition state barrier (see Fig. 6), can be expected to exhibit a positive temperature dependence and, at least at increasingly high temperatures, should be able to compete with the complex-forming mechanism. However, within error limits, the experimentally observed temperature dependence and also the absolute value of the overall rate constant was found to be consistent with a complex-forming mechanism alone. Therefore, no evidence was found for such a direct abstraction pathway.

7.6 Conclusion

The rate constant of the reaction



was determined for the first time at combustion relevant high temperatures of $769 \text{ K} < T < 1307 \text{ K}$. Based on numerical simulations of HCO concentration-time profiles measured behind reflected shock waves, a temperature independent rate constant of

$$k_1 = (7.1 \pm 2.7) \times 10^{12} \text{ cm}^3 \text{ mol}^{-1} \text{ s}^{-1}.$$

was obtained. The determined room temperature rate constant,

$$k_1 = 8.1_{-1.3}^{+2.0} \times 10^{12} \text{ cm}^3 \text{ mol}^{-1} \text{ s}^{-1},$$

was found to be in very good agreement with previous work and hence verifies the applied perturbation approach. The determined high temperature rate constant supports the rate expression given by Xu et al.¹⁷ and also the theoretical prediction that a quasi-direct abstraction pathway dominates the high temperature reaction.

The rate constant of reaction (2),



could also be measured for the first time at temperatures above 713 K. The room temperature rate constant,

$$k_2 = (3.1 \pm 1.2) \times 10^{13} \text{ cm}^3 \text{ mol}^{-1} \text{ s}^{-1},$$

and the inferred branching ratios were found to be in good agreement with previous work. At temper-

atures between 804 K < T < 1183 K, a temperature independent rate constant of

$$k_2 = (3.3 \pm 1.8) \times 10^{13} \text{ cm}^3 \text{ mol}^{-1} \text{ s}^{-1}$$

was determined. A more detailed evaluation of the measured HCO profiles supports a ratio $k_{2a}/k_{2c} \approx 5.6$. Moreover, the high temperature rate constant of reaction (7), OH + (CHO)₂, could be roughly determined to be $k_7 \approx 1.1 \times 10^{13} \text{ cm}^3 \text{ mol}^{-1} \text{ s}^{-1}$. Overall, in close agreement with the theoretical estimate, the measurements of the total rate constant k_2 indicate an essentially temperature independent reaction rate. We recommend the use of $k_2 = 3.2 \times 10^{13} \text{ cm}^3 \text{ mol}^{-1} \text{ s}^{-1}$ over the entire investigated temperature range of 295 K < T < 1183 K. In contrast to the reaction HCO + NO, no evidence for a significant contribution of a high temperature direct abstraction pathway was found.

Acknowledgement

This work was supported by the Deutsche Forschungsgemeinschaft. We acknowledge Prof. F. Temps for helpful discussions and H.-M. Berends for help with the labwork. We also thank Prof. A. Orr-Ewing and R. Dixon for making available high resolution line listings of HNO.

Electronic Supplementary Information. Tables of the Experimental Data and Conditions are available free of charge via the Internet at <http://www.rsc.org>.

Bibliography

- [1] K. A. Bhaskaran and P. Roth, The Shock Tube as a Wave Reactor for Kinetic Studies and Material Systems, *Prog. Energy Combust. Sci.* **2002**, 28, 151–192.
- [2] G. Friedrichs, J. T. Herbon, D. F. Davidson, and R. K. Hanson, Quantitative Detection of HCO Behind Shock Waves by Means of FM Spectroscopy, *Phys. Chem. Chem. Phys.* **2002**, 4, 5778–5788.
- [3] G. Friedrichs, D. F. Davidson, and R. K. Hanson, Validation of a Thermal Decomposition Mechanism of Formaldehyde by Detection of CH₂O and HCO behind Shock Waves, *Int. J. Chem. Kinet.* **2004**, 36, 157–169.
- [4] M. Colberg and G. Friedrichs, Room Temperature and Shock Tube Study of the Reaction HCO

- + O₂ Using the Photolysis of Glyoxal as an Efficient HCO Source, *J. Phys. Chem A* **2006**, *110*, 160–170.
- [5] G. Friedrichs, D. F. Davidson, and R. K. Hanson, Direct Measurements of the Reaction H + CH₂O → H₂ + HCO Behind Shock Waves by Means of vis-UV Detection of Formaldehyde, *Int. J. Chem. Kinet.* **2002**, *34*, 374–386.
- [6] V. Vasudevan, D. F. Davidson, R. K. Hanson, C. T. Bowman, and D. M. Golden, High-Temperature Measurements of the Rates of the Reactions CH₂O + Ar → Products and CH₂O + O₂ → Products, *Proc. Combust. Inst.* **2007**, *31*, 175–183.
- [7] V. Vasudevan, D. F. Davidson, and R. K. Hanson, Direct Measurements of the Reaction OH + CH₂O → HCO + H₂O at High Temperatures, *Int. J. Chem. Kinet.* **2005**, *37*, 98–109.
- [8] J. Warnatz, U. Maas, and R. W. Dibble, *Combustion*, Springer, Berlin/Heidelberg, 3. edition, **2001**.
- [9] J. A. Miller and C. T. Bowman, Mechanism and Modelling of Nitrogen Chemistry in Combustion, *Prog. Energy Combust. Sci.* **1989**, *15*, 287–338.
- [10] C. P. Fenimore, Studies of Fuel Nitrogen in Rich Flames, *Proc. Comb. Inst.* **1979**, *17*, 661–670.
- [11] L. V. Moskaleva and M. C. Lin, The Spin-Conserved Reaction CH + N₂ → H + NCN: A Major Pathway to Prompt NO Studied by Quantum/Statistical Theory Calculations and Kinetic Modeling of Rate Constant, *Proc. Comb. Inst.* **2000**, *28*, 2393–2401.
- [12] J. Wolfrum, Bildung von Stickstoffoxiden bei der Verbrennung, *Chemieingenieurtechnik* **1972**, *44*, 656–659.
- [13] P. C. Malte and D. T. Pratt, Measurement of Atomic Oxygen and Nitrogen Oxides in Jet-Stirred Combustion, *Proc. Comb. Inst.* **1974**, *15*, 1061.
- [14] P. Glarborg, M. U. Alzueta, K. Kjaergard, and K. Dam-Johansen, Oxidation of Formaldehyde and Its Interaction with Nitric Oxide in a Flow Reactor, *Combust. Flame* **2003**, *132*, 629–638.
- [15] J. D. DeSain, L. E. Jusinski, and C. A. Taatjes, Temperature Dependence and Deuterium Kinetic Isotope Effects in the HCO and NO Reaction, *J. Photochem. Photobiol. A* **2005**, *176*, 149–154.
- [16] R. S. Timonen, E. Ratajczak, and D. Gutman, Kinetics of the Reactions of the Formyl Radical with Oxygen, Nitrogen Dioxide Chlorine, and Bromine, *J. Phys. Chem.* **1988**, *92*, 651–655.
- [17] Z. F. Xu, C.-H. Hsu, and M. C. Lin, Ab Initio Kinetics of the Reaction of HCO with NO: Abstraction versus Association/Elimination Mechanism, *J. Chem. Phys.* **2005**, *122*, 234308/1–11.

- [18] Y. Guo, S. C. Smith, C. B. Moore, and C. F. Melius, Kinetics and Product Branching Ratios for the Reaction HCO + NO₂, *J. Phys. Chem.* **1995**, *99*, 7473–7481.
- [19] M. Klatt, *Quantitative Untersuchung der Bildung und des Verbrauchs von H- und O-Atomen sowie OH-Radikalen in verschiedenen Elementarreaktionen bei hohen Temperaturen.*, Ph.D. thesis, Universität Göttingen, **1991**.
- [20] J. V. Michael and J. W. Sutherland, The Thermodynamic State of the Hot Gas Behind Reflected Shock Waves: Implication to Chemical Kinetics, *Int. J. Chem. Kinet.* **1986**, *18*, 409–436.
- [21] M. Colberg and G. Friedrichs, Characterization of a Low-Pressure Shock Tube by Kinetic Measurements of the Thermal Decomposition of Ammonia and Methylamine, *to be published* .
- [22] G. Friedrichs, *Frequenzmodulierte Spektroskopie zur Untersuchung von Reaktionen des Amino- und Methylenradikals hinter Stoßwellen*, Cuvillier-Verlag, Göttingen, **1999**, ISBN 3-89712-741-5, Ph.D. thesis, Universität Göttingen.
- [23] R. Atkinson, D. L. Baulch, R. A. Cox, R. F. Hampson, J. A. Kerr, M. J. Rossi, and J. Troe, IUPAC Subcommittee on Gas Kinetic Data Evaluation for Atmospheric Chemistry, *J. Chem. Phys. Ref. Data* **1997**, *26*, 1329–1499.
- [24] G. Friedrichs and H. Gg. Wagner, Quantitative FM Spectroscopy at High Temperatures: The Detection of ¹CH₂ Behind Shock Waves, *Z. Phys. Chem.* **2000**, *214*, 1723–1746.
- [25] J. E. Flad, S. S. Brown, J. B. Burkholder, H. Stark, and A. R. Ravishankara, Absorption Cross Sections for the $\tilde{A}^2A''(0, 9^0, 0) \leftarrow \tilde{X}^2A'(0, 0^1, 0)$ Band of the HCO Radical, *Phys. Chem. Chem. Phys.* **2006**, *8*, 3636–3642.
- [26] R. J. Kee, F. M. Ruply, and J. A. Miller, Chemkin-II: A Fortran Chemical Kinetics Package for the Analysis of Gas Phase Chemical Kinetics, Sandia report sand89-8009, Sandia National Laboratories, Livermore, CA, **1989**.
- [27] A. A. Konnov, *Detailed reaction mechanism for small hydrocarbons combustion. Release 0.5*, **2000**, <http://homepages.vub.ac.be/~akonnov>.
- [28] M. Frenkel, *Thermodynamics of Organic Compounds in the Gas State*, Thermodynamics Research Center, College Station, TX, **1994**.
- [29] L. Zhu, D. Kellis, and C.-F. Ding, Photolysis of Glyoxal at 193, 248, 308 and 351 nm, *Chem. Phys. Lett.* **1996**, *257*, 487–491.
- [30] J. J. Orlando and G. S. Tyndall, The Atmospheric Chemistry of the HC(O)CO Radical, *Int. J. Chem. Kinet.* **2001**, *33*, 149–156.

- [31] R. C. Millikan and D. R. White, Systematics of Vibrational Relaxation, *J. Chem. Phys.* **1963**, *39*, 3209–3213.
- [32] G. P. Smith, D. M. Golden, M. Frenklach, N. W. Moriarty, B. Eiteneer, M. Goldenberg, C. T. Bowman, R. K. Hanson, S. Song, W. C. G. Jr., V. V. Lissanski, and Z. Qin, GRI-MECH 3.0, http://www.me.berkeley.edu/gri_mech/.
- [33] B. A. Thompson, P. Harteck, and R. R. R. Jr., Ultraviolet Absorption Coefficients of CO₂, CO, H₂O, N₂O, NH₃, NO, SO₂, and CH₄ Between 1850 and 4000 Å, *J. Geophys. Res.* **1963**, *68*, 6431–3436.
- [34] J. L. Bancroft, J. M. Hollas, and D. A. Ramsay, The Absorption Spectra of HNO and DNO, *Can. J. Phys.* **1962**, *40*, 322–347.
- [35] R. N. Dixon and C. A. Rosser, The Characterization of the Complete Set of Bound Vibronic States of HNO in its Excited \tilde{A}^1A' Electronic State, *J. Mol. Spectrosc.* **1985**, *110*, 262–276.
- [36] J. Pearson, A. J. Orr-Ewing, M. N. R. Ashfold, and R. N. Dixon, Spectroscopy and Predissociation Dynamics of the $^1A'$ State of HNO, *J. Chem. Phys.* **1997**, *106*, 5850–5873.
- [37] M. Colberg, *Aufbau und Charakterisierung einer Stoßwellenapparatur zur Untersuchung von Hochtemperaturreaktionen des Formylradikals*, Ph.D. thesis, Universität Kiel, **2006**.
- [38] F. Temps and H. Gg. Wagner, Kinetics of the Reaction of HCO with HCO and O₂, *Ber. Bunsenges. Phys. Chem.* **1984**, *88*, 410–414.
- [39] E. A. Irdam, J. H. Kiefer, L. B. Harding, and A. F. Wagner, The Formaldehyde Decomposition Chain Mechanism, *Int. J. Chem. Kinet.* **1993**, *25*, 285–303.
- [40] W. Tsang and J. T. Herron, Chemical Kinetic Data Base for Propellant Combustion I. Reactions Involving Nitrogen Oxides (NO, NO₂, and N₂O), Nitrosyl Hydride, Nitrous and Hydrocyanic Acid, *J. Phys. Chem. Ref. Data* **1991**, *20*.
- [41] Z. F. Xu and M. C. Lin, A Computational Study of the Kinetics and Mechanism for the Reaction of HCO with HNO, *Int. J. Chem. Kinet.* **2004**, *36*, 205–215.
- [42] C. N. Plum, E. Sanhueza, R. Atkinson, W. P. L. Carter, and J. N. Pitts Jr., Hydroxyl Radical Rate Constants and Photolysis Rates of α -Dicarbonyls, *Environ. Sci. Technol.* **1983**, *17*, 479–484.
- [43] P. H. Wine, N. M. Kreutter, and A. R. Ravishankara, Flash Photolysis-Resonance Fluorescence Kinetics Study of the Reaction OH + NO₂ + M → HNO₃ + M, *J. Phys. Chem.* **1979**, *83*, 3191–3195.
- [44] F. Temps and H. Gg. Wagner, Rate Constants of the Reactions of OH Radicals with CH₂O and HCO, *Ber. Bunsenges. Phys. Chem.* **1984**, *88*, 415–418.

- [45] K. Saito, T. Kakumoto, and I. Murakami, Thermal Unimolecular Decomposition of Glyoxal, *J. Phys. Chem.* **1984**, 88, 1182–1187.
- [46] G. Friedrichs, M. Colberg, J. Dammeier, T. Bentz, and M. Olzmann, HCO Formation in the Thermal Unimolecular Decomposition of Glyoxal: Rotational and Weak Collision Effects, *Phys. Chem. Chem. Phys.* **2008**, 10, 6520–6533.
- [47] E. W. Diau, M. J. Halbgewachs, A. R. Smith, and M. C. Lin, Thermal Reduction of NO by H₂: Kinetic Measurement and Computer Modeling of the HNO + NO Reaction, *Int. J. Chem. Kinet.* **1995**, 27, 867–881.
- [48] T. Ko and A. Fontijn, High-Temperature Photochemistry Kinetics Study of the Reaction Hydrogen Atom + Nitrogen Dioxide → Hydroxyl + Nitric Oxide from 296 to 760 K, *J. Phys. Chem.* **1991**, 95, 3984–3987.
- [49] C. J. Howard, Kinetic Study of the Equilibrium HO₂ + NO = OH + NO₂ and the Thermochemistry of HO₂, *J. Am. Chem. Soc.* **1980**, 102, 6937–6941.
- [50] C.-Y. Lin, H.-T. Wang, M. C. Lin, and C. F. Melius, A Shock Tube Study of the CH₂O + NO₂ Reaction at High Temperatures, *Int. J. Chem. Kinet.* **1990**, 22, 455–482.
- [51] Y. Ninomiya, M. Goto, S. Hashimoto, Y. Kagawa, K. Yoshizawa, M. Kawasaki, T. J. Wallington, and M. D. Hurley, Cavity Ring-Down Spectroscopy and Relative Rate Study of Reactions of HCO Radicals with O₂, NO, NO₂ and Cl₂ at 295 K, *J. Phys. Chem. A* **2000**, 104, 7556–7564.
- [52] A. O. Langford and C. B. Moore, Reaction and Relaxation of Vibrationally Excited Formyl Radicals, *J. Chem. Phys. A* **1984**, 80, 4204–4210.
- [53] O. M. Sarkisov, S. Cheskis, V. A. Nadtochenko, E. A. Sviridenkov, and V. I. Vedeneev, Spectroscopic Study of Elementary Reactions Involving Oxomethyl, Amidogen, and Nitrosyl Hydride, *Arch. Comb.* **1984**, 4, 111–120.
- [54] J. P. Reilly, J. H. Clark, C. B. Moore, and G. C. Pimentel, HCO Production, Vibrational Relaxation, Chemical Kinetics, and Spectroscopy Following Laser Photolysis of Formaldehyde, *J. Chem. Phys.* **1978**, 69, 4381–4394.
- [55] K. Shibuya, T. Ebata, K. Obi, and I. Tanaka, Rate Constant Measurements for the Reactions of HCO with NO and O₂ in the Gas Phase, *J. Phys. Chem.* **1977**, 81, 2292–2294.
- [56] B. Veyret and R. Lesclaux, Absolute Rate constants for the Reactions of HCO with O₂ and NO from 298 to 503 K, *J. Phys. Chem.* **1981**, 85, 1919.
- [57] S. A. Kulkarni and N. Koga, Ab Initio and Density Functional Investigation of Reactions of NO with XCO (X=H, F, Cl), *J. Phys. Chem. A* **1998**, 102, 5228–5235.

- [58] B. M. Morrison Jr. and J. Heicklen, The Reactions of HO with CH₂O and of HCO with NO₂, *J. Photochem.* **1980**, *13*, 189–199.
- [59] B. M. Morrison Jr. and J. Heicklen, The Free Radical Oxidation of CH₂O in the Presence of NO₂ and NO, *J. Photochem.* **1981**, *15*, 131–145.
- [60] S. Meyer and F. Temps, An FTIR Product Study of the Reaction Between HCO and NO₂, *Int. J. Chem. Kinet.* **1998**, *32*, 136–145.
- [61] K. T. Rim and J. F. Hershberger, Product Branching Ratio of the HCO + NO₂ Reaction, *J. Phys. Chem. A* **1998**, *102*, 5898–5902.
- [62] Y. He, E. Kolby, P. Shumaker, and M. C. Lin, Thermal Reaction of CH₂O with NO₂ in the Temperature Range of 393–476 K: FTIR Product Measurement and Kinetic Modeling, *Int. J. Chem. Kinet.* **1989**, *21*, 1015–1027.
- [63] N. I. Butkovskaya and D. W. Setser, Infrared Chemiluminescence Study of the Reactions of Hydroxyl Radicals with Formaldehyde and Formyl Radicals with H, OH, NO, NO₂, *J. Phys. Chem. A* **1998**, *102*, 9715–9728.
- [64] F. Sun, G. P. Glass, and R. F. Curl, The photolysis of NO₂ at 193 nm, *Chem. Phys. Lett.* **2001**, *337*, 72–78.
- [65] J. A. Davidson, C. A. Cantrell, A. H. McDaniel, R. E. Shetter, S. Madronich, and J. G. Calvert, Visible-Ultraviolet Absorption Cross Sections for NO₂ as a Function of Temperature, *J. Geophys. Res.* **1988**, *93*, 7105–7112.

7.7 Supporting information

Table 1: Shock tube experiments for the determination of the rate constant of reaction (1), HCO + NO. Units are mbar, K, ppm, cm, mol, and s.

p	T	$x_0((\text{CHO})_2)$	$x_0(\text{NO})$	$x(\text{HCO})$	$x(\text{H})$	k_1
1000	845	5275	1570	28	70	7.0×10^{12}
1031	859	5275	1570	68	197	5.0×10^{12}
1058	875	5375	1575	34	92	7.0×10^{12}
1095	886	5275	1570	32	93	7.0×10^{12}
1799	1173	3685	1425	60	193	9.0×10^{12}
910	806	5300	2705	58	165	6.0×10^{12}
1167	918	5300	2705	59	173	6.5×10^{12}
1285	983	5300	2705	75	223	5.0×10^{12}
1480	1053	5300	2705	68	205	6.0×10^{12}
1805	1173	4595	2445	70	201	1.3×10^{13}
1015	854	4965	4990	42	121	7.0×10^{12}
1135	906	4965	4990	40	117	7.0×10^{12}
1306	983	4965	4990	100	298	4.0×10^{12}
1547	1041	4965	4990	45	137	7.0×10^{12}
1505	1058	4965	4990	40	120	5.0×10^{12}
1351	1128	10315	4660	150	441	6.0×10^{12}
1819	1179	4505	4880	90	268	6.0×10^{12}
1427	1274	8620	4385	180	559	7.5×10^{12}
1191	1274	8680	4400	160	445	1.3×10^{13}
900	793	10065	2925	105	298	7.0×10^{12}
1060	861	10065	2925	150	437	9.0×10^{12}
1246	938	10560	3010	190	564	6.5×10^{12}
1345	979	10065	2925	65	194	7.5×10^{12}
1917	1182	6385	2375	190	595	9.0×10^{12}
852	769	10315	4930	83	233	8.0×10^{12}
1110	883	10315	4930	80	234	4.5×10^{12}
1436	1013	10315	5085	155	467	6.8×10^{12}
1130	905	2525	1230	18	53	6.5×10^{12}
1606	1078	10365	4570	160	486	6.0×10^{12}
1755	1143	7840	4200	200	601	7.0×10^{12}
1883	1208	4085	1420	90	251	8.0×10^{12}
1330	1220	9710	4550	180	534	6.0×10^{12}
1350	1248	6360	6150	190	568	7.0×10^{12}
1426	1272	8670	4420	220	674	9.0×10^{12}
1242	1307	7980	4375	220	671	1.2×10^{13}

7. Kinetics of the Reactions HCO + NO and HCO + NO₂

Table 2: Shock tube experiments for the determination of the rate constant of reaction (2), HCO + NO₂. Units are mbar, K, ppm, cm, mol, and s.

p	T	$x_0((\text{CHO})_2)$	$x_0(\text{NO}_2)$	$x(\text{HCO})$	$x(\text{H})$	k_2
917	809	5290	1068	40	114	2.5×10^{13}
1141	908	5290	1060	58	170	3.5×10^{13}
1227	952	5290	1060	43	127	3.0×10^{13}
1288	971	5295	1060	53	157	3.0×10^{13}
1297	1041	5010	1047	70	207	3.3×10^{13}
1414	1183	4760	900	90	228	2.0×10^{13}
937	819	4995	2440	35	38	3.0×10^{13}
1146	910	4995	2440	40	117	4.0×10^{13}
1399	1016	4995	2440	75	225	3.0×10^{13}
1437	1099	5995	2965	100	263	4.2×10^{13}
1434	1186	5680	2715	120	286	3.8×10^{13}
925	804	10220	1350	53	151	3.0×10^{13}
999	836	10220	1350	50	144	3.0×10^{13}
1109	883	10220	1350	60	176	3.0×10^{13}
1110	884	10220	1350	70	205	5.0×10^{13}
1137	894	10220	1350	65	191	4.0×10^{13}
1247	940	10220	1350	48	143	4.0×10^{13}
1266	948	10220	1350	110	328	4.0×10^{13}
1251	1004	10435	1075	90	265	2.5×10^{13}

Table 3: Room temperature experiments for the determination of the rate constant of reaction (1), HCO + NO. Units are ppm, cm, mol, and s.
 $p = 51$ mbar, $T = 295$ K.

No.	$x_0((\text{CHO})_2)$	$x_0(\text{NO})$	$x(\text{HCO})$	$x(\text{HCO}^*)$	$x(\text{H})$	k_1
1	5376	0	4.8	11.2	33.6	-
2	5364	533	4.2	9.8	29.4	$(4.5 \times 10^{12})^a$
3	5335	1058	4.05	9.45	28.3	8.0×10^{12}
4	5305	2128	3.9	9.1	27.3	8.0×10^{12}
5	5305	2128	3.9	9.1	27.3	8.0×10^{12}
6	5335	1058	3.81	8.89	26.7	8.0×10^{12}
7	5364	533	3.9	9.1	27.3	8.5×10^{12}
8	5376	0	4.05	9.45	27.0	-

^a This measurement, in particular with regard to the result of a second measurement using the same mixture composition (No. 7), was identified as an outlier and was excluded from averaging.

Table 4: Room temperature experiments for the determination of the rate constant of reaction (2), HCO + NO₂. Units are ppm, cm, mol, and s.
 $p = 50$ mbar, $T = 295$ K.

$x_0((\text{CHO})_2)$	$x_0(\text{NO})$	$x(\text{HCO})$	$x(\text{HCO}^*)$	$x(\text{H})$	k_{2a}	k_{2c}	k_{2d}	k_2
4989	0	1.58	3.68	12.65	-	-	-	-
5020	259	1.86	4.34	13.64	1.23×10^{13}	8.75×10^{12}	1.40×10^{13}	3.51×10^{13}
5058	508	1.62	3.78	11.88	9.60×10^{12}	8.75×10^{12}	1.10×10^{13}	2.75×10^{13}
5041	1024	1.35	3.15	9.9	1.05×10^{13}	7.50×10^{12}	1.20×10^{13}	3.00×10^{13}
5041	1024	1.35	3.15	9.9	1.05×10^{13}	7.50×10^{12}	1.20×10^{13}	3.00×10^{13}
5058	508	1.28	2.98	9.35	9.45×10^{12}	6.75×10^{12}	1.08×10^{13}	2.70×10^{13}
5020	259	1.35	3.15	9.9	1.26×10^{13}	9.00×10^{12}	1.44×10^{13}	3.60×10^{13}

Table 5: Evaluation of the channel branching ratio k_{2a}/k_{2c} and the rate constant of reaction (7), OH + (CHO)₂. Units are mbar, K, ppm, cm, mol, and s.

p	T	$x_0((\text{CHO})_2)$	$x_0(\text{NO}_2)$	$x(\text{HCO})$	$x(\text{H})$	$k(2a)$	$k(2c)$	$k(7)$
1287	971	5295	1060	53	157	2.5×10^{13}	(0) ¹	1.0×10^{13}
1227	952	5290	1060	40	118	2.9×10^{13}	1.5×10^{12}	1.3×10^{13}
1141	908	5290	1060	58	170	4.0×10^{13}	5.3×10^{12}	1.5×10^{13}
917	809	5290	1068	46	131	1.8×10^{13}	2.0×10^{12}	9.0×10^{12}
1251	1004	10435	1075	90	265	2.5×10^{13}	1.8×10^{12}	1.5×10^{13}
1399	1016	4995	2440	72	216	2.5×10^{13}	4.5×10^{12}	1.2×10^{13}
1146	910	4995	2440	43	126	4.0×10^{13}	8.0×10^{12}	1.6×10^{13}
937	819	4995	2440	35	38	1.8×10^{13}	$(4.5 \times 10^{13})^1$	8.0×10^{12}
1266	948	10220	1350	110	328	3.0×10^{13}	6.0×10^{12}	1.5×10^{13}
1248	940	10220	1350	57	170	3.0×10^{13}	8.0×10^{12}	8.0×10^{12}
1137	894	10220	1350	90	265	4.0×10^{13}	1.0×10^{13}	7.0×10^{12}
1109	889	10220	1350	85	294	4.8×10^{13}	3.8×10^{12}	8.0×10^{12}
999	836	10220	1350	65	187	3.5×10^{13}	7.5×10^{12}	8.0×10^{12}
925	804	10220	1350	60	171	2.0×10^{13}	6.5×10^{12}	8.0×10^{12}
					∅	3.02×10^{13}	5.41×10^{12}	

¹ For two measurements, probably due to slight baseline inaccuracies, it was not possible to extract meaningful rate constant values for k_{2c} . For the sake of completeness, the best fit values are reported but have been excluded from averaging.

Table 6: Summary of MP2/6-31G(d) calculation results for estimation of interconversion barrier between O₂N-CHO and ONO-CHO association complexes (see Figure 6). Cartesian coordinates (10⁻¹⁰ m), frequencies (cm⁻¹), and energies (Hartree).

O ₂ N-CHO	
C	-0.853641, -0.576263, -0.000003
O	-1.836310, 0.106776, -0.000002
H	-0.764244, -1.671233, 0.000033
O	1.470273, -0.785180, -0.000002
N	0.544550, 0.045296, 0.000000
O	0.625317, 1.279872, 0.000003
$\tilde{\nu}_i$	111.2, 299.6, 501.4, 550.2, 753.3, 899.2, 989.8, 1328.2, 1349.2, 1824.1, 1843.1, 3143.4
MP2 energy	-318.1789115
zero point energy	0.0309666
ONO-CHO	
C	1.307582, 0.390106, -0.000039
O	1.719961, -0.750790, 0.000007
H	1.949297, 1.286453, 0.000026
O	0.010806, 0.799998, 0.000022
N	-0.995017, -0.483589, 0.000016
O	-2.084476, -0.079454, -0.000016
$\tilde{\nu}_i$	76.3, 211.7, 214.4, 348.5, 564.6, 857.5, 1040.6, 1139.7, 1423.7, 1786.9, 1834.6, 3088.0
MP2 energy	-318.1986282
zero point energy	0.0286745
interconversion barrier	
C	-1.044695, 0.036024, 0.406279
O	-1.827773, -0.459225, -0.327823
H	-1.083366, 0.382383, 1.434030
O	0.304692, 1.046657, -0.233764
N	0.698546, -0.135439, 0.159022
O	1.830794, -0.543739, -0.061521
$\tilde{\nu}_i$	-470.8, 198.5, 386.8, 462.7, 643.2, 752.1, 902.6, 1249.1, 1311.3, 1563.2, 1911.2, 3282.8
MP2 energy	-318.1325476
zero point energy	0.02885

8 Summary and outlook

Difference laser absorption. A new difference amplification laser absorption (DLA) spectrometer has been set up. With this spectrometer it was possible to detect singlet ^1NCN and triplet ^3NCN cyanonitrene radicals in a sensitive ($(\alpha cl)_{\min} = 5 \times 10^{-4}$ @ 1.4 MHz) and quantitative manner. Temperature dependent ^3NCN absorption cross sections of the superposition of the $^3\Pi_1$ subband of the $\tilde{A}^3\Pi_u(000) - \tilde{X}^3\Sigma_g(000)$ transition of the vibrational ground state and the Q_1 band head of the $^3\Sigma^+ - ^3\Pi$ sub-band of the $\tilde{A}^3\Pi_u(010) - \tilde{X}^3\Sigma_g^-(010)$ vibrationally hot Renner-Teller split transition have been determined. Kinetic measurements have been performed at the absorption maximum at $\tilde{\nu} = 30383.11 \text{ cm}^{-1}$. Furthermore, temperature dependent ^1NCN absorption cross sections of the unresolved band head of the $^1\Pi_u(000) - ^1\Delta_g(000)$ transition around $\tilde{\nu} \approx 30045.5 \text{ cm}^{-1}$ have been extracted from high temperature shock tube experiments. At combustion relevant temperatures both absorption cross sections are on the same order of magnitude, thus making possible the investigation of ^1NCN and ^3NCN reactions under similar experimental conditions. It is worth mentioning that these data represent the first directly measured absorption cross sections and high temperature spectra of ^3NCN and ^1NCN . Based on the ^3NCN data, quantitative measurements of NCN concentrations in flames will be possible and, in fact, have already been performed (Klein-Douwel *et al.*, *Combust. Flame*. **2011**, 158, 2090–2104).

NCN₃ decomposition and collision-induced intersystem crossing of NCN. The thermal decomposition of cyanogen azide (NCN₃) has been investigated in order to evaluate the suitability of NCN₃ as an NCN precursor molecule. NCN₃ is explosive, nevertheless, a safe synthesis procedure yielding NCN₃ in very high purities > 99% could be established. It turned out that the pyrolysis of NCN₃ yields stable NCN plateau concentrations by the reaction $\text{NCN}_3 + \text{M} \rightarrow \text{NCN} + \text{N}_2 + \text{M}$ without interfering by-products. This fact reveals that NCN₃ is an almost ideal NCN precursor. The direct product of the NCN₃ pyrolysis is the excited ^1NCN which subsequently undergoes a collision-induced intersystem crossing (CIISC) process to the ^3NCN ground state. From a combination of measured ^1NCN and ^3NCN concentration time profiles behind shock waves, rate constants of the unimolecular NCN₃ decomposition and CIISC rate constants have been extracted. In the investigated pressure and temperature range, the CIISC process is surprisingly slow making possible the quantitative investigation of this electronic relaxation process even behind shock waves. As the thermal NCN₃ decomposition exhibits a much larger temperature dependence than the CIISC, the rate limiting step for the ^3NCN appearance switches from the NCN₃ decomposition at low temperatures to the CIISC at higher tem-

peratures.

³NCN reactions. A consistent ³NCN mechanism has been set up by measuring ³NCN concentration-time profiles following the pyrolysis of NCN₃ behind shock waves. Studies over a wide range of temperatures, total densities and initial NCN₃ concentrations allowed for the determination of the rate constants of the reactions $\text{NCN} + \text{M} \rightarrow \text{C} + \text{N}_2 + \text{M}$ and $\text{NCN} + \text{NCN} \rightarrow 2 \text{CN} + \text{N}_2$. Whereas the reaction $\text{NCN} + \text{NCN}$ has never been addressed before, rate constants of the reaction $\text{NCN} + \text{M}$ are in very good agreement with previous work. Subsequently, the pyrolysis of N₂O has been used as an O atom source to measure rate constants of the reaction $\text{NCN} + \text{O} \rightarrow \text{CN} + \text{NO}$. This reaction is very fast and thus constitutes one of the most important NCN consuming and NO forming reactions. In fact, the measurements reported in this thesis represent the first experimental determination of the rate constants of this key reaction. Furthermore, the rate constants of the reactions $\text{NCN} + \text{NO} \rightarrow \text{CN} + \text{N}_2\text{O}$ and $\text{NCN} + \text{NO}_2 \rightarrow \text{NCNO} + \text{NO}$ have been directly measured by time-resolved detection of NCN following the shock heating of mixtures of NCN₃ and NO or NO₂, respectively. Both reactions are supposed to be dominated by an association-like reaction channel at low temperatures and an alternative abstraction channel at high temperatures. Hence, the temperature dependence is expected to be negative at low and positive at high temperatures. Therefore, low temperature data cannot be extrapolated to combustion relevant temperatures. In this work, the first measurements of reaction rate constants at combustion relevant high temperatures are reported. Whereas in both cases the expected overall temperature dependence and thus the switching of the reaction channels could be experimentally proved, rate constant expressions measured in this work deviate from the theoretically predicted data by up to a factor of three.

HCO reactions. The sensitive time-resolved detection of HCO by means of frequency modulation (FM) spectroscopy, rendered possible the determination of the rate constants of the reactions $\text{HCO} + \text{NO} \rightarrow \text{HNO} + \text{CO}$ and $\text{HCO} + \text{NO}_2 \rightarrow \text{products}$ at room temperature and at high temperatures behind shock waves. Moreover, in an iterative fitting procedure, product branching ratios of the reaction $\text{HCO} + \text{NO}_2$ have been worked out showing that $\text{OH} + \text{CO} + \text{NO}$ are the main products of this reaction at room temperature, whereas the products $\text{H} + \text{CO}_2 + \text{NO}$ constitute the most important reaction channel at high temperatures around $T \approx 1000 \text{ K}$.

Outlook. The established mechanism of the NCN₃ decomposition, singlet-triplet relaxation of NCN (CIISC) and the NCN consumption by the reactions $\text{NCN} + \text{M}$ and $\text{NCN} + \text{NCN}$ together with the determined absolute absorption cross-sections of both ¹NCN and ³NCN opens the door to all kinds of kinetic NCN studies. In this spirit, measurements of the rate constants of the very important reactions $\text{NCN} + \text{H}$ and $\text{NCN} + \text{O}_2$ as well as the reaction $\text{NCN} + \text{H}_2$ are already underway in our workgroup. These measurements rely on the absorption (DLA) spectrometer, which has been set up during this thesis and the new driver gas mixing system, which enhances the reproducibility of the shock tube experiments. The determined spectroscopic properties and absorption cross-sections of NCN can also be useful for the quantitative detection of NCN in flames, exhaust fumes or combustion engines. Such

types of experiments are often used to analyse combustion processes and will in turn help to develop NO_x reduction strategies. In this spirit, also the reported rate constant expressions will find their way into widely used mechanistic models, soon.

Conclusion. The rate constants of several reactions important for the formation of nitrogen oxides in combustion processes have been measured at combustion relevant temperatures for the first time. Combined with subsequent work, which has been made possible by the results of this thesis and which is already underway, a complete set of high temperature NCN reaction rate constants will be available, soon. Together with the NO_x reactions with HCO, these data contribute to an advanced understanding of *prompt*-NO formation in combustion processes.

Danksagung

- Bei meinem hochverehrten Lehrer Prof. Dr. Gernot Friedrichs möchte ich mich für die ausgesprochen gute Betreuung sehr herzlich bedanken. Ich danke außerdem für die Möglichkeit, mit tollen experimentellen Methoden ein aktuelles Thema bearbeiten zu dürfen.
- Prof. Dr. Friedrich Temps danke ich für seine Unterstützung während meiner Diplomanden- und Doktorandenzeit.
- Besonders möchte ich mich bei meinen Praktikantinnen, Staatsexamenskandidaten und Diplomandinnen bedanken: Julia Bock, Nancy Faßheber und Benjamin Oden haben durch Fleiß und Geschick zum Gelingen dieser Arbeit beigetragen.
- Ich danke den Steuerzahlern der Bundesrepublik Deutschland (DFG) und des Landes Schleswig-Holstein (Uni Kiel) für die Finanzierung aller für diese Arbeit nötigen Ausgaben.
- Mark Colberg hat mir alles über Stoßrohre beigebracht und mich ins Institut gelockt. Ohne ihn wäre diese Arbeit nicht geschrieben worden.
- Auf diversen Tagungen und auch am Telefon durfte ich häufig und lange mit Anna Busch und Claudia Kappler (Karlsruher Institut für Technologie) über die verschiedenen Probleme der Cyanonitrenchemie diskutieren. Auch dafür bin ich dankbar.
- Dr. Joachim Gripp bin ich wegen seiner zahllosen Ratschläge und seiner großen Hilfsbereitschaft zu Dank verpflichtet.
- Meister Will, Frank Herzog, Frank Laasch, Andreas Sievers und Olaf Wendt danke ich dafür, meine Fehler ausgebügelt zu haben. Ich möchte mich auch herzlich bei Klaus Will und Michael Carstens für ihre Hilfe bedanken.
- Allen Mitgliedern der Arbeitskreise Friedrichs, Temps und Grottemeyer, besonders meinen Bürokollegen Eike, Carsten und Nancy danke ich für die angenehme Atmosphäre in der Ludwig-Meyn-Str. 8.
- Nancy Faßheber danke ich außerdem für's korrigieren v. A. des Literaturverzeichnisses.
- Ich danke meinen Freunden Katharina, Jan-Hendrik, Jan, Björn, Friedi und Christian, Ameli und Ron, René und Kristina, Julia und Alex, Alex und Tobias für Schweden, Bullerbü, Wittensee, Strongbow's, die Dänische Südsee, Leuchtturm Kiel, etc.
- Meiner Freundin Mina danke ich für ihre Unterstützung und Geduld.
- Bei meinen Eltern und Geschwistern und dem Rest meiner Familie bedanke ich mich für die Sicherheit, mich immer auf sie verlassen zu können.
- Ausdrücklich danke ich dem 1. FC Köln dafür, mehrere Jahre hintereinander nicht abgestiegen zu sein.

Hiermit erkläre ich an Eides Statt, dass die vorliegende Abhandlung - abgesehen von der Beratung durch meinen Betreuer Herrn Prof. Dr. G. Friedrichs - nach Inhalt und Form meine eigene Arbeit ist. Diese Arbeit hat weder in Auszügen noch in ganzer Form einer anderen Stelle im Rahmen eines Prüfungsverfahrens vorgelegen. Sie wurde in ihrer Gesamtheit nicht veröffentlicht und auch nicht zur Veröffentlichung eingereicht. Die Arbeit ist unter Einhaltung der Regeln guter wissenschaftlicher Praxis der Deutschen Forschungsgemeinschaft entstanden.

Johannes Dammeier

Personal data

Name: Johannes Michael Dammeier
Nationality: German
Date and place of birth: 26.04.1981, Cologne
Address: Schauenburgerstraße 39, 24105 Kiel

Education

since 2006: Doctoral candidate on the topic *combustion kinetics*
in the group of Prof. Dr. Gernot Friedrichs, Kiel University
2001 – 2006: Chemistry studies at Kiel University,
optional subject: theoretical chemistry
2000 – 2001: Community service as a paramedic
1991 – 2000: Grammar school: Otto-Hahn-Gymnasium, Bergisch Gladbach

Publications

- J. Dammeier, M. Colberg, and G. Friedrichs, Wide temperature range ($T = 295$ K and $770 - 1305$ K) study of the kinetics of the reactions $\text{HCO} + \text{NO}$ and $\text{HCO} + \text{NO}_2$ using frequency modulation spectroscopy, *Phys. Chem. Chem. Phys.* **2007**, *9*, 4177 – 4188.
- G. Friedrichs, M. Colberg, J. Dammeier, T. Bentz, and M. Olzmann, HCO Formation in the Thermal Unimolecular Decomposition of Glyoxal: Rotational and Weak Collision Effects, *Phys. Chem. Chem. Phys.* **2008**, *10*, 6250 – 6533.
- J. Dammeier and G. Friedrichs, Thermal Decomposition of NCN_3 as a High-Temperature NCN Radical Source: Singlet-Triplet Relaxation and Absorption Cross Section of $\text{NCN}(^3\Sigma)$, *J. Phys. Chem. A* **2010**, *114*, 12963 – 12971.
- J. Dammeier, N. Faßheber, and G. Friedrichs, Direct Measurements of the High Temperature Rate Constants of the Reactions $\text{NCN} + \text{O}$, $\text{NCN} + \text{NCN}$, and $\text{NCN} + \text{M}$, *Phys. Chem. Chem. Phys.* **2011**, DOI: 10.1039/C1CP22123J.
- J. Dammeier, B. Oden, and G. Friedrichs, A Consistent Model for the Thermal Decomposition of NCN_3 and the Singlet-Triplet Relaxation of NCN, *J. Phys. Chem. A* **2011**, submitted.
- J. Dammeier and G. Friedrichs, Direct Measurements of the Rate Constants of the Reactions $\text{NCN} + \text{NO}$ and $\text{NCN} + \text{NO}_2$ Behind Shock Waves, *Int. J. Chem. Kinet.* **2011**, submitted.

Presentations

- G. Friedrichs, J. Dammeier, and N. Faßheber, Shock Tube Study on the Reactions $\text{NCN} + \text{H}$ and $\text{NCN} + \text{O}$, talk, 7th International Conference on Chemical Kinetics, MIT, Cambridge, USA, July 2011.
- N. Faßheber, J. Dammeier, and G. Friedrichs, Experimental Study on the Reactions $\text{NCN} + \text{NO}$ and $\text{NCN} + \text{NO}_2$ Behind Shock Waves, poster, annual meeting of the German Bunsen Society of Physical Chemistry, Berlin, Germany, June 2011.
- J. Dammeier and G. Friedrichs, Investigating NCN Reactions Behind Shock Waves, poster, 33rd Symp. (Int.) on Combustion, Beijing, China, August 2010.
- J. Dammeier and G. Friedrichs, Cyanogen Azide as a High Temperature NCN Radical Source, poster, 30th International Symposium on Free Radicals, Savonlinna, Finland, July 2009.
- J. Dammeier and G. Friedrichs, The Thermal Decomposition of Cyanogen Azide as a High Temperature Source of NCN Radicals, poster, annual meeting of the German Bunsen Society of Physical Chemistry, Cologne, Germany, May 2009.
- G. Friedrichs, M. Colberg, J. Dammeier, T. Bentz, and M. Olzmann, Unimolecular Decomposition of Glyoxal: Shock Tube Experiments and Modeling, talk, annual meeting of the German Bunsen Society of Physical Chemistry, Graz, Austria, May 2007.
- J. Dammeier and G. Friedrichs, Consistent Modeling of the Reaction $\text{HCO} + \text{NO}_2$ over a Wide Temperature Range, poster, annual meeting of the German Bunsen Society of Physical Chemistry, Graz, Austria, May 2007.
- G. Friedrichs, M. Colberg, J. Dammeier, T. Bentz, and M. Olzmann, The HCO -Forming Decomposition Channel of Glyoxal, talk, Int. Workshop on Gas Kinetics, SFB (CRC) 606, Karlsruhe, Germany, November 2006.
- G. Friedrichs, H.-M. Berends, M. Colberg, and J. Dammeier, Shock Tube Study of the Reactions $\text{HCO} + \text{NO}$ and $\text{HCO} + \text{NO}_2$ Using Frequency Modulation Detection of HCO , talk, 31th Symp. (Int.) on Combustion, Heidelberg, Germany, August 2006.
- J. Dammeier and G. Friedrichs, High Temperature Study of the Reaction $\text{HCO} + \text{NO}$ using Frequency Modulation Spectroscopy behind Shock Waves, talk, 1st European Chemistry Congress, Budapest, Hungary, August 2006.